NASA CR-72393

S-F-D Report 54003-F

ANALYTIC DESIGN OF SPACEBORNE AXIAL INJECTION CROSSED-FIELD AMPLIFIERS

by

G. Bernstein

W. C. Sylvernal

Prepared for

National Aeronautics and Space Administration

Contract NAS3-11516

Technical Management
NASA Lewis Research Center
Cleveland, Ohio
Special Projects Office
Peter Ramins

S-F-D laboratories, inc.
Subsidiary of Varian Associates
800 Rahway Avenue
Union, New Jersey

FINAL REPORT

ANALYTIC DESIGN OF SPACEBORNE AXIAL INJECTION CROSSED-FIELD AMPLIFIERS

by

G. Bernstein
W. C. Sylvernal

Prepared for

National Aeronautics and Space Administration

30 September 1968

Contract NAS3-11516

Technical Management
NASA Lewis Research Center
Cleveland, Ohio
Special Projects Office
Peter Ramins

S-F-D laboratories, inc.
Subsidiary of Varian Associates
800 Rahway Avenue
Union, New Jersey

FOREWORD

This final report presents the results of an analytical study program leading to the design of crossed-field amplifiers suitable for a satellite TV relay. The work was performed under Contract NAS3-11516 from the National Aeronautics and Space Administration, Lewis Research Center.

G. Bernstein carried out the electrical design and technical evaluations of the study. W. C. Sylvernal was a principal contributor to the mechanical and structural design.

Thermal analyses, design of the heat transfer system, and evaluation of spacecraft interface problems were carried out in consultation with personnel of the General Electric Space Technology Center at Valley Forge, Pennsylvania. E. Conway of the General Electric Company was a principal contributor to the design of the heat transfer system. G. K. Farney and H. L. McDowell of S-F-D laboratories participated in the design study.

ABSTRACT

Theoretical designs are given for a UHF and an S-band crossed-field amplifier suitable for use in a satellite television relay system. The mode of modulation considered is vestigial side band AM.

A new form of crossed-field amplifier, the axial injection CFA, is presented. This form of amplifier will be able to meet the system requirements for high efficiency, wide dynamic range, low noise, and a minimum life of 20,000 hours. In addition this new type of amplifier is capable of maintaining a high level of efficiency at power levels well below peak synchronizing power, resulting in high average efficiency.

TABLE OF CONTENTS

LIST OF FIGURES

LIST OF TABLES

1.0 SUMMARY

An analytical study program has been carried out to develop the theoretical design of spaceborne crossed-field amplifiers (CFA) suitable for service in broadcast satellite TV applications. The analyses were carried out for two different frequency bands and power levels. The mode of operation was designated as vestigial side band amplitude modulation. A peak synchronizing power of 7.5 kw was the objective at 850 MHz and a peak synchronizing power of 5.0 kw was the objective at 2 GHz.

Some of the major features of the amplifier design included characteristics that previously had not been achieved simultaneously in one crossed-field amplifier tube type. Among these important features are:

a. A very high efficiency at the peak power output level combined with the maintenance of high efficiency at the lower drive levels of the amplitude modulation cycle.

b. A high level of gain exists in the final amplifier tubes; 20 db was taken as a design objective.

c. A large dynamic range is specified. This requires the absence of background noise that is typical of some types of crossed-field amplifiers. This requirement is specified as a dynamic range of 20 db combined with a minimum signal-to-noise ratio of 42 db.

d. The requirement that the amplifier transfer characteristic have an adequate degree of linearity, enhances the value of having the conversion efficiency of the amplifier remain high over a wide dynamic range of input drive levels.

e. The bandwidth requirements of the amplifiers are easily achieved by the slow wave transmission lines used here.

g. A mechanical design and thermal system is developed compatible with direct radiation of waste heat into space.

In order to meet the goals of this program, a set of designs was evolved which utilize a new form of crossed-field amplifier which, in the format presented, was invented at S-F-D laboratories. This device, the axial injection crossed-field amplifier, combines many of the best features of the classical emitting sole crossed-field amplifier with those of the injected beam crossed-field amplifier. The device is capable of achieving the very high efficiency which has been demonstrated for the emitting sole, reentrant stream crossed-field amplifier, together with the low noise, wide dynamic range, and high gain capabilities of the injected beam crossed-field amplifier. The use of a multi-element collector structure to extract the electron stream from the interaction system makes possible a scheme of programmed dc power input leading to the maintenance of a high level of conversion efficiency even at reduced drive levels. Finally, employing an external electron gun to produce the hollow beam, which is used in the interaction space of this tube, makes possible the long life operation that experience has shown can be achieved with thermionically emitting cathodes. This was of great importance in view of the required minimum operating life of 20,000 hours.

An arrangement of heat pipes is used to conduct the waste heat from the internal tube parts to a connecting radiator system, which then rejects the heat directly into outer space. The temperature profiles within the system are such that the hottest points within the tube structure are kept at about 300°C. This is consistent with long life operation. The heat pipe radiator system itself was designed so that partial failure of some heat pipes would not result in an operational failure.

The electronic interaction calculations were carried out by adapting a design format from existing analyses for the classical injected beam crossed-field amplifier. In addition these calculations were partially verified by using a digital computer program which was adapted to the axial injection mode of operation for a crossed-field

amplifier. Experimental verification of the basic performance characteristics postulated for the axial injection crossed-field amplifiers was achieved in experimental models built on a program of research sponsored by S-F-D laboratories.

The analyses carried out in the course of this study program lead to the conclusion that the following program objectives are feasible.

	UHF Design	S-band Design
Peak synchronizing power	7.5 kw	5.0 kw
Peak picture power	3.5 kw	2.3 kw
Average picture power	2.6-3.0 kw	1.75-2.0 kw
Gain	20 db	20 db
Estimated conversion efficiency		
at saturated output	84%	80%
at peak of synchronizing power	80%	77%
at peak picture power	75%	68%
at average picture power	69%	64%

Therefore, this study program has resulted in the evolution of an analytic amplifier design using a new type of crossed-field amplifier which has the following features: high efficiency over a wide range of modulation conditions, a high operating gain level, wide dynamic range, a linear regime with good efficiency, the long life expectation that goes with current derived from a thermionic emitting cathode having low emission density loading, and a mechanical thermal system compatible with space operation.

2.0 INTRODUCTION

This section indicates the key elements of the problems that were considered in developing a theoretical design for the spaceborne crossed-field amplifiers which were to be suitable for relaying amplitude modulated television signals via satellite rebroadcast.

The relevant prior art is reviewed and the approach used in this investigation is then discussed. The section concludes with a listing of the analytical procedures used in the performance of the study program.

2.1 Objectives of the Program

The objectives of this program were to develop analytical designs at both UHF and S-band frequencies for crossed-field amplifiers suitable for transmitting vestigial side band, amplitude modulated, TV signals via satellite relay.

The peak power levels of the amplifiers were in the multi-kilowatt range, and their operating characteristics were to include high efficiency, two years operating life, and adequate dynamic range and linearity. A thermal system design which allowed direct radiation of waste heat into space was required. A detailed outline of program objectives is presented in Section 3.2.

2.2 State of the Art Prior to this Program

The status and operating characteristics of established forms of crossed-field amplifiers was reviewed prior to this program to evaluate their possible application to the requirements of this program. Of the various possible types, it was found that only two - the emitting sole, reentrant stream crossed-field amplifier and the injected beam crossed-field amplifier - had been sufficiently well established to merit serious consideration.

This review showed that both of these tube types had some of the required operating characteristics of the TV relay amplifier. However, both of these tube types had deficiencies in their operating properties which led to the ultimate selection of a new form of crossed-field amplifier as being best qualified to meet the requirements of this program. A review of the state of the art for the emitting sole crossed-field amplifier and then the injected beam crossed-field amplifier is presented below.

2.2.1 The Emitting Sole Crossed-field Amplifier

A crossed-field amplifier is a microwave tube which converts dc power into microwave power using an electronic conversion process similar to that which is used in magnetron oscillators. Within this broad definition there are a large number of crossed-field amplifier types. Only two of these have achieved any significant state of development to date. These two tube types are the emitting sole crossed-field amplifiers and the injected beam crossed-field amplifiers. These tubes differ primarily in the method by which the electron current utilized for interaction is injected into the crossed-field interaction region.

In the emitting sole amplifier the current is obtained from the negative electrode, called the sole. This is usually secondary emission resulting from back bombardment of the sole by electrons which are absorbing energy from the circuit wave. The method for obtaining current is similar to that which is used in magnetron oscillators. However, the current for the crossed-field amplifier can be obtained from a non-thermionic emitting cathode. In tubes of this type, a dc voltage is applied between the sole electrode and the anode together with the axially applied magnetic field which is orthogonal to the dc electric field. The current flow is initiated from the sole electrode by the presence of a strong RF signal on the slow wave circuit. The exact mechanism by which the current flow

is initiated is not completely understood, but it is known to be a predictable process when properly used. This particular feature is of interest primarily in the utilization of crossed-field amplifiers in high power radar applications with narrow pulse, low duty cycle modes of operation with a fixed RF drive at the saturation level.

The several kinds of emitting sole crossed-field amplifiers that exist may be divided into one of two classes depending on whether the amplifier uses a reentrant or non-reentrant electron stream. In the non-reentrant tube shown schematically in Figure 1, dc potentials are applied and current flow is initiated by an input RF signal which is amplified during its passage through the amplifier. This is accomplished by the exchange of energy between the dc power supply and the RF field during the passage of the current from the sole electrode to the anode. The process continues throughout the length of the amplifier interaction region, and that portion of the current which has not reached the anode at the end of the amplifier circuit is permitted to exit from the interaction region and be collected. This form of non-reentrant device is of limited efficiency compared to a reentrant stream device and is not considered further in this review.

The reentrant tube geometry is indicated schematically in Figure 2. The shortcoming of limited efficiency is overcome by permitting the unused electrons to reenter the interaction space, traveling from output to input, and thereby to continue to interact with the circuit wave to develop additional microwave power. The increased efficiency obtained by this geometry usually is an improvement by a factor of two or more over that obtained with a non-reentrant emitting sole amplifier. However, it is apparent that such a reentering electron stream could contain electronic modulation leading to regenerative or degenerative gain depending upon the relative phase of the modulation.

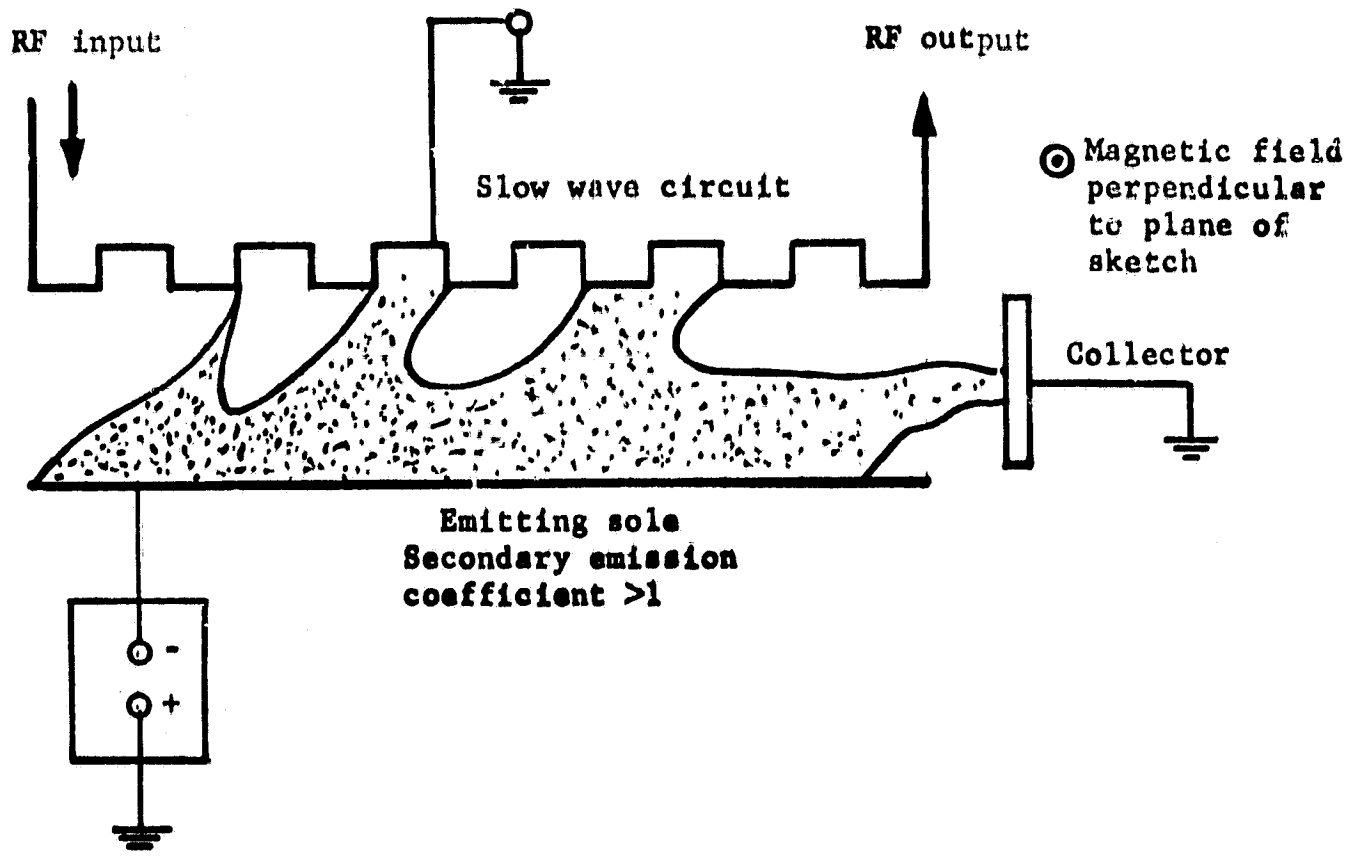

FIGURE 1 SCHEMATIC DIAGRAM OF NON-REENTRANT EMITTING SOLE AMPLIFIER

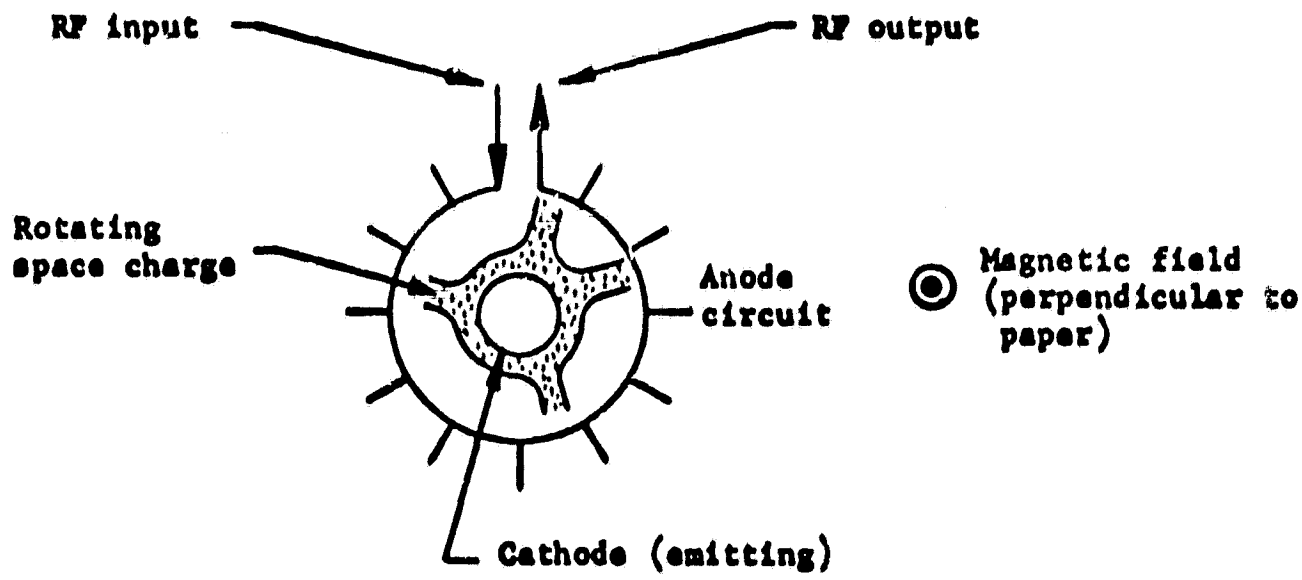

a. Lack of drift space between output and input allows electronic regeneracy

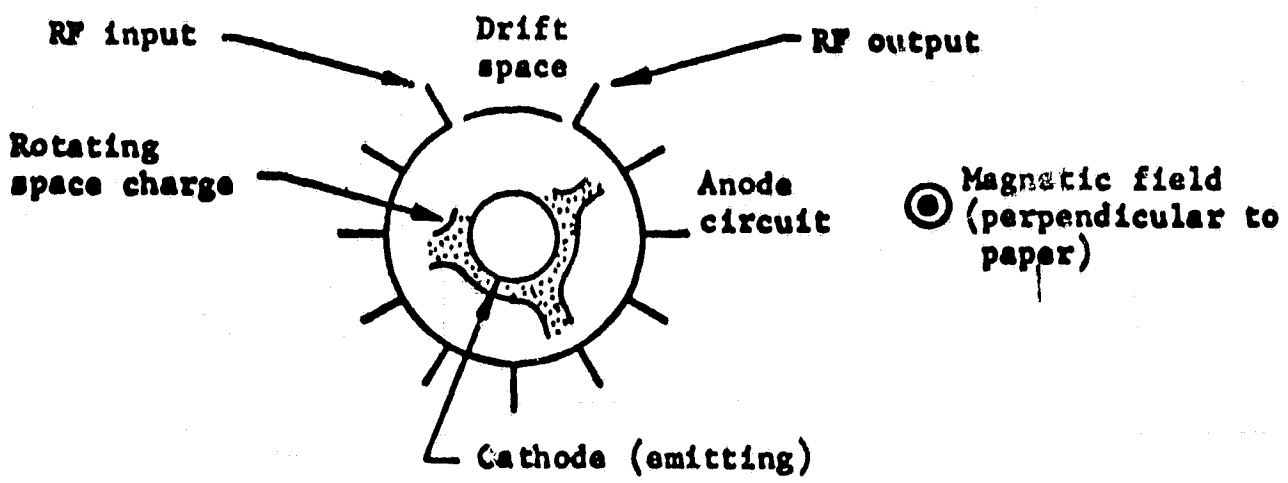

b. Drift space causes electron spoke debunching preventing RF feedback via electron stream reentrancy

FIGURE 2 REENTRANT STREAM EMITTING SOLE CROSSED-FIELD AMPLIFIER

In general, therefore, two types of reentrant stream, emitting sole crossed-field amplifiers have emerged. One of these attempts to utilize the maximum regenerative amplification that is possible, and the other attempts to demodulate the electron stream permitting continued use of reentrant electrons without suffering from cyclic variations in gain due to regeneration. The regenerative amplifier, using a maximum of regeneration, provides a large improvement in efficiency but is limited both in gain and in bandwidth because of the regenerative oscillation that would occur in various circuit modes. Thus, the limitations in gain compromise the benefits provided by a high efficiency final amplifier, since a relatively high level driver tube is needed, thus reducing the net efficiency. Most highly efficient regenerative amplifiers have gains which are restricted to the level of about 10 db. An alternative approach pioneered by S-F-D laboratories utilizes a drift space between the RF output and RF input which is free of RF fields so that the reentering electron stream can become self-debunching as a result of the strong internal space charge forces, thereby removing the electronic modulation. The RF field free region is called a drift space as is shown in Figure 2b. Amplifiers of this type have been developed at S-F-D laboratories for radar applications with gains on the order of 15 db and efficiencies in excess of 50%. Bandwidth is limited only by the characteristics of the slow wave circuit chosen.

The emitting sole crossed-field amplifier has almost no usable dynamic range and operates effectively only at its saturation power level. The reduction of the effective drive in this type of amplifier results in a large amount of background noise, so that this type of device does not effectively have a small signal regime. Thus, an amplitude modulation of the RF drive is not feasible.

There was no accumulated evidence that current emission resulting from secondary bombardment of the sole electrode would occur for the 20,000 hours of life required by this program. This type of long life history existed only for thermionically emitting cathodes. In addition, the performance of the secondary emission cathode in a CW mode within a high gain amplifier was even less predictable since the emission capabilities in the presence of low RF input signals could become unreliable.

This occurs since the secondary emission ratio of a cathode material is a function of the back bombardment voltage. There is a minimum voltage below which the secondary emission ratio is less than unity and the emission process is no longer self-sustaining. The back bombardment voltage is directly related to the RF field strength in the interaction space, and the RF field strength is proportional to the square root of the input signal power. It follows that a crossed-field amplifier with a secondary emission cathode does not have a small signal regime where the amplification process is continuously maintained as the drive level is reduced toward zero.

The generation of current by the process of back bombardment of the sole electrode in the emitting sole amplifier is detrimental to the conversion efficiency when such an amplifier is operated in a CW mode. Our experience had shown that the power wasted in back bombardment of the sole electrode can be about 20% of the dc power input. This estimate is based on calorimetric measurements performed at S-F-D laboratories on CW crossed-field devices. A value of 5% to 10% of the dc input power is more typical of high peak power pulsed amplifiers and magnetrons. In the case of high peak power, low duty cycle applications, the average power represented by this back bombardment power might not be appreciable, compared to the heater power required for thermionic emission. However, in the case of a CW mode of operation, an efficient thermionic emission system could be designed which would consume far less power than 20% of the total dc input.

Thus, the emitting sole crossed-field amplifier was rejected for this application because of severe limitations in dynamic range, excessive noisiness in the presence of reduced input drive, uncertain life expectancy of the secondary emission process, and uncertainty over the performance of the secondary emission process under conditions of low RF drive. At low RF drive, the large amount of uncontrolled space charge results in a high diocotron or slipping stream gain factor within the electron stream itself. This is the source of the background noise in the presence of low RF drive and is discussed in further detail in Section 3.0.

2.2.2 The Injected Beam Crossed-field Amplifier

The conventional injected beam crossed-field amplifier differs from the emitting sole amplifiers in that the electron current for interaction is obtained from a region external to the RF interaction portion of the tube. This is shown schematically in Figure 3. In this case, an electron gun is used to supply current from a thermionic emitting cathode. The electron stream is generated and launched into the crossed-field interaction region so that the whole electron stream is initially synchronous with the RF circuit wave. Amplification of the circuit wave is obtained in a fashion similar to that utilized in the emitting sole tubes. The RF wave on the circuit increases as a result of an exchange of energy between the electrons and the circuit wave as the electrons move toward the anode. In this device, it is not intended that the out-of-phase electrons be accelerated back to the sole electrode and cause subsequent secondary emission. Indeed, the tube geometry is so designed as to avoid this if at all possible, and the sole electrode is usually biased negative with respect to the cathode to further inhibit back bombardment. It is intended that the electron stream move through the interaction region, causing the conversion of potential energy between the sole and the anode to

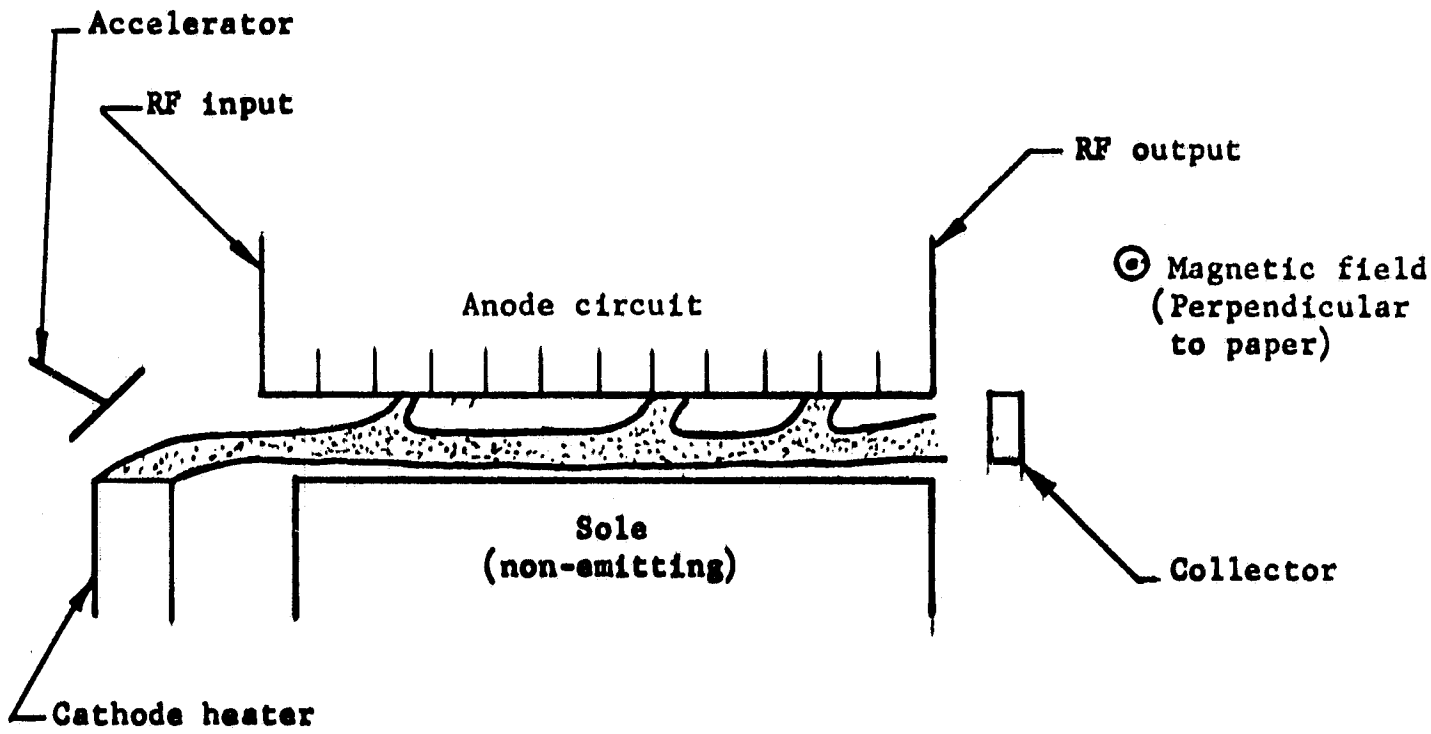

FIGURE 3 CONVENTIONAL INJECTED BEAM CROSSED-FIELD AMPLIFIER

result in amplification of the circuit wave. The current travels through the interaction region and that portion not collected on the anode exits at the far end and is collected upon a separate collector assembly.

Tubes of this type have achieved stable gain on the order of 20 db for large instantaneous bandwidths. These tubes have a wider dynamic range than the emitting sole amplifier, because of the external current injection scheme, and they are relatively noise free because of the high beam impedance - i.e., lower space charge density. A high space charge density results in high diocotron gain in the electron stream which is a major source of noise generation in the emitting sole type of crossed-field device. The established efficiency of this form of device is considerably below that achieved by the reentrant stream, emitting sole type of amplifier. Despite high efficiencies which are theoretically predictable, typical published efficiencies for CW tubes are on the order of 40% or less.

These results have been obtained with, at most, a single stage of collector depression. Theoretical studies of multi-element collector techniques have been carried out with respect to the injected beam crossed-field amplifier. However, it appears that only single stage systems have actually been applied thus far to optimize saturation efficiency for CW amplifiers.

Although the conventional injected beam crossed-field amplifier does possess the desirable properties of large dynamic range and an acceptable signal-to-noise ratio in the output signal, it was rejected as not being best suited for the purposes of this program for the reasons which follow.

1. Efficiency Under Conditions of Amplitude Modulation

   As usually used, the electronic efficiency of the conventional injected beam crossed-field amplifier decreases as the RF drive level is reduced, approximately in direct proportion with single stage collection. Thus, in an amplitude modulated television

signal where the average power level is about one-third of the peak of the synchronizing power level, the average efficiency of the device would only be one-third of that achieved near saturation conditions.

2. Concentration of Dissipation

Since the electron stream is injected entirely at the entrance to the RF interaction region, current collection on the anode or slow wave circuit near the end of the tube is highly concentrated in one particular region, thus increasing the thermal loading on the circuit unnecessarily. This situation was avoided in the form of crossed-field amplifier which was utilized in this program.

3. Cathode Loading and Efficiency

In designing the electron gun of a conventional injected beam CFA, the following considerations place limits on minimum cathode loading and efficiency. All CFAs achieve the conversion of dc to RF energy by converting the potential energy of the electrons directly into RF energy. In order to do this at maximum efficiency, a large ratio of cathode-anode voltage, to synchronous voltage, V_a/V_o, must be used. The synchronous voltage is the effective voltage in electron volts corresponding to the drift velocity of the electron stream, which is set equal to the phase velocity of the circuit wave, v_p. A high V_a/V_o results in the need for a large operating magnetic field, B. The magnetic field is almost directly proportional to this voltage ratio as indicated by Equation (1), where $\omega_c = (e/m)B$, $\beta = \omega/v_p$, ω = radian frequency, and y = distance from outer surface of beam to anode

$$\frac{\omega_c}{\omega} = \left[\frac{\frac{V_a}{V_o} - 1}{2\beta y}\right] \qquad (1)$$

As shown in Figure 3, the emitting area available from the cathode is equal to the cathode length which, in turn, is equal to the circuit height in the direction of magnetic field multiplied by the width of the cathode in the direction of the beam drift velocity. Experience and analyses have shown that in this type of electron gun, excessive anomalous RF noise will occur unless the width of the cathode is kept

in the range of 0.5 to 1 cyclotron wavelengths. For a given drift velocity, the cyclotron wavelength varies inversely as the magnetic field. A design which uses a large ratio of anode-cathode voltage to synchronous voltage results in a large magnetic field, a small cyclotron wavelength, and a low value of maximum cathode width if the noise suppression criteria are to be met.

The situation is illustrated by the following numerical example. In Section 4.0 the RF design of two axial injection crossed-field amplifiers are evolved to meet the requirements of this program. The properties of this new type of crossed-field amplifier are described in Section 3.0. The following parameters from the design of the S-band amplifier (Table I) are pertinent here.

TABLE I

S-BAND DESIGN PARAMETERS

Circuit height	1"
Magnetic field	3300 gauss
Synchronous voltage	800 volts
Cathode-anode voltage	12 kv
Ratio cathode-anode voltage to synchronous voltage	15
Cathode current	1 ampere
Cathode emission density	0.2 amp/cm^2

The high value of the ratio of cathode-anode voltage to synchronous voltage of 15 results in an operating magnetic field of 3300 gauss. If these operating parameters are now applied to the design of an electron gun for a conventional injected beam crossed-field amplifier, the following situation arises. In a typical Charles gun design, the drift velocity at the end of the gun corresponds to about 400 electron volts and this, in combination with the magnetic field of 3300 gauss, results in a cyclotron wavelength of 0.051". If one takes 0.6 of this

length as a safe factor for the suppression of anomalous noise, the allowable width of the cathode in the direction of beam propagation is 0.031". The total cathode area, therefore, is given by the product of 0.031" times 1". This area is equal to 0.196 cm^2. In order to emit a current of 1 ampere, the resulting emission density is 5.1 amp/cm^2. This emission density is not available from an ordinary oxide coated cathode and in the case of a dispenser cathode, the resulting high temperature operation would compromise the life requirements of this program. The emission density used for the axial injection crossed-field amplifier design resulting from this study program was 0.2 amp/cm^2.

It would be possible, in the case of the gun design just postulated, for the conventional injected beam crossed-field amplifier to reduce the emission density to 1 amp/cm^2 by making the cathode width three cyclotron wavelengths. Experience (Ref. 1) indicates that in this situation the problem of anomalous noise may be dealt with by putting a metallic grid above the cathode surface. However, this would be an undesirable expedient in an amplifier where the objective is an operating life of 20,000 hours. Past experience indicates that grids eventually become coated with cathode emitting material and the operating life of the structure is greatly reduced.

The axial injection crossed-field amplifier which was chosen as best suited to meet the needs of this program utilizes a hollow electron beam which is generated by a magnetron injection gun. Experience with this type of gun in O-type devices and in experimental work done at S-F-D laboratories using axial injection crossed-field amplifiers indicates that an anomalous noise is not generated in the same fashion as in guns used for the conventional injected beam crossed-field amplifier. To achieve this in the magnetron injection gun, it is necessary to maintain a taper angle between the cathode surface and the magnetic field.

Thus, for the conventional injected beam crossed-field amplifier, the high magnetic field requirements for high efficiency and the need to restrict the cathode width to contain gun noise result in an excessively high current emission density at higher frequencies and power levels.

2.3 Approach used in this Investigation

The axial injection crossed-field amplifier was chosen as the device having the highest potential capability of meeting the requirements of this program. In the format presented here this device is new to the crossed-field amplifier art and was first explored on internally sponsored research programs at S-F-D laboratories. The axial injection crossed-field amplifier uses a system of electron optics similar to that of the voltage tunable magnetron to generate a hollow beam external to the interaction space. The beam is then injected into the interaction space. After the generation of RF energy, the beam is removed from the interaction space by a multi-element collector system placed outside the interaction space at the end opposite to that occupied by the electron gun. A more detailed discussion of the operating principles of the axial injection crossed-field amplifier is provided in Section 3.1.

2.4 Analyses Performed

Analyses were carried out to verify and optimize the approach used in this program. These included

1. Selection of the slow wave circuit
2. Calculation of the interaction processes between the electron beam and RF field using small signal theory, as well as a digital computer simulation model
3. Analysis of the operation of a multi-element collector and its effect on efficiency
4. Electron gun design

5. An analysis of thermal requirements and the design of a heat pipe and radiator system for waste heat disposal
6. A mechanical design to meet environmental specifications.

A more detailed summary of these analyses is provided in Section 3.3.

The results of initial experiments on the axial injection crossed-field amplifier carried out at S-F-D laboratories were evaluated for pertinence to the requirements of this program.

2.5 Contributions of this Program

The sequence of design analyses carried out on this program has established the design and operating parameters necessary to meet the requirements of the program for two amplifiers suitable for satellite TV relay applications. In addition, the program explored and defined the capabilities of a new type of CFA which, in a number of ways, has extended the range of capabilities previously available in a single CFA type. A more detailed listing of the contributions of this program is given in Section 3.4.

3.0 THE AXIAL INJECTION CROSSED-FIELD AMPLIFIER

The amplifier designs resulting from the analyses carried out on this study program are based on the use of the axial injection CFA. Since this device is new to the crossed-field amplifier art, this section starts with a review of the physical principles upon which this device is based. This is followed by a detailed listing of the objectives of this program and a detailed summary of the analyses performed. This section then concludes with a listing of the contributions of this program in terms of the designs evolved utilizing the axial injection CFA.

3.1 Review of Principles of Axial Injection CFA

In the review of the physical principles of the axial injection CFA which follows, the sketches shown are for purposes of illustration and do not represent a specific physical embodiment of the device. The collector array, for instance, is a schematic rather than a specific design format.

Figure 4 shows a schematic drawing of the tube. Beam trajectories shown are those obtained with a low RF input signal. The tube is constructed in circular format, with the slow wave circuit or delay line wrapped around 80% of the circumference of the anode. The delay line is at anode or ground potential. For this application, a forward wave line with the appropriate dispersion would be employed. The characteristics of this line determine the bandwidth capabilities of the tube. A non-emitting electrode, called the sole, is located concentrically within the delay line. This electrode is operated at a potential which is negative with respect to the delay line, so that a radial dc electric field exists between the sole and the delay line. In conjunction with an axial magnetic field, this provides the crossed-field interaction environment requirement in a CFA. An electron

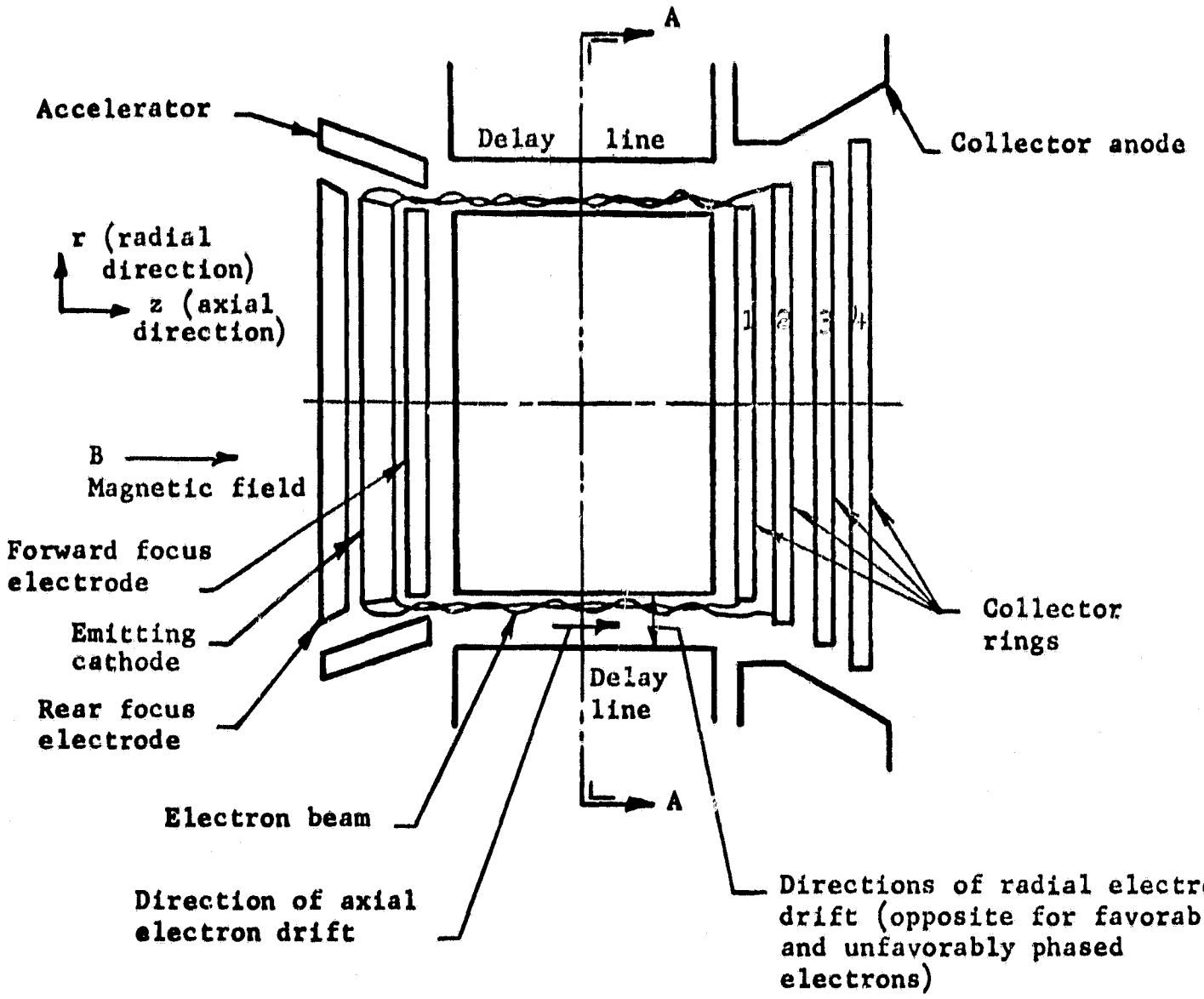

FIGURE 4 SKETCH OF THE AXIAL INJECTION CFA

Electron beam in interaction space circulates in the circumferential direction (perpendicular to paper) with a velocity greater than the axial (z direction) drift velocity. Trajectories are shown for a condition of low RF input drive

gun employing a thermionic cathode is mounted concentric with the interaction space, but is axially displaced to one end of it. A concentric multi-section collector is located at the opposite end.

Figure 5 shows a cross-section through the interaction space through the plane A-A of Figure 4. The disposition of the tube electrodes in this cross-section appears similar to that of an emitting sole crossed-field amplifier. The interaction space is reentrant, allowing electrons to recirculate from the output back to the input. Between the output and the input, there is the usual drift space in which the electron charge is debunched so that RF feedback from output to input is avoided. This is a necessity for reasonable bandwidth and high gain levels. It has been found that a high degree of debunching can be obtained in this manner and that RF feedback through the recirculating beam from output to input is negligible. In the usual emitting sole crossed-field amplifier, the negative surface opposite to the slow wave circuit would be a cathode and would supply electrons to the interaction. In the present type of tube, however, this surface is made into a non-emitting sole, which is biased negative with respect to the cathode electrode. This prevents electrons from striking the sole and insures that the sole will be non-emitting. At the same time, the sole bias forces the beam away from the sole surface, which acts as a shorting plane for the RF fields, and into a region of high RF field strength.

Returning to Figure 4, we see that the cathode is displaced axially to one end of the interaction space. Here it is incorporated into an electron gun which is similar in many regards to the electron guns employed in voltage tunable magnetrons. Electrons from the gun are injected into the interaction space by a component of velocity which is parallel to the tube axis, and is imparted by the electric fields of the gun. This has given rise to the term "axial injection" to describe this type of CFA. A collector assembly consisting of a

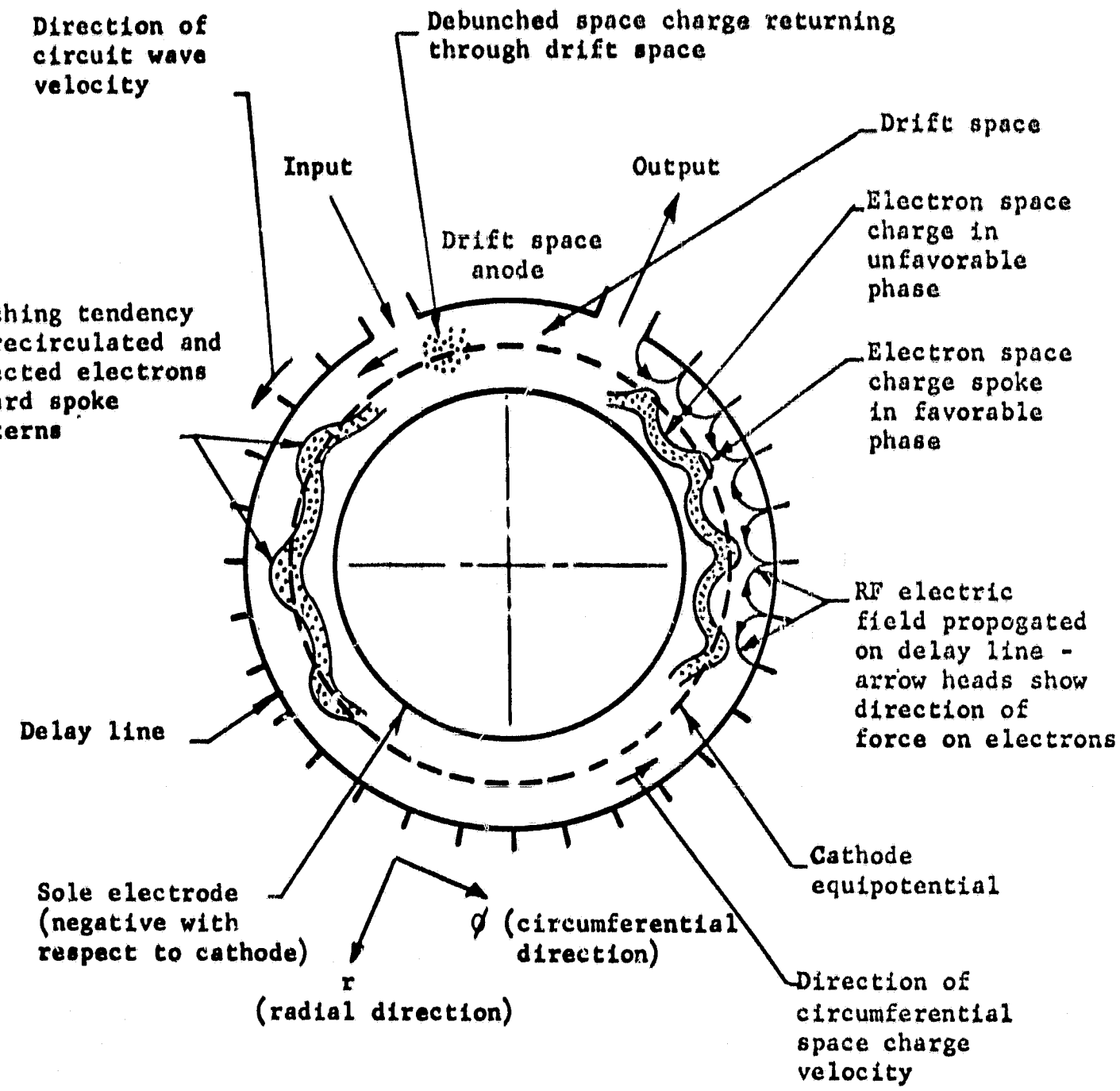

FIGURE 5 CROSS-SECTION THROUGH A-A IN FIGURE 4 SHOWING A SKETCH OF THE SPACE CHARGE DISTRIBUTION

number of rings is located at the end of the interaction space opposite to the gun. This is a multi-section collector in which the rings are operated at successively higher potentials ranging from cathode potential to anode potential. Electrons leaving the interaction space are collected on a ring at a potential close to that at which they leave the interaction space. In this manner, the energy dissipated on the collector segments is minimized. The multiple section collector is intended to maintain a high efficiency of operation over a wide range of output powers. For a tube intended for operation at saturated output most of the time, a simpler collector with fewer rings could be employed. It should be noted that all the electrons arriving at the various collector rings have approximately the same circumferential velocity and axial drift velocity. Only their potentials vary. This is in contrast to O-type devices, such as TWTs and klystrons, which have a large velocity spread in the spent beam that depends on the level of RF drive. Thus, the axial injection CFA lends itself much more readily to current collection by a series of rings at fixed potentials.

Electrons originate in the gun, following a trajectory as shown in the developed view of the tube in Figure 6. This sketch shows an interaction space which has been unwrapped and in which we are looking down upon the beam from the delay line on the anode. An electron acquires a circumferential drift velocity equal to the ratio of electric to magnetic fields in the interaction space (E/B ratio). The voltage and magnetic field are adjusted so that this circumferential drift velocity is in synchronism with the velocity of the circuit wave. The electron also acquires an axial drift velocity as a result of the electric fields in the gun which launch the electron into the interaction space. As will be described in more detail later, the potentials applied to the gun electrodes can control both the amount of current injected and the axial drift velocity with which it is

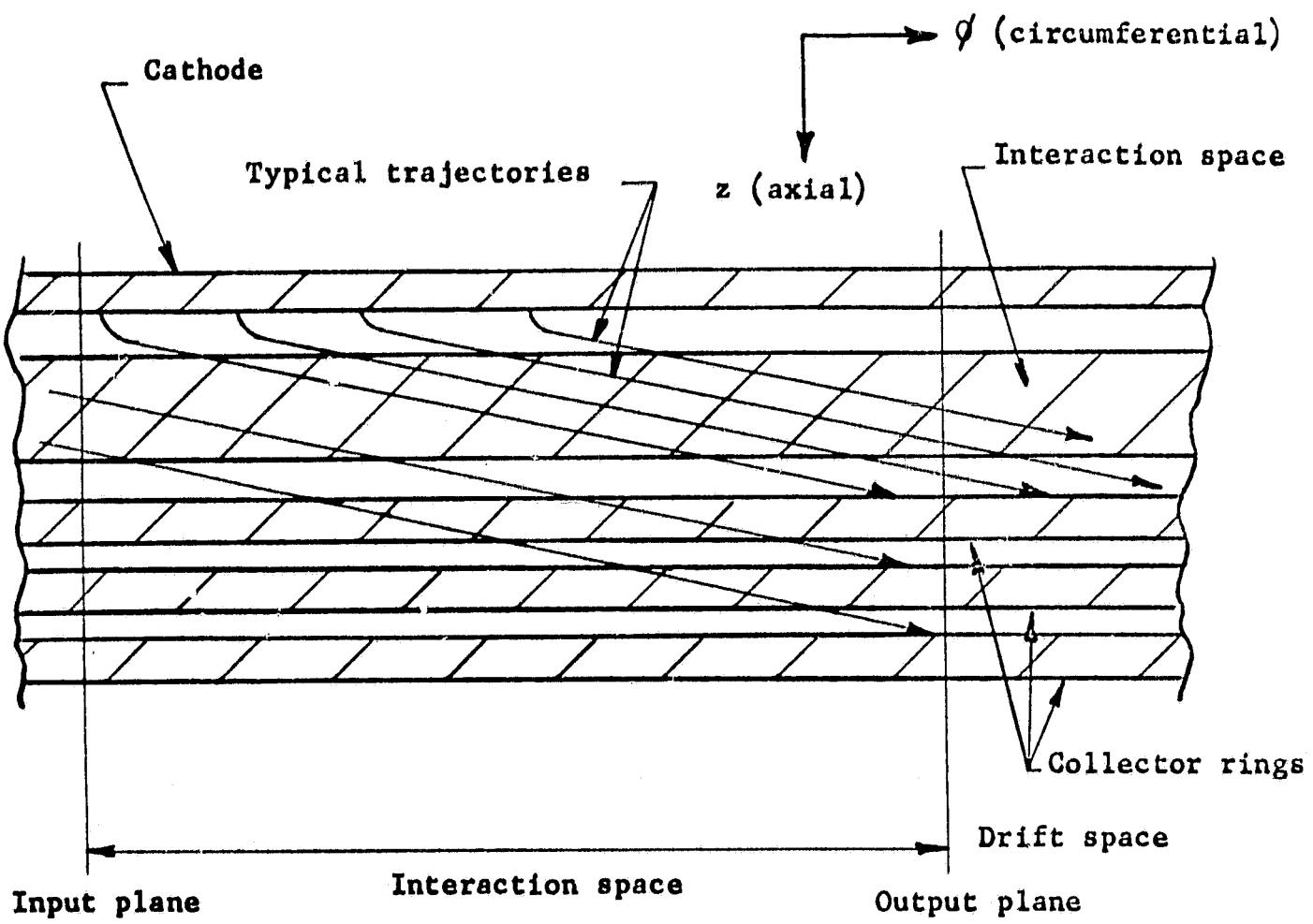

FIGURE 6 SKETCH OF THE INTERACTION SPACE WHICH HAS BEEN DEVELOPED (UNWRAPPED) IN THE ϕ-z PLANE

We are looking from the delay line toward the sole

injected. As shown in Figure 6, the circumferential drift velocity is several times greater than the axial drift velocity so that the electron travels through a significant fraction of the circumference of the tube before it is removed from the interaction space. The axial drift velocity is introduced as a means of transporting the electrons across the interaction space from the gun to the collector on the opposite side. This transport of electrons to the collector, i.e., the draining of electrons from the interaction space, is necessary to insure that the tube will operate with a large dynamic range and will not generate large amounts of noise at low drive levels.

Under low level RF input power conditions when the RF fields of the circuit wave are weak, the electrons will drift across the interaction space to the depressed collector. Here, each electron will be collected at a potential near that with which it exits from the interaction space. Figures 4 and 5 show the electron beam under these conditions. At the collector, much of the unused potential energy in the electron stream will be recovered and the tube will operate efficiently, even under low RF input power conditions. When the tube is driven to its full RF input power by applying a higher RF input signal, most of the favorably phased electrons which give up energy to the RF field will be drawn up to the anode circuit before they have had a change to exit from the interaction space on the collector end. The unfavorably phased electrons will be collected on the first collector ring which operates at cathode potential. The trajectories in this case are shown in Figures 7 and 8. Under these conditions of operation, most of the current will be collected on the anode and efficient operation will be obtained in a manner similar to that in a conventional emitting sole crossed-field amplifier.

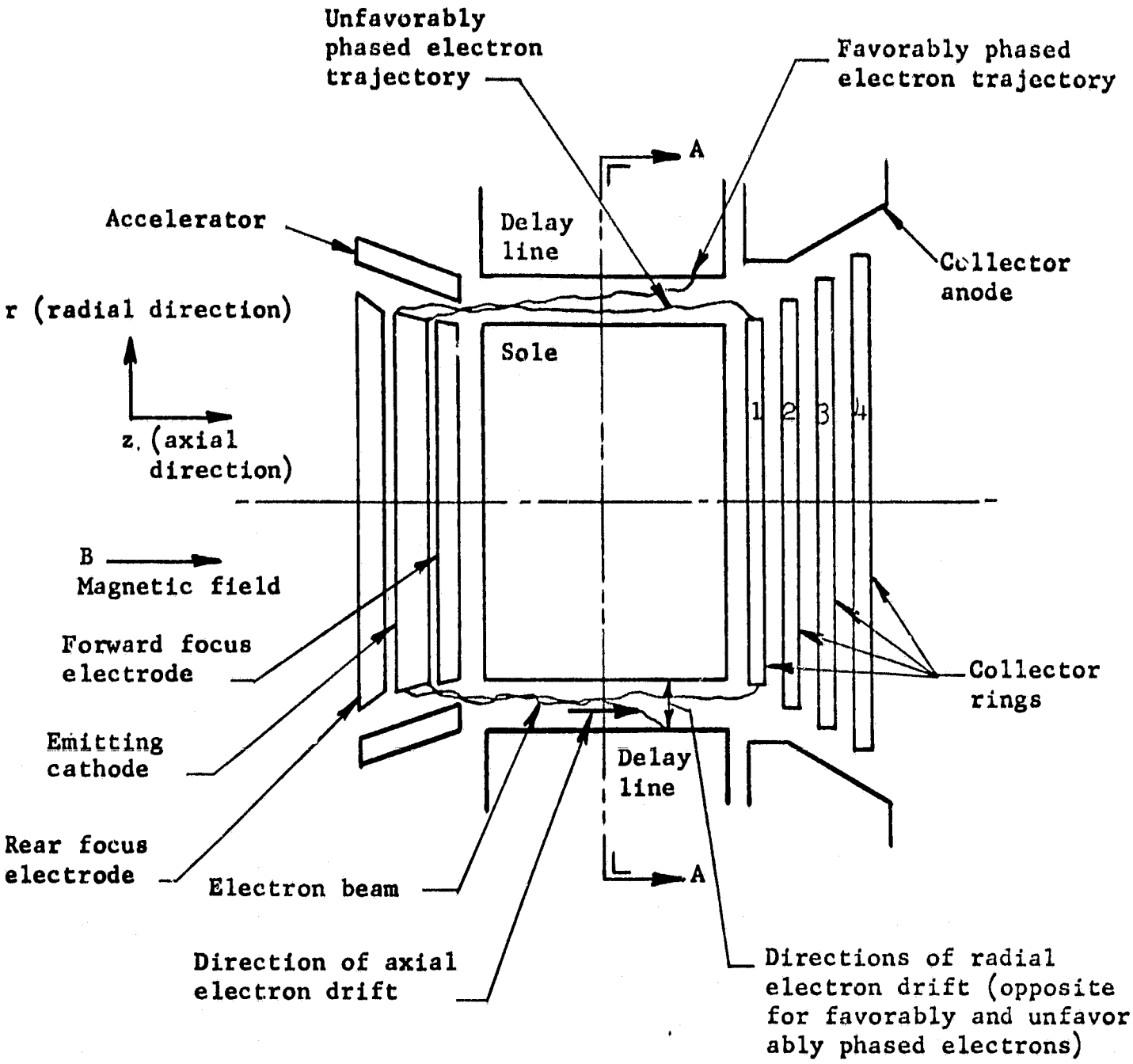

FIGURE 7 SKETCH OF THE TUBE SHOWING TRAJECTORIES WHEN TUBE IS DRIVEN TO SATURATION

The favorably phased electrons are collected on the delay line while the unfavorably phased electrons are collected on the first collector ring at cathode potential

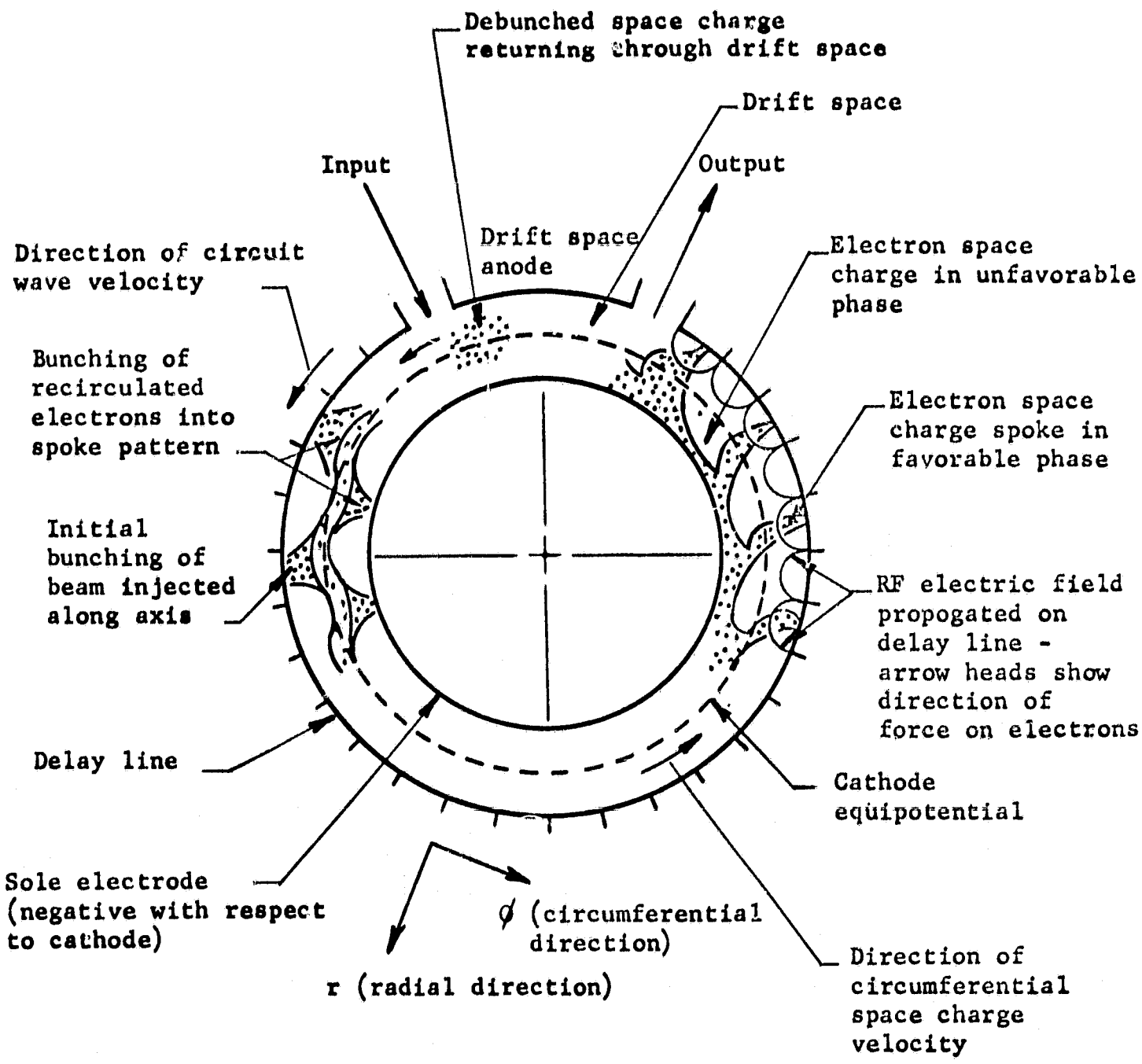

FIGURE 8 **CROSS-SECTION THROUGH A-A IN FIGURE** 7 **SHOWING A SKETCH OF THE SPACE CHARGE DISTRIBUTION WHEN THE TUBE IS DRIVEN TO SATURATION**

It should be noted that there are three components of velocity to the electron trajectories. The circumferential drift velocity (indicated in Figure 5 as the Ø-directed velocity) is determined by the E/B ratio in the interaction space. The axial drift velocity from the gun to collector (indicated in Figure 4 as the z-directed velocity) is determined by the dc electric fields in the gun. The radial drift velocity (indicated in Figure 4 as the r-directed velocity) is imparted by the RF electric fields of the circuit wave. Electrons located in favorable phase for interaction move toward the anode, gaining energy from the dc field and simultaneously giving it up to the RF field. Electrons located in the unfavorable phase move toward the sole, gaining energy from the RF field and moving against the dc field force. Amplification is obtained because a greater amount of energy is added to the RF circuit wave by interaction with the favorably phased electrons than is subtracted by interaction with the unfavorably phased electrons.

The basic power supply arrangement for the axial injection tube is similar to that used for a conventional injected beam CFA. For the multiple segment depressed collector, a tapped main power supply is employed. Following the usual technology for modern power conditioners, the collector supplies are derived from a common, variable pulse width, regulated converter which has multiple secondary taps. This is discussed in greater detail in the section on power conditioner requirements. Only a few collector rings are required to provide high efficiency at saturated output. The remaining rings are added to provide enhanced efficiency over a wide range of amplitude modulation levels.

The capability to program the dc power input as a function of RF drive level makes possible the maintenance of a high level of efficiency over a wide dynamic range of output power. For 20 db of

dynamic range, only a device that uses controlled dc power input, i.e., recovery of unused dc power, can hope to maintain high efficiency over the specified dynamic range.

The use of a power supply with multiple voltages is established technology in VHF distributed amplifiers where different voltages are desired for tubes having different positions along the line. This is an example of a situation where multiple voltages have been employed to increase efficiency, even though a single voltage could have been employed. Actually, the provision of multiple voltages does not have much effect on power supply efficiency so that their use can increase the overall system efficiency significantly. The accelerator and sole supplies draw essentially no current and are not a factor in efficiency considerations.

The axial injection crossed-field amplifier, thus, will make available the wide dynamic range and zero signal stability of the conventional injected beam crossed-field amplifier, combined with the high efficiency of the distributed emission, reentrant stream form of crossed-field amplifier. In addition, the use of a multi-element collector structure will assure a minimum variation in efficiency over a wide dynamic range.

This follows since the RF drive level determines the extent of the radial excursion of the electron beam above the radius of injection. This, in turn, determines the range of collector elements at which most of the current will arrive. Thus, at low RF drive levels, the current is collected at lower potential elements with respect to the cathode potential. Since the dc input to the amplifier is the summation of current collected multiplied by the potential of the collector element, it follows that at reduced RF drive levels a smaller amount of dc power is programmed into the amplifier. Thus the output power level is a larger percentage of the dc power input over a range of drive levels than if the dc power input had remained constant and corresponded to the full saturated output capability of the amplifier.

Thus the use of a multi-element collector in this application differs from the manner in which a multi-element collector is used in an O-type device. In an O-type amplifier, the depressed collectors are used to recover kinetic energy from the beam. The multi-element collector as used here controls the original input power.

The specific details of the manner in which the depressed collector of an O-type amplifier operates indicate that the design problem for such a collector is more complex than in the case of the axial injection CFA. The reason for this is as follows. There is a substantial spread in the kinetic energy of the spent beam of an O-type amplifier. Before collection of the spent beam on the various collector elements can occur, this velocity distribution must be converted into a spatial distribution. In addition, this conversion from velocity distribution to appropriate spatial distribution must be accomplished without reflecting electrons back into the interaction space of the O-type amplifier. Such reflections can result in bombardment of the electron gun and the circuit as well as in RF regeneration.

The basic interaction process in the CFA can be viewed as a process which sorts the electrons at different energy levels into different position locations. Therefore, when the spent beam is to be collected, the spatial sorting necessary to introduce electrons of different energy levels to the appropriate collector elements has already been accomplished. In addition, if an electron should be reflected from the collector region of the axial injection CFA back into the interaction space, it cannot travel through the interaction region in the wrong direction, since the crossed electrostatic and magnetostatic fields always produce a force on the electron in the same circumferential direction. The reflected electron must travel in the same direction as the direction of RF wave propagation and thus a possible reflected electron cannot cause RF regeneration.

The foregoing operating characteristics were made possible by the major features of axial injection which are summarized as follows:

1. Maintenance of electron recirculation results in a maximum efficiency capability since partially interacted electrons can be reused by reentering through the drift tube area. RF regeneration is avoided by using a drift space between the input and output ports.

2. Control of noise and attainment of zero signal stability occurs through the use of a hollow beam axial injection gun and through the use of an electron collector to drain unused space charge in the interaction space. The use of high current density cathodes and fine grids of conventional injected beam crossed-field amplifiers is avoided.

3. Provision is made for a geometry which permits incorporation of a multiple electrode collector which maximizes efficiency at every output power level. This also makes possible efficient operation somewhat below the saturation power level in order to meet necessary linearity requirements.

4. The concept of distributed emission is maintained, which results in a more even distribution of dissipation upon the anode and also insures a minimum emission density loading on the gun cathode. This contributes to long life possibilities.

3.2 Outline of Program Objectives

An outline of the program objectives to be achieved by the axial injection CFA analytical designs follows. The power handling capabilities of the two CW crossed-field amplifiers when relaying a TV signal were

Frequency	850 MHz	2 GHz
Peak synchronizing power	7.5 kw	5.0 kw
Peak picture power	3.5 kw	2.3 kw
Average picture power	2.6-3.0 kw	1.75-2.0 kw
Minimum picture power	1.3 kw	0.9 kw
Sound power	0.75 kw	0.5 kw

It was stipulated that the thermal system should be designed to handle steady state powers ranging from minimum picture power plus sound power to peak picture power plus sound power. These are then in the range of 2.05 kw to 4.25 kw for the 850 MHz design and 1.4 kw to 2.8 kw for the 2 GHz tube. Actual thermal design of the UHF amplifier was carried out with a 5 kw average power handling capability.

The following major requirements define the important operating characteristics of the amplifier.

3.2.1 Efficiency

Since the prime power source for operating the TV relay transmitter within the orbiting satellite was an array of solar cells, the highest order of priority was placed upon obtaining maximum conversion efficiency within the microwave amplifier because of the extremely high cost per unit of prime power obtained from the solar cell array. An early appraisal of the requirements of this program resulted in a conversion efficiency objective of 80% or better under conditions of saturated power output. In addition, it was desired to maintain a high level of efficiency under conditions of amplitude modulation of the RF drive. This would constitute a unique improvement over many existing types of amplifiers, where the efficiency was reduced in nearly direct proportion to the reduction in RF drive level in the course of a modulation cycle. These features would be achieved in the proposed design by combining the high saturation efficiency of the reentrant stream crossed-field amplifier together with a scheme for programming the dc power input at lower drive levels by the use of a properly designed multi-element collector.

3.2.2 Gain

The gain level chosen for the amplifiers for each of the frequency bands in this study program was 20 db. This value was selected using trade-off considerations which will be considered

elsewhere in this report. With this choice of gain level, low power microwave amplifiers which were within the state of the art could be used to drive the crossed-field output amplifiers from the 1 watt drive level. This choice of gain for the final amplifier stage would make the overall system efficiency relatively insensitive to the efficiency of the driver stage.

3.2.3 Life

A minimum operating life of 20,000 hours was designated for the amplifier chain in order to provide a practical amortization period for the transmitter and satellite vehicle. The axial injection crossed-field amplifier chosen in this study program utilizes thermionic emission from a cathode placed external to the RF interaction space as a source for the electron stream. This was the only type of current emission system for which accumulated data existed, verifying the possibility of life expectancy of 20,000 hours and more.

3.2.4 Dynamic Range

A minimum linear dynamic range of 20 db was specified in order to properly handle the amplitude modulated signal. This dynamic range would be obtained in the axial injection crossed-field amplifier by injecting the current into the interaction space from an external source as is done in the classical injected beam crossed-field amplifier. However, the very high efficiencies of the emitting sole crossed-field amplifier would be retained. This large dynamic range was not achievable in the classical emitting sole crossed-field amplifier because of the high background noise existing at low drive levels.

3.2.5 Linearity

A 0.5 db maximum deviation from linearity of small signal gain was specified when operating 3 db below saturation. The ability of the proposed axial injection crossed-field amplifier to operate below saturation level with a high degree of efficiency made it possible to chose an operating range where linearity requirements could be satisfied.

3.2.6 Signal-to-noise Ratio

A signal-to-noise ratio of at least 42 db over the specified bandwidth was required. The use of space charge control via the axial injection feature of the amplifier made it feasible to meet this requirement. This feature has been demonstrated in experimental work carried on at S-F-D laboratories.

3.2.7 Bandwidth

A bandwidth of 6 MHz between the 3 db points was specified for both operating frequencies. The slow wave circuits that were selected for incorporation in these amplifiers have bandwidths far in excess of that required. These particular circuits were chosen from considerations other than those of bandwidth.

3.2.8 Mechanical Design

A mechanical configuration for the amplifier tubes has been arrived at which will adequately meet the environmental shock and vibration specifications. This was based on design experience achieved on other development programs carried out by S-F-D laboratories.

3.2.9 Thermal System

A thermal system design that uses direct radiation into space for disposal of waste heat was specified. Such a design has been evolved using a system of heat pipes which transmit the waste heat from the tube structure to the radiator structure. This design was worked out in consultation with personnel at the Valley Forge Space Technology Center of the General Electric Company. This work was carried out directly under a sub-contract let to the General Electric Company.

3.3 Summary of Analyses Performed

The areas in which analyses were carried out to verify and optimize the approach used in this program are enumerated below. In addition, reference is made to experiments obtained on programs sponsored by S-F-D laboratories which verify the principles of operation for the axial injection crossed-field amplifier.

3.3.1 Selection of Slow Wave Circuit

Design trade-offs were carried out to select a suitable slow wave circuit or delay line for use in the UHF and S-band amplifiers. The desired characteristics were maximum possible interaction impedance, coupled with a minimum of insertion loss per unit length of circuit. This would result in a maximum circuit efficiency. The total conversion efficiency is the circuit efficiency multiplied by the electronic efficiency of the device. This led to a consideration of three possible delay lines, with the same circuit eventually being chosen for both the UHF and S-band designs. In order to achieve a high value of interaction impedance, high surge impedances (characteristic impedance) were accepted as part of the delay line characteristic, and a low dispersion phase characteristic helped assure low insertion loss. Trade-off calculations were then carried out with the operating voltages, currents,

and magnetic fields as variable factors. The results sought in the trade-off calculations were minimum circuit length for maximum circuit efficiency, optimal electronic efficiency, establishment of maximum permissible noise level and diocotron gain in the electron stream to assure dynamic range, and reasonable internal temperature to assure the life expectancy desired. The size and weight were factors given consideration, but were considered after maximum conversion efficiency and adequate dynamic range were assured.

Since the axial injection crossed-field amplifier is a relatively new device, a complete set of analytical relationships for the interaction process is still being developed. In order to carry out the above trade-off calculations, a design procedure was synthesized from existing small signal analyses for the conventional injected beam crossed-field amplifier.

3.3.2 Computer Calculations

Preliminary computer simulation calculations were carried out both to verify the above design procedures and to yield additional information on the operating characteristics of the device. Preliminary computer results were also obtained on the distribution of current as a function of the potential at which various electrons leave the interaction system of the tube. These computer calculations were carried out at the end of this study program, after successfully modifying an S-F-D laboratories computer program for an injected beam crossed-field amplifier, so as to accommodate the mode of operation of the axial injection tube. This program, as modified, allows for continuous injection of current over the active length of delay line, keeps track of the axial transit time of each unit of electron charge, and removes the electron charge from the system when it has been in the interaction space for a time duration of one axial transit. In addition, an iterative procedure to simulate the effect of electron reentrancy was carried out.

3.3.3 Multi-element Collector Operation

A detailed analysis on the operation of a multi-element collector and its effect on efficiency was carried out. Calculation of electronic efficiency under different conditions of drive level and presumed current distributions in the collector region were undertaken so that the importance of the number of elements in the multi-element collector structure could be evaluated. In addition, the effects of secondary emission on the collector elements were considered and schemes for minimizing its importance were evaluated.

3.3.4 Electron Gun Design

A design analysis of the electron gun needed to produce a hollow beam used in the interaction space of the amplifier was undertaken. The electron gun used is of the magnetron injection variety and the Kino's analysis (Ref. 2) was used to guide the calculations. The relative distribution of rotational and axial energy in the electron stream, however, is unique to the requirements of the axial injection amplifier. Velocity distributions that appeared realistic in the electron gun design were then introduced as considerations in the overall design of the interaction space geometry.

3.3.5 Thermal Requirements

The thermal requirements of the crossed-field amplifier were assessed and maximum operating temperatures for the internal tube parts were assigned to assure the required life expectancy. A system of heat pipes was designed to convey the waste heat from the amplifier to an appropriate metallic radiator for direct radiation of the waste power into space. An appropriate selection was made from the various possibilities that exist in the heat pipe and radiator design art.

3.3.6 Mechanical Design

A mechanical design was carried out so that the total tube structure would be capable of meeting the shock and vibration characteristics specified for this program. The mechanical design was integrated into a permanent magnet package. Permanent magnets supply the magnetic field required for the operation of this tube. These magnets are surrounded by a shield of ferro-magnetic material which minimizes the effect of the magnetic field of the tube on the rest of the spacecraft environment.

3.3.7 Review of Initial Experimental Results

The results of initial experiments on the axial injection amplifier carried out by S-F-D laboratories were reviewed. These results verified the operating principles in the areas of extended dynamic range, the operation of multi-element collectors, and the effect of this collector structure on the conversion efficiency. The very first of these series of experiments contained a crude single-element collector. This tube was operated first in a mode which simulated emitting sole operation with no axial removal of the electron stream. The axial injection mode of operation was then introduced with an immediate improvement of 26 db in the overall dynamic range and the achievement of a signal-to-noise ratio of over 50 db, which was the limit of resolution of the spectrum analyzer being used for the measurement. Even with this single-element collector, a ten-to-one reduction in output power resulted in less than a three-to-one variation in conversion efficiency. In subsequent experiments with a simple three-element collector, efficiencies approaching 70% were obtained and the principle of switching the electron stream current to different collector elements as a function of RF drive was verified. These early experiments were by no means carried out with optimum designs, but rather were verification experiments carried out using vehicles fabricated from readily available piece parts.

3.4 Outline of Program Contributions

The areas in which the design analyses carried out on this program have made contributions to amplifier capabilities, are outlined below.

3.4.1 Efficiency

By retaining the distributed emission, reentrant stream characteristics of the emitting sole crossed-field amplifier, the high level of efficiency at saturation power levels has been retained. The use of the non-regenerative version of a reentrant stream amplifier makes possible an extended circuit length and high gain level. The extended circuit length insures an adequately low thermal flux density, and the high gain level assures that the overall transmitter amplifier package will have a high level of efficiency that is insensitive to the actual efficiency of the driver tube.

3.4.2 Gain

The use of a drift section in the delay line structure to assure no electronic feedback via the reentering electron stream has made possible the design objective of 20 db RF gain. The use of a circuit with a high interaction impedance makes possible the achievement of this gain in a minimum circuit length, with the consequent minimum circuit losses.

3.4.3 Dynamic Range

A method of space charge control in the interaction region of the crossed-field amplifier has been provided by the use of external injection of the electron stream and a collector structure that efficiently withdraws unused portions of the circulating electron current. This eliminates the background noise which is typical of the emitting sole crossed-field amplifier and provides a dynamic range capability comparable to the classical injected beam crossed-field amplifier.

3.4.4 Amplitude Modulation Capability

The use of the multi-element collector scheme makes possible a programming of the dc power input to the amplifier as a function of RF drive level. Thus a high level of efficiency is sustained not only at the saturation power level but at greatly reduced drive levels. This is of particular importance in an amplifier to be used for relaying amplitude modulated television signals, where the average power level is approximately one-third of the peak power level during a typical modulation cycle. Thus, for example, in the UHF design with a peak synchronizing power of 7.5 kw, a conversion efficiency of better than 80% is predicted. At the reduced power output level of 3.7 kw, it is expected that a conversion efficiency of 69% might be maintained. In the case of the S-band design, the conversion efficiency at the peak of synchronizing power of 5 kw would be on the order of 77%. However, at the average power level of 1.7 kw, it is predicted that a conversion efficiency of 64% might be maintained. The peak of synchronizing power level in both these cases was set below the saturation power of the amplifiers to assure linearity. The saturation power level efficiency in both cases would be somewhat higher than the numbers just quoted.

3.4.5 Bandwidth

The axial injection crossed-field amplifier as presented in this program is a traveling wave device utilizing a forward wave slow wave circuit. From considerations of low insertion loss, non-dispersive circuits have been selected so that the bandwidth capability of this device is far in excess of the required 6 MHz. The bandwidth of the device is essentially set by the dispersion characteristic of the delay line and with the particular circuits chosen, bandwidths on the order of an octave are available. All the design procedures carried out on this program were aimed at optimizing the design for

the amplification of amplitude modulated signals. However, because of the inherent bandwidth of the device, it is felt that an optimal design had been achieved for the amplification of frequency modulated signals if such an application were deemed desirable.

3.4.6 External Electron Gun

The use of an external electron gun in the specific form presented in this program results in a number of desirable features. The thermionic cathode used to obtain the required current emission makes possible the prediction of the life expectancy required by this program. It is only for thermionic cathodes that sufficient accumulated data exist to demonstrate the achievement of tens of thousands of hours of life, if the cathode operating temperature and emission density loading are kept sufficiently low. Use of the external electron gun allows a degree of space charge control that eliminates the background noise which is typical of emitting sole crossed-field amplifiers. This scheme of current injection is similar to that used in voltage tunable magnetrons which are well known for their very low noise properties. Generating the required hollow beam from the ringed cathode in the external electron gun results in a low emission density and thus, avoids the drawback of heavy cathode loading that exists in the conventional injected beam crossed-field amplifier.

4.0 RF DESIGN

This section of the report will present the considerations that entered into the selection of the delay line for the amplifier design, and the tradeoff calculations that were carried out to select design geometry and operating parameters. The small signal calculations are also presented. An analysis of the manner in which the collector element parameters affect conversion efficiency under varying drive level conditions is also presented. Preliminary verifying results from computer calculations are submitted.

4.1 Choice of Slow Wave Circuit

The slow wave circuits chosen for use in the UHF and S-band amplifier designs must exhibit the following desirable characteristics:

1. low insertion loss
2. high interaction impedance
3. adequate thermal capabilities
4. reasonable axial dimensions for the frequencies involved.

Items (1) and (2) are directly connected in maintaining the highest possible circuit efficiency. The net conversion efficiency of the amplifier is equal to the electronic conversion efficiency multiplied by the circuit efficiency, which accounts for the ohmic losses on the slow wave circuit.

The interaction impedance, as used in the calculations presented in this program, is the impedance defined by Pierce (Ref. 3). That is, it is a measure of the RF field strength at the point of interaction for a given power flow on the slow wave circuit or delay line. A high interaction impedance, therefore, makes possible the achievement of the desired gain level in a minimum active circuit length. A low insertion loss per unit circuit length then helps to minimize the total insertion loss of the circuit and results in a high value of circuit efficiency. An analysis of the properties of slow wave circuits indicates that one may obtain a very high interaction

impedance by using a highly dispersive circuit. However, a high unit insertion loss is an accompanying defect to this approach to obtaining high interaction impedances. A dispersive circuit leads to a high interaction impedance and a decreased circuit length. However, the following argument indicates that this approach results in a higher total insertion loss than with a non-dispersive circuit,and therefore decreased circuit efficiency.

The interaction impedance , K, is given by:

$$K = \frac{E^2}{2\beta^2 P}$$

where E = RF field strength

$\beta = \omega/v_p$

ω = radian signal frequency

v_p = phase velocity of circuit

P = power flowing on slow wave circuit

$P = Wv_g$

W = energy stored per unit length of circuit

v_g = group velocity of circuit wave

A common convention, when characterizing the delay lines used in crossed-field amplifiers, is to define the interaction impedance in terms of the RF fields at the surface of the delay line. The exponential decay of the fields as a function of distance to the electron stream is accounted for directly in the gain calculation. Hence, rewriting K in terms of the foregoing quantities, we have

$$K = \left(\frac{E^2}{2W}\right)\left(\frac{v_p}{\omega^2}\right)\left(\frac{v_p}{v_g}\right)$$

Now, E^2/W is a function of the geometry of a given circuit, and v_p and ω are set by the desired operating frequency and synchronous voltage. As will be discussed in Section 4.2.2, the gain, G, in decibels, follows the proportionality $G \sim L\sqrt{K}$ where L is the circuit length in wavelengths. For a given value of gain

$$L \sim \frac{1}{\sqrt{K}} \sim \sqrt{\frac{v_g}{v_p}} \qquad (2)$$

It may be generally shown - as in Pierce (Ref. 3) - that the insertion loss of a slow wave circuit has the following dependence:

$$\alpha \sim \frac{v_p}{v_g}$$

where α = insertion loss in db per wavelength

The total circuit insertion loss, α_{tot}, is given by

$$\alpha_{tot} = \alpha L$$

$$\alpha_{tot} \sim \frac{v_p}{v_g}\sqrt{\frac{v_g}{v_p}}$$

$$\alpha_{tot} \sim \sqrt{\frac{v_p}{v_g}}$$

Therefore, obtaining a high value of interaction impedance by making $v_g \ll v_p$ results in a greater overall insertion loss. For this reason, a non-dispersive circuit ($v_p/v_g \cong 1$) was chosen for the amplifier study carried out here. The choice was restricted to relatively low dispersion slow wave circuits with high interaction impedance. This led to the consideration of the helix and the helix loaded bar circuits for the UHF and S-band applications and, in addition, the meander line above a ground plane for the S-band application.

A transmission line propagating a given amount of power does this with a minimum of insertion loss under conditions of high voltage and low current operation. A low value of unit insertion loss on the delay line will be achieved if the surge impedance of the delay line is high. The surge impedance is the effective impedance to which the external 50 ohm transmission line must be matched. Unit insertion loss of the delay line in nepers per unit length is given by equation (3).

$$\alpha = \frac{R_s}{2Z_o} \qquad (3)$$

where α is the insertion loss in nepers per unit length

R_s is the effective series resistance of the delay line per unit length

Z_o is the surge or iterative impedance of the delay line.

The match to the input and output transmission lines is most easily made if the surge impedance of the delay line is 50 ohms. This is not a good reason for choosing a 50 ohm surge impedance when maximum circuit efficiency is the prime objective. Therefore, the surge impedance of the delay line chosen to meet the needs of this program was on the order of several hundred ohms. These circuits can be matched quite easily to the 50 ohm external transmission line over the limited bandwidth of 6 MHz. Development work at S-F-D laboratories on this type of circuit shows that an adequate match can be obtained over a much wider frequency range, and in some cases, over a frequency range approaching an octave.

Of the various circuits considered, the helix of rectangular cross-section and the helix loaded bar circuit are the ones that most effectively combined the desired features. The dispersion and interaction impedance characteristics of the helix slow wave circuit are well known. The helix is quite capable of maintaining a constant phase velocity over several octaves of frequency bandwidth. No

further qualitative description of its properties will be given at this point. Since the helix loaded bar circuit, which is the circuit that was finally chosen for both the UHF and S-band amplifier designs, has been less completely described in the specific format used in this program, a short description of its geometry follows.

Figure 9 is a sketch of the geometry of this circuit. The circuit consists of a series of thin capacitive metal bars mounted above a ground plane on slabs of ceramic. The ceramic used is beryllium oxide because of its thermal capabilities. These bars are connected to an inductive loading coil so that the circuit becomes a quasi-lumped element, artificial transmission line. The equivalent circuit of this structure is shown at the top of figure 9. As is indicated, the beam flows between the sole element of the crossed-field amplifier and the capacitive bars. The circuit interacts with the RF field which fringes between the bar elements. This is due to the voltage that exists across the series capacitance which is shown in the equivalent circuit. By an appropriate choice of capacitance, inductance per section of circuit, and mutual inductance between sections of circuit, the dispersion and impedance characteristics may be made highly similar to that of the helix. A typical set of experimental characteristics obtained on a helix loaded bar circuit designed for operation in the UHF region is shown in Figure 10. The almost constant phase velocity and the high interaction impedance, which varies approximately inversely as the square of the phase shift per section over the mid-range of the characteristics, are similar to the helix circuit. The major difference between the helix and the helix coupled bar circuit, therefore, is the vastly greater thermal capability of the helix loaded bar circuit. This results from the very short heat transmission path from the circuit bar on which electron current impinges to the ground plane which effectively acts as the heat sink for the system. The rectangular helix slow wave

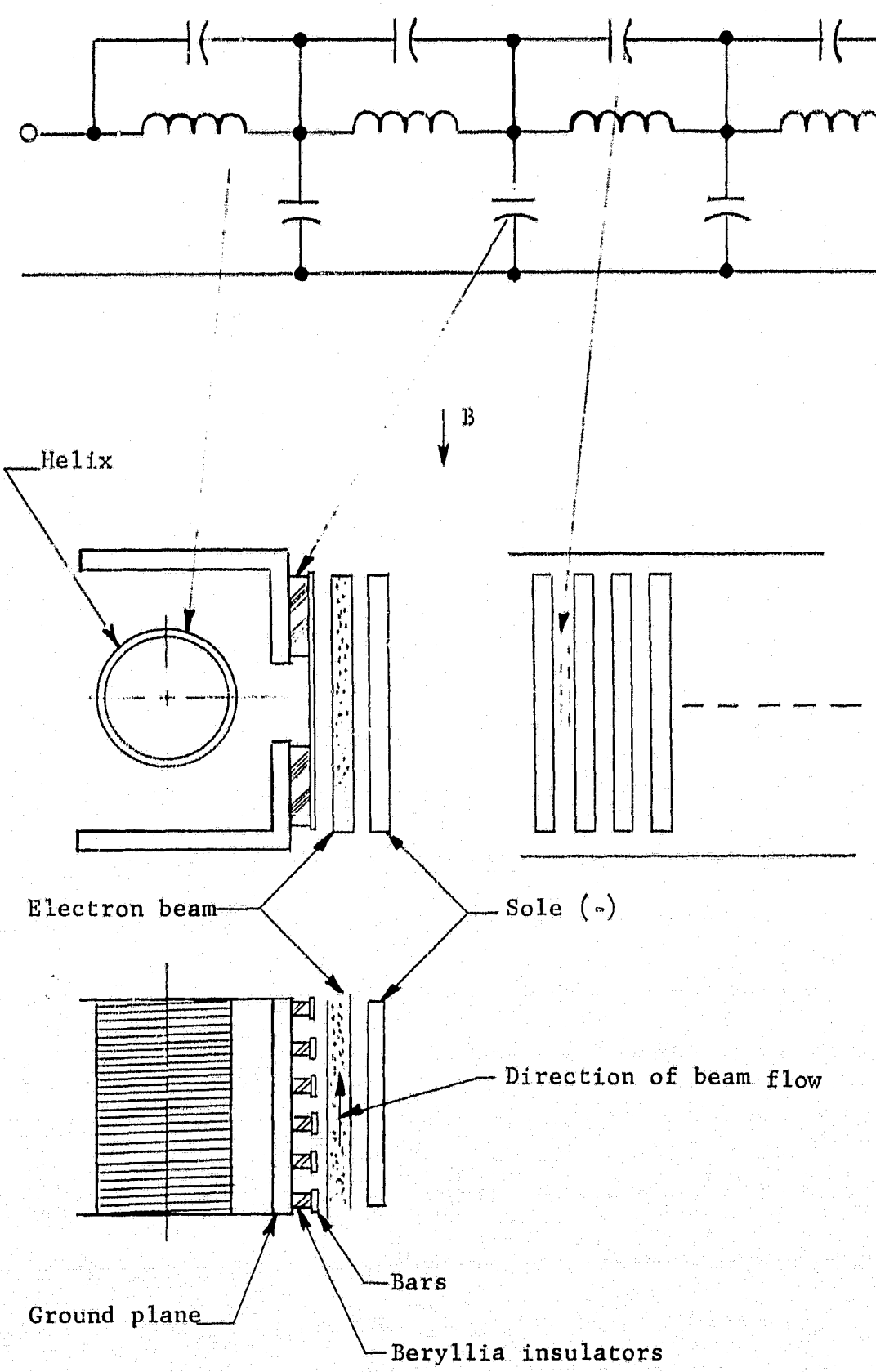

FIGURE 9 THE HELIX COUPLED BAR CIRCUIT

Sketch at the top shows the low frequency equivalent circuit of this line

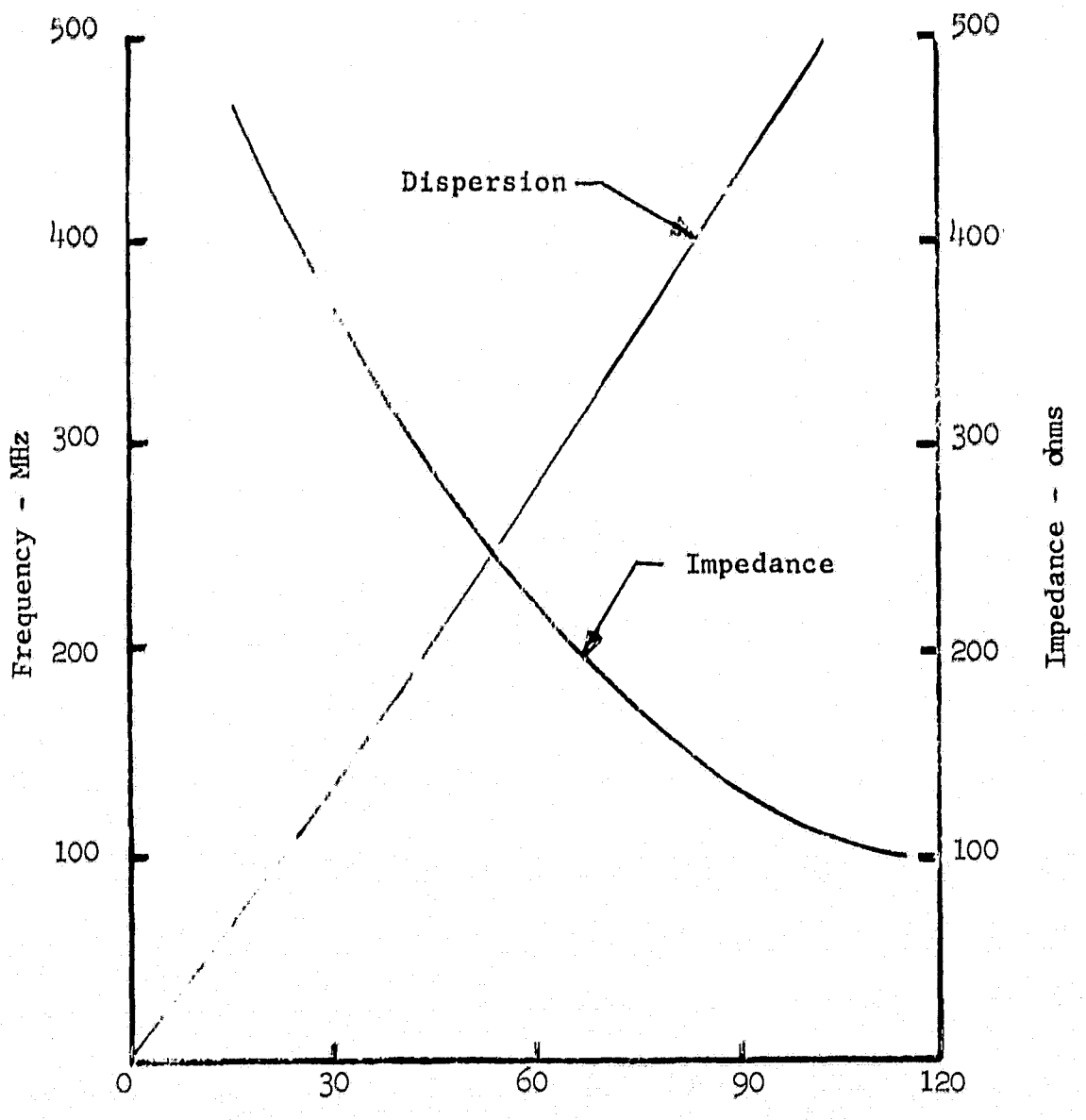

FIGURE 10 DISPERSION AND INTERACTION IMPEDANCE AS A FUNCTION OF PHASE SHIFT PER CIRCUIT SECTION FOR EXPERIMENTAL HELIX COUPLED BAR CIRCUIT

circuit can be supported on top and bottom by beryllium oxide slabs but the heat flow path then includes the length of the entire inside bar of the helix which faces the electron stream. Trade-off calculations were carried out in parallel for the two circuits and verify that the helix loaded bar circuit was indeed preferable for the applications of this program.

4.2 Relations Used in Small Signal Design Calculations

The design relationships that were used to calculate the variations of insertion loss and interaction impedance that could be expected from the delay lines for varying values of phase shift per section are discussed below. In addition, the relationships used to calculate the electronic interaction properties are tabulated.

The trade-off calculations that are subsequently presented consider variations in value of phase shift per section for the circuit and variations in operating magnetic field. Optimal operating parameters are then chosen. Certain other parameters in these comparisons are fixed. The frequency of operation has been specified. The ratio of cathode-anode voltage to synchronous voltage is fixed for a given calculation set, and the interaction impedance is specified.

4.2.1 Circuit Insertion Loss and Interaction Impedance

4.2.1.1 Properties of the Helix Slow Wave Circuit

A typical geometry for a helix of rectangular cross-section as used in a crossed-field amplifier is such that the transverse depth of successive turns is frequently equal to or greater than the turn-to-turn spacing. Thus, the sheath helix model used to analyze the properties of a helix, as used in an O-type traveling wave tube, is not appropriate to this case.

It has been found in circuit development work carried out at S-F-D laboratories that a reasonable approximation for the insertion loss and interaction impedance of the helix may be calculated by considering the helix as a strip line which is wound upon itself. This helix is of toroidal geometry and is of rectangular cross-section. The impedance is calculated at the circuit surface. The usual exponential decay of field strength as the point of observation is moved radially away from the circuit surface applies, and the effect of current distribution is accounted for in the gain calculations. This approximate calculation yields the following relationships for interaction impedance and circuit insertion loss parameters using the geometry indicated in Figure 11.

The interaction impedance for a given helix circuit structure may be determined experimentally or by an approximate calculation. The experimental measurement may be made by the standard technique of resonating a section of the slow wave circuit by placing shorts at both of its end points. One of the resulting resonances is observed, and the shift in resonant frequency when the RF fields are perturbed by a piece of dielectric material of known geometry and dielectric constant is measured. These data are used to calculate the interaction impedance. However, an approximate analytical calculation is best suited for the type of parametric study being done on this program.

As already mentioned, the rectangular helices used as delay lines in these amplifiers have a cross-sectional aspect ratio that is far removed from the idealized sheath helix. When used in a crossed-field amplifier, the width of the turn, w, is typically of the same order of magnitude as the pitch, p, in order to provide adequate thermal capability. An appreciable fraction of the RF field energy is stored in the space between adjacent turns. The classical helix analysis which assumes a thin transverse thickness, w, compared to the

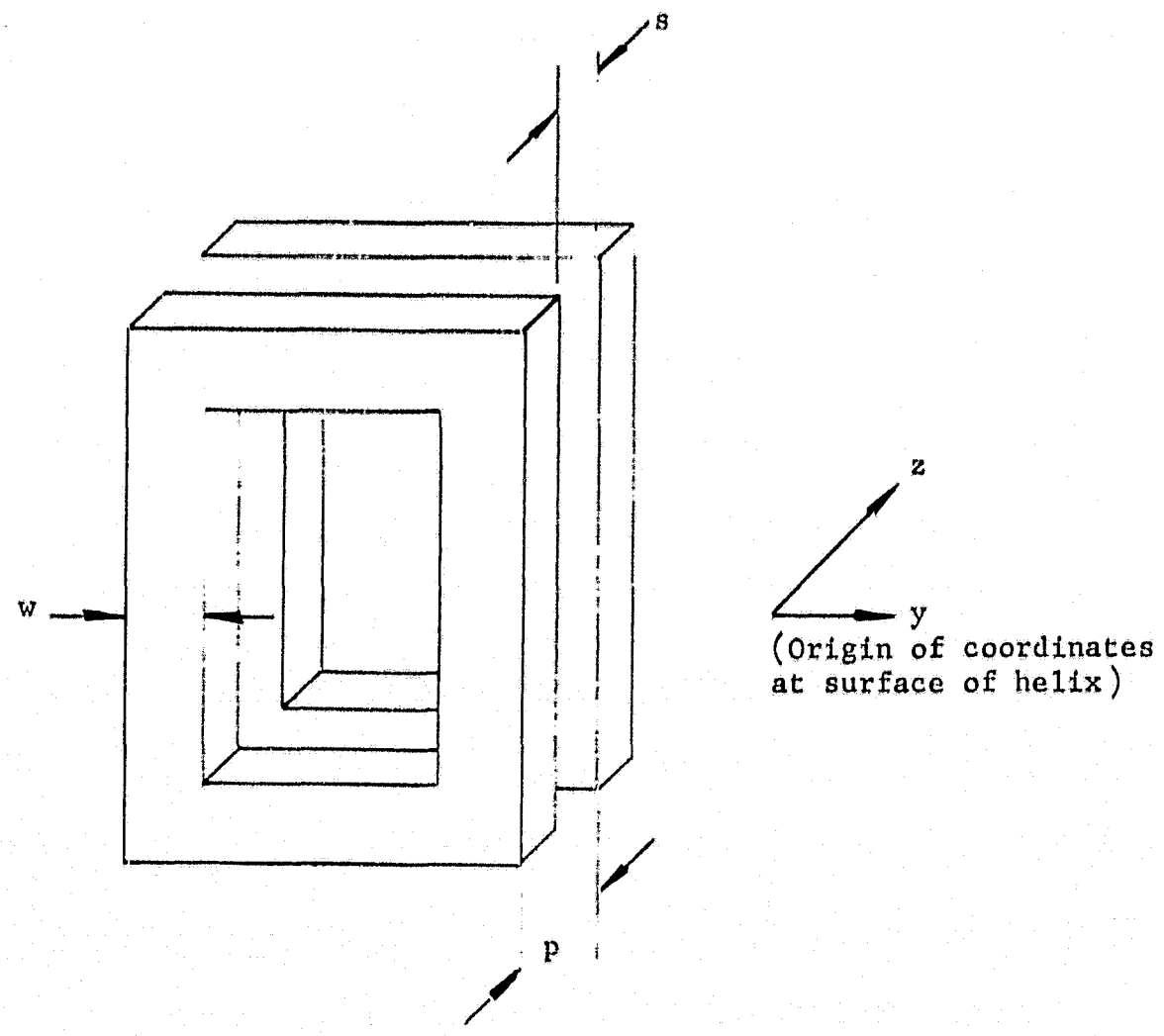

p = pitch of helix

s = spacing between adjacent turns

FIGURE 11 SKETCH OF RECTANGULAR HELIX FOR CALCULATION OF INTERACTION IMPEDANCE

pitch, p, is useless here. A somewhat different approach is needed to calculating the interaction impedance. A useful estimate can be made by regarding adjacent helix turns as forming a section of strip line and then calculating the stored energy within and without the strip line as the basis for the impedance estimate.

Rewrite the expression for interaction impedance as follows:

$$K = \frac{E^2}{2\beta^2 P} = \frac{E^2}{2\beta^2 W v_g}$$

where W = energy stored per unit length of transmission line

v_g = group velocity of circuit wave

Consider a linear version of the helix as shown in Figure 11, where y corresponds to the radial direction and z corresponds to the circumferential direction or propagation direction. To calculate the stored energy, W, consider two regions, one outside the strip line and one within the strip line. Outside the strip line, RF electric fields are given by

$$E_z = E_o(\sin \beta z)e^{-\beta y}$$

$$E_y = E_o(\cos \beta y)e^{-\beta y}$$

where E_z = RF electric field in z-direction

E_y = RF electric field in y-direction

E_o = amplitude of fundamental space harmonic

$$\text{Energy/unit volume} = \epsilon(E_z^2 + E_y^2) = \epsilon E_o^2 e^{-2\beta y}$$

where ϵ = dielectric constant of space around the helix

The energy per unit length of line in the z-direction, W_1, is given by

$$W_1 = 2\bar{L} \int_o^\infty \epsilon E_o^2 e^{-2\beta y}\, dy$$

$$W_1 = \frac{\bar{L}\epsilon E_o^2}{\beta}$$

where $\bar{L}$ = mean perimeter of helix turn

The factor 2 approximates the summation of fields inside and outside the helix. Since much of the field energy is stored between adjacent turns, the fields decay rapidly away from the helix surface. Thus one inside surface does not "see" the fields at the opposite inside surface. The factor 2 is used as if the fields were symmetrical going from the inside to the outside of a helix section.

If a voltage, V, is taken to exist across the strip line, and a uniform electric field, V/p, is assumed to exist across the strip line, then E_o (which is taken at the outer surface of the helix), is given by

$$E_o = M\left(\frac{V}{p}\right)$$

where p = pitch of circuit

M = geometric factor for calculating space harmonic component of RF electric field

$$M = \frac{\sin \frac{\beta s}{2}}{\frac{\beta s}{2}}$$

where s = spacing between adjacent turns

The assumption of a uniform electric field across the strip line is a fair approximation for the low order space harmonic terms. Only the fundamental term is of interest here. Then

$$W_1 = \frac{L}{p} \frac{\epsilon M^2 V^2}{\beta p}$$

For the helices considered for use in the non-dispersive region

$$\frac{L}{p} \approx \frac{c}{v_g} = \frac{c}{v_p}$$

where c = speed of light

$$W_1 = \frac{\epsilon M^2 (\frac{c}{v}) V^2}{\beta p}$$

Within the strip line,

$$Z_o = \frac{V^2}{2Wc}$$

where Z_o = strip line characteristic impedance.

The energy per unit length along the strip line is

$$W = \frac{V^2}{2Z_o c}$$

Along the helix in the z-direction, this becomes

$$W_2 = \frac{V^2}{2Z_o c} \frac{c}{v_g} = \frac{V^2}{2Z_o v_p}$$

The net interaction impedance, K, is given by

$$K = \frac{E^2}{2\beta^2 P} = \frac{M^2 (\frac{V}{p})^2}{2\beta^2 (W_1 + W_2) v_g}$$

$$K = \frac{M^2\left(\frac{V}{p}\right)^2}{2\beta^2 v_g\left[\frac{\epsilon M^2 V^2 \frac{c}{v_g}}{\beta p} + \frac{V^2}{2Z_o v_g}\right]}$$

$$K = \frac{1}{\left[2\epsilon c(\beta p) + \frac{(\beta p)^2}{M^2 Z_o}\right]}$$

$$K = \frac{1}{(0.005)(\beta p) + \frac{(\beta p)^2}{M^2 Z_o}} \qquad (4)$$

The expression given in equation (4) has its greatest accuracy at the mid-range frequencies and larger values of the phase shift per section, βp. At the higher frequencies, the first term in the denominator of equation (4) becomes relatively unimportant and the interaction impedance is seen to vary inversely as the square of the phase shift per section. This was the relationship assumed in estimating helix properties as a function of βp. The effect of dielectric loading has been neglected since the helix is supported in such a manner that the dielectric-support pieces do not bridge any helix turns. The validity of this assumption is verified since the phase velocities measured experimentally agree within a few percent with that calculated by the approximate relationship, $L/p = c/v_p$.

The expression given for the interaction impedance, K, has been found experimentally to give reasonably accurate results except for very small values of θ, the phase shift per section of circuit. This is illustrated by the following comparison of calculated and experimentally measured values of interaction impedance for a helix circuit used in a UHF crossed-field amplifier.

Phase Shift per Section (degrees)	$\frac{K\ (calculated)}{K\ (measured)}$
13	2.26
39	0.866
78	1.06

As will be seen, the designs arrived at in this study centered about a phase shift per section of 90°. Thus, in this region, the expression given is a reasonable guide to estimating the parametric variation of the interaction impedance.

The insertion loss per unit length of the helix circuit is estimated directly from the value of the surface resistivity for copper. Calculating the series resistance, R_s

$$\frac{R_s}{2} = 2.52 \times 10^{-7} \sqrt{f} \frac{L}{w} \quad \text{per turn}$$

where f = frequency

$\bar{L}$ = the mean perimeter of a helix turn

w = width of circuit element

This expression is corrected for the estimated operating temperature of the copper.

The attenuation factor, α, in db per unit length in the z direction of Figure 11 is then

$$\alpha = 8.68 \frac{R_s}{2Z_o} \frac{1}{p}$$

The ensuing trade-off calculations will show that as θ is increased for a given helix geometry, the interaction impedance decreases but the total insertion loss decreases if the radial depth of the turn

and the synchronous voltage are kept constant. This follows from the relations

$$K \cong \frac{M^2 Z_o}{(\beta p)^2} = \frac{M^2}{\phi^2}$$

$$v = \frac{\omega}{\beta} = \frac{\omega p}{\phi}$$

where v = phase velocity

$\phi = \Theta\pi/180^\circ$, phase shift per section in radians

If the phase velocity is kept constant, i.e., $p \sim \Theta$, then

$$Z_o \sim s \sim p$$

Therefore

$$K \sim \frac{p}{\Theta^2} \sim \frac{\Theta}{\Theta^2} \sim \frac{1}{\Theta}$$

As shown in Section 4.2.2,

$$G \sim N\sqrt{K}$$

where N = number of circuit wavelengths

Therefore

$$G \sim \frac{N}{\sqrt{\Theta}}$$

and for constant gain, $N \sim \sqrt{\Theta}$.

The total attenuation, α_{tot}, is

$$\alpha_{tot} \sim \frac{n\bar{L}}{Z_o} \sim \frac{n\bar{L}}{p} \sim \frac{n\bar{L}}{\Theta}$$

where n = total number of circuit sections

For a non-dispersive helix

$$\bar{L} \cong \frac{\theta}{2\pi} \lambda$$

where λ = free space wavelength at given frequency

Therefore

$$\alpha_{tot} \sim n \frac{\theta}{2\pi} \frac{1}{\theta}$$

but

$$\frac{n\phi}{2\pi} = N$$

where N = total number of circuit wavelengths

Thus

$$\alpha_{tot} \sim \frac{N}{\theta}$$

However, for constant gain

$$N \sim \sqrt{\theta}$$

Therefore

$$\alpha_{tot} \sim \frac{\sqrt{\theta}}{\theta} = \frac{1}{\sqrt{\theta}}$$

The foregoing is a specific relationship for the case where the width of the helix turn, w, is kept constant as θ is varied.

Thus, the optimal value is a compromise between the variation of interaction impedance and unit insertion loss as a function of phase shift per section for the circuit.

4.2.1.2 Properties of the Helix Loaded Bar Circuit

The interaction impedance of the helix loaded bar circuit is calculated from the equivalent transmission line parameters of the circuit. These are the capacitance, inductance, and mutual inductance per unit length. This is the impedance which appears across the capacitance between bars. A surge impedance (characteristic impedance) for this transmission line, in terms of the voltage appearing between the capacitive bar and the ground plane, may also be calculated from the transmission line parameters. The calculation of both the interaction and surge impedances is carried out by a straightforward application of standard network theory to a transmission line with lumped elements. Thus, it will not be elaborated on further at this point.

The surge impédance is the impedance to which the external 50 ohm transmission line must be matched. Although the use of a high surge impedance makes the problem of external match somewhat more difficult, it also results in a higher interaction impedance and, most important, in a lower effective unit insertion loss. Unit insertion loss is again calculated by taking the effective series resistance of the line per unit length and dividing by twice the characteristic impedance of the line. This gives the attenuation factor in nepers per unit length. The effective series resistance of the helix loaded bar circuit is calculated by adding up four components of loss. The first component is the actual ohmic loss in the skin of the inductive coil calculated at the frequency of operation. In addition, there are ohmic losses due to the charging currents that flow into the capacitive bar from the connection to the loading coil. These currents effectively flow in the braze interface between the bar and the beryllium oxide ceramic and in the interface between the ceramic and the ground plane. To calculate this loss factor, it is assumed that these charging currents are flowing in a skin depth

of pure molybdenum on the presumption that the molybdenum-manganese technique is being used to make the braze. Two additional, but less important, contributors of loss are the actual losses in the dielectric and the series transmission line current flowing across the width of the bar. These last three components of loss are converted into equivalent series resistances, taking into account the phase shift between currents flowing in the capacitive section and inductive section of the transmission line. Thus, the entire loss of the line is reduced to an equivalent series resistance. The loss per unit length of line is then calculated.

The four components of loss may be tabulated as follows:

1. <u>The series resistance per unit length in the inductive coil, R_{s_1}</u>. A coil diameter and coil wire size are chosen for the proper values of self-inductance and mutual inductance between circuit sections. The series resistance of round copper wire, R_s, is given by

$$R_s = \frac{83.2\sqrt{f}}{d}$$

where f = frequency

d = wire diameter in centimeters

Thus,

$$R_{s_1} = \frac{R_s \pi \bar{D} m}{p}$$

where $\bar{D}$ = mean diameter of coil

m = number of turns per circuit section

p = pitch of circuit section

R_{s_1} is one of the major components of circuit loss.

2. <u>Loss due to series current flowing across the height of the copper bars (return path in ground plane), R_{s_2}</u>

$$\frac{R_{s_2}}{2} = 2.52 \times 10^{-7} \sqrt{f} \sqrt{\frac{\rho_2}{\rho_1}} \frac{h}{w}$$

where f = frequency

ρ = unit volumetric resistivity of metal

ρ_2/ρ_1 = ratio of resistivity of molybdenum to copper (about 3)

h = axial height of circuit bar

w = width of circuit bar

R_{s_2} is a minor loss factor.

3. Loss due to shunt or capacitive charging current, R_{s_3}.

This current creates loss by flowing axially in the interface between circuit bar and ceramic, and ceramic and ground.

Assume the worst case, where the coil is connected at one end of the bar so that the charging current must flow along the entire length of the bar.

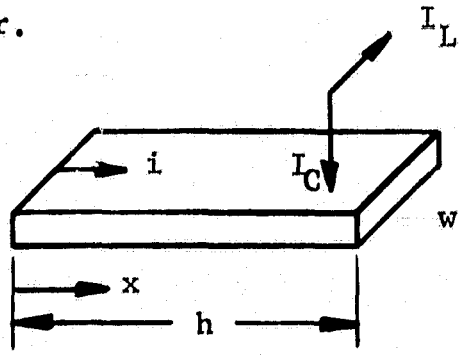

If the coil is connected at the right hand end of the bar and the capacitive or shunt current flowing from the series coil into the bar is I_C, then the current amplitude along the bar, i, as a function of distance from the free end is

$$i = \frac{x}{h} I_C$$

If the resistance per unit length axially in the braze interface is r, then the power dissipated along the bar, P_d, is

$$P_d = \int_o^h r\left(\frac{x}{h} I_C\right)^2 dx$$

$$P_d = \frac{I_C^2}{h^2} \frac{h^3}{3} r$$

$$P_d = \frac{hr}{3} I_C^2$$

The resistance is the same as if all the current flowed in one-third of the bar height. Thus, with a factor of 2 for the top and bottom interface of beryllium oxide bar,

$$\frac{R_{s_3}}{2} = 2.52 \times 10^{-7} \sqrt{f} \sqrt{\frac{\rho_2}{\rho_1}} \frac{h}{3w} \left(\frac{I_C}{I_L}\right)^2$$

where h = axial height of bar

w = width of bar in circumferential direction

I_C = amplitude of shunt current

I_L = amplitude of series current

The ratio I_C/I_L is introduced to convert R_{s_3} to an equivalent series resistance. For 90° phase shift per circuit section, $I_C/I_L = \sqrt{2}$ For 60° phase shift per section, $I_C/I_L = 1$, and so forth. R_{s_1} and R_{s_3} are the major loss components.

4. <u>Effective series resistance representing the dielectric losses in the beryllium oxide (BeO) slab</u>, R_{s_4}

$$R_{s_4} = \frac{\delta}{\omega C} \left(\frac{I_C}{I_L}\right)^2 \frac{1}{p}$$

where δ = loss tangent of BeO, $\delta = 3 \times 10^{-4}$

C = capacitance of circuit bar to ground

$\omega = 2\pi f$

R_{s_4} is a minor loss component.

The total resistance, R_T, therefore is

$$R_T = R_{s_1} + R_{s_2} + R_{s_3} + R_{s_4}$$

The unit insertion loss, α, is

$$\alpha = 8.68 \frac{R_T}{2Z_o} \text{ db per unit length}$$

The foregoing relations were used to calculate the effective insertion loss per unit length in the trade-off calculations made for the helix loaded bar circuits.

4.2.1.3 The Meander Line Circuit

In the trade-off calculations for the S-band circuit, the possibility of using a meander line above the ground plane is briefly considered. In this case, the attenuation is calculated in a straightforward fashion, simply treating the line as a convoluted transmission line formed by a strip line above a ground plane. The major component of forward resistance is due to the ohmic losses in the brazed joints, the beryllium oxide ceramic and the ground plane. This, once again divided by twice the strip line or surge impedance, yields the attenuation factor to be used in the trade-off calculations.

4.2.2 Relations Used for Small Signal Gain Calculations

The relations used to calculate the operating characteristics of the axial injection crossed-field amplifier were adapted from relationships that have been developed for the conventional injected beam crossed-field amplifier. In these relations, an effective circulating current is defined in terms of the cathode injection current and the number of circumferential revolutions that a given electron makes in the time of one axial transit through the interaction space. Effective circulating current is the cathode current multiplied by this ratio as is demonstrated in Section 4.0. An interaction space model, therefore, may be set up for calculation purposes as is indicated by Figure 12. The key relationships used in the calculation are given in Table II. When applying these relationships, all voltages were taken with respect to cathode voltage. This was true even though the delay line was actually at ground potential.

The terms used in Table II are defined as follows.

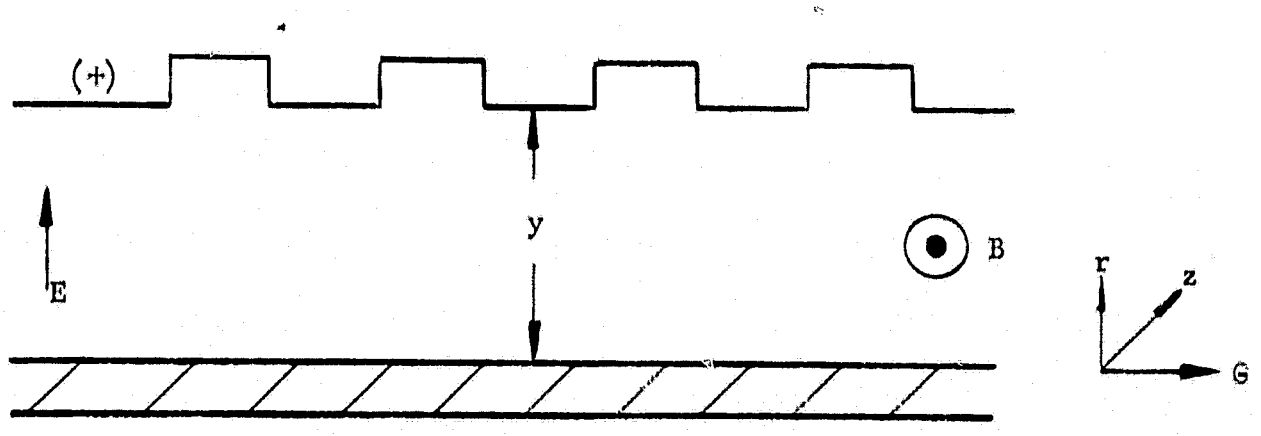

FIGURE 12 SKETCH OF INTERACTION SPACE GEOMETRY

TABLE II

DESIGN RELATIONSHIPS FOR CALCULATION OF ELECTRICAL PERFORMANCE

$$\frac{\omega_c}{\omega} = \left[\frac{\frac{V_a}{V_o} - 1}{2\beta y}\right] \tag{1}$$

$$D = \left[\frac{1}{2}\,\frac{\omega}{\omega_c}\,\frac{I_c}{V_o}\,K\right]^{\frac{1}{2}} e^{-\beta y} \tag{2}$$

$$K = \frac{E^2}{2\,\beta^2 P}$$

$$G = -6 - \frac{\alpha N}{2} + 55DN \quad (db) \tag{3}$$

$$N = \frac{G + 6}{55D - \frac{\alpha}{2}}$$

$$I_c = 1.56hBV_o 2k\left[1 - \frac{k}{2}\right] \tag{4}$$

where $k = \frac{\Delta v}{v} = 1 - \sqrt{1 - Q}$

$$Q = \frac{I_c}{1.56hBV_o}$$

$$S = \frac{1}{2D}\left[\frac{\Delta v}{v}\right] \tag{5}$$

Equation (1)

ω_c = cyclotron radian frequency

$\omega_c = (e/m)B$

B = operating magnetic field

e/m = charge-to-mass ratio for electron

V_a = cathode-anode voltage

V_o = synchronous voltage

$\beta = \omega/v_p$, propagation constant of delay line

y = distance from outer surface of beam to anode

Equation (2)

D = gain parameter

I_c = circulating beam current

Equation (3)

G = small signal gain in db

α = insertion loss in db per circuit wavelength

N = number of wavelengths on the circuit

Equation (4)

h = axial height of circuit

B = axial magnetic field

v = circumferential velocity of outer surface of beam

Δv = difference in circumferential velocity between outer and inner surface of the beam

Equation (5)

S = diocotron gain parameter

The relations of Table II are applied to the selection of a slow wave circuit and optimized operating parameters in the manner described below.

In Section 4.3, each set of trade-off calculations has several fixed parameters. The ratio of anode-to-synchronous voltage, V_a/V_o, is set and the interaction impedance, K, appropriate to the

circuit frequency and the phase shift per section is selected. The frequency is set and the phase shift per section is fixed for a given set of calculations. The variable parameters are βy (the electrical spacing of the electron stream from the circuit), and ω_c (the cyclotron radian frequency), which is directly proportional to the applied magnetic field. The synchronous voltage, V_o, has been chosen from the circuit design and the circulating current, I_c, is chosen on the basis of a desired power output and expected efficiency. The expected conversion efficiency, η, is the circuit efficiency, η_c, multiplied by the electronic efficiency, η_e. These efficiencies are defined as follows

$$\eta_e = \frac{P}{P_{dc}}$$

$$\eta_c = \frac{P_o}{P}$$

$$\eta = \frac{P_o}{P_{dc}}$$

where P = RF power generated

P_{dc} = dc power input

P_o = RF power output

The calculation of electronic efficiency is discussed in Section 4.4.

The second relationship in Table II is used to obtain a gain parameter, D. The third relationship is used to give the necessary number of circuit wavelengths to obtain the desired gain. At this point the insertion loss per unit length that has been calculated for the circuit at the given frequency and phase shift is utilized. Having calculated the total number of wavelengths, the total insertion loss is determined. The fourth relationship in Table II is the Brillouin condition for space charge limited flow in a crossed electric and magnetic field system. This relationship is used to calculate the

relative slip in circumferential velocity between the outer surface of the beam and the inner surface of the beam, k (the velocity differential divided by the velocity of the outer surface). This then leads to a calculation of the diocotron gain parameter, S, in terms of the velocity slip factor and the electronic gain parameter, D.

One of the boundary limits in the trade-off calculations is the maximum permissible value of the diocotron gain factor, S. It can be shown that the diocotron gain within the electron stream is approximately given by the factor S times the electronic gain of the tube. The maximum value of S in these trade-off calculations was set at about 2 since the electronic gain selected for these calculations was 20 db. This gives a possible diocotron gain of about 40 db. The background noise which may be generated in the beam would then be on the order of 40 db above thermal noise level. This is more than adequate to meet the dynamic range and signal-to-noise requirements of this program, since the designated dynamic range is 20 db with a signal-to-noise ratio of 42 db minimum and 55 db desirable. Thus, within a 6 MHz bandwidth, the background noise power level should be between 62 db and 75 db below the peak of synchronizing power level. The thermal noise in a 6 MHz bandwidth is approximately -106 dbm. If the electron gun has a typical 40 db noise figure, the noise level in the electron stream would be -66 dbm. If the diocotron gain is 40 db, then -26 dbm of noise power might appear at the output of the tube.

It is desirable that the noise level be as much as 75 db below 7.5 kw or -7 dbm. This is a 19 db safety factor for the signal-to-noise ratio of 55 db and a 33 db safety factor with respect to the requirement for a minimum signal-to-noise ratio of 42 db. The limit of the diocotron gain parameter, S, was chosen on this basis.

This portion of the analysis is guided by the general considerations that have been developed by R.W. Gould (Ref. 4).

The determination of an appropriate level of gain upon which to base the crossed-field amplifier designs employed the following considerations. If it is postulated that the crossed-field amplifier will achieve a conversion efficiency of 80% and that this crossed-field amplifier (CFA) is then driven by a low level traveling wave tube driver whose conversion efficiency is 30%, then the efficiency of the entire amplifier chain (driver plus crossed-field output amplifier) is given by

$$\eta = \frac{P_o}{\frac{P_o}{0.8} + \frac{P_o}{(0.3)G}} = \frac{1}{1.25 + \frac{3.33}{G}} \qquad (5)$$

where P_o = output power of CFA

G = power gain of CFA

The value of this expression is plotted as a function of the CFA gain, G, in Figure 13. From this graph, it is seen that increases in CFA gain beyond the 20 db point result in an increasingly smaller benefit in total package efficiency while increasing the risk of system instability. Thus, a design gain objective of 20 db was chosen as being the point at which additional increments in output amplifier gain produce unimportant increases in efficiency but do place greater pressure on the quality of the match that the antenna load presents to the output amplifier.

4.3 Trade-off Calculations for Comparison of Circuits and Selection of Operating Parameters

The following sub-sections summarize the details of the trade-off calculations used in the final selection of the circuits and the determination of the design parameters for the two amplifiers.

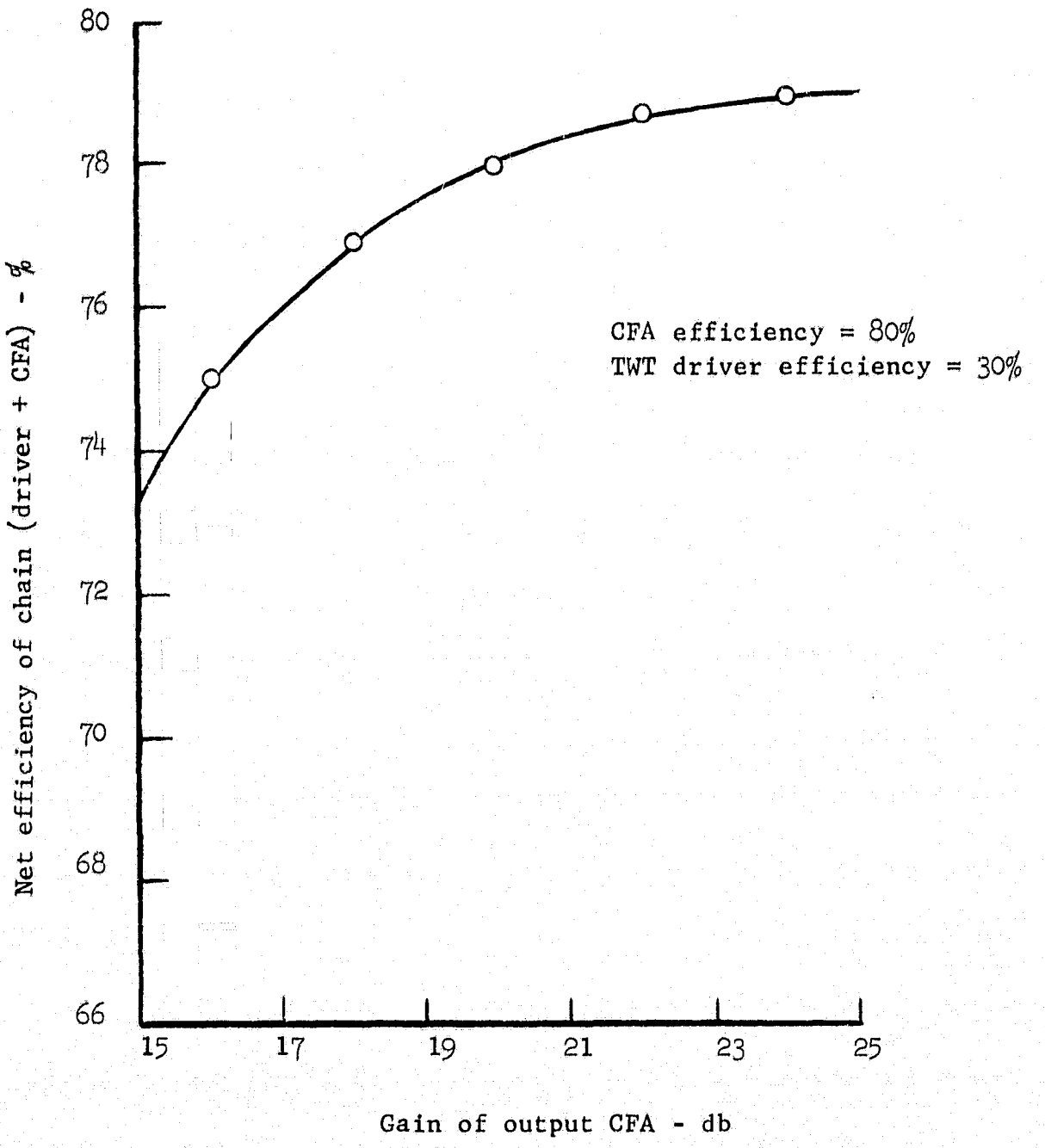

FIGURE 13 CHAIN EFFICIENCY VERSUS CFA GAIN

For each of the slow wave structures that were investigated, the performance of the circuit for a range of values of magnetic field were examined. This was done at each of two different values of phase shift per section for each circuit. These calculations were carried out for a fixed small signal gain level of 20 db and a ratio of cathode-anode voltage to synchronous voltage of 15 to insure a high level of electronic efficiency.

The first priority in the selection of circuits and operating parameters was given to achieving the lowest total insertion loss for the circuit that was consistent with a diocotron gain parameter, S, of not more than 2 to 3. The lowest insertion loss criterion was set up to achieve a maximum circuit efficiency. The constraint of a maximum allowable value of diocotron gain was to assure compliance with the dynamic range and signal-to-noise ratio requirements.

The second consideration was then applied to those configurations which met the attenuation and S parameter criteria. This was the achievement of a maximum thermal conductance for the slow wave circuit and its support structure. The result is a minimum circuit operating temperature while allowing for the design of an efficient heat transfer and radiation system. For those design candidates which met the trade-off selection criteria equally well, a final choice was made on the basis of minimum size and weight.

4.3.1 The UHF Amplifier

In the early phase of this study program, the peak synchronizing power output for the UHF amplifier had been designated as 15 kw. At a later point in the program, this design objective was reduced to 7.5 kw at the direction of NASA Lewis Research Center. Trade-off calculations had already been carried out for the 15 kw design; the results of these calculations are presented here, along

with the final calculations for the 7.5 kw design. The early calculations also show the trend of results that led to the final selection of operating parameters.

The results of seven sets of calculations will be presented here. These led to the selection of the helix loaded bar circuit and the final design parameters for the amplifier. The first five sets of calculations were carried out for the 15 kw peak power design with the last two leading to a scaling of the results to the 7.5 kw level. Much of the detail of the original calculations was still adequate to select the circuit, and a scaling of the operating parameters was carried out. All the calculations for the UHF design (with one exception) were done for an interaction impedance level of 200 ohms. Experience has shown this to be a feasible value in the UHF band, both for the helix circuit and the helix loaded bar circuit.

Measurements on the helix loaded bar circuit are illustrated in Figure 14. Experimentally determined values of interaction impedance are plotted against phase shift per section. These were taken on a circuit which operated in the UHF frequency band and had a synchronous voltage of 500 volts.

No measurements have been made on a helix circuit which has a synchronous voltage of 945 volts as developed for the UHF design here. However, measurements made on UHF circuits in the range of 100-150 volts indicate that these circuits, when scaled to 945 volts, should achieve about 200 ohms of interaction impedance.

The meander line was not considered for the UHF application because of its excessive size at this frequency. The ratio of anode voltage to synchronous voltage was set at 15, which was close to an optimal value. The selection of a higher value for this ratio results in somewhat increased electronic efficiency but reduced gain per unit length of given circuit. Therefore, the circuit efficiency would be decreased. In addition, magnetic field requirements are increased as the ratio of anode voltage to synchronous voltage is increased.

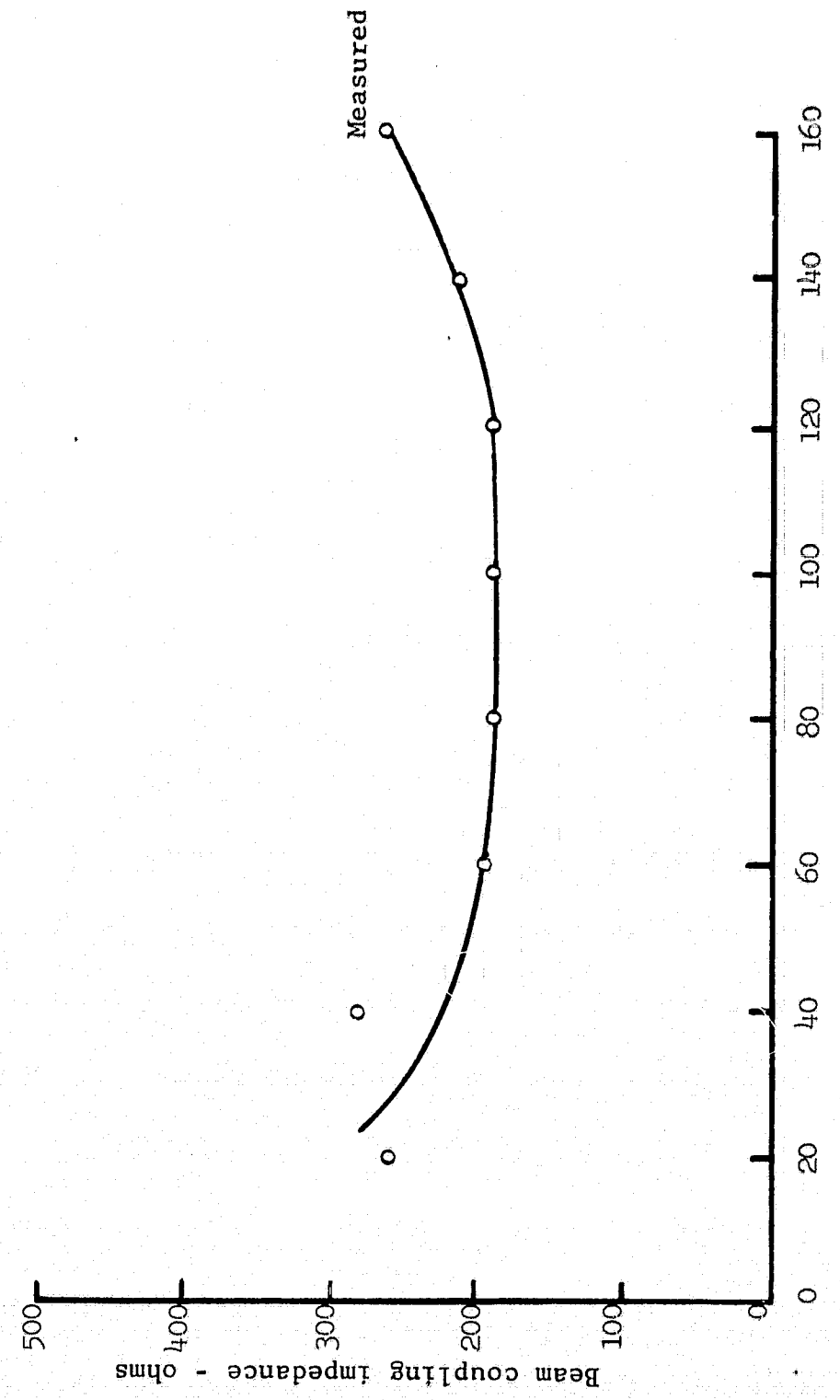

FIGURE 14 BEAM COUPLING IMPEDANCE FOR HELIX LOADED BAR CIRCUIT

The designs consider two values of phase shift per section, 60° and 90°. This was done to examine the effect that centering the design at different points would have on the dispersion characteristics fo the circuits. As will be seen, a lower phase shift per section yields an unimportant improvement in thermal capability but is accompanied by a higher insertion loss. Thus, the final selection led to the choice of 90° phase shift per section as the operating point. The details are first given for the 15 kw design. The 7.5 kw scaling then follows.

The UHF designs for 60° and 90° phase shift per section for the helix and bar circuits have the following values in common.

Frequency	850 MHz
Gain	20 db
Anode voltage	18 kv
Delay line synchronous voltage	1.2 kv
Peak power output	15 kw
Average power output	5 kw
Propagation constant, β	6.59 rad/in
Cathode current	1.6 amps
Circulating current	1.6 amps
Interaction impedance	200 ohms

Table III considers the specific case where the phase shift per circuit section, θ, is 90°, and Table IV treats the specific case where the phase shift per circuit section is 60° Within each table, the running variable is the spacing in electrical radians between the beam and the delay line, which physically means that the running variable is the operating magnetic field. The explanation and significance of the various symbols follow. Since some of the variables have the same value for either the helix or the bar circuit design, they have been combined into one table. Those values that are distinct to one circuit or the other are called out in separate columns.

TABLE III

DESIGNS OF UHF HELIX (U-1) AND HELIX LOADED BAR (U-2) CIRCUITS WITH $\theta = 90^{\circ}$

1.	βy, rad	1.0	1.5	2.0
2.	ω/ω_c	7.00	4.66	3.50
3.	f_c, MHz	5950	3960	2980
4.	B, gauss	2120	1410	1060
5.	D, db	0.0506	0.0377	0.0264
6.	55D, db	2.78	2.08	1.45
7.	N	10	13	19
8.	n = 4N	40	52	76
9.	L = p(4n + 6), in	11.05	13.92	19.7
10.	ID = L/π, in	3.52	4.44	6.26
11.	α_{tot}, db			
	a. Helix circuit	0.25	0.325	0.475
	b. Bar circuit	0.140	0.182	0.266
12.	$\Delta T(max)$, ^{o}C			
	a. Helix circuit	383	289	202
	b. Bar circuit	48.8	37.3	26.1
13.	Q	0.159	0.239	0.318
14.	$\Delta v/v$	0.08	0.126	0.174
15.	S = $(\Delta v/v)/2D$	0.79	1.67	3.29
16.	$P_d(max)$, w	63.9	48.1	33.6
17.	y, in	0.152	0.228	0.304

TABLE IV

DESIGNS OF UHF HELIX (U-3) AND HELIX LOADED BAR (U-4) CIRCUITS WITH $\theta = 60^{\circ}$

1.	βy, rad	1.0	1.5	2.0
2.	ω/ω_c	7.00	4.66	3.50
3.	f_c, MHz	5950	3960	2980
4.	B, gauss	2120	1410	1060
5.	D, db	0.0506	0.0377	0.0264
6.	55D, db	2.78	2.08	1.45
7.	N	10	13	19
8.	n = 6N	60	78	114
9.	L = p(6n + 9), in	11.02	13.9	19.7
10.	ID = L/π, in	3.52	4.42	6.27
11.	α_{tot}, db			
	a. Helix circuit	0.25	0.325	0.475
	b. Bar circuit	0.198	0.257	0.376
12.	$\Delta T(max)$, $^{\circ}C$			
	a. Helix circuit	212	163	112
	b. Bar circuit	34.2	26.8	18.0
13.	Q	--	--	--
14.	$\Delta v/v$ (helix only)	0.142	0.224	0.314
15.	S = $(\Delta v/v)/2D$ (helix only)	1.4	2.97	5.95
16.	$P_d(max)$, w	42.5	32.7	22.4
17.	y, in	0.152	0.228	0.304

For purposes of the thermal aspect of the 15 kw design, it was allowed that 1.5 kw may be dissipated on either the delay line or the multi-element collector structure.

Examining Table III, βy (Line 1) is the normalized spacing from the top of the electron stream to the delay line, where β is the propagation constant in radians per inch and y is the physical distance in inches. The parameter, ω_c/ω, is the ratio of cyclotron radian frequency, for the magnetic field used, to the signal frequency, and is given in Line 2. This sets the value of operating magnetic field B in gauss, which is given in Line 4. Line 5 is the gain parameter D, as given by equation (6)

$$D = \left[\frac{1}{2}\,\frac{\omega}{\omega_c}\,\frac{I_c}{V_o}\,K\right]^2 (e^{-\beta y}) \qquad (6)$$

where I_c = circulating current
V_o = synchronous voltage
K = interaction impedance

This is related to the net gain in db of the tube as given by the relation

$$G = -6 - \frac{\alpha}{2} + 55\ DN \qquad (7)$$

where α = circuit insertion loss in db
N = number of circuit wavelengths

In Line 6, 55D is essentially the gain per circuit wavelength in db. In Line 7, N is the number of circuit wavelengths required to give 20 db of gain, taking the circuit insertion loss for the particular circuit into account. In Line 8, n gives the number of active circuit sections. L in Line 9 is the linear length corresponding to the inside diameter of the circuit. This includes a blank section which

is the drift tube space provided for debunching the electron stream so that no electronic reentrancy occurs. Line 10 gives the inside or bore diameter of the circuit corresponding to L. Line 11 gives the insertion loss of the helix and the bar circuit.

Line 12 gives the maximum temperature rise for the circuit element having the highest thermal flux density. This is the temperature rise from the hottest point on the circuit through to the far side of the supporting beryllium oxide element. The maximum power density is obtained by dividing the power dissipation (in this case, 1.5 kw), by the number of active circuit elements and then allowing for a 70% non-uniformity factor in the power distribution along the circuit. In both the bar circuit and the helix designs, the axial circuit height was 1 inch.

Line 13 contains an intermediate parameter, Q, which is given by equation (8) in mks units.

$$Q = \frac{I_c}{1.56\ hBV_o} \tag{8}$$

where h = circuit height

B = magnetic field

Q is used to calculate the highly important velocity slip parameter given in Line 14. Equation (9) gives the relationship between Q and $\Delta v/v$, which is the velocity slip, from the top edge of the beam facing the delay line to the bottom edge of the beam, divided by the velocity at the top edge of the beam. The velocity at the top edge corresponds to the synchronous voltage, V_o.

$$\frac{\Delta v}{v} = 1 - \sqrt{1 - Q} \tag{9}$$

Line 15 contains the S parameter,

$$S = \frac{1}{2D}\frac{\Delta v}{v}$$

It should be remembered that D is the gain parameter. The S parameter is the significant factor in determining the noisiness of the beam. The diocotron gain of the beam is equal to S times the gain of the amplifier. As previously explained, a maximum value of about 2 was set for S. Looking at Table III, it is seen that this limitation permits a βy of no more than 1.5 with a corresponding magnetic field of 1410 gauss. Also, the bar circuit has the lower attenuation value and, in addition, is far superior in thermal characteristics. The helix of this circuit design was 1" high and 0.73" wide, having a radial thickness of 0.040".

In Table IV an evaluation is made using 60° phase shift per section where the circuit pitch is 0.160". The bar circuit is still taken to be 1" high. However, the helix circuit height is reduced to 0.600". It is seen that in this case, for the helix circuit, βy must be restricted to no more than 1, which means a higher magnetic field 2120 gauss. The 60° bar circuit insertion loss was no better than for the 90° design. The insertion losses for the helix circuit for the 90° phase shift per section and 60° phase shift per section cases are the same due to a coincidence of numbers. It turns out that for either helix, the attenuation per wavelength is about 0.025 db. A reasonably clear choice is indicated by these two tables. The helix loaded bar circuit operating at 90° phase shift per section has lower insertion loss and better thermal properties. A maximum βy of 1.5 is set by dynamic range considerations.

The depth of the helix circuit turn in the 60° case is 0.080", while it is only 0.040" in the 90° case. Additional design analyses were carried out on the helix circuit, allowing the radial depth of

the helix, Δr, to remain at 0.080" and analyzing its performance characteristics at a phase shift per section of 90°. This resulted in a reduction of the coupling impedance, K, to 113 ohms, with no advantage being gained in any of the other characteristics and a price being paid in a bigger, heavier circuit. The results of this design calculation are given in Table V.

The next step was to revise the UHF design in terms of the new set of operating power levels. Previous calculations indicated the superior characteristics of the helix loaded bar circuit when operating at 90° phase shift per section. Therefore, a recalculation of performance characteristics for new voltages and currents in this region was carried out. These results are shown in Table VI. The operating parameters in the region of $\beta y = 1.5$ formed the basic design from which further refinements were then made.

One more variation was investigated for the 7.5 kw design. This was the possibility of establishing a higher voltage, lower current design. Accordingly an additional set of calculations were carried out and are shown in Table VII. The calculations were carried out for the helix loaded bar circuit and represent an extension of design U-6 to an operating anode voltage of 18 kv. Tabulated results indicate that for the value of $\beta y = 1.5$, the significant electrical parameters have not changed. The maximum temperature drop from the hot point on the bar to the heat sink has been reduced from 33°F to 16°F but the price paid is an increase in the circuit bore diameter from 4.3" to 6.1". This indicates that the 18 kv design is simply bigger than the 14.2 kv design with no apparent advantage. Therefore, the final operating parameters were based on design U-6.

A final modification to the geometry of the helix loaded bar circuit was arrived at when an analysis of the electron gun and electron beam requirements had been carried out. The details of this problem will be found in Section 5.0. However, to achieve a

TABLE V

DESIGN OF UHF HELIX (U-5) CIRCUIT WITH $\theta = 90^{\circ}$

r = 0.080"
K = 113 ohms

1.	βy, rad	1.0	1.5	2.0
2.	ω/ω_c	7.00	4.66	3.50
3.	f_c, MHz	5950	3960	2980
4.	B, gauss	2120	1410	1060
5.	D, db	0.0380	0.0283	0.0198
6.	55D, db	2.09	1.56	1.09
7.	N	13	17	24
8.	n = 4N	52	68	96
9.	L = p(4n + 12), in	15.4	19.2	25.9
10.	ID = L/π, in	4.89	6.11	8.25
11.	α_{tot}, db	0.216	0.282	0.398
12.	$\Delta T(max)$, ^{o}C	156.8	120.0	85.1
13.	Q	--	--	--
14.	$\Delta v/v$	0.080	0.126	0.174
15.	S = $(\Delta v/v)/2D$	1.05	2.23	4.39
16.	$P_d(max)$, w	49.0	37.5	26.6
17.	y, in	--	--	--

TABLE VI

SELECTED UHF HELIX LOADED BAR CIRCUIT (U-6)

Peak of synchronizing power = 7.5 kw
$\theta = 90^{o}$

1.	βy, rad	1.0	1.5	2.0
2.	ω/ω_c	7.00	4.66	3.50
3.	f_c, MHz	5950	3960	2980
4.	B, gauss	2120	1410	1060
5.	D, db	0.0506	0.0377	0.0264
6.	55D, db	2.78	2.08	1.45
7.	N	10	13	19
8.	n = 4N	40	52	76
9.	L = p(n + 12), in	11.08	13.63	18.74
10.	ID = L/π, in	3.53	4.34	5.97
11.	α_{tot}, db	0.156	0.203	0.296
12.	$\Delta T(max)$, ^{o}C	41.0	31.5	21.5
13.	Q	--	--	--
14.	$\Delta v/v$	0.080	0.126	0.174
15.	S = $(\Delta v/v)/2D$	0.79	1.67	3.29
16.	$P_d(max)$, w	42.5	32.7	22.3
17.	y, in	0.135	0.202	0.269

TABLE VII

HIGHER VOLTAGE UHF HELIX LOADED BAR CIRCUIT (U-7)

Peak of synchronizing power = 7.5 kw

V_a = 18 kv

V_o = 1.2 kv

I_k = 1 amp

1.	βy, rad	1.0	1.5	2.0
2.	ω/ω_c	7.00	4.66	3.50
3.	f_c, MHz	5950	3960	2980
4.	B, gauss	2120	1410	1060
5.	D, db	0.0398	0.0297	0.0208
6.	55D, db	2.19	1.63	1.14
7.	N	12	17	23
8.	n = 4N	48	68	92
9.	L = p(4n + 12), in	14.4	19.2	25.0
10.	ID = L/π, in	4.59	6.11	7.95
11.	α_{tot}, db	0.137	0.194	0.262
12.	$\Delta T(max)$, ^oC	21.96	15.53	11.50
13.	Q	--	--	--
14.	$\Delta v/v$	0.0646	0.0989	0.134
15.	S = $(\Delta v/v)/2D$	0.812	1.66	3.22
16.	$P_d(max)$, w	27.9	19.73	14.6
17.	y, in	0.152	0.228	0.304

practical electron gun design and still get the desired ratio of cathode current to effective circulating current in the interaction space, the height of the circuit bar needed to be doubled. Electrically, this yields only a small and not important increase in circuit insertion loss. In order to keep the same bar capacitance, the distance from the ground plane is also doubled. Thus, the thermal impedance between the bar and the point of heat sink is not changed either.

The final circuit geometry chosen for the UHF design coupled with the thermal calculations indicate that a maximum tube temperature of about 300°C can be achieved. This allows a radiator temperature in the range of 200°C to 250°C. Thermal calculations for the heat pipe and radiator design are given in Section 6.1.

A comparison of the various UHF designs is given in Table VIII. The prime constraints in the trade-off considerations were the S factor, the circuit loss, and the differential temperature of the hottest point above heat sink temperature. These factors are given in the table. It then becomes clear why design U-6 was finally chosen.

In order to accommodate linearity requirements, the design value for the saturated power level in the tube was set at about 10 kw. This was done so that the peak synchronizing power level of 7.5 kw would be in the linear region of response.

The salient characteristics of the UHF design are summarized in Table IX. Thus the trade-off calculations have led to the selection of circuit and operating parameters using the following criteria in order of priority.

1. Efficiency and assurance of adequate dynamic range.
2. Low thermal impedance of circuit and support structure leading to a low temperature design for maximum life
3. Minimum size and weight.

TABLE VIII
COMPARISON OF UHF DESIGNS

Design	Circuit	Circuit ID in	V_a kv	I_k amp	θ deg	S	Circuit Loss db	ΔT °C
U-1*	Helix	4.4	18	1.6	90	1.67	0.33	289
U-2*	Bar	4.4	18	1.6	90	1.67	0.18	37
U-3*	Helix	4.4	18	1.6	60	2.97	0.33	163
U-4*	Bar	4.4	18	1.6	60	1.67	0.26	27
U-5**	Helix	6.1	18	1.6	90	2.23	0.28	120
U-6	Bar	4.3	14.2	1.3	90	1.67		33
U-7	Bar	6.1	18	1.0	90	1.66	0.20	16

*Peak power = 15 kw
**Interaction impedance = 113 ohms
Peak power = 15 kw

TABLE IX
CHARACTERISTICS OF THE UHF DESIGN

(All voltages are given with respect to cathode voltage, even though the delay line is actually at ground potential)

Anode voltage	14.2 kv
Synchronous voltage	0.945 kv
Sole voltage	-7 kv
Cathode current	1.3 amps
Magnetic field	1410 gauss
Circuit attenuation	0.29 db
Circuit bar capacitance	1.01 pf
Inductance per circuit section of loading coil	0.0632 μh
Coupling impedance	200 ohms
Surge impedance	372 ohms
Base period of circuit	0.213"
Capacitive bar	2" high by 0.140" wide
Circuit type	Helix loaded bar circuit
Circuit ID	4.34"
Sole	3.64"
Anode-sole spacing	0.349"
Distance top of beam to delay line at point of injection	0.202"
Beam thickness	0.005"
Beam velocity slip	0.07
Inductive loading coil	
2 turns per circuit section	
Mean diameter	0.534"
Wire diameter	0.053"
Coil material	copper clad stainless steel
Approximate tube dimensions	7" diameter by 3-1/2" high
Approximate outer dimensions in shielded package using Alnico 9 permanent magnets (each magnet about 2" high)	11" diameter by 8" high

4.3.2 The S-band Amplifier

A set of trade-off calculations has been carried out for the S-band amplifier design following the same general format as was used in the case of the UHF amplifier. In addition to the helix and the helix loaded bar circuit, brief consideration was given to the meander line. This is a convoluted strip line above a ground plane. However, this design was soon discarded when it became apparent that for the same geometric porportions, this circuit had considerably higher insertion loss.

Calculations were again carried out for 60^{o} and 90^{o} phase shift per section. The interaction impedance was taken to be 100 ohms for each of the circuits. Experience and a survey of the circuit properties indicated this level was achievable at the frequency of 2.0 GHz, if low dispersion were maintained. In these calculations the gain level was again set at 20 db, and the ratio of anode voltage to synchronous voltage was taken to be 15 to 1. The S-band designs for the 60^{o} and 90^{o} phase shift per section calculations for the helix and the helix loaded bar circuit have the following values in common.

Frequency	2 GHz
Gain	20 db
Anode voltage	12 kv
Delay line synchronous voltage	800 volts
Peak power output	5 kw
Average power output	2 kw
Propagation constant, β	18.9 rad/in
Cathode current	1.0 amps
Circulating current	1.0 amps
Interaction impedance	100 ohms

The helix loaded bar circuit, operating with a phase shift per section of 90°, also turned out to be the optimal choice for the S-band amplifier. The temperature differential calculation allows for a maximum of 800 watts to be dissipated either on the anode circuit or the collector circuit.

The details of the optimum design, S-1, are given in Table X. Once again, the maximum allowable βy is 1.5. This yields an S factor of about 2 and corresponds to a minimum magnetic field of 3300 gauss.

Calculations were also carried out to determine the effect of using a more fine-grained circuit structure. A 60° phase shift per section was used. The pertinent results of this calculation, design S-2, along with other S-band calculations carried out, are exhibited in Table XI. The results of the various sets of calculations are compared on the basis of the trade-off criteria; the S-band parameter, the circuit loss, and the temperature differential ΔT. Included in the table are the results of calculations for a helix circuit, design S-5. The appropriate helix has a coupling impedance of 100 ohms and operates at 90° phase shift per section. For comparative purposes, a 0.45" circuit height was used, the same as for the bar circuit. This resulted in a helix turn radial dimension of 0.380". An inspection of Table X shows that the S-5 helix design has an insertion loss and S-factor comparable to the helix loaded bar circuit design S-1. However, it also has a much higher temperature differential between the hot spot on the circuit and the point of heat sink.

Included on the table are the calculations for the meander line carried out both for a 40° phase shift per section (design S-3), which makes the line height comparable to that of the helix and the helix loaded bar circuit, and for a 90° phase shift per section (design S-4). In both these cases, the investigation was pursued no further since it was obvious that the circuit insertion loss was

TABLE X

SELECTED S-BAND HELIX LOADED BAR CIRCUIT (S-1)

Circuit height = 0.45"
$\theta = 90^{\circ}$
f = 2 GHz

1.	βy, rad	1.0	1.5	2.0
2.	ω/ω_c	7.00	4.66	3.50
3.	f_c, MHz	14,000	9320	7000
4.	B, gauss	5000	3329	2500
5.	D, db	0.0347	0.0258	0.0180
6.	55D, db	1.91	1.42	0.99
7.	N	14	19	27
8.	n = 4N	56	76	108
9.	L = p(4n + 12), in	5.64	7.30	9.96
10.	ID = L/π, in	1.80	2.33	3.17
11.	α_{tot}, db	0.507	0.689	0.979
12.	ΔT(max), ^{o}C	12.78	9.41	6.61
13.	Q	--	--	--
14.	$\Delta v/v$	0.0726	0.112	0.151
15.	S = $(\Delta v/v)/2D$	1.05	2.17	4.21
16.	P_d(max), w	15.2	11.2	7.87
17.	y, in	0.0526	0.0789	0.105

TABLE XI
COMPARISON OF S-BAND DESIGNS

Design	Circuit	V_a kv	I_k amp	θ deg	S	Circuit Loss db	ΔT °C
S-1	Bar	12	1	90	2.17	0.69	9
S-2	Bar	12	1	60	2.17	1.5	5.7
S-3	Meander	12	1	40	2.17	5.3	-
S-4*	Meander	12	1	90	0.82	1.6	-
S-5	Helix	12	1	90	2.17	0.74	208

*Circuit height = 1 inch

excessive compared to the other possibilities. The thermal capabilities of this line are about the same as that of the helix loaded bar circuit. Thus, in this case, it offered no special advantages.

The final set of operating parameters for the S-band amplifier, therefore, were based on design S-1. As in the case of the UHF amplifier design, analyses of the electron stream and gun requirements later led to the conclusion that the height of the circuit should be increased to obtain a desirable ratio of cathode current to circulating current. The height of the circuit bars in the eventual design was raised from 0.45" to 1". Again, the distance of the circuit bar above the ground plane was adjusted to maintain the same bar capacitance to ground. The net effect of the increased circuit height was a small increase in circuit insertion loss and about a 30% increase in the magnetic gap. In order to accommodate the linearity requirements, the actual saturated power level of the tube was set at about 6.6 kw so that the peak synchronozing power level of 5 kw would be in a linear region. It was estimated that the saturation power level conversion efficiency would be about 80%. The technique of estimating this efficiency is discussed in Section 4.4.

The S-band design parameters, based on design S-1 with the circuit bar height modified, are given in Table XII.

As was done in the case of the UHF design a selection of circuit and operating parameters was made based on the trade-off calculations. The selection criteria were again, minimum insertion loss, adequate reduction of possible noise, circuit thermal capability, and minimum size and weight. The criteria were ranked in the order listed.

Sketches of the interaction gap geometry and associated potential distributions for the UHF and S-band designs are shown in Figures 15 and 16 respectively.

TABLE XII
CHARACTERISTICS OF S-BAND DESIGN

(All voltages are given with respect to cathode voltage, even though the delay line is actually at ground potential)

Anode voltage	12 kv
Synchronous voltage	0.8 kv
Sole voltage	-6 kv
Cathode current	1 amp
Effective circulating current	1 amp
Magnetic field	3300 gauss
Circuit bar capacitance	0.87 pf
Inductance per circuit section of loading coil	0.0134 μh
Circuit insertion loss	1.2 db
Coupling impedance	100 ohms
Surge impedance	190 ohms
Base period of circuit	0.083"
Capacitive bar	1" high by 0.060" wide
Circuit type	Helix loaded bar circuit
Circuit ID	2.330"
Sole	2.050"
Anode-sole spacing	0.138"
Distance top of beam to delay line at point of injection	0.079"
Beam thickness	0.003"
Beam velocity slip	0.05
Inductive loading coil	
1 turn per circuit section	
Mean diameter	0.354"
Wire diameter	0.040"
Approximate tube dimensions	4.0" diameter by 2.3" high
Approximate outer dimensions in shielded package using Alnico 9 permanent magnets (each magnet about 3.1" high	7.5" diameter by 9.0" high

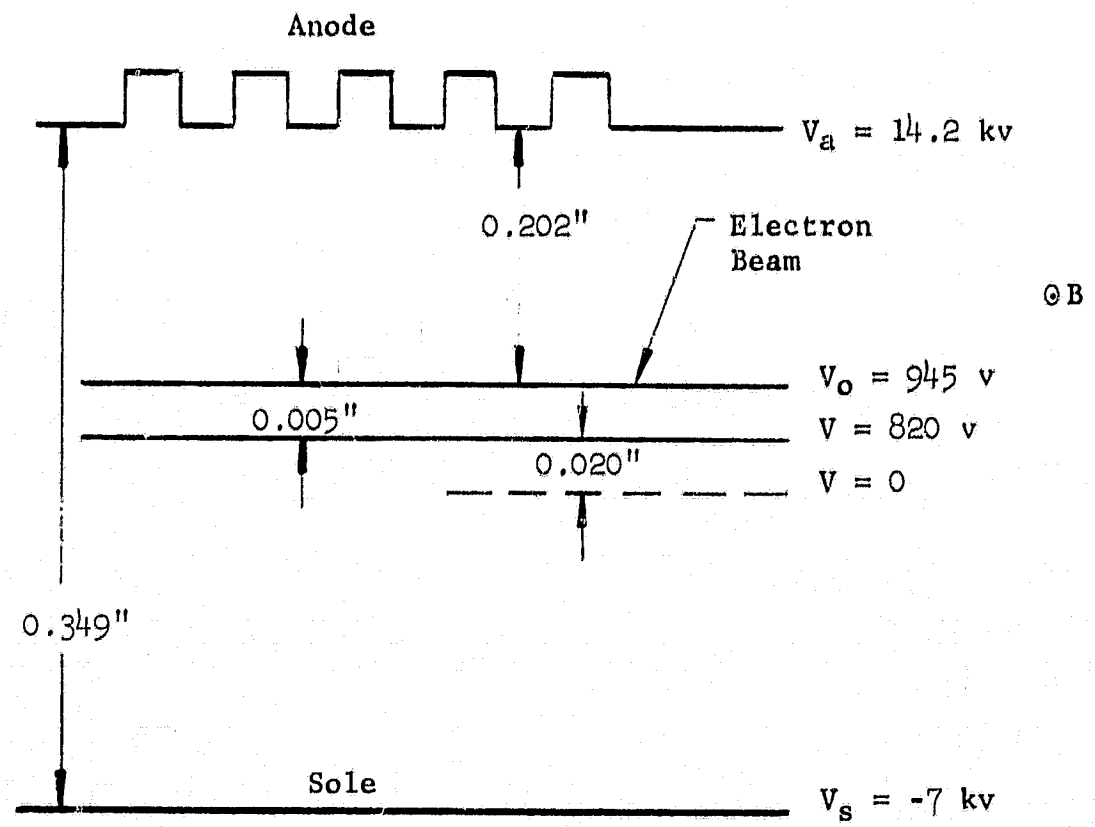

Anode ID = 4.34"

Sole OD = 3.64"

Cathode diam = 3.88"

FIGURE 15 SCHEMATIC OF INTERACTION GAP FOR UHF DESIGN

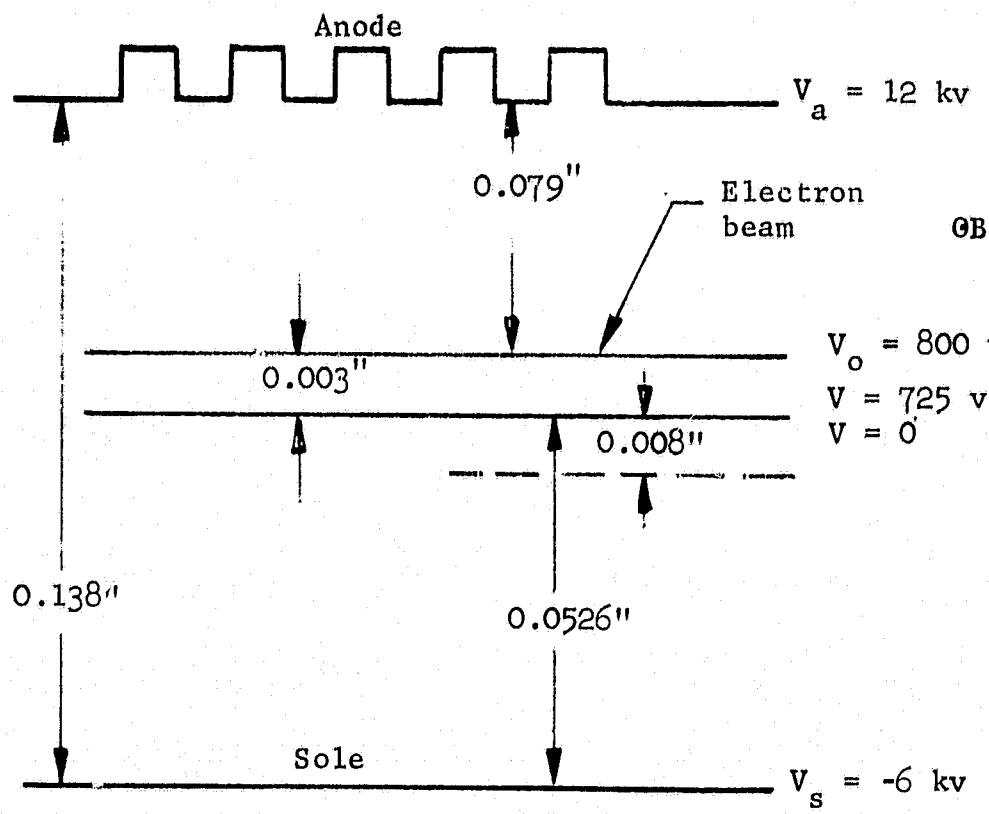

Circuit ID = 2.33"
Sole OD = 2.05"
Cathode diam = 2.15"

FIGURE 16 SCHEMATIC OF INTERACTION GAP FOR S-BAND DESIGN

4.4 Collector Design and Efficiency Analysis

In this section the relationship of electronic conversion efficiency, as a function of collector geometry and as a function of potential distribution within the electron stream arriving at the collector, will be examined. Since the potential distribution in the current stream arriving at the collector is a function of the RF drive level, the analysis is then essentially being made in terms of collector geometry and variation in RF drive level. Some reasonable mathematical models are set up for the current distribution for three regions of drive level. This analysis is first performed in terms of energy balances between the RF and dc systems within the tube. In Section 4.4.1 the effect of possible secondary emission from the collector elements is taken into account and procedures for minimizing the impact of any possible secondary emission is considered at that point.

The use of these results in estimating overall conversion efficiency is then discussed in terms of their application to the amplifiers being designed for this study program. Verification of efficiency results from computer calculations on the tube model are discussed in Section 4.4.4 on computer results. The concept of switching the electron beam to various collector elements as a function of RF drive level is verified. The consequent effect on efficiency is discussed based upon experimental work from S-F-D laboratories' study programs at other power levels.

4.4.1 Electronic Efficiency as a Function of Collector Parameters and Current Distribution

In this report electronic efficiency, η_e, is defined as the RF power generated divided by the dc power input. Electronic efficiency is a function of the details of the RF interaction process and the manner in which the dc power is applied to the amplifier.

The manner in which the dc power is applied to the amplifier is in turn a function of the procedure by which the spent beam is removed from the interaction region by the multi-element collector structure.

The collector structure is taken to be a series of concentric rings placed axially after the interaction structure at the end opposite to the electron gun. The potential difference between these rings is a constant increment. This increment is equal to the potential difference between cathode and anode divided by the number of collector elements. Thus, if cathode potential is taken as zero, then the collector elements moving radially outward from the first ring assume a series of values starting at close to cathode potential, the last ring being close to anode potential.

Some electrons moving in the accelerating RF fields exit from the interaction space below cathode potential. In the discussion that follows, their distribution is presumed to be in the range between cathode and anode potential in order to simplify the analysis somewhat. Later, comments are made on the extension of the analysis to include electrons which exit below cathode potential. Power supply requirements for recovering this class of electrons are discussed in Section 8.0.

Each collector ring is placed at the appropriate radial position so that it terminates its corresponding potential line in the interaction region.

Consider now an array of N collector elements. For convenience of analysis, the delay line itself is taken as the last element in this array. The RF energy converted for collector element, n, $E_{RF}(n)$ is

$$E_{RF}(n) = I_n \left(V_n - kV_o - \frac{\Delta V}{2}\right) \qquad (10)$$

where $n = 1, 2, 3, \ldots, N$

V_n = potential of nth collector element with respect to cathode

I_n = current collected by nth collector element

V_o = synchronous voltage of slow wave circuit

ΔV = voltage increment between adjacent collector rings

k = factor to account for cycloiding beam

Equation (10) is also valid for RF energy converted when the electrons are below cathode potential, if the collector potential, V_n, is given the proper algebraic sign with respect to cathode potential.

V_o is the kinetic energy of the electron due to circumferential synchronous velocity of the electron stream. The factor, k, may vary instantaneously from 0 to 4 for the worst case of a badly cycloiding beam. The instantaneous variation of electron velocity components over one cyclotron period, for such a badly cycloiding beam, would be

$$u_\theta = u_o (1 + \sin \omega_c t)$$

$$u_r = u_o \cos \omega_c t$$

where u_θ = instantaneous velocity amplitude in circumferential direction

u_r = instantaneous velocity amplitude in radial direction

u_o = dc component of drift velocity corresponding to V_o

ω_c = radian cyclotron frequency

t = time

The worst case, $k = 4$, corresponds to a maximum instantaneous velocity, $u = 2u_o$. Since the electrons strike the collector at all phases of the cyclotron cycle, the average value of impact energy corresponds to the average value of

$$u^2 = \left[u_o(1 + \sin \omega_c t)\right]^2 + \left[u_o \cos \omega_c t\right]^2$$

The average value of u^2 reduces to

$$\overline{u^2} = 2\, u_o^2$$

Thus, for the worst case of a badly cycloiding beam, the average value of k would be 2. In a well-behaved beam, which is physically realizable, an average value of k = 1.1 or 1.15 appears reasonable. Any recovery of the drift energy of the stream would reduce this value even further.

On arriving at the collector structure, some electrons will just miss collection at the nth element and will be accelerated through a potential rise, ΔV, to arrive at the (n + 1) element. The average electron therefore dissipates an amount of energy $\Delta V/2$ when arriving at the collector structure.

The dc power input to section, n, is $P_{dc}(n)$ where

$$P_{dc}(n) = I_n V_n \tag{11}$$

Therefore the net electronic efficiency, η_e, for the amplifier is given by

$$\eta_e = \frac{\sum_{n=1}^{N_c} I_n\left(V_n - kV_o - \frac{\Delta V}{2}\right)}{\sum_{n=1}^{N_c} I_n V_n} \tag{12}$$

where N_c = number of collector elements

(This does not include possible secondary emission losses at the collector)

Define a current weighting factor, a_n, where

$$a_n = \frac{I_n}{I_k}$$

$$\sum_{n=1}^{N_c} a_n = 1$$

Since $\Delta V = V_a/N_c$, where V_a = anode potential and $V_n = n\,\Delta V$, the expression for efficiency, equation (12), becomes

$$\eta_e = \frac{\sum_{n=1}^{N_c} a_n\left(n - \frac{1}{2} - kN_c\,\frac{V_o}{V_a}\right)}{\sum_{n=1}^{N_c} na_n} \qquad (13)$$

Equation (13) states algebraically that the system may be considered as a sequence of energy converters in parallel, with the efficiency of each particular converter section being a function of the rank of the converter in the array. The total efficiency of the system is then calculated by summing all the outputs and all the dc power inputs. The total electronic efficiency, η_e, is a linear function of the running index, n.

In order to use equation (13) to calculate the electronic efficiency, it is necessary to know the current distribution factor, a_n, as a function of exit potential, V_n. The data for this function are obtainable either from highly detailed experimental results or

from a reliable computer simulation model. The axial injection crossed-field amplifier is a relatively new device and a useful computer simulation model has just been obtained. While experimental verification of the axial injection principle has been achieved, detailed experimental readout of the current distribution in the collector region has not yet been completed. However, by postulating some reasonable physical models for the current distribution under different conditions of RF drive level, some useful estimates of achievable efficiency may be made using equation (13). The impact of the number of collector rings and the factor k can be evaluated.

Now consider the sketches in Figure 17. These are plots of the current distribution in the collector region as a function of exit potential and are based on a knowledge of the physical processes that are occurring in the interaction space. When the tube is being driven at medium drive levels but is still below saturation, the current distribution should appear essentially as shown in the middle sketch, labeled, "just at saturation drive". It is known that the electrons will be sorted into two main groups. Some of the electrons are in the proper RF phase to deliver energy to the RF wave. These electrons will do this by converting potential energy and moving radially outward in the interaction system toward the higher potential values near the anode voltage, V_a. Pi radians away in RF phase is another group of electrons that absorb energy from the RF wave. These electrons are driven down to lower potential values and form a cluster exiting toward the collector rings which are well below the mid-ring which is at one-half anode potential. It should again be pointed out that the analytical discussion is simplified by not considering the electrons which exit below cathode potential. This was done so that the general trends which relate efficiency to collector design parameters could be established. Additional analysis of this point is carried out at the end of this section.

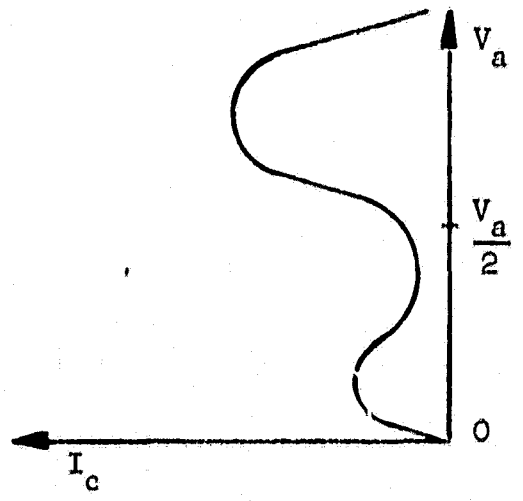

a. Tube driven well into saturation

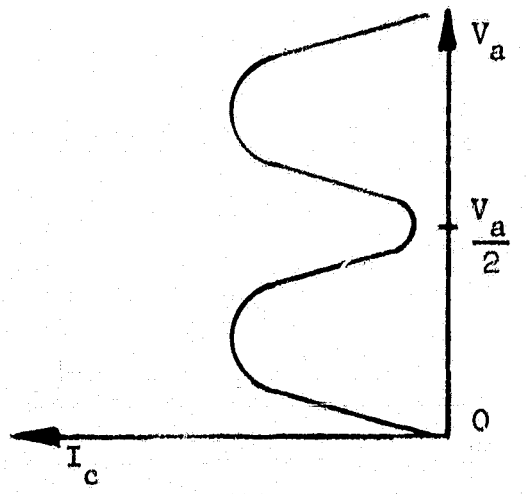

b. Just at saturation drive

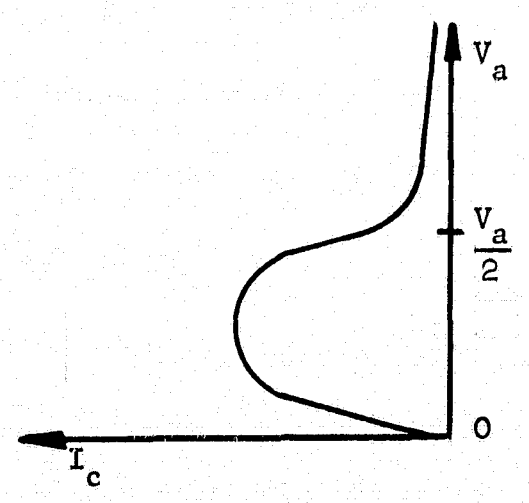

c. Low drive well below saturation

FIGURE 17 PROFILES OF COLLECTOR CURRENT DISTRIBUTION VERSUS EXIT POTENTIAL FOR DIFFERENT DRIVE LEVELS

In calculating efficiency using experimental data or computer simulation results, the actual distribution of current versus exit potential is to be used. In the region of low level drive, very little of the available potential energy of the system will be converted and most of the current will exit at lower potentials. This is shown in the lower sketch, but the phase sorting effect is not clearly delineated. The upper sketch of Figure 17 is an approximation of what might occur with the tube driven well into saturation. Here the phase focusing effects of the strong RF field drive a preponderance of the current into the proper RF phase for delivering energy to the RF field. Therefore, a great deal of the current is collected in and around the anode potential, although there is still a residual mass of electron current which has interacted with the out of phase component of RF field. This current still exits at lower values of potential.

Now consider the intermediate condition, just at saturation drive. As sketched, the current is shown to be distributed symmetrically above and below the middle collector ring - that is, above and below the mid-potential value of $V_a/2$. For ease of analysis, let a_n become a continuous variable and approximate the current distribution as a double peaked sinusoid as follows:

$$a_n = \frac{1}{N_c}\left(1 - \cos\frac{4n\pi}{N_c}\right)$$

$$\int_0^{N_c} a_n \, dn = 1$$

is satisfied. Equation (13) then becomes

$$\eta_e = \frac{\int_0^{N_c} \frac{1}{N_c}\left(1 - \cos\frac{4n\pi}{N_c}\right)\left(n - \frac{1}{2} - kN_c\frac{V_o}{V_a}\right) dn}{\int_0^{N_c} \frac{n}{N_c}\left(1 - \cos\frac{4n\pi}{N_c}\right) dn}$$

$$\eta_e = 1 - \frac{1}{N_c} - 2k\frac{V_o}{V_a} \qquad (14)$$

Figure 18 is a plot of equation (14) for values of k equal to 0.75, 1, and 2. The ratio of anode voltage to synchronous voltage is taken to be 15 in this case, corresponding to design values used in the initial UHF and S-band amplifier designs. As might be expected, the lower values of k result in decreasing sensitivity to the number of collector rings needed for approaching the asymptotic value of efficiency which results from a very large number of rings. With k equal to 1, at least 10 collector rings appear desirable, with appreciable benefits resulting with as many as 15. The plot of equation (14) is extended to the cases for V_a/V_o equal to 20 and 25 in Figures 19 and 20 respectively.

The results plotted in Figure 18 were obtained with the assumption that the current distribution as a function of collector index number, n, was symmetrical about the middle collector ring. However, any current distribution function which was symmetrical about this mid-point would have given a similar result, since an examination of equation (13) shows that the expression is a linear function of n. Therefore, for this general physical condition, the results are relatively insensitive to the precise details of the current distribution and the calculations provide a useful measure of what might be expected.

(Current distribution, two symmetric sinusiods,
just below saturation drive)

$$\eta_e = 1 - \frac{1}{N_c} - 2k \frac{V_o}{V_a}$$

$$\frac{V_a}{V_o} = 15$$

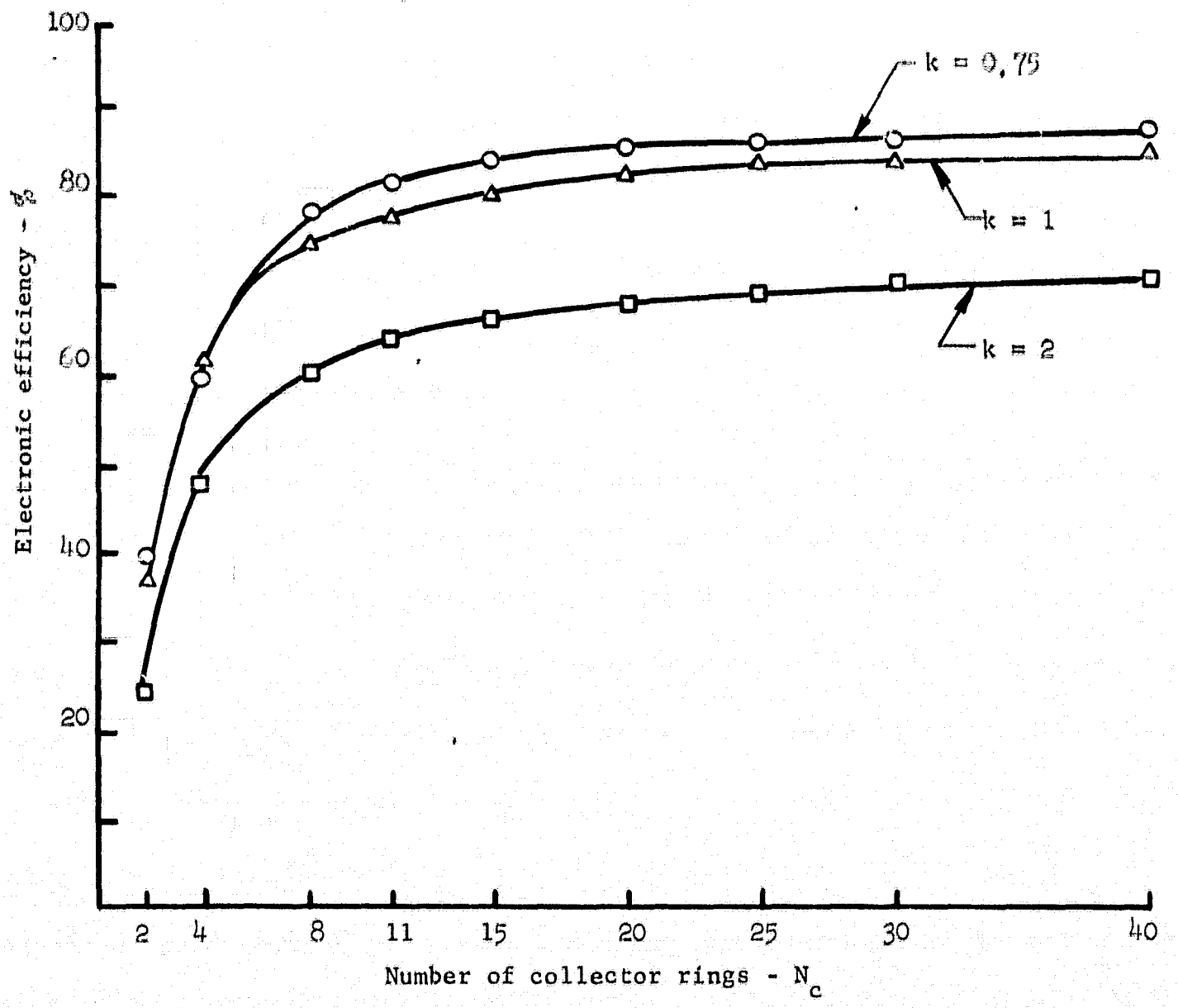

FIGURE 18 ELECTRONIC EFFICIENCY VERSUS NUMBER OF COLLECTOR RINGS, INTERMEDIATE DRIVE LEVEL, $V_a/V_o = 15$

(Current distribution, two symmetric sinusoids,
just below saturation drive)

$$\eta_e = 1 - \frac{1}{N_c} - 2k \frac{V_o}{V_a}$$

$$\frac{V_a}{V_o} = 20$$

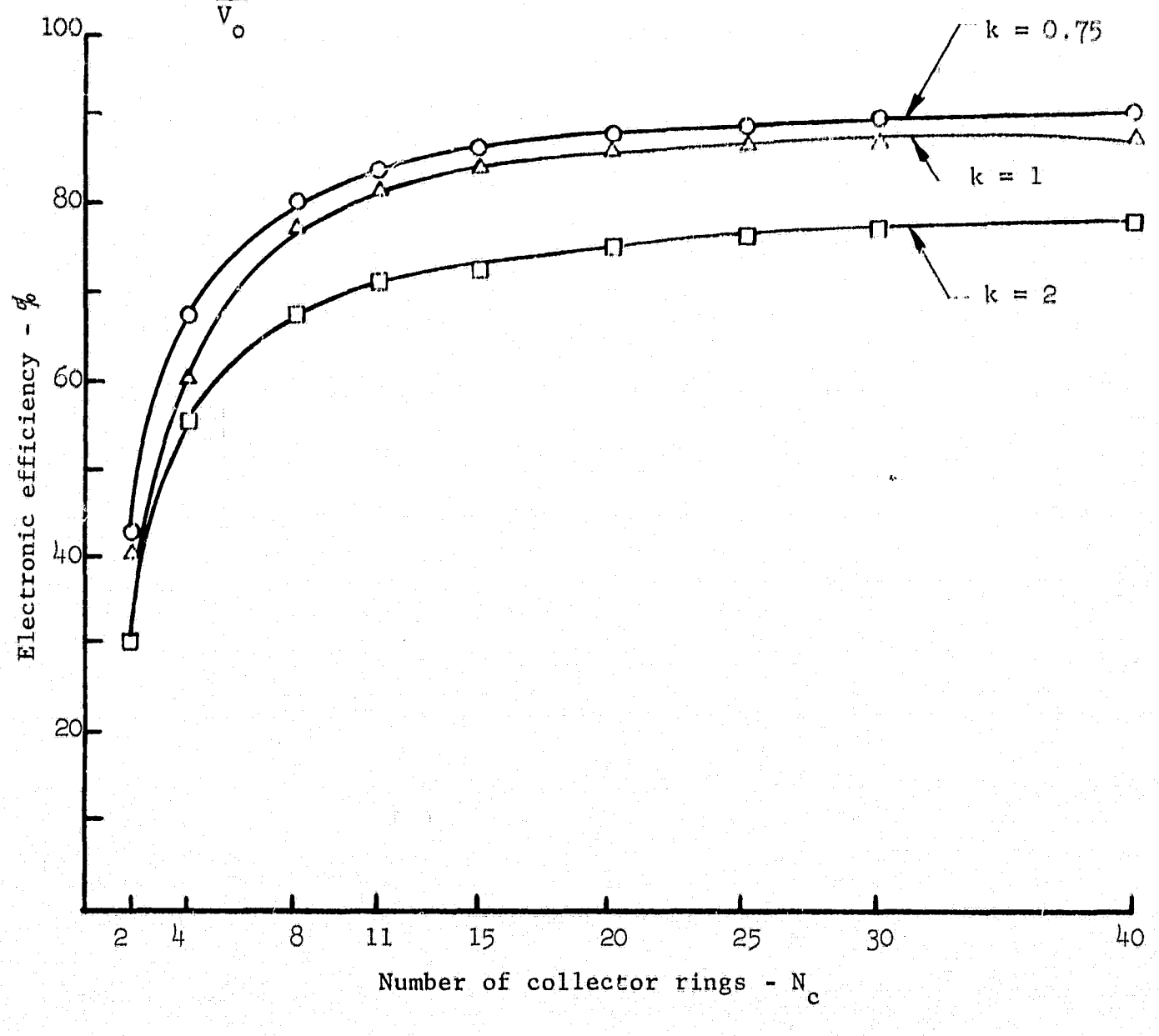

FIGURE 19 ELECTRONIC EFFICIENCY VERSUS NUMBER OF COLLECTOR RINGS, INTERMEDIATE DRIVE LEVEL, $V_a/V_o = 20$

(Current distribution, two symmetric sinusoids,
just below saturation drive)

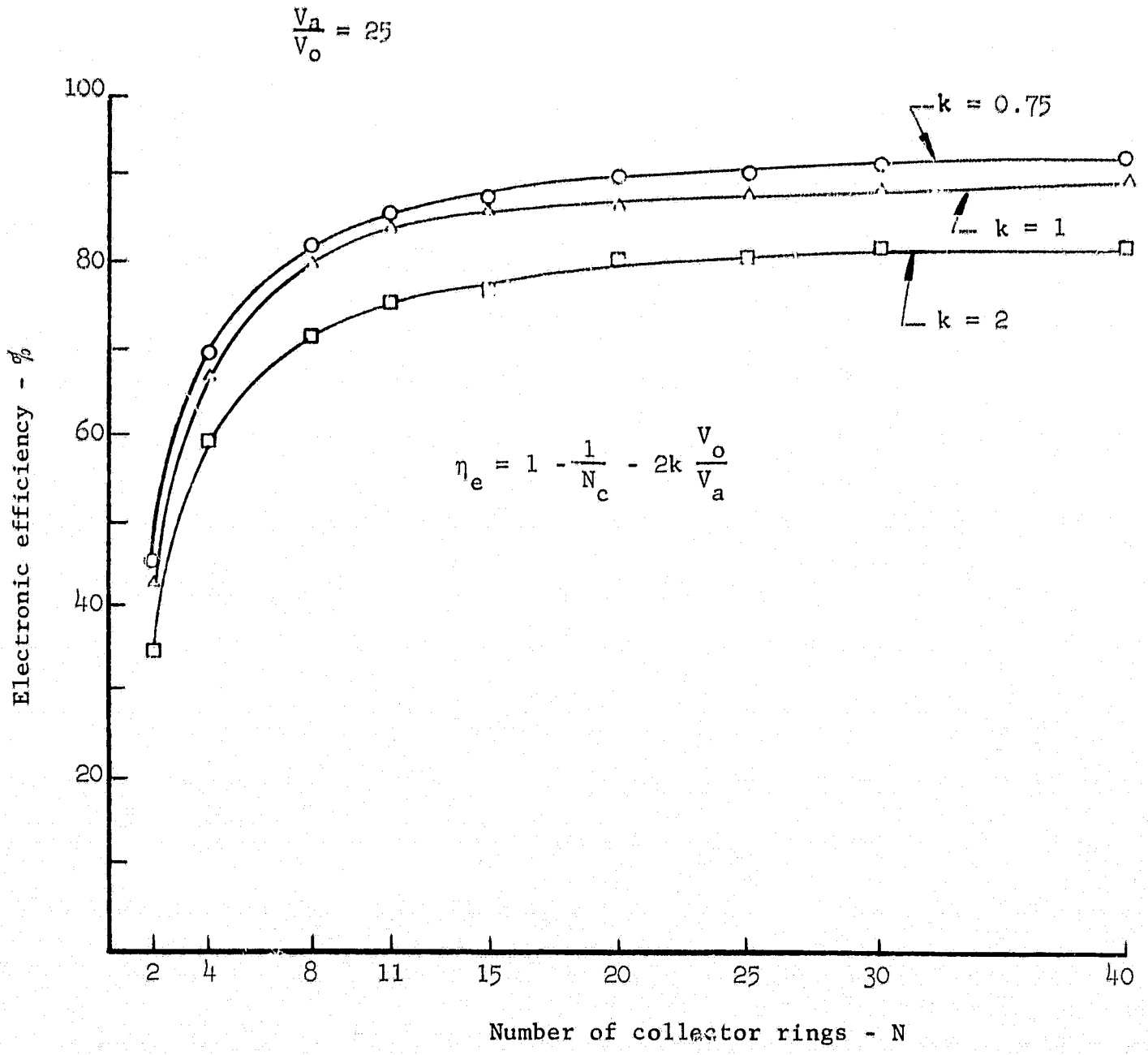

FIGURE 20 ELECTRONIC EFFICIENCY VERSUS NUMBER OF COLLECTOR RINGS, INTERMEDIATE DRIVE LEVEL, V_a/V_o = 25

Next, consider the two other cases sketched in Figure 16, that of small signal drive and saturation drive. Proceeding along similar lines, assume that all the current at low drive exits at a potential less than one-half the anode potential and the current distribution as a function of collector index number is again a sinusoid and is given as follows:

For Low Drive

$$a_n = \frac{2}{N_c}\left(1 - \cos\frac{4n\pi}{N_c}\right)$$

$$0 \leq n \leq \frac{N_c}{2}$$

While in the case of saturation drive, make the idealized assumption that all of the current exits at a potential greater than one-half the anode voltage and is again given by a sinusoidal distribution as a function of collector ring index number as follows:

For Saturation Drive

$$a_n = \frac{2}{N_c}\left(1 - \cos\frac{4n\pi}{N_c}\right)$$

$$\frac{N_c}{2} \leq n \leq N_c$$

This is sketched in Figure 21.

Substituting the above expressions into equation (13) and carrying out the indicated operations results in the following expressions for efficiency under conditions of low drive and saturation drive:

Low Drive: $\eta_e = 1 - \frac{2}{N_c} - \frac{V_o}{V_a}$ (15)

Low drive and saturation drive, sinusoid current distributions

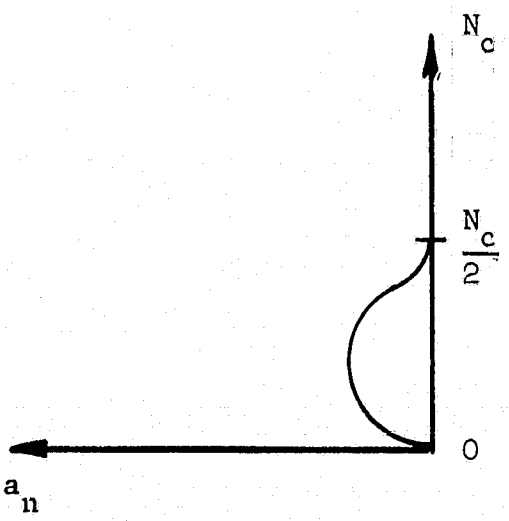

$$a_n = \frac{2}{N_c}\left(1 - \cos\frac{4n\pi}{N_c}\right)$$

$$0 \leq n \leq \frac{N_c}{2}$$

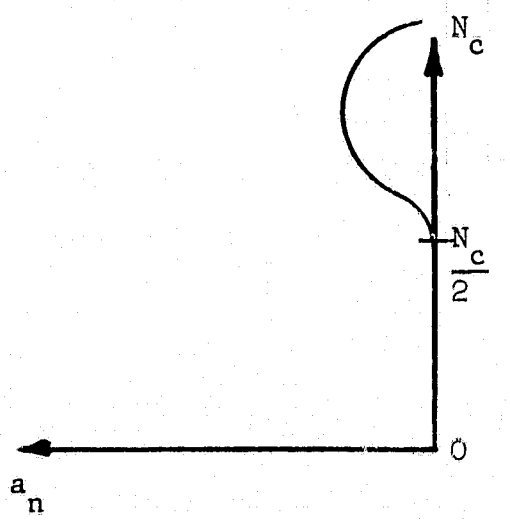

$$a_n = \frac{2}{N_c}\left(1 - \cos\frac{4n\pi}{N_c}\right)$$

$$\frac{N_c}{2} \leq n \leq N_c$$

FIGURE 21 COLLECTOR CURRENT MODEL FOR LOW DRIVE AND SATURATION DRIVE

Saturation Drive:

$$\eta_e = 1 - \frac{2}{3N_c} - \frac{4}{3} k \frac{V_o}{V_a} \qquad (16)$$

A plot of equation (15) which gives the electronic efficiency for the low drive saturation is exhibited in Figure 22. Here again values of k are taken equal to 0.75, 1, and 2. The ratio of anode voltage to synchronous voltage is again 15. It is seen here that the electronic efficiency is highly sensitive to the number of collector rings, since the energy loss represented by $\Delta V/2$ is comparatively important, compared to a low value of k, has an important influence on the calculated efficiency. The plots of equation (15), as extended to values of V_a/V_o equal to 20 and 25, are exhibited in Figures 23 and 24.

A plot of equation (16) which gives the estimated electronic efficiency for the case of saturation drive is shown in Figure 25 for the same range of parameters as in Figure 22. In this case since most of the current exits at potential values close to or at the anode voltage, the energy losses due to the finite number of collector rings and unrecovered synchronous injection energy are relatively unimportant. Therefore, the curves exhibit a lesser dependence on the value of k and the number of collector rings. Extensions of the plot of equation (16) to values of V_a/V_o of 20 and 25 are exhibited in Figures 26 and 27 respectively.

The foregoing discussion shows that, in all cases, large increases in electronic efficiency can be achieved by using a number of collector rings at least equal to the number at the knee of the curve in the various figures presented. Indeed, in most cases it seems worthwhile to use as many collector rings as are compatible with technology capability. The sensitivity to the number of collector rings is decreased for low values of k and for higher values of saturation drive. This follows immediately from the fact that the

(Low drive, all current collected below $V_a/2$, sinusoid model)

$$\eta_e = 1 - \frac{2}{N_c} - 4k \frac{V_o}{V_a}$$

$$\frac{V_a}{V_o} = .15$$

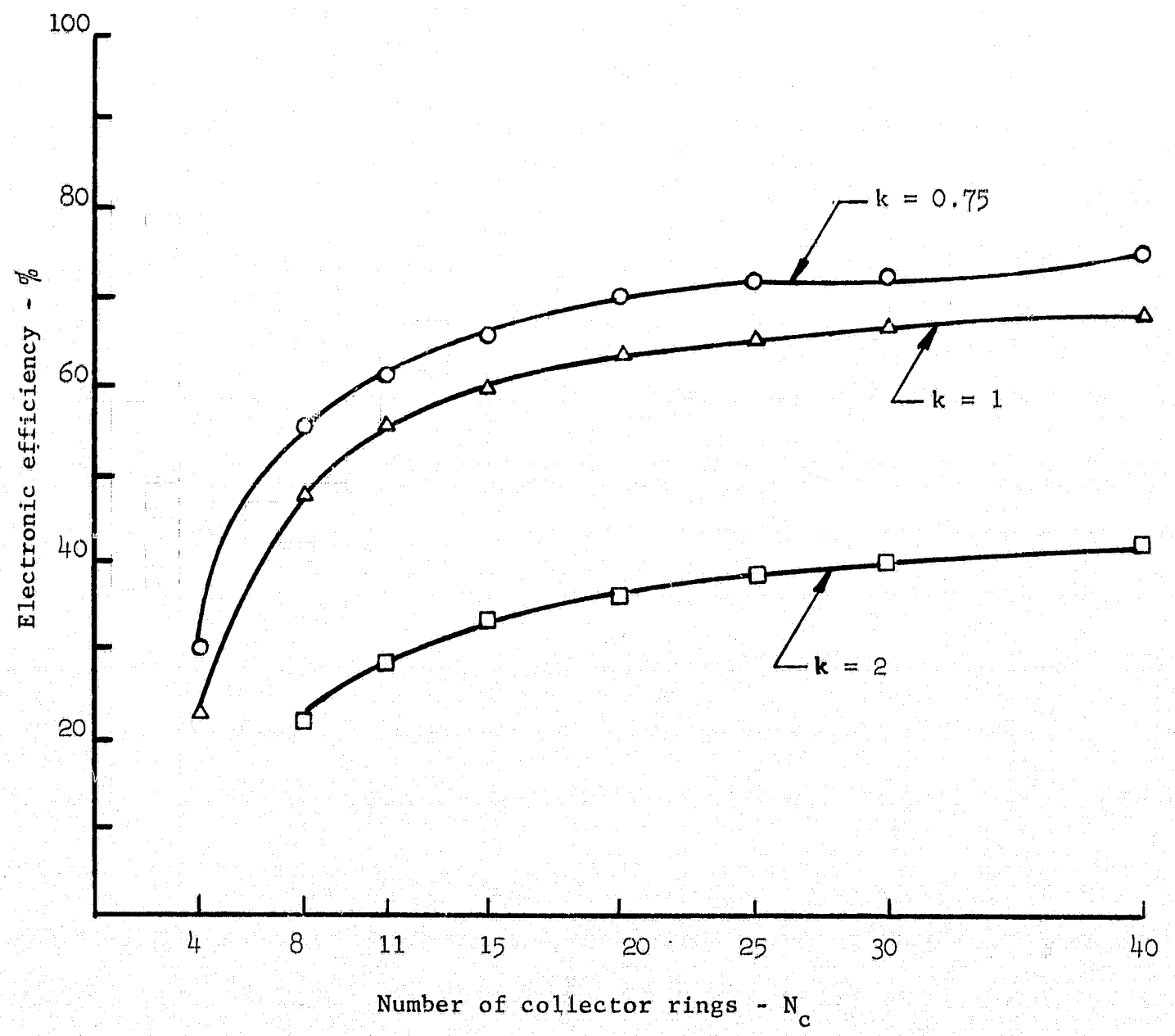

FIGURE 22 ELECTRONIC EFFICIENCY VERSUS NUMBER OF COLLECTOR RINGS, LOW DRIVE, $V_a/V_o = 15$

(Low drive, all current collected
below $V_a/2$, sinusoid model)

$$\eta_e = 1 - \frac{2}{N_c} - 4k \frac{V_o}{V_a}$$

$$\frac{V_a}{V_o} = 20$$

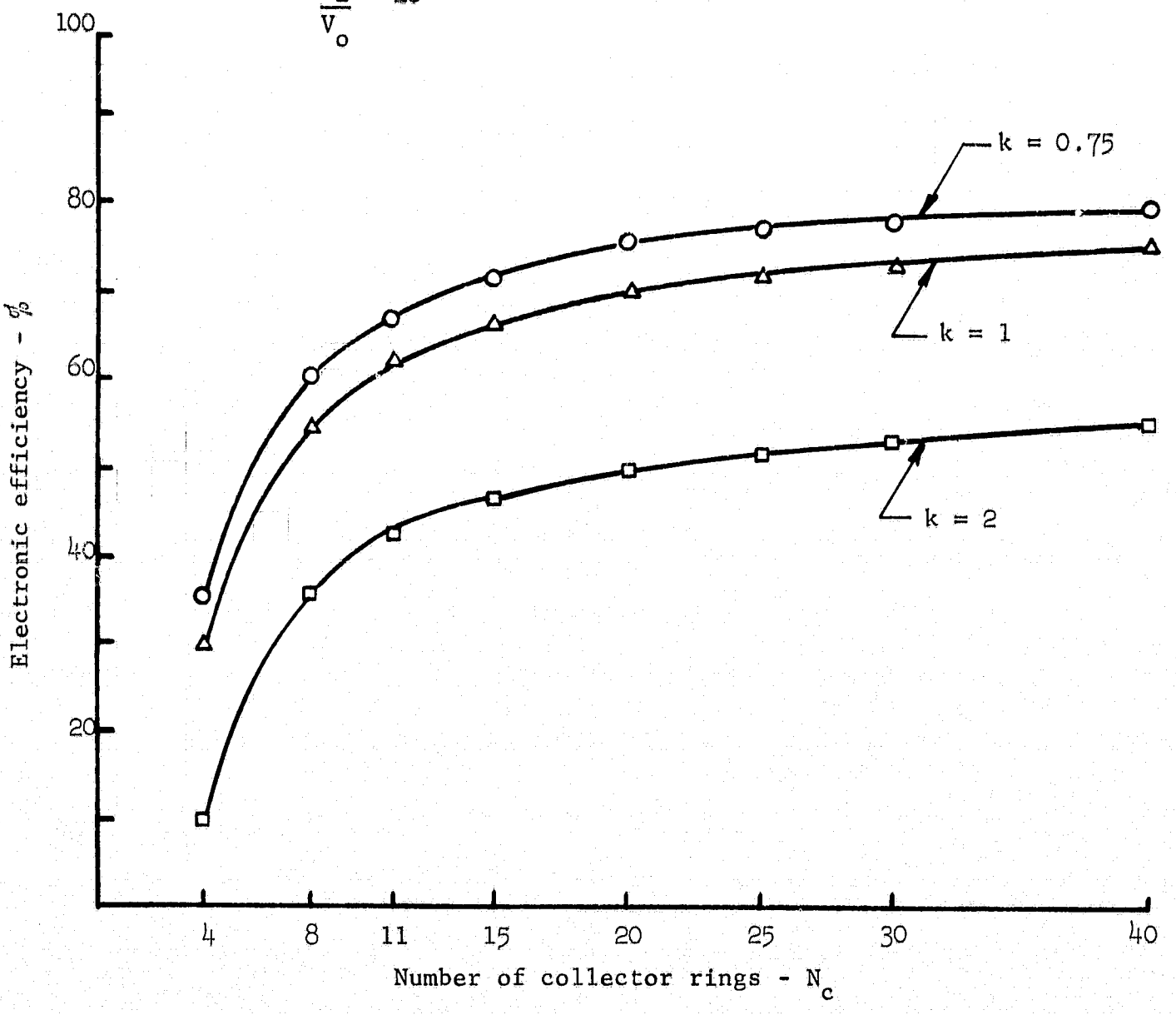

FIGURE 23 ELECTRONIC EFFICIENCY VERSUS NUMBER OF COLLECTOR RINGS, LOW DRIVE, $V_a/V_o = 20$

(Low drive, all current collected
below $V_a/2$, sinusoid model)

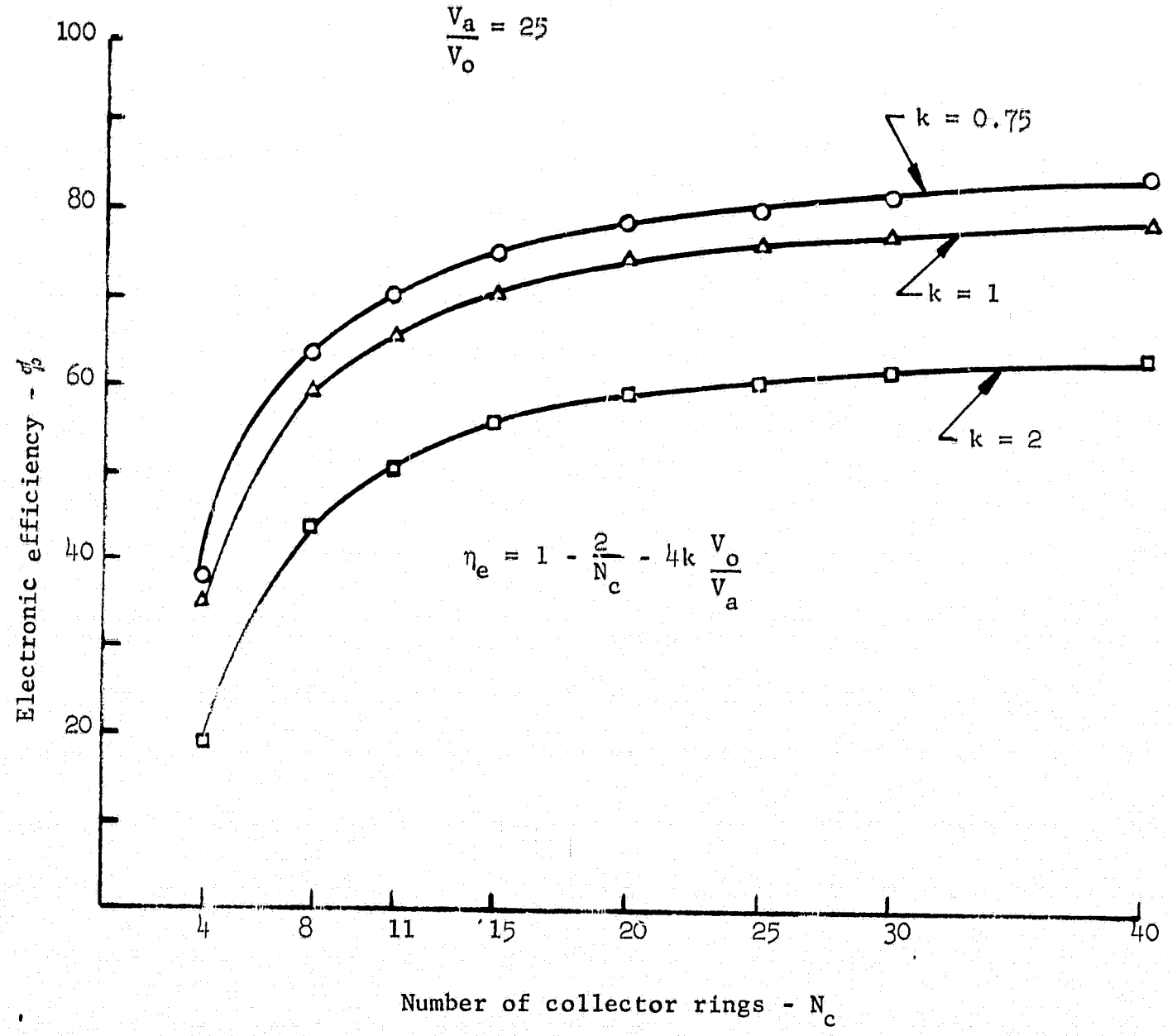

FIGURE 24 ELECTRONIC EFFICIENCY VERSUS NUMBER OF COLLECTOR RINGS, LOW DRIVE, V_a/V_o = 25

(Saturation drive, most current collected above $V_a/2$, sinusoid model)

$$\eta_e = \frac{2}{3N_c} - \frac{4}{3} k \frac{V_o}{V_a}$$

$$\frac{V_a}{V_o} = 15$$

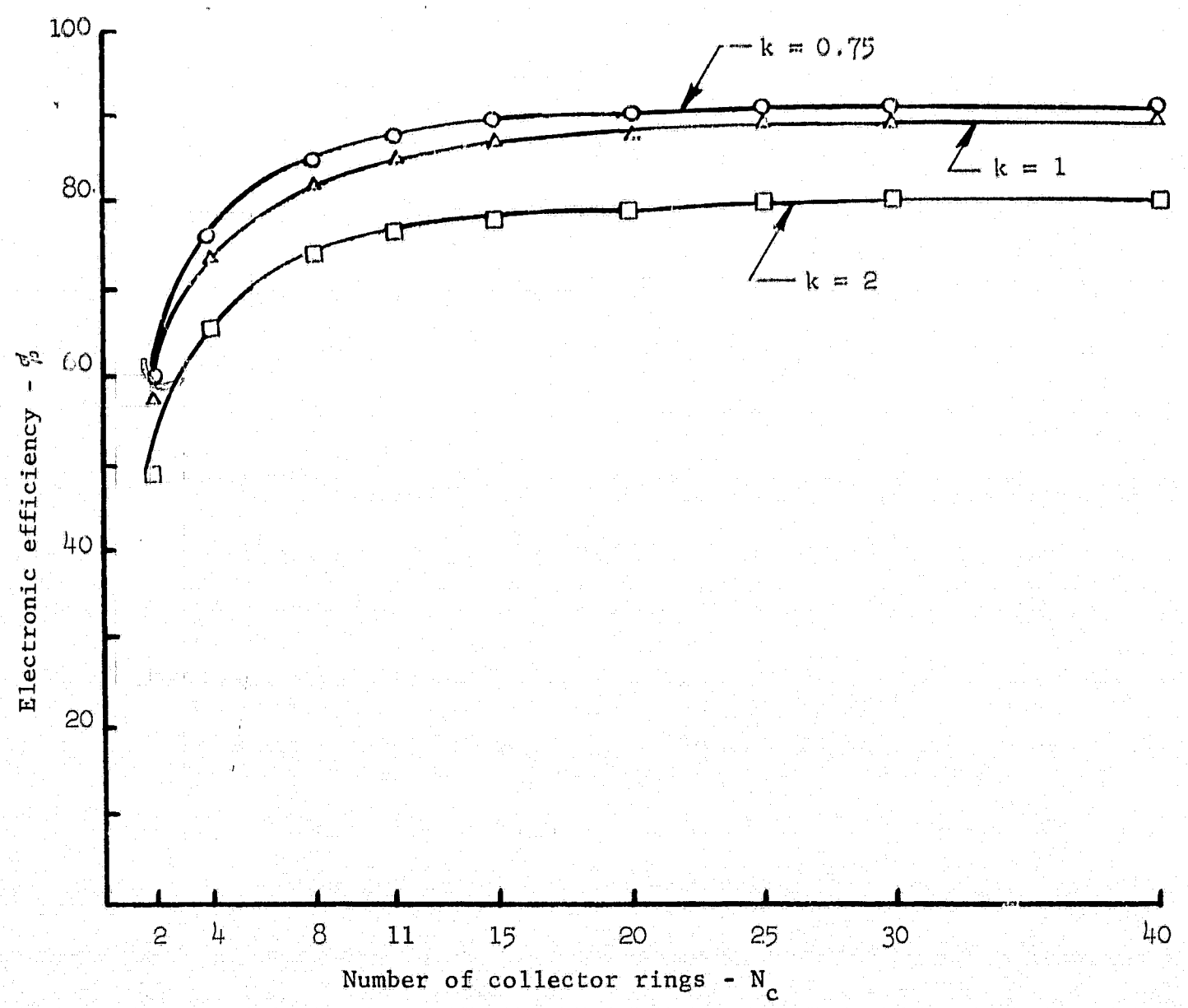

FIGURE 25 ELECTRONIC EFFICIENCY VERSUS NUMBER OF COLLECTOR RINGS, SATURATION DRIVE, $V_a/V_o = 15$

(Saturation drive, most current collected above $V_a/2$, sinusoid model)

$$\eta_e = 1 - \frac{2}{3N_c} - \frac{1}{4} k \frac{V_o}{V_a}$$

$$\frac{V_a}{V_o} = 20$$

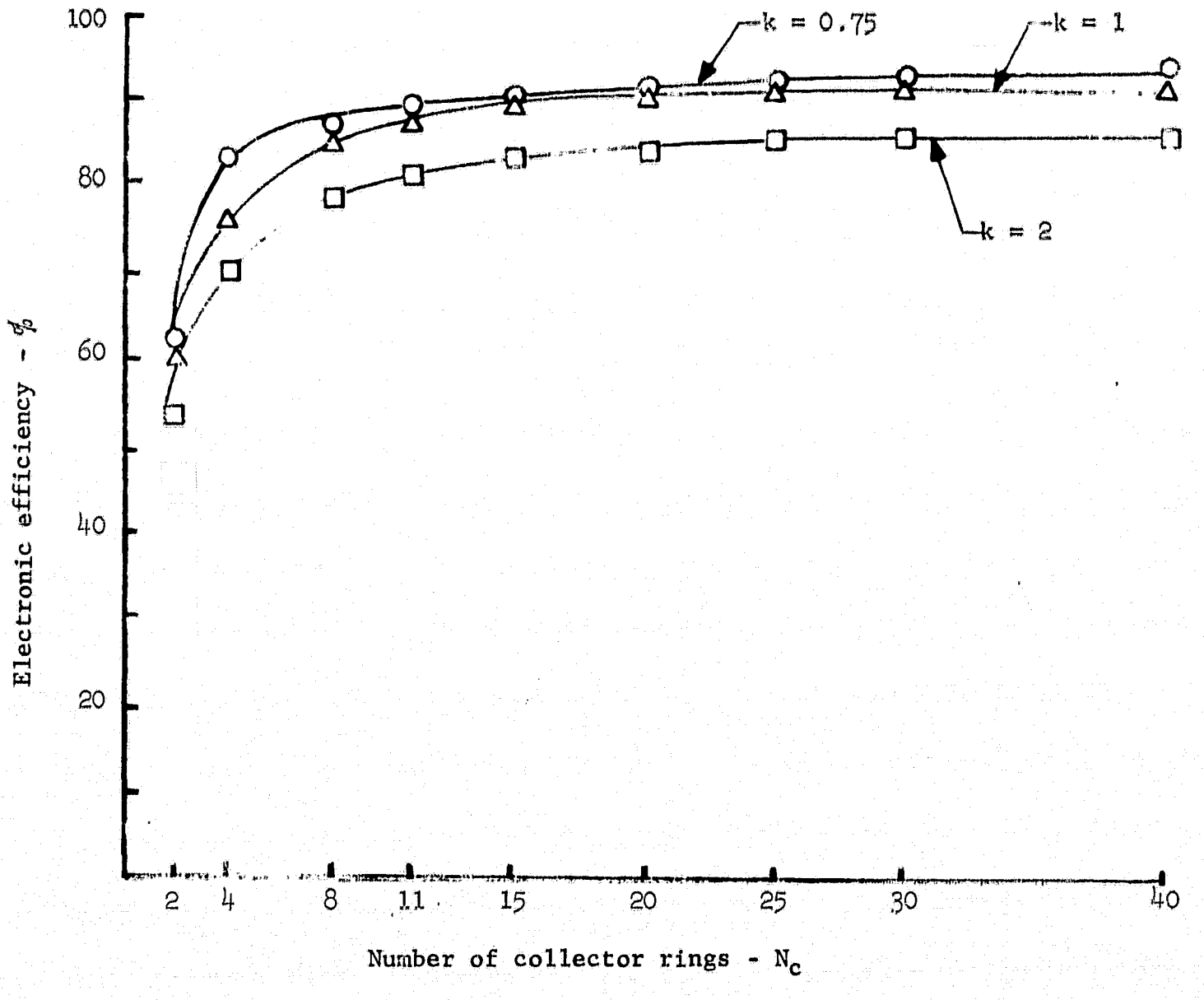

FIGURE 26 ELECTRONIC EFFICIENCY VERSUS NUMBER OF COLLECTOR RINGS, SATURATION DRIVE, $V_a/V_o = 20$

(Saturation drive, most current collected above $V_a/2$, sinusoid model)

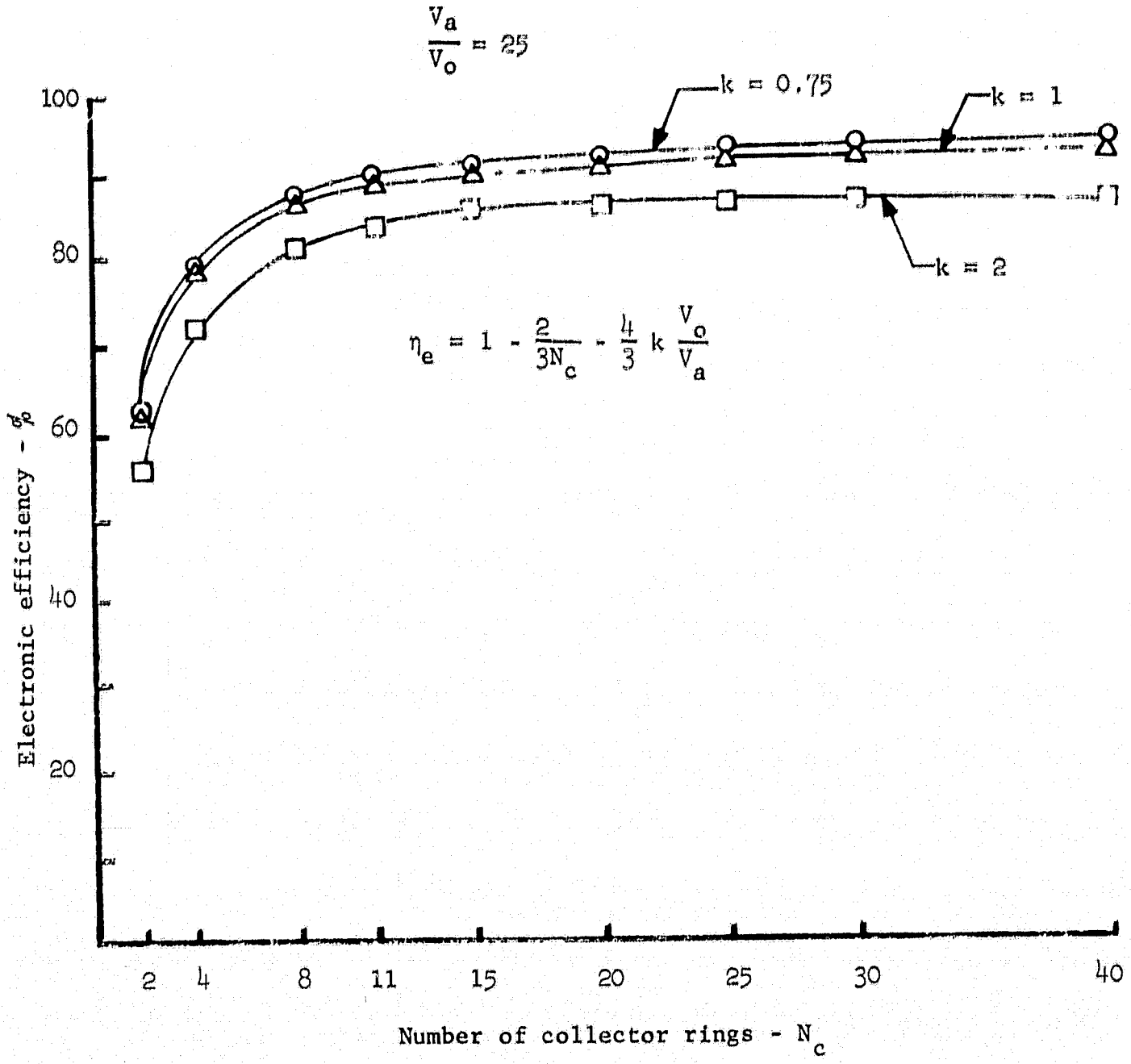

FIGURE 27 ELECTRONIC EFFICIENCY VERSUS NUMBER OF COLLECTOR RINGS, SATURATION DRIVE, $V_a/V_o = 25$

net efficiency calculated is simply a summation over a series of potential energy converters. Thus when the unit efficiency of each of these converters is high, the summation result is relatively insensitive to the number of elements.

Actual experimental results and results from computer simulation calculations indicate that some number of electrons will exit from the interaction space at a potential which is below that of the cathode potential. This occurs in a potential region between the cathode and the sole potential. Although the foregoing analysis has been carried out by considering only the potential region between cathode potential and anode potential, an extension of this procedure may be carried out to include the region below cathode potential. The electrons which exit in the negative potential region may be recovered by extending the collector structure radially inward below the potential corresponding to the cathode. This negative potential represents RF energy taken from the circuit wave by out-of-phase electrons. The general comments made previously on the number of collector elements are still valid. There is a physically realizable packing density for collector rings in the potential space between the cathode and anode. This density level may also be directly extended to the region of negative potential. The recovery of this negative potential energy calls for a somewhat different power conditioner arrangement than that used to recover electrons in the positive potential region. A process of dc to dc conversion is required and is believed to be well within the present state-of-the-art. The details of this process are discussed in Section 8.0.

In estimating electronic efficiency the analysis, equations (12) through (16), may be modified to include collection of electrons at potentials below cathode potential. The basic equation (12) is correct as given for electrons collected above and below cathode potential if V_n, the collector potential with respect to the cathode, is taken algebraically, i.e., V_n is a negative number for potentials

below cathode potential. The summation is still carried out over all collector elements, including the ones below cathode potential. The current weighting factor, a_n, is used once again

$$a_n = \frac{I_n}{I_k}$$

where $\sum_n a_n = 1$

but the potential interval between collectors is redefined

$$\Delta V = \frac{V_a + V_r}{N_c} \qquad (17)$$

$$V_n = n\Delta V$$

where V_a = anode potential with respect to cathode

N_c = total number of collector elements

V_r = lowest negative potential below cathode at which current collection will occur

Equation (13) may now be rewritten as follows

$$\eta_e = \frac{\sum_{n=-N_n}^{N_p} a_n \left[n - \frac{1}{2} - \frac{kN_c \frac{V_o}{V_a}}{1 + \frac{V_r}{V_a}} \right]}{\sum_{n=-N_n}^{N_p} n\, a_n} \qquad (18)$$

where N_n = number of collector elements below cathode potential

N_p = number of collector elements above cathode potential

The total number of collector elements, N_c, allowing for one element at cathode potential, is

$$N_c = N_n + N_p + 1$$

The summation index n is now a negative number for those elements which are below cathode potential. For example, consider a modification of the current distribution in Figure 17b, which shows the distribution of current with the RF drive level just below saturation. This distribution has been modified, Figure 28, to include the current collected below cathode potential. As before, we use a double sinusoid for the model and let a_n become a continuous variable,

$$a_n = \frac{1}{N_c}\left(1 - \cos\frac{4n\pi}{N_c}\right) \qquad (19)$$

Substituting this expression into equation (18)

$$\eta_e = \frac{\displaystyle\int_{-N_n}^{N_c-N_n} \frac{1}{N_c}\left(1 - \cos\frac{4n\pi}{N_c}\right)\left[n - \frac{1}{2} - \frac{kN_c\,\frac{V_o}{V_a}}{1 + \frac{V_r}{V_a}}\right] dn}{\displaystyle\int_{-N_n}^{N_c-N_n} \frac{n}{N_c}\left(1 - \cos\frac{4n\pi}{N_c}\right) dn} \qquad (20)$$

Then performing the indicated integration

$$\eta_e = 1 - \frac{2\left[\frac{1}{2} + \frac{kN_c\,\frac{V_o}{V_a}}{1 + \frac{V_r}{V_a}}\right]}{N_c - 2N_n + \frac{N_c}{\pi}\sin 4\pi\frac{N_n}{N_c}} \qquad (21)$$

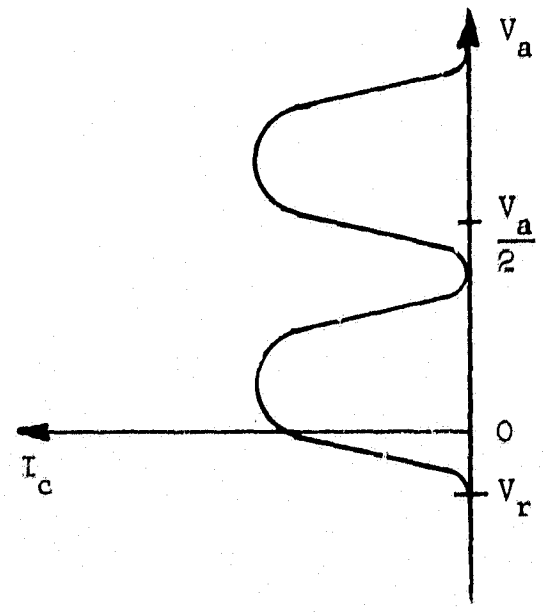

Just at saturation drive

FIGURE 28 MODEL OF PROFILE OF COLLECTOR CURRENT DISTRIBUTION VERSUS EXIT POTENTIAL WITH CURRENT BELOW CATHODE POTENTIAL INCLUDED

If the number of collector elements per unit length along the radial direction is constant,

$$\frac{V_r}{V_a} = \frac{N_n}{N_c - N_n}$$

Expression (21) then becomes

$$\eta_e = 1 - \frac{\frac{1}{N_c} + 2k\left[1 - \frac{N_n}{N_c}\right]\frac{V_o}{V_a}}{1 - 2\frac{N_n}{N_c} + \frac{1}{2\pi}\sin\left(4\pi\frac{N_n}{N_c}\right)} \qquad (22)$$

It is of interest to compare a typical calculation performed while neglecting the current below cathode potential i.e., $N_n = 0$, equation (14), with the same calculation utilizing $N_n \neq 0$, equation (22).

Consider the situation plotted in Figure 19 for efficiencies below saturation drive, where

$$\frac{V_a}{V_o} = 20$$

$$k = 1$$

$$N_c = 15$$

$$N_n = 0$$

The electronic efficiency, η_e, is 83%.

Now use the same set of parameters but with $N_n \neq 0$. In equation (22) take a value of $N_n/N_c = 0.2$. This would be a reasonable value, based on experimental experience and the computer simulation results given in Section 4.5. In this case equation (22) yields an electronic efficiency, η_e, of 79% for drive levels below saturation.

Thus, the more complex model of current distribution gives results which are close to those calculated. This illustrates the relative importance of various parameters in the collector design.

4.4.2 Modification of Electronic Efficiency due to Possible Secondary Emission from Collector Elements

The analyses presented in Section 4.4.1 may be directly modified to include the effect of possible secondary emission upon the electronic efficiency. It is felt that the effective secondary emission ratio for electrons striking the collector ring elements can be kept in the range of 0.1 to 0.3. The techniques available for doing this will be discussed in Section 4.4.3.

Secondary emission introduces a power loss equal to the secondary current emitted times ΔV, the potential difference between adjacent collector rings. It is not felt that any appreciable number of secondary electrons will return to the interaction space, but should this occur, these returned electrons will simply reenter the circulating electron stream and contribute to the energy conversion process.

Any secondary electrons which enter the interaction space are generated at the time of impact of the primary electron. Thus they are in phase coherence with the RF wave, as was the primary electron. Any noise associated with the discrete nature of the secondary emission process is, therefore, of the same order as the shot noise that accompanies the secondary current emitted from a thermionic cathode. Whether this background shot noise is significant depends upon the existence of a noise gain mechanism in the primary beam. A low level diocotron gain mechanism has been provided in the design analysis for the beam-circuit interaction. Thus the small amount of secondary emission current that may return to the interaction space joins the primary beam without affecting the noise considerations.

Since the secondary electrons travel in the same circumferential direction as the primary beam they do not provide a mechanism for RF feedback.

The effect of secondary emission on the electronic conversion efficiency may be estimated by modifying equation (12). Electronic efficiency, η_e, then becomes

$$\eta_e = \frac{\sum_{n=1}^{N_c} I_n\left(V_n - kV_o - \frac{\Delta V}{2}\right)}{\sum_{n=1}^{N_c} \left[I_n(1 - \delta) + \delta I_{n-1}\right] V_n + \delta I_n \Delta V} \qquad (23)$$

where δ = secondary emission coefficient

I_n = primary beam current impinging on nth ring

ΔV = potential difference between adjacent collector rings

$(I_n \delta \Delta V)$ is the energy dissipated on the (n + 1) collector ring due to secondary emission from the nth ring. If this current in turn produces secondary emission at the (n + 1) ring, the current generated is $(I_n \delta^2)$. Thus, if the process is repeated b times, the secondary emission current generated at the bth event is $(I_n \delta^b)$. If $\delta \ll 1$, this quantity becomes insignificant. Thus, only the first order event which sends current from element n, to element (n + 1) is considered in equation (22). For a sufficient number of collector elements and with I_n a reasonably smooth function of V_n

$$-\delta I_n + \delta I_{n-1} \cong 0 \qquad (24)$$

Equation (22) may then be simplified to

$$\eta_e = \frac{\sum_{n=i}^{N_c} I_n(V_n - kV_o - \frac{\Delta V}{2})}{\sum_{n=1}^{N_c} I_n(V_n + \delta\Delta V)} \qquad (25)$$

using

$$a_n = \frac{I_n}{I_k}$$

and

$$\Delta V = \frac{V_a}{N_c}$$

(N_c = total number of collector elements)

Equation (24) becomes

$$\eta_e = \frac{\sum_{n=1}^{N_c} a_n(n - \frac{1}{2} - kN_c \frac{V_o}{V_a})}{\sum_{n=1}^{N_c} a_n(n + \delta)} \qquad (26)$$

Using the function for a_n which approximates the distribution when driving just below the saturation level, equation (19),

$$a_n = \frac{1}{N_c}(1 - \cos \frac{4n\pi}{N_c})$$

Substitute it into equation (26) and carry out the summation by integrating from 0 to N,

$$\eta_e = \frac{1 - \frac{1}{N_c} - 2k\frac{V_o}{V_a}}{1 + \frac{2\delta}{N_c}} \qquad (27)$$

where δ = secondary emission coefficient

Equation (27), under the conditions assumed in the derivation, differs from the expression previously derived only by the extra term in the denominator. The previous expression did not consider secondary emission. It is seen that for large values of N, the number of collector rings, the effect of secondary emission on the calculated electronic efficiency becomes of rapidly decreasing importance if δ is small. A plot of the values calculated from equation (27) is given in Figure 29. Here V_a/V_o is taken as 15, and k is taken as 1. The parameter, δ, is allowed to take on the values 0.1, 0.2, and 0.3. The value ($\delta = 0$) is replotted from Figure 13 for comparison. It is seen that for a large number of collector rings, the curves all converge toward the ($\delta = 0$) values. Once again this emphasizes the benefits to be obtained from a large number of collector rings in the structure design.

Thus, the possibility that some secondary emission may occur from the elements of the collector structure of the axial injection crossed-field amplifier does not present the serious problem that it might in the case of an O-type amplifier. This follows from the fact that any secondary electrons which reenter the interaction system do not create the danger of causing regeneration but merely are added to the circulating electron stream which is already reentrant by design. By taking appropriate measures, the value of secondary emission coefficient may be kept low, thus reducing the

(Current distribution, two symmetric sinusoids, just below saturation drive)

$$\eta_e = \frac{1 - \frac{1}{N_c} - 2k\frac{V_o}{V_a}}{1 + \frac{2}{N_c}}$$

$\frac{V_a}{V_o} = 15$, $k = 1$

δ = Secondary emission coefficient

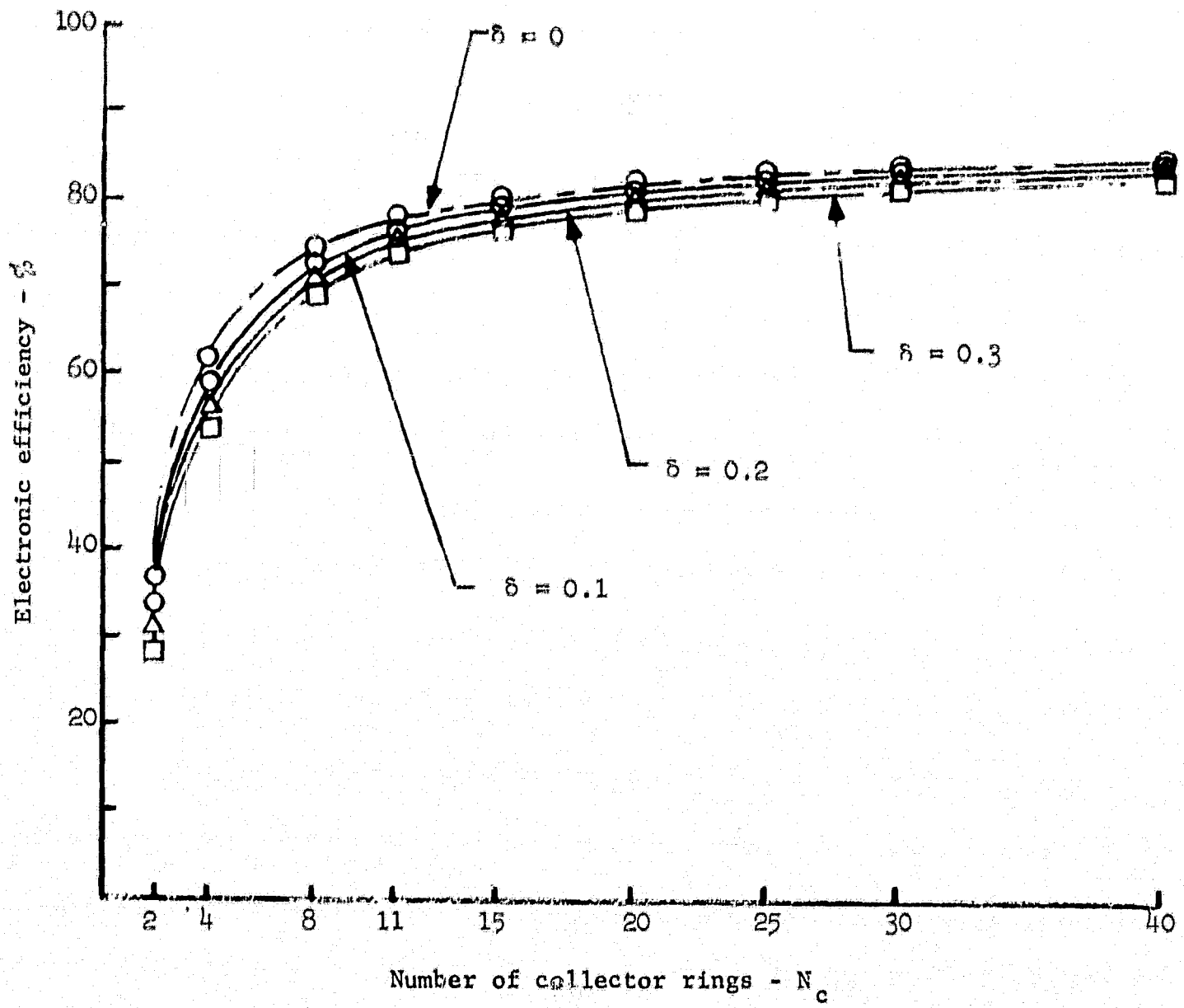

FIGURE 29 ELECTRONIC EFFICIENCY VERSUS NUMBER OF COLLECTOR RINGS WHEN SECONDARY EMISSION OCCURS

power loss caused by secondary electrons going from one collector element to the ring of next higher potential. In addition a large number of collector elements reduces this loss factor to a minimum value.

The collector structure, as used in conjunction with the axial injection crossed-field amplifier performs a potential sorting operation in the emerging electron stream. Therefore, it has none of the limits of effectiveness that accompany the use of multi-element collector structures in O-type amplifiers, where the collector structure must inevitably perform a velocity sorting function.

4.4.3 Suppression of Secondary Emission

Secondary emission from the collector elements results from the impact of electrons with an energy approximately equal to that of the synchronous voltage. This emission can be suppressed by choosing suitable materials and field shaping techniques. The materials to be used should produce a secondary emission coefficient that is less than unity. Among such materials are titanium and, under more recent development, a deposit of tungsten carbide (Ref. 5). The texture of the surface is also of importance in determining the secondary emission coefficient. A rough textured or fluffy surface usually results in a lowered secondary emission coefficient. However, it is felt that the most important contribution to the suppression of secondary electrons will be made with field shaping techniques that set up potential gradients which tend to return the secondary electrons to the emitting element.

One form of this technique is shown schematically in Figure 30. This is a technique that is usable when the collector structure consists of a series of coplanar, concentric rings. Figure 30 shows a few typical rings from the array of collector elements. The direction of ascending voltage is V_1, V_2, V_3, and V_4.

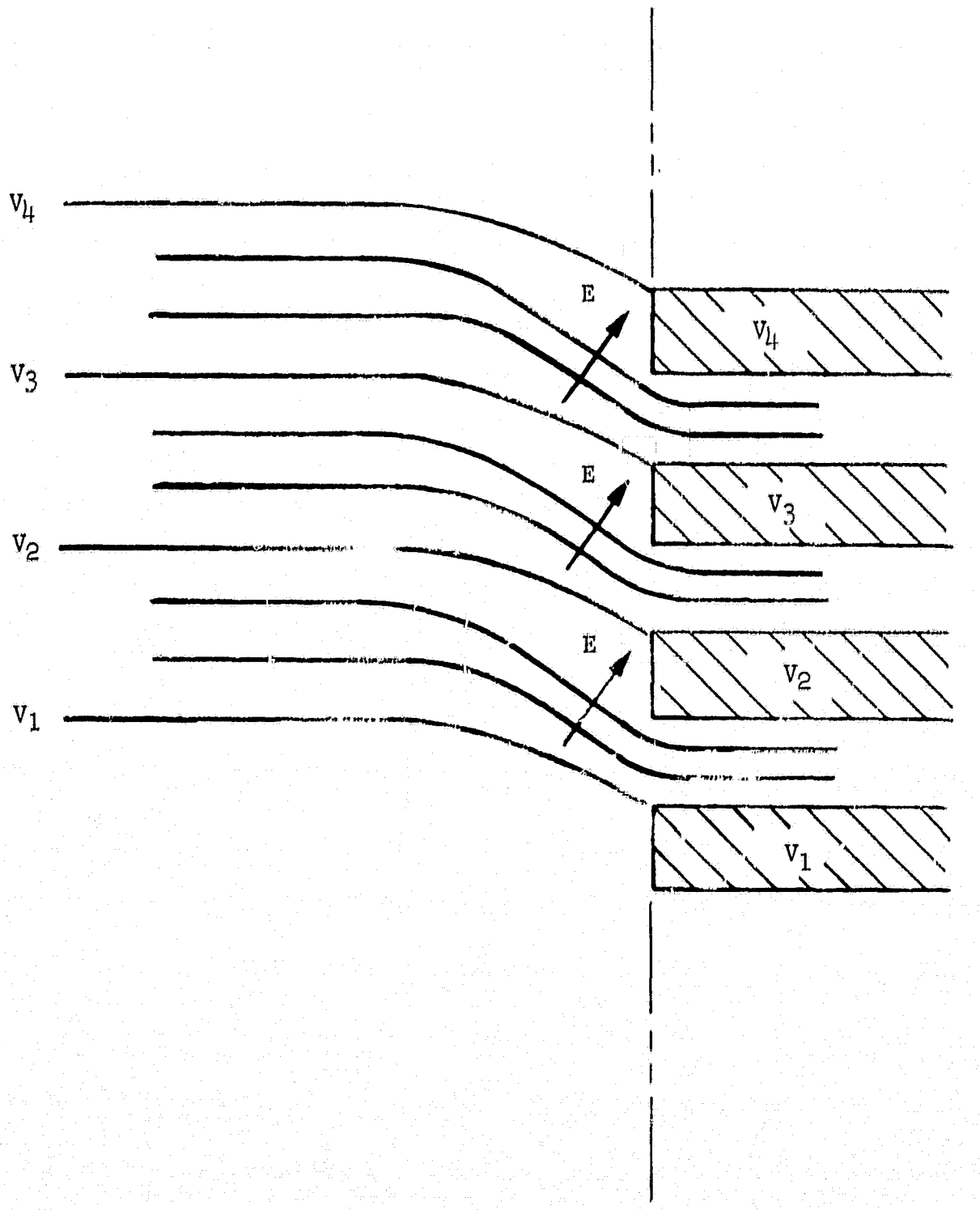

FIGURE 30 TRAPPING OF SECONDARY ELECTRONS IN COLLECTOR REGION BY FIELD SHAPING, COPLANAR CASE

The rings, as shown, are offset geometrically from the corresponding potential line in the interaction space from which the electrons are coming. The potential gradient is such that any electrons striking the front or bottom surface of the ring will be driven back into the element from which they were emitted. The electrons that are emitted from the top surface of a given collector ring are those that will be accelerated to the ring of next higher potential. Thus it is only from a small fraction of the available secondary emission area on the ring that any secondary emission may occur. The effective secondary emission coefficient for the metalic coating material used on the collector ring is decreased by this area reduction factor.

In Section 7.0 some variations on the structural details of the collector assembly are discussed. In particular reference is made to the situation in which all the collector element tips are not coplanar but are displaced from each other axially as well as radially. Field shaping techniques may still be employed to return the secondary electrons to the emitting element. This situation is sketched in Figure 31. The elements are arranged so that the one nearest sole potential is also closest to the interaction space, receding with increasing potential as shown. The forward edge of the collector element may be tapered, as shown, so that most of the electron collection occurs from the surface where a potential gradient exists, tending to drive electrons back into the surface. Thus, although the coplanar arrangement is the first choice for electrical design reasons and minimizes the total length of the magnetic gap, field suppression techniques may still be carried out if a variant of the collector structure seems desirable from the point of view of optimum mechanical design.

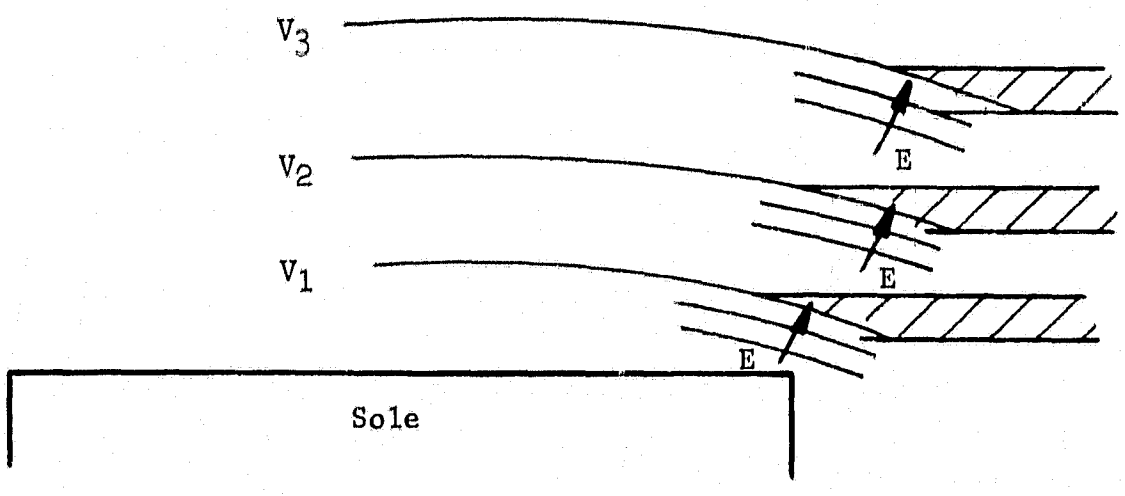

FIGURE 31 TRAPPING OF SECONDARY ELECTRONS IN COLLECTOR REGION BY FIELD SHAPING, NON-COPLANAR COLLECTOR

4.4.4 Circuit Efficiency

The preceding sections have evaluated the factors that determine the electronic efficiency, η_e, of the amplifier. The electronic efficiency of the amplifier was defined as the RF power generated, P, divided by the dc power input, P_{dc}

$$\eta_e = \frac{P}{P_{dc}}$$

This definition does not account for circuit losses which occur during RF power generation. The circuit efficiency, η_c, is defined as the RF power output, P_o, divided by the RF power generated

$$\eta_c = \frac{P_o}{P}$$

Therefore the conventional conversion efficiency, η, is given by

$$\eta = \eta_e \eta_c = \frac{P_o}{P_{dc}}$$

The circuit efficiency, η_c, is a function of the insertion loss of the delay line and of the nature of the power distribution along the delay line between the input and output ends. When the RF drive level applied to the amplifier is below that needed to produce saturation, the power distribution along the delay line as a function of length is typically exponential. In this case, a simple analytical expression is easily developed for the circuit efficiency.

The circuit efficiency for the delay line, η_c, thus is given by

$$\eta_c = \frac{P_o}{P_o + P_d}$$

where P_o = RF power output from line
P_d = power dissipated on the line due to RF energy flow

In a low loss system this may be written as

$$\eta_c \cong 1 - \frac{P_d}{P_o} \tag{28}$$

Below saturation drive the power distribution along the delay line is exponential as follows

$$P = P_i e^{bz}$$

where P = power level at any point on the line
P_i = power at input of the line
b = gain in nepers per wavelength
z = distance along the line measured in wavelengths

Let α be the line attenuation factor in nepers per wavelength. The power dissipated over a differential line length, dz, is given by

$$dP_d = \alpha P \, dz$$

Therefore, if N is the total number of wavelengths on the delay line, the total dissipated power is

$$P_d = \int_o^N \alpha P \, dz$$

$$P_d = \int_o^N P_i \, e^{bz} \, \alpha \, dz$$

$$P_d = P_i \frac{\alpha}{b} (e^{bN} - 1) \tag{29}$$

Substituting equation (29) into (28), the expression for circuit efficiency becomes

$$\eta_c = 1 - \frac{P_i \frac{\alpha}{b} (e^{bN} - 1)}{P_i e^{bN}}$$

$$\eta_c = 1 - \frac{\alpha}{b} (1 - e^{-bN}) \qquad (31)$$

For a high gain amplifier,

$$\eta_c \cong 1 - \frac{\alpha}{b} \qquad (32)$$

Equation (31) has been used in estimating the circuit efficiency, η_c, from the calculated values of α for both the UHF and S-band amplifier designs, with drive levels below saturation. Thus, for the UHF amplifier, the delay line is 13 wavelengths long and the insertion loss is 0.0221 db per wavelength. The gain factor is 2.08 db per wavelength. Equation (32) yields a theoretical small signal circuit efficiency of 98.8%, where the total line insertion loss is 0.287 db for the 2" bar height.

In the case of the S-band amplifier with the 1" bar height, the total calculated insertion loss is 1.2 db. The circuit is 19 wavelengths long giving an α of 0.0615 db per wavelength. The gain factor is 1.42 db per wavelength. Equation (32) then gives a theoretical small signal circuit efficiency for the S-band amplifier of 95.7%.

It is to be understood that, as the saturation region is approached, the distribution of power along the line is no longer exponential. This means that it is no longer true that most of the

power in the line passes through only a very small part of the line near the output end. In the case of saturation or near saturation, the power distribution along the delay line may be approximated as being linear or perhaps nearly constant along the last 20% of the line. Therefore a fair approximation, based on experience, is to presume that one-half the total output power sees the entire attenuation in the last 20% of the line. This may be used then to give an approximate circuit efficiency under saturation conditions.

The electronic efficiencies for the UHF and S-band amplifiers were obtained from the curves in Section 4.4.2 using a value of k approximately equal to unity. The circuit efficiency was estimated as just described. This formed the basis for the first order estimate of the efficiency in the case of both UHF and S-band amplifiers.

In the computer calculations which are described in Section 4.5, there is no need to separate the electronic and circuit efficiencies. The insertion loss of the delay line is an input parameter to the computer program. The effect of the line insertion loss is taken into account continuously, as the power growth along the delay line is traced out by sequential calculation steps beginning at the input end and proceeding to the output end.

4.4.5 Experimental Verification of Collector Operation and Effect on Efficiency

A few small experimental tubes have been built in the UHF region in order to verify the basic principles of the axial injection amplifier. This was done on a research program sponsored by S-F-D laboratories. These tubes were not of optimum design but were constructed from readily available tube parts, with the main intent being to verify the basic operating principles.

The first tube built for this sequence of experiments had a simple one-element collector. This amplifier verified that an extended dynamic range was established by the removal of unused space charge as

the beam moved axially through the system to the insulated collector. This initial tube exhibited efficiencies on the order of 45%. A succeeding tube had a three-element collector. On this particular vehicle, it has been possible to obtain conversion efficiencies at saturated power levels in the range of 70% to 75%.

Some of the response characteristics of this tube under a particular set of operating parameters are exhibited in Figures 32 and 33. Figure 32 is a plot of the RF power output of the tube as a function of RF drive power. This set of operating parameters was optimized to give a linear response or to reduce the noise output to an absolute minimum. The major value of this particular set of data is to illustrate the operation of the three-element collector in maintaining efficiency over a range of drive levels and programming dc power input into the tube. The lower double curve is the power output from the tube; the dashed line represents power output at the signal frequency and the difference represents a small amount of background noise. Over the range of power levels at which the tube was tested, the power output at the signal frequency increased from 2.8 watts with 50 mw of drive signal to 73 watts with 13 watts of drive signal. The integrated noise power from the tube at the low signal drive was about 1.5 watts spread over a very wide frequency range. Efficiency at the 73 watt power output level was 55% and at the low drive conditions was 8.5%. These data show the effect of RF control of the dc power input to the amplifier. The power output from the tube is reduced by a factor of 25, but over this range the efficiency is only reduced by a factor of 6.5. This occurs because the dc input power of the tube is reduced by a factor of 4 as the RF drive signal is lowered. This variation of net dc input is plotted on the upper curve in Figure 32. It should once again be emphasized that the operating parameters in this particular tube are not optimized for absolute minimum of background noise level or for linearity of amplifier response characteristics. The data plotted

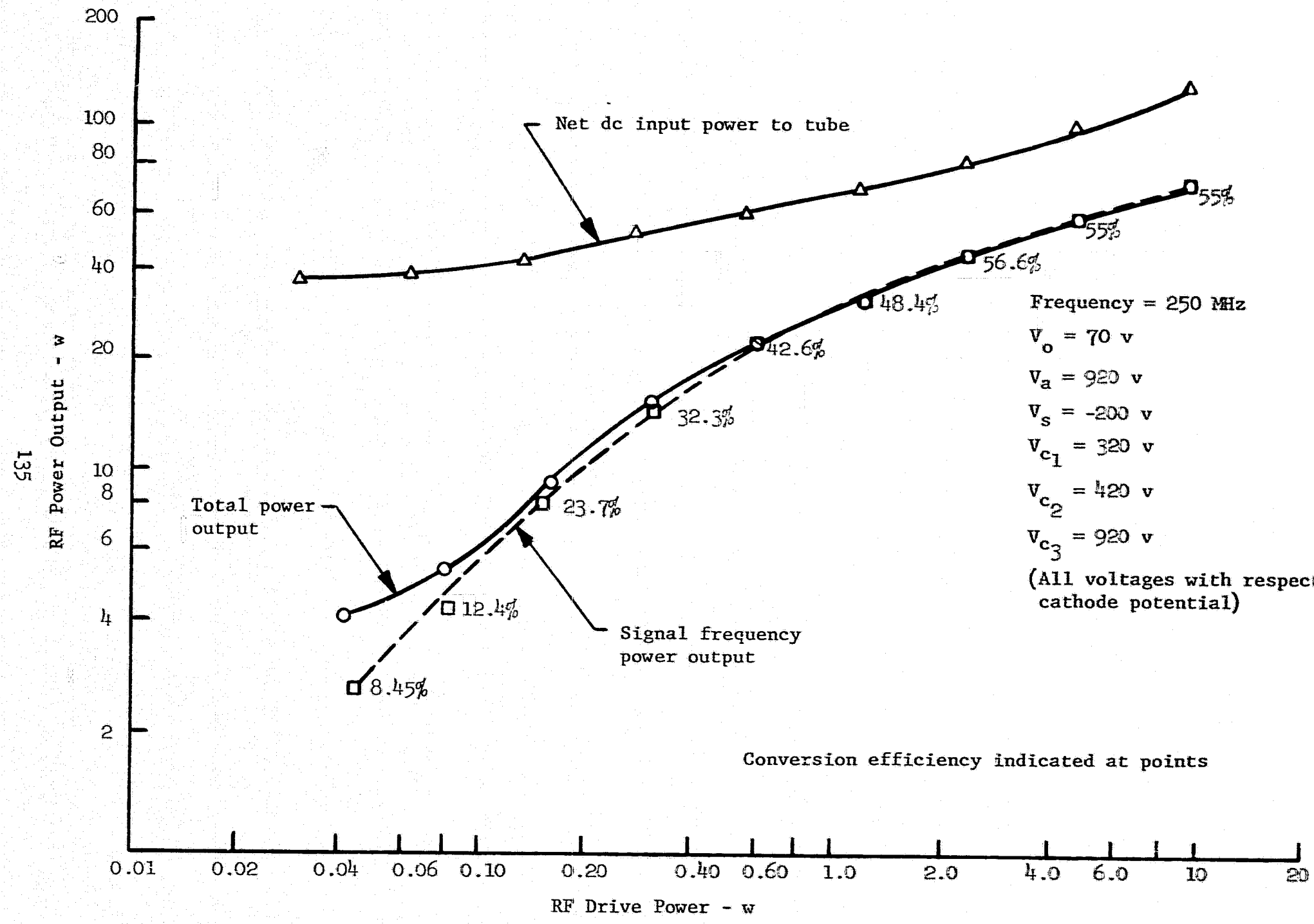

FIGURE 32 GAIN CHARACTERISTICS OF SECOND UHF AXIAL INJECTION AMPLIFIER

Frequency = 250 MHz
V_a = 920 v
V_s = -200 v
V_{c_1} = 320 v
V_{c_2} = 420 v
V_{c_3} = 920 v

(All voltages with respect to cathode)
Current to collector 3 (I_{c_3}) is negligible under these conditions

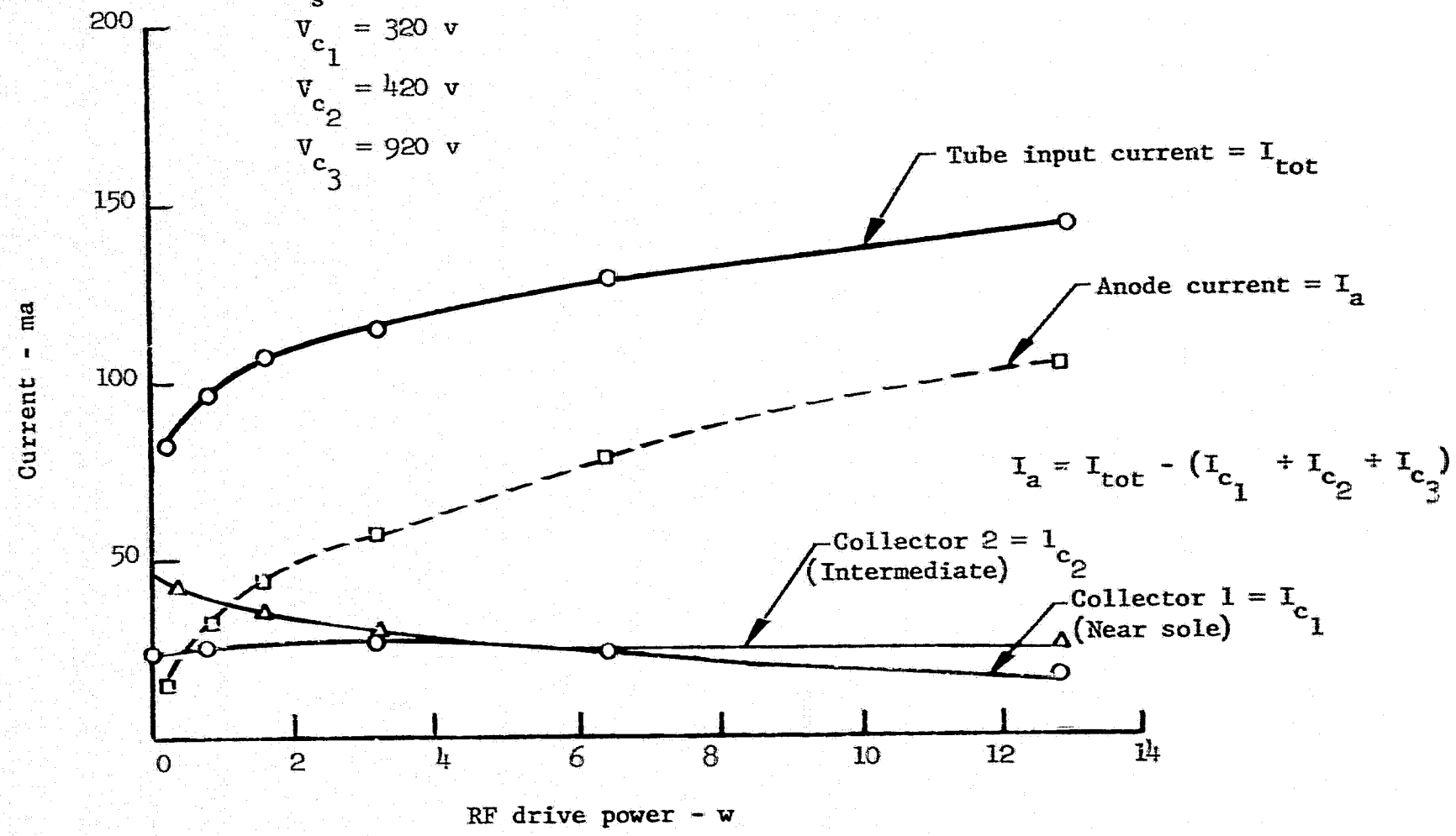

FIGURE 33 CURRENT AS A FUNCTION OF DRIVE LEVEL FOR SECOND UHF AXIAL INJECTION AMPLIFIER

in Figure 33 illustrate the switching of the current to various collector elements as a function of RF drive level. The data in Figure 33 are taken under exactly the same operating parameter settings as the data for Figure 32. The amount of anode current is clearly seen to increase as the RF drive is increased. The current on the collector having the lowest potential near the sole is seen to drop by a factor of 2 in going from the zero drive level of 10 watts of drive. The anode current is seen to go from a value of 20 ma at zero drive conditions to a value of about 75 ma at 10 watts of drive. The geometry of even this simple three collector system was far from optimized, for all the collector elements were not equally effective. However, the general principle of control of current exit potential, as a function of the RF drive, is illustrated by the results.

4.5 Results of Computer Calculations

At the start of this study program, no computer simulation program existed which would adequately describe the interaction process occurring in the axial injection crossed-field amplifier. Existing computer programs for analyzing the interaction processes in crossed-field amplifiers were set up to solve a two dimensional problem. Given an array of current charges, they typically trace the trajectories of the electrons in the current stream as they move in both the radial and circumferential direction while calculating the transfer of energy that occurs between the electron stream and the fields which are produced by the traveling wave on the delay line.

As has been indicated in preceding sections of this report, an initial design procedure was synthesized from the analytical expressions which exist for the injected beam crossed-field amplifier. It was expected that this procedure would be verified both by experimental results and by computer calculation. A computer program was needed that was capable of handling the three dimensional problem

of the axial injection crossed-field amplifier. An attempt was made to modify an existing program for the conventional injected beam crossed-field amplifier. The unmodified program did not allow any reentrancy in the calculation since it assumed that all electrons would be collected on the delay line or on a collector system at the end of the run through the interaction space. It also allowed only for the injection of all the current at the input end of the circuit. The approach used is Lagrangian and the current is simulated by an array of charge rods. The program permits the rods to be arranged either in a single layer or in multiple layers to simulate finite beam thickness and circumferential velocity slip within the beam. The radial position of the top of the beam upon entry into the interaction space may also be specified. As the program was originally set up, the rods were introduced over the two π radians of phase angle corresponding to a single RF wavelength. This simulates entrance of the beam at all values of RF phase. The other input parameters to the program are the sole and cathode voltages with respect to the anode and magnetic field. The values of circuit interaction impedance and RF drive level are specified, along with the pitch and phase shift per section of the circuit. This specifies the point on the dispersion curve at which the circuit is operating. An iterative series of calculations then traces this cluster of electrons down the delay line over the specified length. The circuit insertion loss is specified and even circuit severs may be taken into account. The time step over which this calculation is iterated may be specified.

In order to adapt the program to simulate the process of axial injection, the rods were introduced in pairs at regular intervals along the circuit so that a distributed input current was achieved. The two rods which were injected at a given point on the transmission line were π radians apart in RF phase. Thus, their introduction represented no RF information at the frequency of the calculation. In addition, a control variable was set up so that the

amount of time that each pair of rods spent in the system was specified. Thus, when any charge rod had been in the system a length of time equal to the time of the axial transit through the tube, it was removed from the system and noted as having been taken up by the collector structure (or anode, if this occurred sooner). The program records the point at which this occurs (in wavelengths down the circuit), the radial and phase coordinates, and the exit potential, if this was desired.

The feature of electron stream reentrancy was handled by taking all the charges remaining in the interaction space at the end of the first pass through the delay line, rearranging them in pairs, and introducing them again at the input to the interaction system for a succeeding pass. They were arranged so that the new radial position of each pair of electrons was the average position which these two rods occupied at the termination of the succeeding run. Thus, they entered for the succeeding pass with the total potential of the charge cluster unchanged.

However, the phase of these reentering electrons was scrambled so that no RF information remained on the reentering electron stream. Thus, all of the reentering electrons were reintroduced at the start of the second pass. An account was still being kept of their lifetime in the interaction system, and they were removed at the point in time originally specified. In addition to these reentering electrons, the original distributed injection was repeated so that the total current stream was now made up of reentering, as well as freshly injected, charge rods. This, then, gave a reasonable simulation to the process by which the electron stream was formed in the interaction space. This iteration could be repeated several times to insure that a self-consistent set of conditions had been achieved.

As mentioned, the calculation, which traces the growth of RF power on the delay line, is carried out in a sequence of time steps which are small compared to an RF cycle. At the end of each time step, the distance down the transmission line, the gain, the power level at that point, the amplitude of the RF wave, the phase angle between the circuit wave, and the RF current were printed out. At regular intervals in this procedure, a complete read out of information was given on the charge rods in the interaction space. These were the radial coordinate, the circumferential location with respect to the phase of the RF wave, the increments in velocity, and the position from the last time step. As rods were collected on either the anode or the collector, a read out of this fact was obtained. In the case of collection on the collector, a read out of the radial coordinate was given, and in all cases the power dissipated on the circuit element was calculated and noted.

The successful modification and testing of this program was achieved only at the very end of this study program. Therefore, it was used only to check the S-band amplifier design, because of the limited time available. It is felt that the information obtained from the runs on the S-band amplifier can be expected to verify the similar features of the UHF design. A set of computations were obtained at two drive levels, 50 watts and 5 watts. Listed below are the input parameters to the computer runs:

Sole to line spacing	0.138"
Slow wave structure pitch	0.083"
Slow wave structure height	1.00"
Phase shift per circuit section	$\pi/2$
Frequency	2.0 GHz
Interaction impedance	100 ohms
Circulating beam current	1 amp
Cathode-anode voltage	12 kv
Sole to anode voltage	19.55 kv
Synchronous voltage	809 volts
Magnetic field	3307 gauss

Number of rod layers in simulation	1
Position of beam top from delay line	0.079"
Fraction of cyclotron period calculation is advanced per step along the line	0.1
Length of line	6.3"
Circuit insertion loss	0.189 db per inch
Lifetime of electrons	7.3" of circumferential travel (this allows for the drift space)

On the initial circulation through the interaction space, the total current input was represented by an array of 30 charge rods. The time step of 0.1 cyclotron wavelengths means that 878 calculations of charge rod coordinates and interaction processes were carried out while traversing the interaction length of 6.3". It should be realized that on successive passes to simulate the reentrancy, the total number of charge rods was changed but the current in the system at any one time was relatively constant, as would be the case for axial injection combined with reentrancy.

4.5.1 Verification of Gain

The results of the computer runs, both at the 5 watt drive level and the 50 watt drive level, verify the analytical calculation of 20 db of gain to a high degree of accuracy. It should be recalled that reentrancy was simulated by a series of cascaded runs where the charge rods remaining from the preceding run were rearranged and reintroduced as initial input current for the run under consideration. Therefore, it took at least two or more iterations before the results were meaningful. It was, therefore, apparent that a reentrant or closed cycle situation was being approximated by cascading a series of open ended runs. If the process were a perfect simulation, then after a given number of iterations, the charge rods left in the

interaction system at the end of the run would equal in number and have the same coordinate positions as the rods remaining in the previous run. Thus, a perfect closure of the calculation would have been achieved. However, it is not necessary to achieve this closure exactly to obtain very useful results, particularly if successive iterations converge or oscillate about a perfect closure position. This will be examined in more detail shortly.

A three iteration calculation was carried out for the 50 watt drive case and a two iteration calculation for the 5 watt drive case. The results are as follows:

	Gain	RF Power Output
5 watt drive, second iteration	23.5 db	1130 watts
50 watt drive, second iteration	20.17 db	5200 watts
50 watt drive, third iteration	21.4 db	6931 watts

It should be pointed out immediately that this set of gain numbers cannot be used directly to check linearity since there is a small imbalance in the technique used to simulate reentrancy and it was not practical to run a very large number of iterations. Information about the linearity will be derived in another manner from the computer output in Section 4.5.3 These gain numbers, however, do verify the magnitude of gain level that was predicted.

4.5.2 Verification of Efficiency

The conversion efficiency of the amplifier is the RF power output divided by the total power input. In the actual device the total power input is simply the sum of the individual dc inputs to the anode and collector. Since, as has been pointed out, a closed cycle situation is being represented by a series of open ended calculations, the efficiency, η, at the end of any given iteration may be written in the following manner.

$$\eta = \frac{P_{RF}}{P_{dc} + (P_{RL} - P_{RR})}$$

where P_{dc}, P_{RL}, and P_{RR} are power quantities obtained by summations of the form

$$P = \Sigma V_n I_n$$

where V_n is an entrance or exit potential for a specific charge rod calculated from its spatial coordinates

I_n is the current represented by the charge rod

P_{dc} is the power summation for all the charge rods arriving at the anode or collector during the given iteration

P_{RL} is the power summation for all the charge rods remaining in the interaction space at the end of the run. These are the rods that would be reintroduced during the next iteration with rearranged coordinates and the value of $\Sigma V_n I_n$ kept the same

P_{RR} is the power summation for those charge rods which are introduced at the beginning of the run as reentering rods

If the cycle of iterations closed perfectly, then after a number of repeated runs, P_{RL} would always equal P_{RR} and in a computational sense would merely be a circulating component of power.

In the case of the 50 watt drive run after the second iteration

$$P_{RL} - P_{RR} = 1188 \text{ watts}$$

and after the third iteration

$$P_{RL} - P_{RR} = -1269 \text{ watts}$$

This is a swing of about plus or minus 14% around an exact energy balance, and indicates that the situation of exact balance is being bracketed by the two iterations.

The efficiency for the second iteration was

$$\eta_2 = \frac{5200}{4987 + 1188} = 84.2\%$$

and the efficiency for the third iteration was

$$\eta_3 = \frac{6931}{8941 - 1269} = 90.3\%$$

Taking the mean value of these two results gives 87%, which is the efficiency that would prevail if there were an infinite number of rings in the collector structure. This value is then corrected by the ratio of efficiency for ten rings to the asymptotic value for an infinite number of rings, as given in Figure 24. Then the efficiency for a finite number of collector rings is

$$\eta = 87\left(\frac{0.850}{0.911}\right) = 81\%$$

Therefore, the estimated efficiency from the computer calculations for the S-band amplifier operating at peak synchronizing power output is 81%. This compares closely with the 77% estimated from the analytical design procedures that have been described.

At the 5 watt drive level the results of two iterations yielded the following efficiency.

$$\eta = \frac{1131}{872 + 1096} = 57.4\%$$

Note that the energy balance term, 1096 watts, is about the same as for the second iteration, 50 watt drive. Correcting this value for a finite number of collector rings yields

$$\eta = 57.4\left(\frac{0.850}{0.911}\right) = 53.4\%$$

A reduction in output power by a factor of 6 has resulted in a reduction in efficiency by a factor of 1.5.

4.5.3 Verification of Linearity

The iterative procedure used to account for current reentrancy in the computer calculations results in some computational closure error. Therefore, a rigorous proof of gain linearity cannot be attempted at this point by examining the results of computer runs for different drive levels. This is true since there will be small fluctuations in resultant gain due to computational technique rather than the physics of the situation.

However a plausibility argument concerning gain as a function of drive level may be presented and used to examine the computer results. Generally a traveling wave amplifier which has a linear response as a function of RF drive is characterized by the following relationships:

$$P = P_i e^{bz} \tag{33}$$

$$G = -A + Bz \tag{34}$$

where under conditions of constant drive

P = RF power at any point, z, on the delay line

P_i = RF power input

b = gain constant in nepers per unit length

z = distance along delay line measured from input

G = power gain at point, z, in db

A = constant of the amplifier

B = constant determined by amplifier parameters

If an examination of the computer results indicates a power range within which the above characteristics exist, then it is reasonable to infer that the amplifier is linear within that power range. Therefore the most meaningful way to obtain some information about linearity of response from the computer calculations that have been carried out is to examine the distribution of power level along the length of the delay line. This will now be done for the 50 watt drive situation. As one advances along the delay line, the growth of power should be exponential or linear in db, until a point of saturation sets in. In the linear region, the gain in db is given by an expression of the form

$$G = -6 - \frac{\alpha l}{2} + 55DN \quad (db)$$

where α = insertion loss in db per wavelength

D = gain parameter

N = number of wavelengths on circuit

An examination of the range over which this linearity prevails indicates the upper power level at which the departure from linearity occurs and the extent of this deviation. This information can be taken directly from the computer output and is plotted for the case of the second iteration in Figure 34. Cumulative gain and power level on the delay line as a function of distance from the input measured in wavelength are plotted in this figure. The dashed line which is superimposed upon the gain curve is a plot of the idealized linear situation and fits the expression G = -A + 52.6DN. It is seen that at the peak of synchronizing power level, 5 kw, departure from linearity is just beginning and amounts to 0.4 db out of a total gain of about 20 db. This falls within the designated specification for amplitude linearity as given by the program requirements. Further comments on experimental verification of linearity are made in Section 4.6.

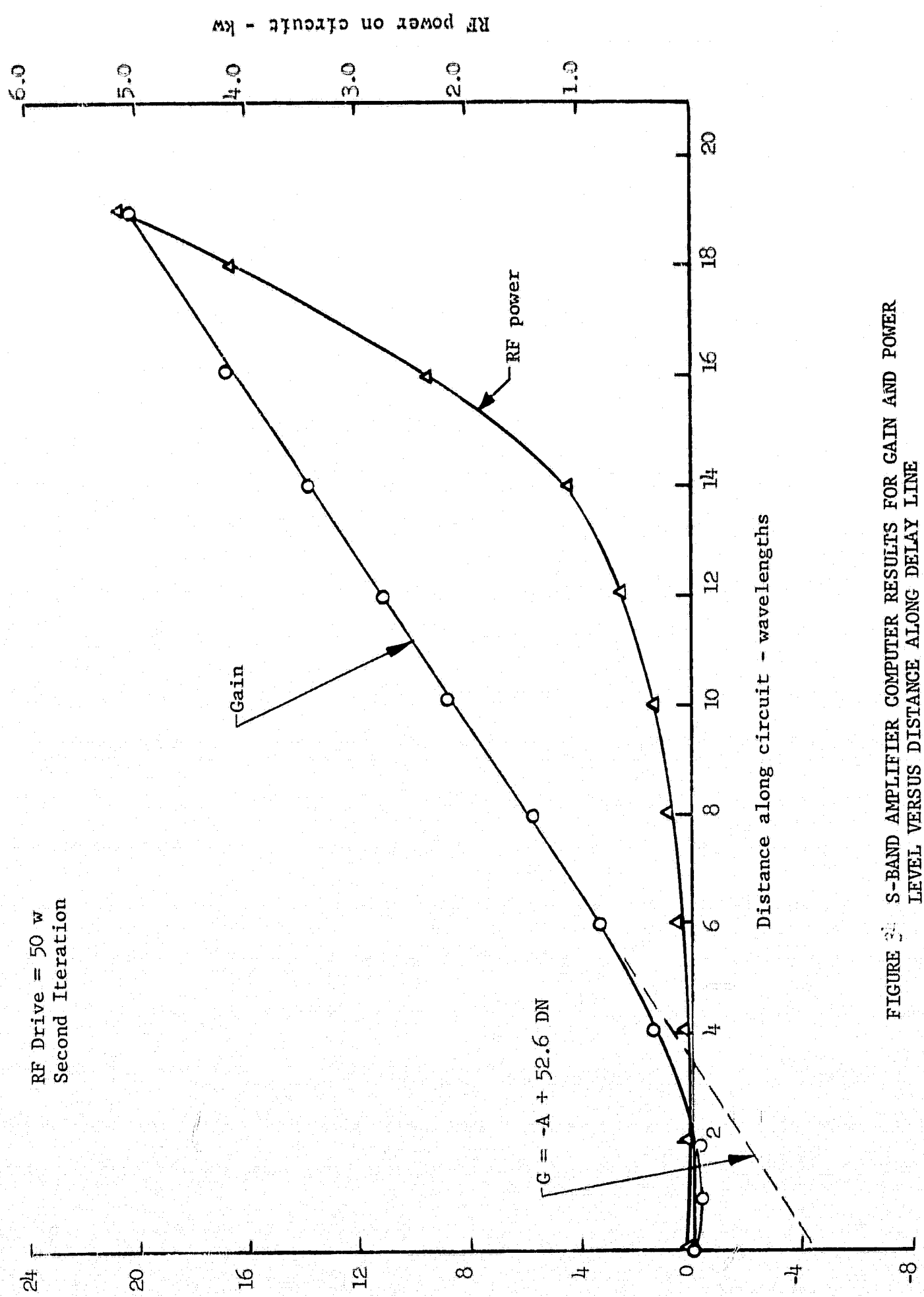

FIGURE 3: S-BAND AMPLIFIER COMPUTER RESULTS FOR GAIN AND POWER LEVEL VERSUS DISTANCE ALONG DELAY LINE

It is interesting to note that the slope of the gain curve in Figure 34 is 1.36 db per wavelength, (52.6DN instead of 55DN). In design S-1 which contains the set of tradeoff calculations from which the S-band amplifier design parameters were obtained, the value of 55D is given as 1.42 db per wavelength. A close correlation between these two numbers is arrived at by different computational techniques.

4.5.4 Current Distribution at Entrance to Collector Structure

An examination was made of the computer results to determine the distribution of current as a function of exit potential for those rods that were entering the collector structure. This was done to verify that the idealized distributions, used in the analysis of the collector design presented in Section 4.4 were reasonable models.

The efficiencies calculated and presented in Section 4.5.4 were obtained using the current distributions indicated by the computer results. It is of interest to compare the conversion efficiencies resulting from the computer calculations, with that estimated from the idealized sinusoid models used in Section 4.4.1. The comparison is tabulated below for the S-band amplifier design.

Using Current Profile from Computer Calculations	Using Idealized Model of Current Distribution
(10 collector elements)	(10 collector elements)
50 watts drive - 81%	Saturation drive - 80%
5 watts drive - 53.4%	Low level drive - 52.8%
	(η_c = 95.7%)

These sets of efficiency numbers demonstrate that for the cases examined here, the idealized models of current distribution in the collector region give a good approximation to the results obtained from the computer calculations.

The current distributions as a function of exit potential obtained from the computer calculations are presented in Figures 35 and 36. Figure 35 presents the results of the second iteration in the case of 5 watts of RF drive. The range of exit potentials was divided into 1.2 kv intervals going from the cathode potential of zero volts to the anode potential of 12 kv. The negative potential region below the cathode was also examined. The number of rods exiting within each of these potential intervals was counted. This count was normalized by dividing by the total number of rods exiting to the collector during this run. A plot is given, somewhat in the manner of a histogram, of exit potential versus the normalized value of current. It is seen, in Figure 35 that all of the current is indeed grouped below the 6 kv potential, which is the halfway point between the cathode and the anode, and some of the current is exiting at a potential less than cathode potential. As has already been explained, this represents some electrons that have acquired additional energy from the RF wave. Therefore, the idealized model, which was used for the small signal case and assumed that all the current was collected at a potential less than half the total cathode-anode potential, is seen to have been a reasonable one to use. Figure 36 is a similar plot for the case of 50 watts of RF drive. It is seen that, in this particular situation, most of the current is in the upper half of the potential range and indeed half of it falls in the last potential interval. This includes charge rods going to the anode and charge rods going to the collector in the potential interval between 10.8 kv and 12 kv. Once again the grouping of current as a function of exit potential is such that the model used to approximate saturation conditions seems to have been a reasonable one. This is the plot of current output for the third iteration where the RF output level is 6931 watts. In the case of the second iteration with an output power level of 5200 watts, a similar current

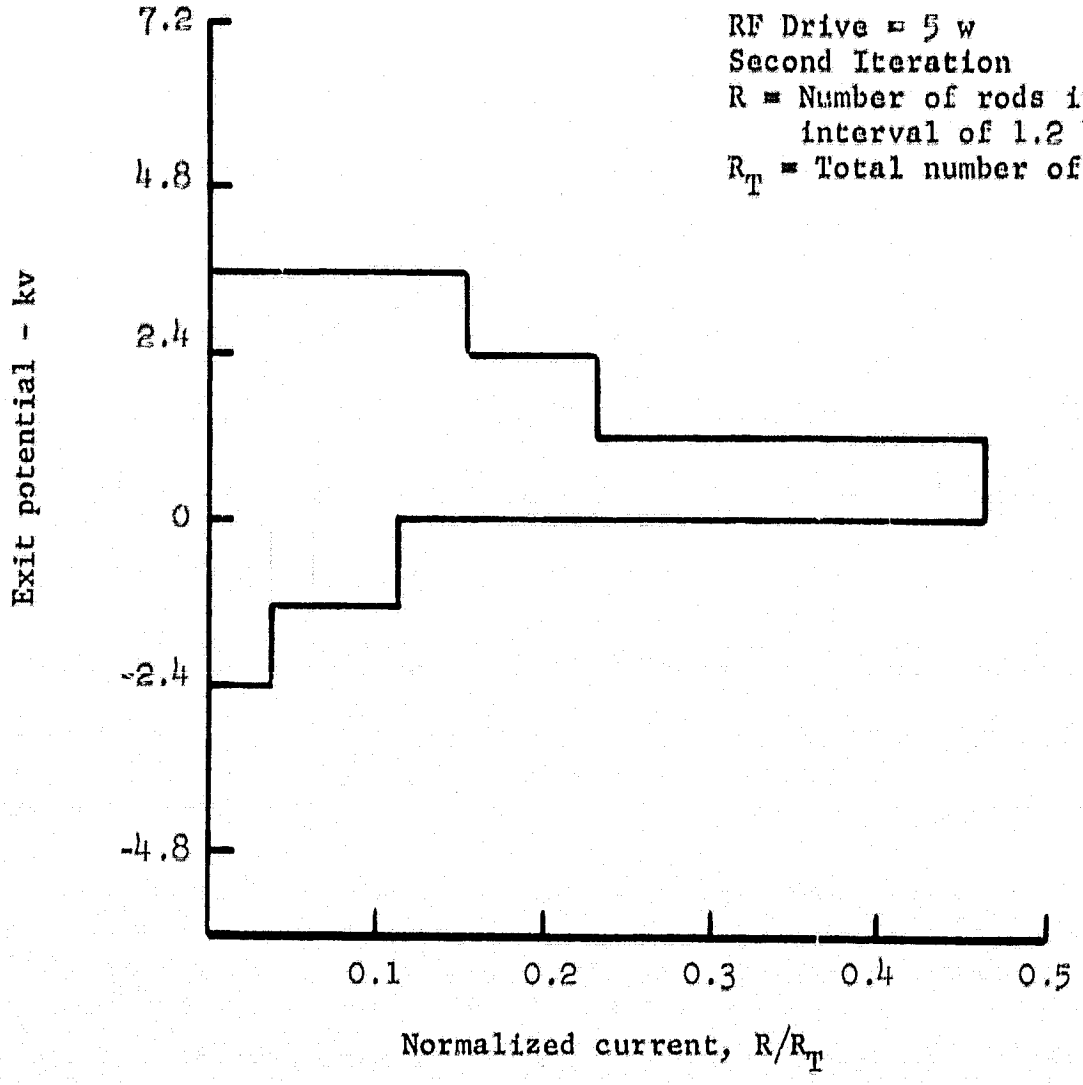

RF Drive = 5 w
Second Iteration
R = Number of rods in each potential interval of 1.2 kv
R_T = Total number of rods to collector

FIGURE 35 S-BAND AMPLIFIER CURRENT VERSUS EXIT POTENTIAL AT COLLECTOR STRUCTURE, COMPUTER RESULTS

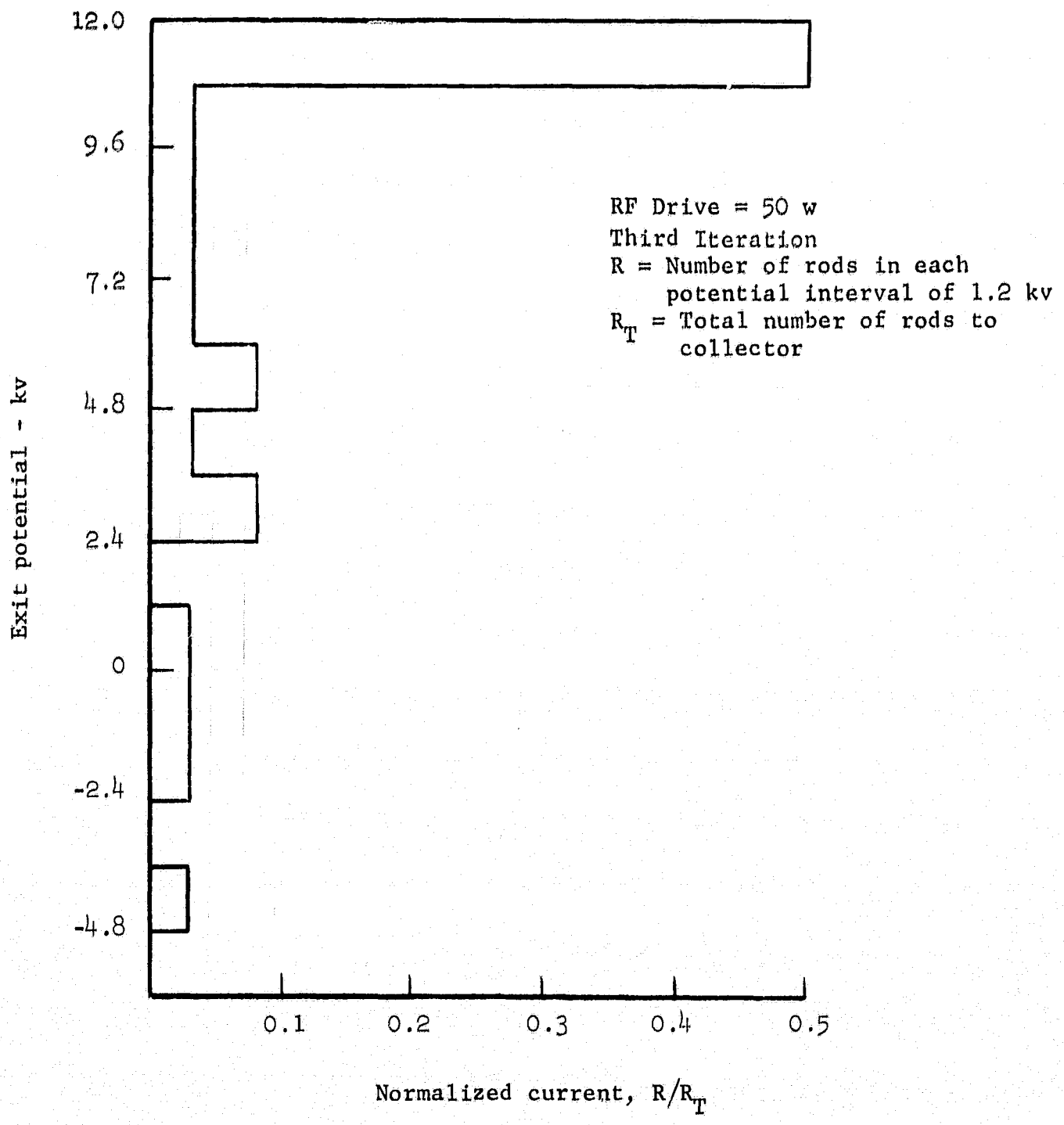

FIGURE 36 S-BAND AMPLIFIER CURRENT VERSUS EXIT POTENTIAL AT COLLECTOR STRUCTURE, COMPUTER RESULTS

distribution prevailed but in that case only 24% of the current appeared in the top potential interval. This was still a nearly saturated situation, but somewhat less saturated than the third iteration represents.

4.6 Some Additional Comments on Linearity and Some Experimental Results

In Section 4.5, it appeared that the design arrived at would meet the specification for amplitude linearity over a dynamic range of at least 20 db; that is, from the peak synchronizing power level down to the lowest signal level to be utilized. Some additional experimental verification of linearity of response and modulation capability was obtained on the second of the UHF experimental tubes built during the course of the S-F-D laboratories sponsored program on axial injection principles. This is the tube which has a three-element collector structure operating at a signal frequency of 150 MHz. The RF drive into the amplifier was sinusoidally modulated at a 10 kHz modulation rate. The percent of RF modulation was 80%. Both the drive level and the output power level were swept over a dynamic range of 19.1 db. The results of this experiment are shown in Figure 37.

Figure 37a is a photograph of the modulated carrier. This was obtained by putting the output of the axial injection amplifier into a Hewlett-Packard spectrum analyzer, and then examining the signal after the second IF strip where the carrier has been translated to 20 MHz. The RF signal was then fed directly into an oscilloscope which was capable of 20 MHz response. Figure 37b shows the output from square law detectors of both the input signal to the amplifier and the output signal from the amplifier. The scope was calibrated and the two tracers were originally superimposed with no visible difference in the detected envelope. The tracers are separated by 1 cm on the photograph for ease of inspection. The voltage and current adjustments while this particular set of measurements was

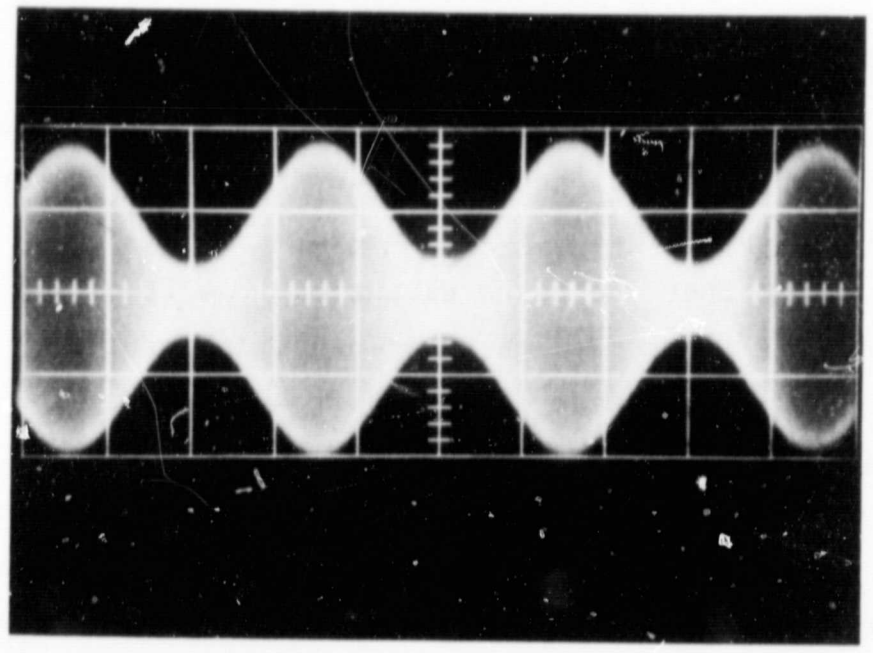

a. Modulated carrier, power range 19 db

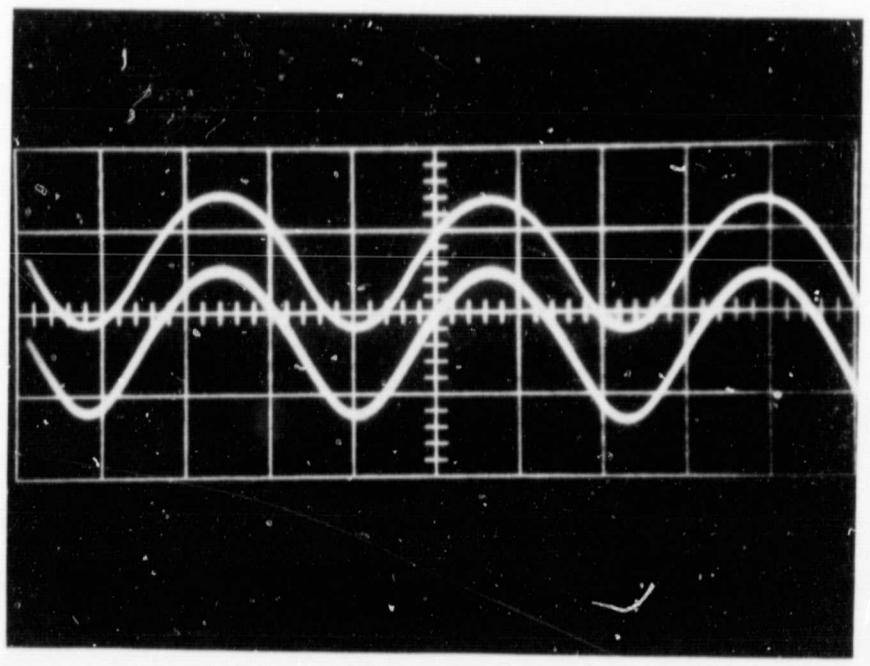

b. Detected input and output

FIGURE 37 SINUSOIDAL MODULATION OF THE RF DRIVE ON EXPERIMENTAL UHF AXIAL INJECTION AMPLIFIER

being made were such that the net conversion efficiency of the amplifier was about 30%. Even though the operating parameters were not optimized, it is significant to note that the efficiency measured with and without modulation was essentially the same.

It was specified that the phase deviation from linearity should be no more than 1.2^{o} over the operating bandwidth of the amplifier. One major source of phase deviation from linearity is dispersion in the delay line. It has already been indicated that the delay line chosen for this application has a constant $d\omega/d\beta$ over the 6 MHz bandwidth. Thus this will not be a source of phase deviation Phase deviations may also result from multiple reflections from poor input and output matches. These reflections can give a periodic variation of phase as a function of frequency. However, it is felt that the specification of an input and output VSWR of 1.05:1 is readily achievable over the narrow band specified for this amplifier.

4.7 Suitable Driver Sources for the Axial Injection CFA

Suitable microwave amplifiers are required to drive both the UHF and S-band axial injection amplifiers from a 1 watt level. In the case of the UHF amplifier, a driver with about 75 watts of output is required with approximately 19 db of gain. In the case of the S-band amplifier, a driver with approximately 50 watts of output is required with approximately 17 db of gain. These power output levels should be sufficiently below the saturation compression level so that the proper linearity requirements are observed. If the highest possible efficiency were required in the drivers, a development of low level axial injection crossed-field amplifier drivers might be considered. However, the axial injection CFA tubes designed as output amplifiers in this study program have 20 db of gain. As a result, the total chain efficiency is relatively insensitive to the efficiency of the driver tube. Therefore, available devices which may be considered as present state-of-the-art should also be considered.

4.7.1 The UHF Amplifier Chain

In the case of the UHF amplifier chain, one possibility would be to use two planar triodes, such as the Eimac 8757, to achieve a two-stage, Class A, linear amplifier with tuned circuit plate loads. This should be adequate to provide the required 6 MHz bandwidth. The Eimac 8757 has a 3/8" threaded connection for direct bolting to a heat sink block. This would be compatible with the heat pipe features of the thermal system that was evolved for the high powered axial injection CFA. This particular triode operates with about 900 volts of dc plate voltage and draws about 140 ma of plate current. The two-stage amplifier would weigh about 2 lbs.

Another planar triode suitable for use as a driver amplifier in the UHF chain is the General Electric L-65-S. It operates at a plate voltage of about 800 volts and a cathode current of 0.4 ampere. The required gain and bandwidth should be achievable in a single stage.

The RCA 8226 is a beam tetrode that could be adapted to the driver requirements.

A possible objection to the use of planar triodes is the uncertainty that a close-spaced grid adds to the question of life expectancy. Generally gridless devices can be expected to have a higher degree of life expectancy assurance.

An alternate possibility is to use a traveling wave tube amplifier. Consultation with the TWT division of Varian Associates indicates that a tube capable of 100 watts of RF output (to allow for compression) would be about 22" long, weigh 10-12 lb, and be focused by periodic permanent magnets. An efficiency of 30% at peak synchronizing power might be achieved with some collector depression.

Another possible UHF driver amplifier would be the scaled Microwave Associates traveling wave tube, MA-2001, which operates at 800 MHz.

Still another possibility is a scaled version of the Watkins-Johnson S-band amplifier, discussed below, which has a saturated power output of 100 watts and an efficiency at saturation of 50%.

It should be remembered that the crossed-field amplifier is transparent between the input and output ports, except for the insertion loss that exists on the slow wave circuit. Therefore, any RF power reflected from the output antenna will be returned through the crossed-field amplifier and will be diminished only by this insertion loss. As a result, it is desirable to place a circulator between the driver amplifier and the crossed-field amplifier output tube. For the narrow bandwidth involved, the necessary circulators are available in the present state-of-the-art. A typical circulator, capable of handling 100 watts of power, might weigh 2-3 lb.

4.7.2 The S-band Amplifier Chain

If the driver tube in the S-band amplifier chain is to be chosen from presently available devices, then the logical choice would be a traveling wave tube amplifier. Space-qualified TWT's, at the proper frequencies and power range, are already in existence. They are described below for reference purposes.

S-band space qualified traveling wave tube (TWT) amplifiers having outputs in the 20-50 watt range are now available as state of the art devices. Typical of these tubes are the X1250 and EM1264 TWT's manufactured by the Eimac Division of Varian Associates. Traveling wave tubes having power outputs in the indicated range would be suitable as drivers for the axial injection crossed-field amplifier which has been proposed in this design study. The crossed-field amplifier having 5 kw of RF output and 20 db of gain would therefore require 50 watts of RF input drive.

Both the X1250 and EM1264 TWT's have been designed for the 2.2-2.3 GHz telemetry band. The X1250 TWT has an output power of 50 watts and could undoubtedly be scaled somewhat higher. The EM1264 is essentially the same tube scaled down to a half-power version so that the output power is 20 watts. The overall efficiency of the TWT package is about 30% and each tube has about 30 db of gain.

For reference purposes, some of the operating characteristics and descriptive details concerning the Eimac X1250 and EM1264 traveling wave tubes are included as Appendix I.

Another suitable S-band TWT amplifier is the Watkins-Johnson WJ-395-1 which uses periodic permanent magnet focusing and has a saturated power output of about 100 watts. Some recently published characteristics of the WJ-395-1 are listed in Table XIII.*

An S-band circulator suitable for use between the driver tube and S-band axial injection CFA would weigh about 1-1/4 lb. Western Microwave Laboratories is one of the companies from which such a component is available.

*This data sheet supersedes WJ-395-1 Technical Data Sheet dated July 1968

TABLE XIII

TECHNICAL DATA FOR WJ-395-1

Performance Characteristics	
Frequency range	2.2-2.3 GHz
Saturation power output	100 w min
Saturation gain	33 db min
Overall efficiency, including heater[1]	42% min
Electrical Requirements	
Heater voltage	4-5 v
Heater current	1.0 a max
Anode voltage[2]	3.3-3.8 kv
Anode current	1.0 ma max
Helix voltage[2]	2.5-2.8 kv
Helix current	18 ma max
Collector voltage[2]	1.8-2.3 v
Collector current	115 ma max
Mechanical Characteristics	
Tube length	13.5 inches max
Tube width	1.8 inches max
Tube height, excluding connectors	1.6 inches max
Tube weight	2.8 pounds max
dc connectors	Flying leads
RF connectors	OSM (Female)
Cooling	Conduction from bottom surface
Focusing	PPM
Environmental Characteristics	
Heat sink temperature	-20°C to +85°C
Vibration	
a. Sinusoidal (2 min/octave)	0.5 inch, double amplitude, 5 to 18 Hz, ±20 g peak, 18 to 2000 Hz
b. Random (5 min/axis)	0.1 g^2/Hz, 20 to 2000 Hz
Acceleration (1 min/axis)	100 g
Shock	75 g, 11 msec

1 Overall efficiency = RF output power, divided by total dc input.
2 These voltages are referenced to cathode. Helix at ground potential.

5.0 BEAM OPTICS AND ELECTRON GUN DESIGN

The method of generating the hollow beam utilized in the interaction space of the amplifier is described in this section. The desired distribution of axial and circumferential velocity within the beam in order to achieve optimum electronic performance and a low current emission density loading on the cathode of the gun is examined. The beam is derived from a magnetron injection gun. The analytical relations used to explore the design requirements are based on those developed by G. S. Kino (Ref. 2, 6).

5.1 Velocity Components within the Hollow Beam

The circumferential velocity of the outer surface of the hollow beam must be equal to the phase velocity of the RF wave on the delay line. The ratio of this velocity to the axial, z-directed, drift velocity through the interaction space determines the ratio of effective circulating current to the axial current injected from the cathode. An inspection of the magnitudes of these velocities shows that, in general, the kinetic energy represented by the circumferential velocity component is far greater than the kinetic energy represented by the axial velocity component. This is a reversal of the situation usually found in hollow beams designed for O-type amplifiers where the axial kinetic energy is the prime energy input into the system. In the case of the axial injection crossed-field amplifier, the axial drift velocity serves only to transport the stream from the gun to the collector region.

The parameters that have been evolved for the UHF and S-band amplifier designs have been based upon the condition that the cathode current from the electron gun be equal to the circulating current in the interaction space. In order for this condition to exist, the electron stream must make one full circumferential excursion during the time of its axial transit through the interaction space. Whether or not this condition is met depends on the ratio of circumferential

to axial drift velocities. More generally, the ratio of circulating current to cathode current is equal to the number of circumferential excursions that an electron makes in its axial traverse through the interaction space. A schematic diagram of the pertinent geometry and a derivation of the foregoing relationship are given in Figure 38. Figure 38b is an unwrapped view of the cylindrical surface on which the current flows upon injection. It is a planar sketch, with left-to-right corresponding to the circumferential direction, and top-to-bottom being the axial direction from cathode end to collector end.

Figure 38a indicates that continuity requirements set the input current from the electron gun equal to the output currents to the delay line and to the collector. This, however, does not define the value of circulating current. The reasoning presented under sketch b of Figure 38 establishes the value that the circulating current bears to cathode current under conditions of low level drive. This is the situation in which all of the cathode current goes to the collector with none arriving at the delay line. Since the circuit height, h, and diameter, D, are usually fixed by other design considerations, the ratio of circulating current to cathode current is determined by adjusting the ratio of circumferential velocity to axial velocity. These velocity values are determined by the design of the electron gun and the transition region between the gun and interaction space.

5.2 Initial Design of Magnetron Injection Gun based on Kino Analysis

A first round of design calculations for the magnetron injection gun for the UHF and S-band amplifiers was carried out. The objective was to restrict the emission density at the cathode to 200 ma/cm^2. This would allow a cathode operating temperature in the range of 700°C to 800°C in order to assure long life. With this constraint on the emission density, the design calculations checked

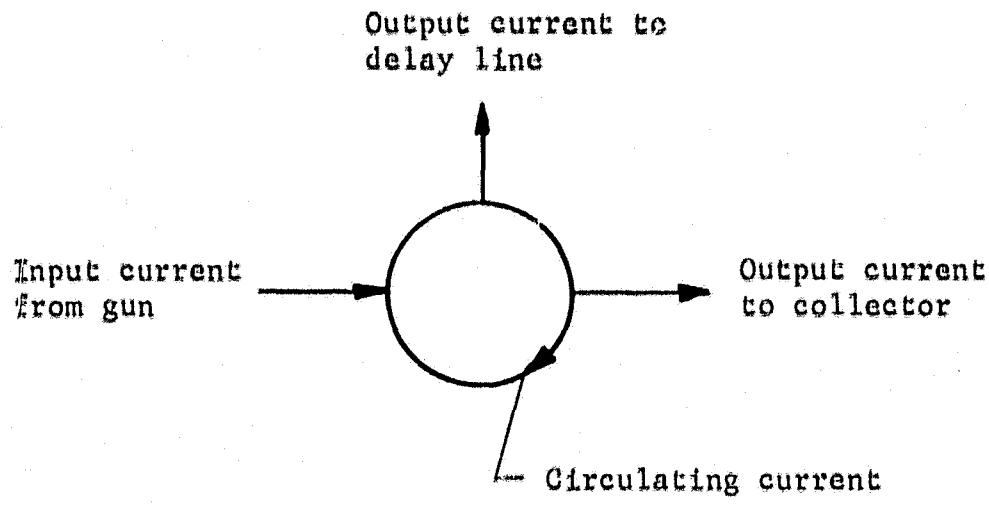

a. A symbolic representation of input, output and circulating currents

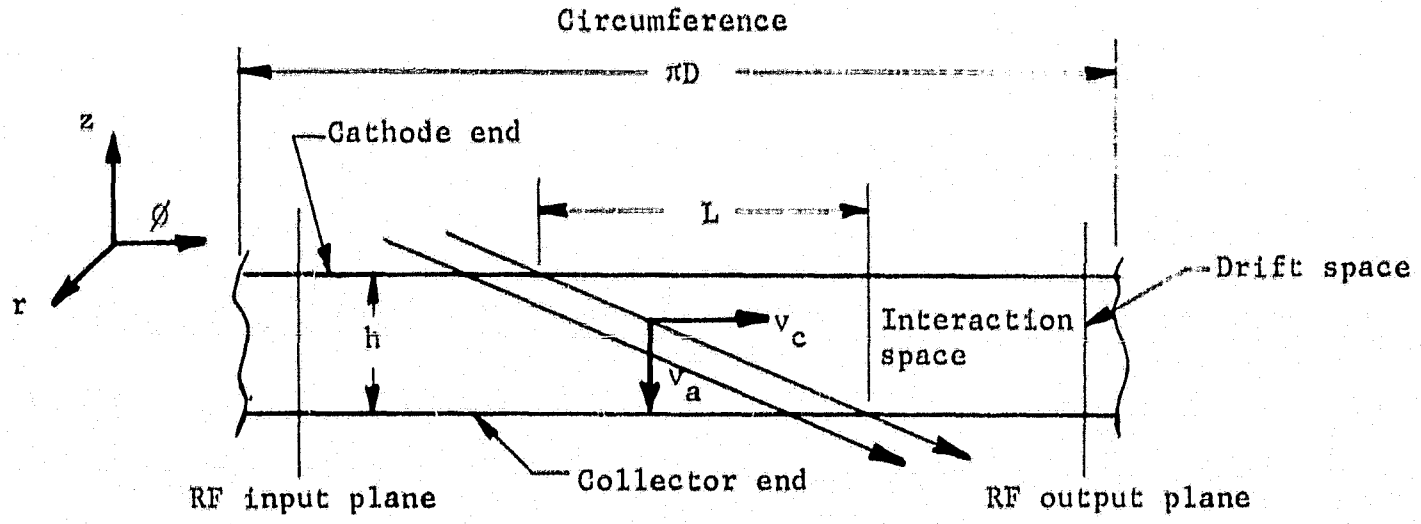

b. Unwrapped view looking down from anode toward unwrapped interaction space

Each electron has circumferential and axial drift velocities, v_c and v_a respectively. Let ρ_o be the space charge density in the beam under low level conditions when the beam is uniform throughout the interaction space and let t be the beam thickness in the radial direction (out of the paper). The circumferential current is then $\rho_o thv_c$ and the axial current is $\rho_o t\pi Dv_a$ where D is the beam diameter on injection. The ratio of these currents $I_c/I_a = (h/\pi D)(v_c/v_a)$. However h/v_a is the transit time t for an electron through the interaction space and $v_c t = L$ is the circumferential distance an electron travels while in the interaction space. Thus $I_c/I_a = L/\pi D$ or the ratio of circumferential to axial current is equal to the fraction of the full circumference that a trajectory covers in its traverse across the interaction space.

FIGURE 38 INPUT, OUTPUT, AND CIRCULATING CURRENTS

out circumferential and axial velocities of the beam as it emerged from the gun region. The intent was to adjust the axial velocity to the desired value in the interaction space by shaping the field in the region between the gun and the interaction space. The average circumferential velocity in the interaction space is automatically set to the synchronous value due to the balance of forces created by the dc electric and magnetic fields. A smooth transition is necessary to avoid excessive cycloiding or scalloping of the beam. Some of the pertinent relations from the Kino analysis are quoted here and reference is made to the sketch in Figure 39. The cathode is a cylindrical trapezoid having a small taper angle, θ, with a magnetic field applied parallel to the main axis of the cathode. This is also the axial magnetic field of the interaction space itself. An appropriately shaped accelerator is placed above the cathode area and a focus electrode is attached to the back end of the cathode. The beam exits axially to the right on the sketch and picks up circumferential velocity as it exits due to its acceleration in the crossed-dc electric and magnetic fields. The Kino analysis is actually carried out in planar coordinates, as shown in the sketch. The y direction corresponds to the radial direction in the gun and the x direction corresponds to the circumferential, or θ, direction in cylindrical coordinates. It is this velocity in the θ direction that must eventually be equal to the synchronous velocity of the RF wave on the delay line. Some pertinent relationships from the Kino analysis are presented here for reference. These relations are based on the assumption that the charge density, potential, velocity, etc., are functions only of y and that the dc electric field in the gun region exists in the y direction. The normalized coordinates are defined as follows

$$X = \frac{x}{a} \qquad Y = \frac{y}{a} \qquad Z = \frac{z}{a}$$

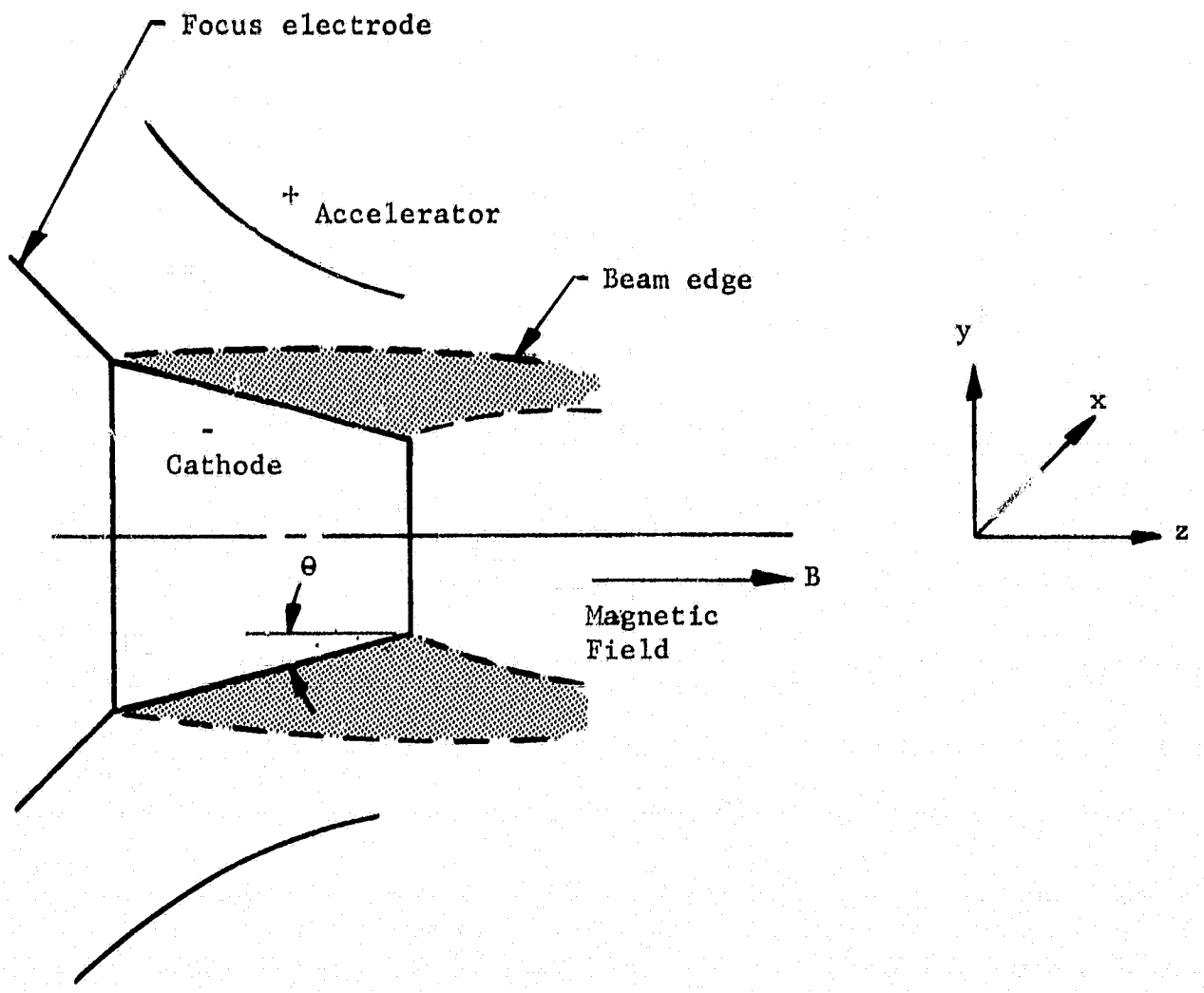

FIGURE 39 MAGNETRON INJECTION GUN SKETCH USING RECTANGULAR COORDINATES FOR KINO-TAYLOR ANALYSIS

$$a = \frac{\frac{e}{m} J_o}{\epsilon_o \omega_c^3}$$

where e/m = ratio of electron charge to mass

J_o = current density at cathode

ϵ_o = dielectric constant of free space

$\omega_c = (e/m)B$ = cyclotron frequency in radians

An electron trajectory in terms of normalized transit time, $T = \omega_c t$, is:

$$X - X_o = \frac{T^2}{2} \cos \theta$$

$$Y = T + \frac{T^3}{6} \sin^2 \theta$$

$$Z - Z_o = \frac{T^3}{6} \sin \theta \cos \theta$$

where X_o and Z_o are the coordinates of the point on the cathode where the electron starts.

The equation of the beam edge is given by

$$Y = \left(\frac{6}{\sin \theta \cos \theta}\right)^{\frac{1}{3}} Z^{\frac{1}{3}} + Z \tan \theta$$

By differentiating the expressions for x and y coordinates and substituting for T in terms of Z, the axial velocity of the top surface of the beam is obtained.

$$\frac{dz}{dt} = \frac{a}{2} \omega_c (6Z)^{\frac{2}{3}} (\sin \theta \cos \theta)^{\frac{1}{3}}$$

The circumferential velocity is:

$$\frac{dx}{dt} = a\omega_c \left(\frac{6Z}{\sin\theta \cos\theta}\right)^{\frac{1}{3}} \cos\theta$$

This led to the design parameters given in Tables XIV and XV for the first set of gun designs for the UHF and S-band amplifiers.

Based on this initial set of design values, it had been planned to use the cathode with the 4 degree tapered angle. It was the intent in the case of the UHF amplifier to reduce the axial velocity with which the beam emerged from the gun from 41 ev to 6.4 ev, and in the case of the S-band amplifier to reduce the axial velocity from 62.7 ev to 3.6 ev. The ratio of circumferential and axial velocity then would be such that one circumferential excursion occurred during an axial transit. Thus the circulating current and cathode current would be equal.

It will be noted from the small value of the y coordinates that, on exiting from the cathode itself, not much energy has been transferred to the electron stream and it has just left the cathode surface.

5.3 Modification of Design Because of Axial Velocity Slip

A closer detailed examination of the electron dynamics of the beam formation in the gun region indicated that the axial velocity of the emerging electron stream could not be adjusted as originally indicated. The reason is that when the beam emerges from the emitting region of the electron gun, a differential in axial velocity exists between the outer edge of the beam and the inner edge of the beam. As the beam proceeds to grow in axial and circumferential velocity in the region which is still under the influence of the gun electrodes, this differential continues to

TABLE XIV

INITIAL DESIGN PARAMETERS FOR THE UHF ELECTRON GUN

I_k = 1.3 amps

B = 1410 gauss

J = 0.2 amps/cm^2

Cathode area = 1.01 in^2

Cathode diameter = 3.88 in

Cathode length = 0.083 in

$$a = \frac{\frac{e}{m} J_o}{\epsilon_o \omega_c^3} = 2.6 \times 10^{-6}$$

θ degrees	Trajectory - y inches	Exit Velocity (Energy) v_θ (volts)	v_z (volts)
2	0.008	31.7	26.0
3	0.009	24.2	34.5
4	0.010	20.1	41.3
5	0.011	17.3	47.9

In the interaction space:

Circumferential velocity (energy), V_o = 945 volts

Axial velocity (energy) = 6.4 volts

for one circumferential excursion during axial transit.

TABLE XV

INITIAL DESIGN PARAMETERS FOR THE S-BAND ELECTRON GUN

I_k = 1 amp
B = 3330 gauss
J = 0.2 amps/cm^2
Cathode area = 0.775 in^2
Cathode diameter = 2.15 in
Cathode length = 0.115 in

$$a = \frac{\frac{e}{m} J_o}{\epsilon_o \omega_c^3} = 2.0 \times 10^{-7}$$

θ degrees	Trajectory - y inches	Exit Velocity (Energy) v_θ (volts)	v_z (volts)
2	0.0013	7.1	39.4
3	0.0017	5.4	52.2
4	0.0022	4.5	62.7
5	0.0027	3.9	72.5

In the interaction space

Circumferential velocity (energy), V_o = 800 volts
Axial velocity (energy) = 3.6 volts

for one circumferential excursion during axial transit.

increase slowly. The physical reason for this is that the outer and inner portions of the beam are made up of electrons which have originated at different points on the cathode surface. Thus for any given cross-section of the beam in an x-y plane, the inner surface electrons have traveled a shorter trajectory from the cathode surface and therefore have developed a smaller value of velocity.

A detailed derivation of a complete set of expressions for the velocity slip between the top and bottom of the beam is presented in Appendix II. It is shown in the expressions presented that the differential in axial velocity between the top and bottom of the beam, expressed in electron volts, is proportional to the two-thirds power of the ratio of sin θ to the current density, J_o. This indicates that, for a given current density, it would be desirable to minimize the taper angle of the cathode. A reevaluation of the design in terms of a 2 degree taper angle has been carried out, and some values of axial velocity are plotted from the relations that are given in Appendix II.

A graph of the axial velocities of the beam outer edge and beam inner edge is shown in Figure 40. These velocities are plotted as a function of the axial distance measured from the corner of the cathode furthest from the interaction space. The values plotted are for the case of a cathode taper angle of 2 degrees. It is seen that at a distance of 0.083" from the origin (this is the length of the cathode emitting surface), the upper edge of the beam has an axial drift velocity of 26 ev; the lower edge, of course, has a drift velocity of 0 ev, since the lower edge of the beam is just being formed. As the gun electrodes are continued further, this differential between outer edge and inner edge axial velocity increases slowly. It, thus, is not possible to decrease the axial velocity of the outer edge of the beam to 6.4 ev without decreasing the axial velocity of the inner edge of 0 ev and then reversing it. In other words, part of the beam would be cut off.

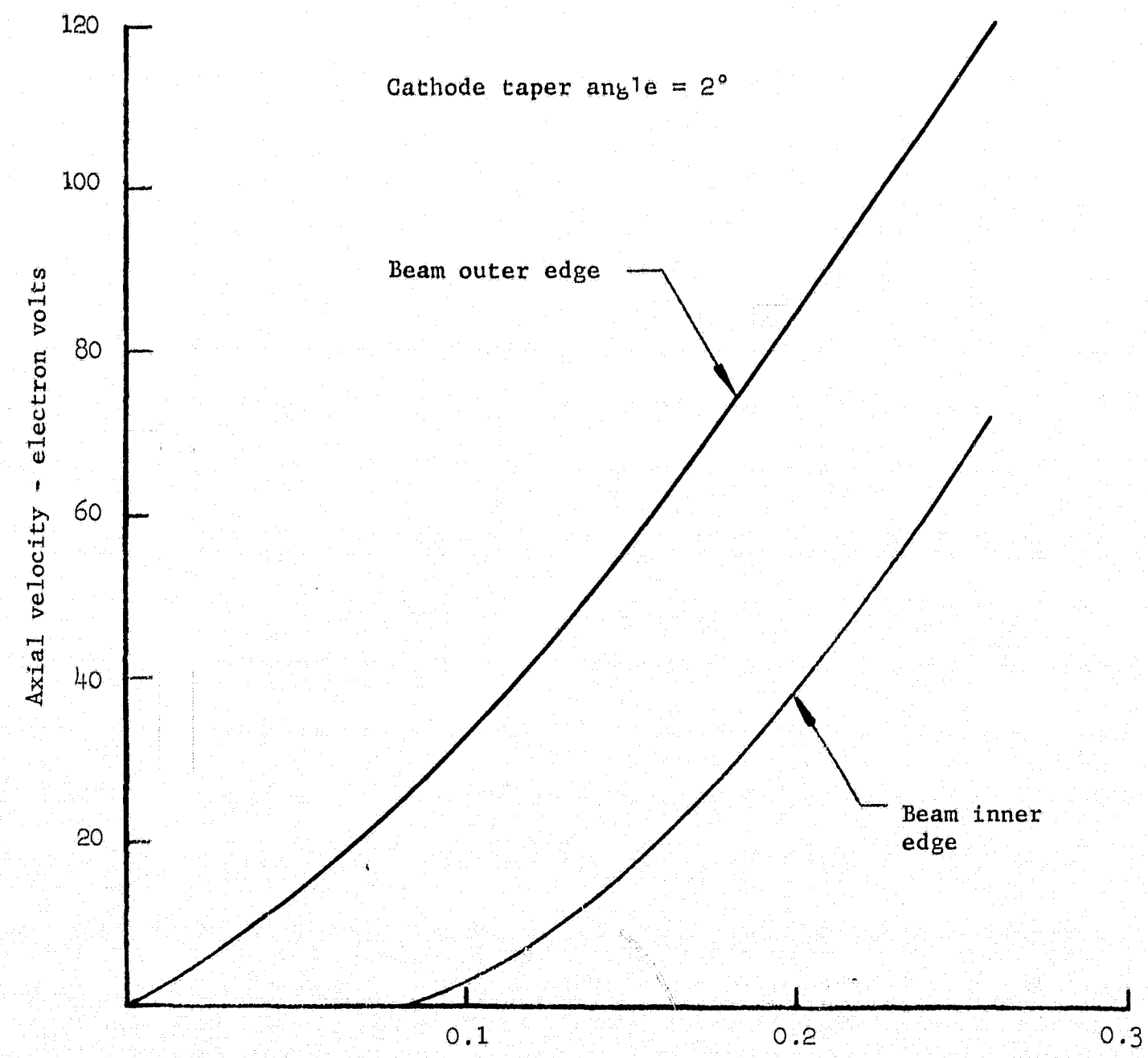

FIGURE 40 AXIAL VELOCITIES OF INNER AND OUTER BEAM EDGES IN REGION OF ELECTRON GUN FOR UHF DESIGN

It appears that operation of the amplifier must be carried out with the axial velocity of the outer edge of the beam at 40 ev. This means that for the original circuit geometry, the electron stream would make less than one-half of a revolution before exiting from the interaction space. This would not be desirable since degradation in efficiency might occur. Many of the electrons would not have undergone a high degree of interaction with the RF field before exiting from the interaction space. These electrons would exit at lower values of potential, thus weighting the distribution function of current versus exit potential more heavily in the region of low potentials. As has been indicated by the analysis on efficiency and collector design, this would result in a net lowering of efficiency. In addition if the cathode current remained fixed, the effective circulating current would be reduced. It would then be necessary to increase the circumferential length of the circuit to obtain the objective 20 db of gain. This increased circuit length would add some insertion loss and would also tend to decrease efficiency. If on the other hand the circulating current were kept at the original design value of 1.3 amps, the cathode current would need to be increased, resulting in heavier cathode loading. It was, therefore, decided to resolve the situation by making the following design modification. The axial circuit height was increased from 1" to 2". This now means that an axial drift velocity of 25.5 volts will insure one complete circumferential revolution during one axial transit through the interaction space. An electron gun based on the cathode taper angle of 2 degrees will be used. The gun electrode configuration is extended a distance of approximately 0.060" axially past the end of the emitting area, which is 0.083" long. It is seen from Figure 40 that at this point, the outer edge electron has an axial velocity of 16 ev. The beam will then enter a region where no further axial acceleration occurs. The dynamics of the situation are now such that the outer

edge electron will make 0.7 revolutions in its passage through the interaction space and the inner edge electron will make 1.3 revolutions in its passage through the interaction space, thus yielding an average transit time of one complete circumferential revolution.

Thus, by increasing the axial circuit height and working with a higher average axial electron velocity, the circulating current is maintained about equal to the cathode current. Increasing the height of the circuit from 1" to 2" results in a calculated increase of insertion loss from 0.203 db to 0.287 db. This is not considered significant. In addition, the magnetic air gap of the amplifier is increased from 2.5" to 3.5". This increase of 40% in the magnetic air gap increases the overall height of the shielded magnetic package to 8". This results in the addition of about 6 lb of magnet weight and 1 lb of magnetic shielding material. The increase in amplifier package volume and weight is essentially the only price paid in order to maintain those operating features of the amplifier which have the highest priority in carrying out design trade offs.

A similar situation exists in the case of the S-band amplifier design and a similar solution is achieved. In the original design, the axial drift velocity of the electron stream would have to be about 4 ev in order to have the circulating current equal to the cathode current. Figure 41 contains a plot of outer edge and inner edge beam velocities in the gun region of an S-band design with a cathode taper angle of 2 degrees. In this case, the axial length of the emitting cathode area is 0.115", and it is seen that the smallest differential between outer edge and inner beam edge axial velocities is 40 ev. To resolve the situation, the axial height of the capacitive bar in the S-band circuit was increased from 0.45" to 1". The axial velocity needed to assure that cathode current equals circulating current is now increased to 17.5 ev. If the gun electrodes are continued to a region which goes 0.035" past

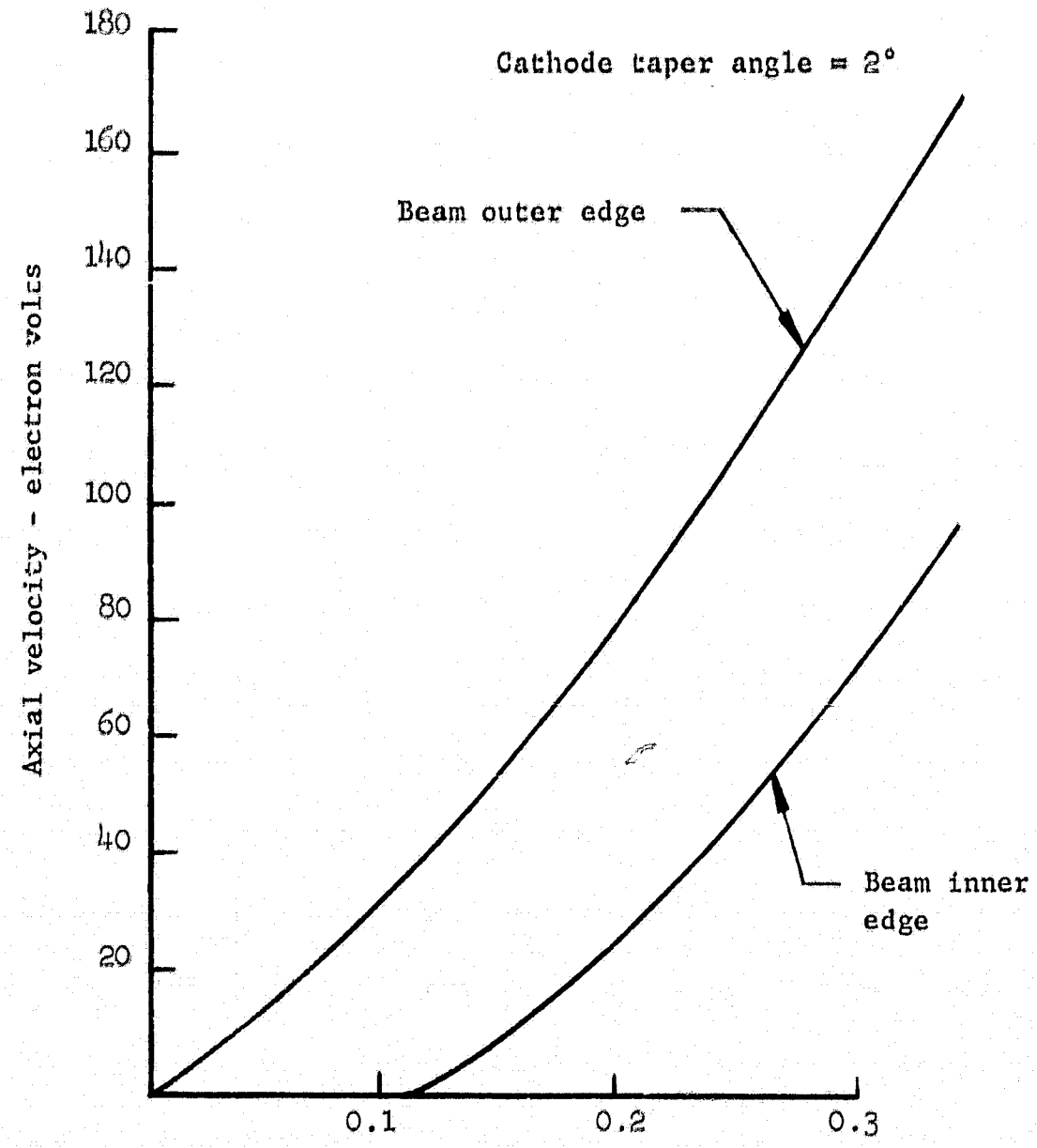

FIGURE 41 AXIAL VELOCITIES OF INNER AND OUTER BEAM EDGES IN REGION OF ELECTRON GUN FOR S-BAND DESIGN

the emitting area, it is seen that the outer edge electron will have an axial velocity of 56 ev and the inner edge electron will have an axial velocity of 8 ev. This corresponds to 0.5 revolutions for the outer edge electron and 1.5 revolutions for the inner edge electron. Thus, on the average, one complete revolution is being made for a single axial transit, and the condition of having circulating current equal to cathode current is approximately maintained.

The increase in the height of the capacitive bar from 0.45" to 1" in the case of the S-band design increases the circuit insertion loss from a calculated value of 0.69 db to 1.2 db. It is felt that this, too, is not a significant increase. As a result of the increased circuit height, the magnetic air gap for the S-band design is increased from 1.75" to 2.3", about 30%. The Alnico-9 magnet would then have to be lengthened, which would increase the total shielded package length to 9 inches. This would result in the addition of 3 lb of magnet and 0.5 lb of magnetic shield.

In both the case of the UHF circuit and the S-band circuit, the spacing between the capacitive bar and the ground plane will be increased in proportion to the new length of the bar, so that the bar capacitance is kept constant. This means that there will be no change in coil dimensions. In addition, the thermal impedance between the capacitive bar and the ground plane is also kept constant.

Thus, by making an adaptation of the interaction space and circuit design, it becomes feasible to maintain the desired objective of a low emission density at the cathode - i.e., about 200 ma/cm^2. The active length of circuit and the efficiency of energy conversion is maintained.

The possibility exists that a magnetron injection gun with modified coordinates other than those based on the Kino type of analysis may have intrinsically lower velocity slips within the generated beam. This would be a subject for a separate investigation,

and it was decided that a consistent and usable design should be presented in this study program based on what is calculable. It has been experimentally observed in the UHF work carried out at S-F-D laboratories that excessive slowing of the beam can indeed cut off part of the beam and this combined with the extended analysis, led to the revised design.

Some details of the support structure for the ringed cathode of the magnetron injection gun and the associated heater structure are indicated in Section 7.0. A straightforward analysis of the heater power requirements for operating the cathodes at 720°C results in a figure of 40 watts for the UHF design and 32 watts for the S-band design. This temperature presumes the use of an oxide coated cathode.

If developments in cathode technology should indicate that the dispenser type of cathode is more desirable for this type of long life, high powered application, the corresponding figures for a cathode temperature of 820°C would then be 53 watts for the UHF case and 41 watts for the S-band amplifier case. These powers resulted from estimating the conduction and radiation losses from the heater system. It may well be that a reduction in these powers is possible by using a directly-heated cathode, which consists of a pre-formed tungsten ring having an impregnated tungsten surface. This type of technology is under development at present, and its usage should be carefully considered in a future extrapolation of the results of this study program.

6.0 THERMAL DESIGN

This section deals with the problems of removing the waste heat from the internal tube structure and of disposing this heat by direct radiation into space. It was decided to keep the maximum operating temperature at the hottest point within the tube in the range of 200°C to 300°C. This would assure that the evaporation rate of metal from the circuit and collector elements would never by great enough to compromise the life expectancy of the tube. The design arrived at uses heat conduction from the critical collector and circuit elements through supporting beryllium oxide insulators to a circular copper block within the tube that acts as a heat sink. From this point of heat sink, the heat is conducted to a radiating structure. To connect the copper heat sink within the tube to the radiating structure, it was decided to utilize a system of heat pipes and thus, eliminate the necessity for using any mechanical pumping elements to circulate heat transfer coolant. This choice was made in order to remove the mechanical pump as one additional failure mechanism which might compromise the life expectancy of the tube while in orbit. This section then considers the three basic design areas of temperature distribution within the tube, the considerations that enter into the selection of the heat pipe design, and the considerations that enter into the radiator design.

The material presented in this section has been developed in consultation with scientific personnel of the Space Technology Center of General Electric Company, Valley Forge, Pennsylvania.

6.1 Heat Pipe and Radiator Design Considerations

As outlined, the approach taken to the thermal design of the CFA is to maintain the temperature of the hottest part below a temperature which would permit excessive evaporation of copper. The temperature drop from each heat producing element to the heat transfer

interface is determined. This interface, then, is limited to a temperature below the maximum limit minus the highest temperature drop from element to heat pipe. The maximum temperature limit in the trade-off considerations that follow, will be taken over a range from 250°C to 400°C, to show the effect on radiator size and weight.

The following subsections first develop the relevant parameters and then apply them to the two crossed-field amplifiers considered in this study.

6.1.1 Operating Characteristics of Heat Pipes

A heat pipe is a closed volume containing a two-phase fluid with the liquid phase in contact with the wall. If one portion of the surface enclosing the volume is heated, vapor is formed which increases the local vapor pressure. The resulting movement of the vapor, to equalize the pressure, unbalances the equilibrium at other liquid-vapor interfaces, causing vapor to condense. The result is the transfer of the latent heat of vaporization from the surface where the liquid was vaporized to the surface where the vapor condensed. Since heat transfer coefficients are very high in vaporization and condensation, large quantities of heat can be moved over long distances with little temperature change. Return of condensate to the evaporator surface provides a continuous cycle.

Gravity to return condensate has long been used successfully in vacuum tube cooling applications and in residential and commercial steam heating systems. In the absence of gravity, however, a positive means of pumping the condensate must be provided. A mechanical pump may be desirable in some applications, but the addition of an active element in an otherwise passive system would reduce the inherent reliability. A capillary return, however, has a reliability consistent with the remainder of the system and has been shown to be capable of flow rates adequate for most applications.

The heat pipe concept has been demonstrated both on the ground and in orbit. Two heat pipe experiments have been flown successfully to date. The first was flown "piggyback" on an ATS Agena Vehicle (Ref. 7) and the second on GEOS/B (Ref. 8). Both adequately demonstrated the operation of the heat pipe in a 0 g environment.

Several parameters can be used to describe the performance of a heat pipe. The liquid should have high density and latent heat of vaporization to minimize the required flow rate. The liquid viscosity should be low to minimize the resistance to flow, and the surface tension and wetting angle should provide an adequate capillary rise. The same type of general requirements can be described for the properties of the vapor and for the geometry; but, since the choice must be made from real fluids and manufacturable geometries, properties must be considered in light of all other relevant material properties and geometric constraints. Cotter (Ref. 9) presents an integrated analysis of heat pipe performance. Equations are developed to describe the vapor flow for two flow regimes, the case where the radial Reynolds number is much less than one and the case where it is much greater than one. The pressure drops in the vapor, in the liquid and due to gravity are summed and equated to the maximum capillary pressure rise to determine the heat flow limits. After optimizing the geometry and equating the gravity term to zero to simulate orbital operation, the equations for maximum heat flow are determined. For a radial Reynolds number much greater than one;

$$Q = \frac{4\pi r_w^2 \lambda}{3}\left[\frac{2\rho_v \sigma_\ell e\gamma^2 \cos^2\theta}{(\pi^2 - 4)\mu_v \mu_\ell}\right]^{\frac{1}{3}} \qquad (35)$$

and for a radial Reynolds number much less than one,

$$Q = \frac{\pi r_w^3 \gamma (\cos\theta) \lambda}{3L} \left[\frac{e\rho_v \rho_L}{3b\eta_v \eta_\ell}\right]^{\frac{1}{2}} \qquad (36)$$

where r_w = outer radius of the wick
λ = latent heat of vaporization
γ = surface tension
θ = contact angle between the fluid and the wick
L = heat pipe length
ρ_v = density of the vapor
ρ_ℓ = density of the liquid
η_v = viscosity of the vapor
η_ℓ = viscosity of the liquid
e = void fraction of the wick
b = capillary geometry constant

The radial Reynolds number, R_r, is defined as:

$$R_r = \frac{1}{2\pi\eta_v} \frac{d\dot{m}_v}{dz}$$

where $\frac{d\dot{m}_v}{dz}$ = the rate of increase of mass flow with axial distance.

Equations (35) and (36) have two principal drawbacks. First, they do not adequately describe the performance of low thermal conductivity fluids, since they do not allow for nucleate boiling. Second, a model over the range of radial Reynolds numbers in the neighborhood of one, which is frequently encountered in practice, is not developed. These equations, however, are very useful in providing a basis for comparison of fluids. Figure 42 shows the results of

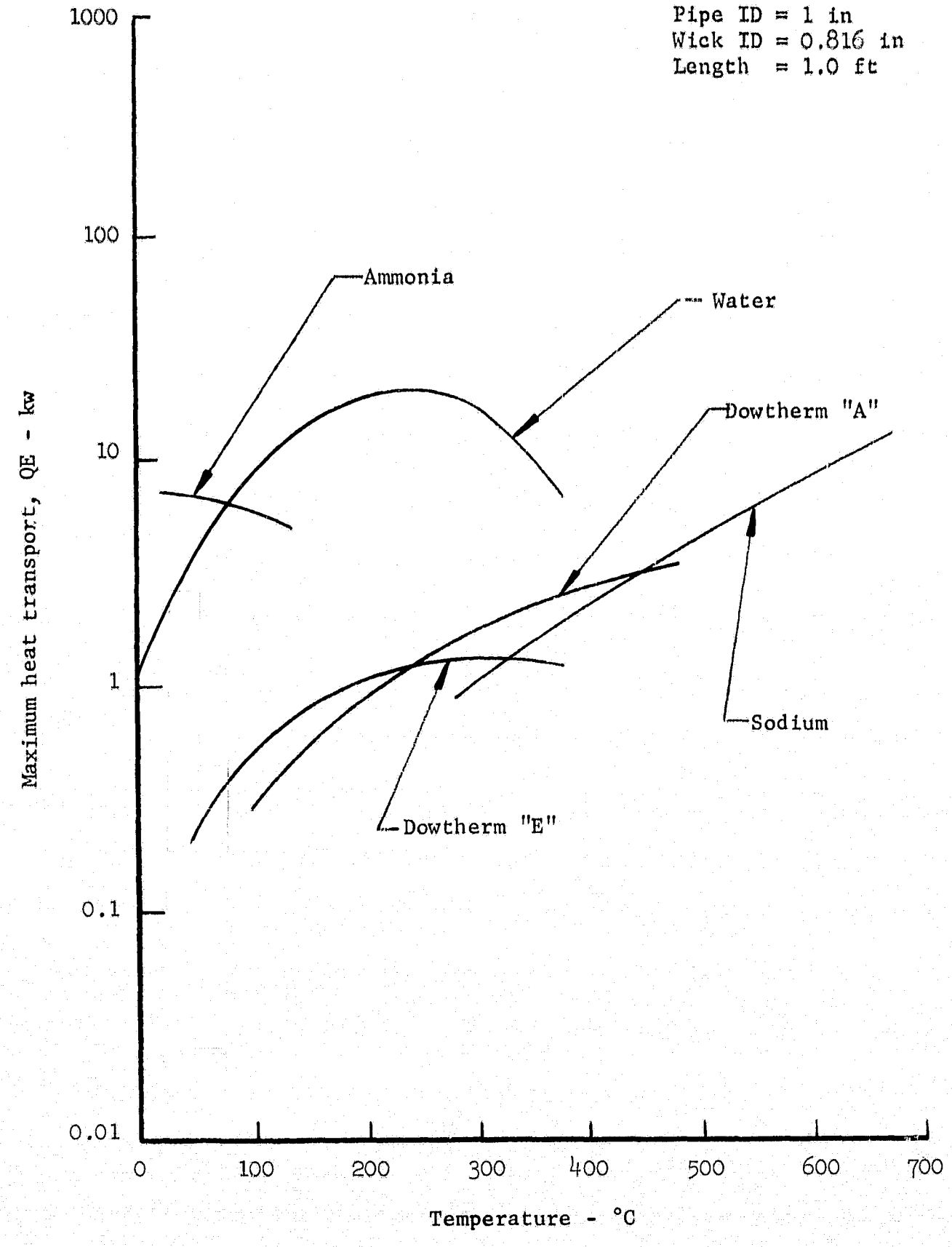

FIGURE 42 MAXIMUM HEAT PIPE CAPACITY VERSUS TEMPERATURE

equation (33) over a range of temperatures for a 1" diameter, 12" long heat pipe. Equation (35), rather than equation (36), was used since heat pipes considered in this study are not likely to have very small values of radial Reynolds number. In addition to relative performance, the vapor pressure of the fluid is an important consideration, since the heat pipe wall must be thick enough to contain it. Figure 43 shows the vapor pressure of the fluids included in Figure 42 as a function of temperature. Figure 42 leads to the choice of water as the appropriate fluid for the system under study here, since a radiator temperature of about 200°C is desired to minimize internal tube temperature.

The use of equation (35) to predict performance of heat pipes where the fluid selected has a low thermal conductivity can lead to an inadequate design, particularly where the power density in the evaporator is high. Comparison with test data shows the calculated maximum heat transport can be as much as a factor of 6 higher than what can actually be obtained when the evaporator is operating near the maximum heat flux.

The evaporator is a critical area in many heat pipe applications due to high power and limited area. The heat fluxes resulting from such a combination can be high enough to reach the point at which the vapor flowing from the evaporator surface interferes with the evaporation at the surface. If the heat flux is high enough, the liquid cannot reach the surface fast enough to remove the heat and the temperature increases drastically. This is the burnout heat flux and is the limit of evaporator capacity. Kunz (Ref. 10) and past experience indicate that values of boiling burnout heat flux as high as 300 w/in^2 can be reliably attained with water. Other fluids considered in this study should approach this value. While considerably higher power densities are no doubt possible, it may be necessary to verify this by testing the specific configuration.

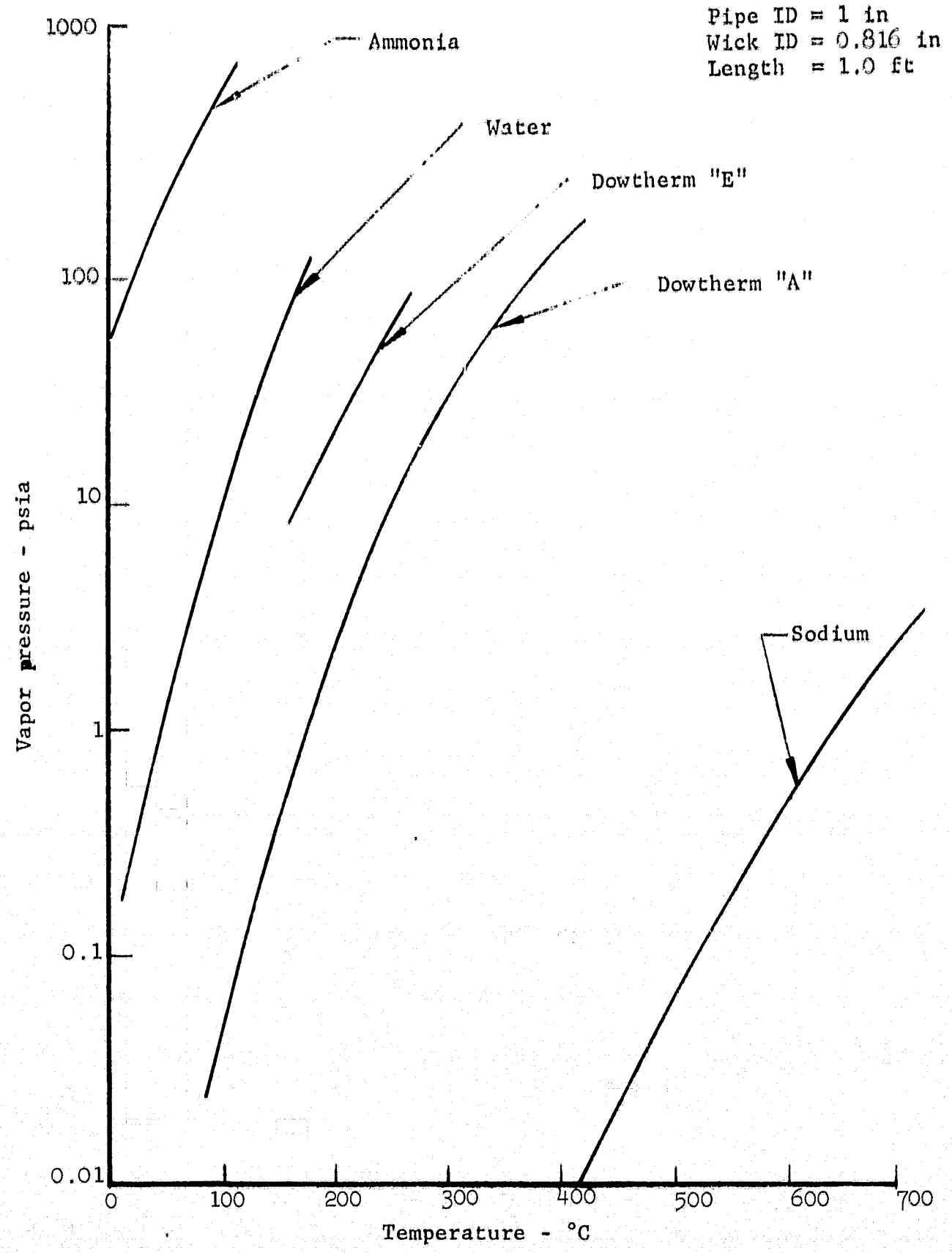

FIGURE 43 VAPOR PRESSURE VERSUS TEMPERATURE IN HEAT PIPE

6.1.2 Radiator Design

Radiators provide the sole practical means of rejecting heat in space over long periods of time. Thus, they are a necessary part of almost all spacecraft. The radiator directly influences the successful operation in space of a high power, crossed-field amplifier, since the radiator sets the maximum internal operating temperature.

The most simple radiator, for purposes of analysis, is one which has an isothermal surface. The net heat radiated from the surface is

$$q = \epsilon A \sigma (T^4 - T_s^4) \qquad (37)$$

where q = net heat radiated
ϵ = surface emittance
A = surface area
σ = Stefan-Boltzmann constant
T = surface temperature
T_s = equivalent sink temperature

Where weight is a consideration, an isothermal radiator is not optimum. The temperature of the fin, and thus the heat rejection per unit area, decreases as the distance from the heat source increases. Instead of integrating the heat rejection for each fin configuration, a parameter called fin effectiveness, η, is established (Ref. 11 and 12). This parameter allows the simple computation of the net heat radiated in a format similar to equation (37). Taking the radiator temperature, T_r, at the fin root, equation (37) becomes

$$q = \epsilon \eta A \sigma (T_r^4 - T_s^4) \qquad (38)$$

In equation (38), η is the ratio of the heat radiated by the fin to the heat which would be radiated by an isothermal surface of the same emissivity and area.

A circular fin is a disk with a heat source at its center. This is the situation that would exist if the CFA were in the center of the radiator with no further heat pipe extension. Figure 44 shows the heat which can be rejected by a circular fin as a function of temperature. In each case, the fin has been optimized for minimum weight, which is also shown on the figure. The theory used, from Ref. 11, does not account for gradients through the thickness of the fin; but for a high thermal conductivity material such as aluminum, fins of the thickness investigated (0.060") should perform in the manner predicted by one-dimensional heat transfer theory.

The straight fin, investigated by Ref. 12, would be used in conjunction with a heat pipe or active loop, heat transport device. The heat pipe or coolant line would provide the fin with a constant temperature over a given length of fin root. The fin root length can be computed such that the fin weight is minimized. Minimizing fin weight, however, results in a relatively large area, thus leaving the final trade off between area and weight to the requirements of a specific spacecraft. Figures 45 and 46 show the weight and area per kilowatt for a weight-optimized heat pipe radiator. Each system is designed for a 1/2" heat pipe, including attachment mechanisms, which weighs 0.4 lb/ft of length. A system of 1/2" heat pipes is used in the proposed design.

As shown in the preceding discussion, the choice of a fin is primarily a trade off between area and weight. For the purpose of this study, designs will be based on the limits, minimum weight in one case and minimum area (isothermal surface) in the other. The relationship between area and weight per unit power as a function of temperature for a minimum area fin is shown on Figures 47 and 48.

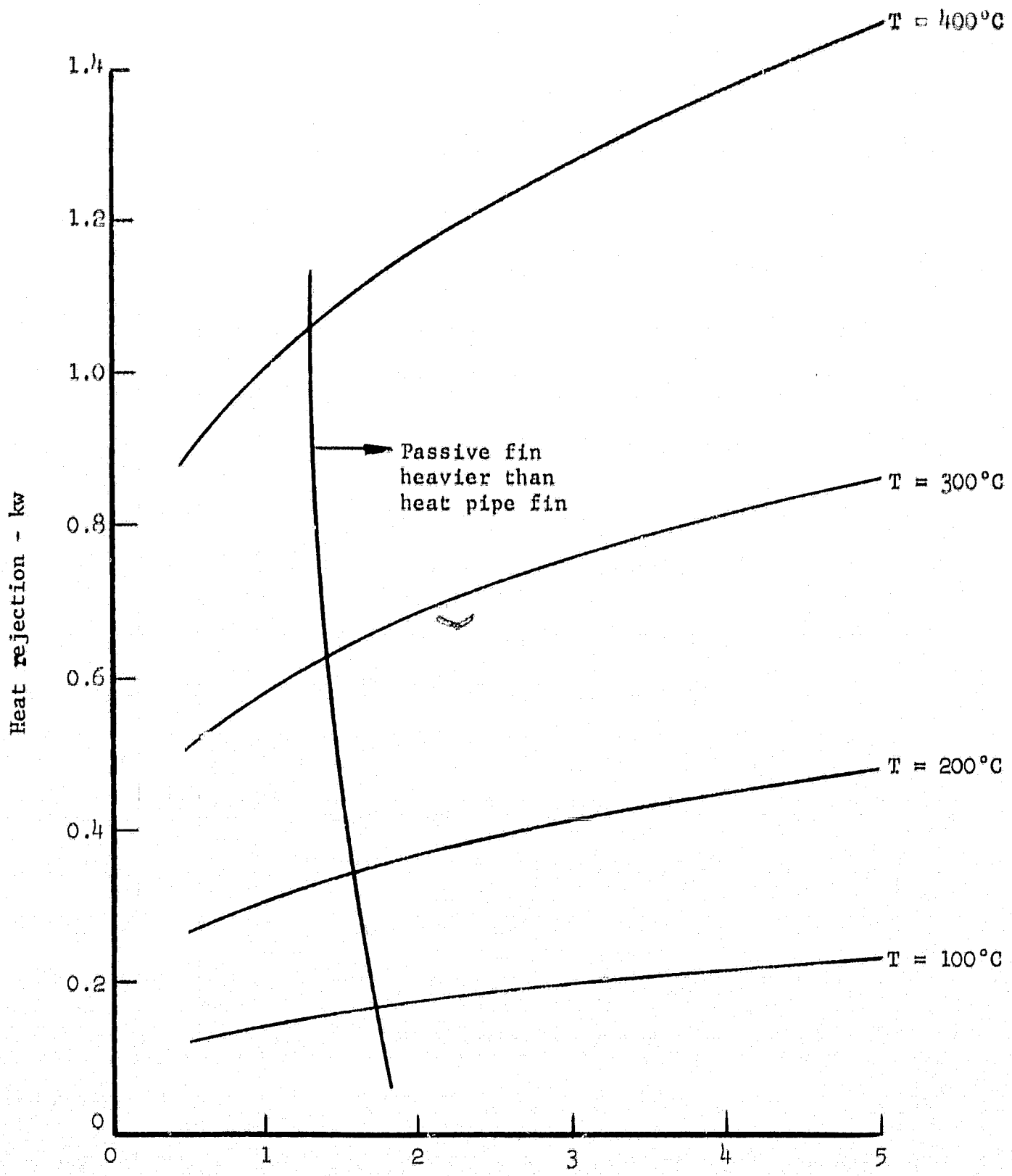

FIGURE 44 RADIATION CHARACTERISTICS OF A CIRCULAR FIN

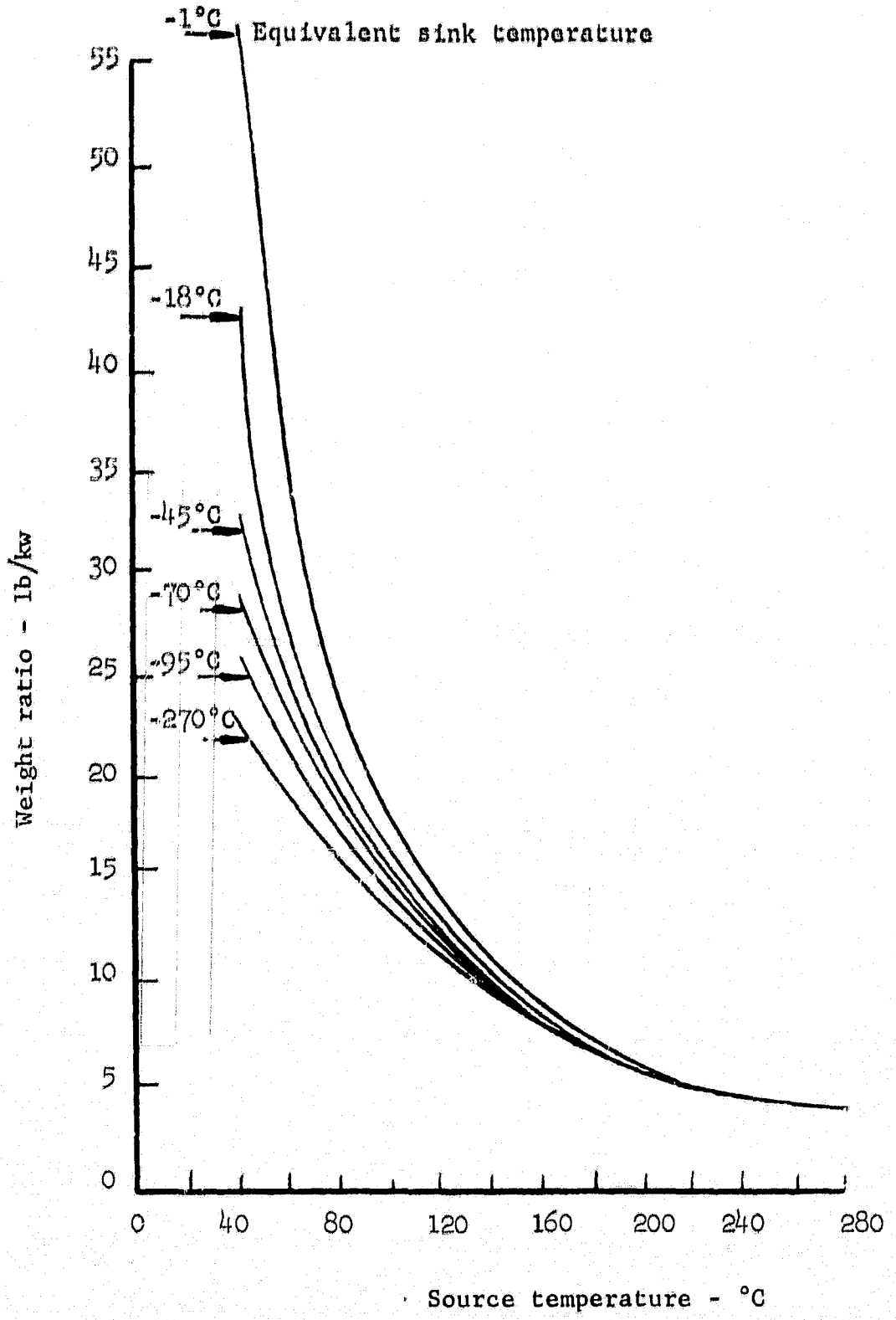

FIGURE 45 WEIGHT REQUIREMENTS FOR A MINIMUM WEIGHT RADIATOR

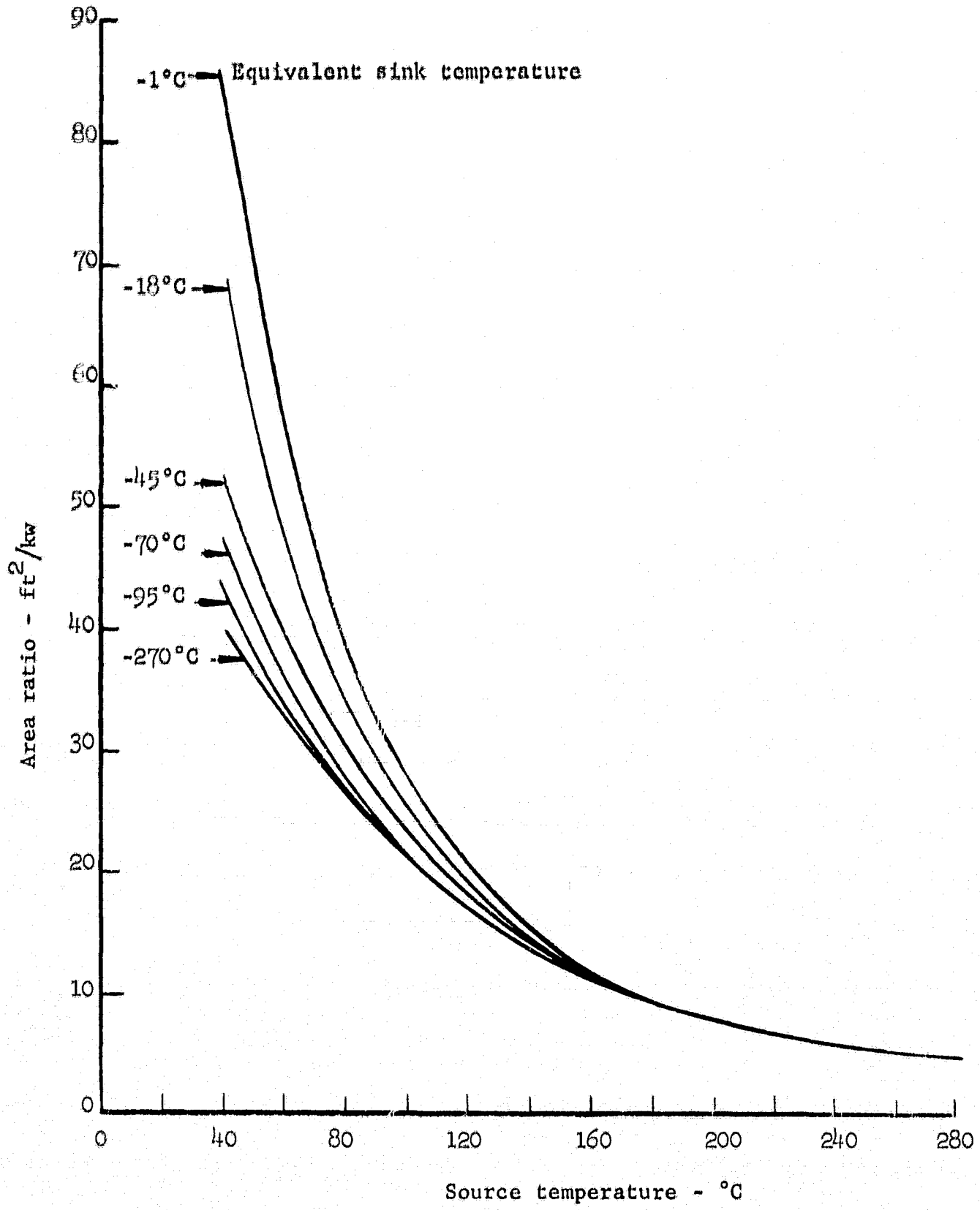

FIGURE 46 AREA REQUIREMENTS FOR A MINIMUM WEIGHT RADIATOR

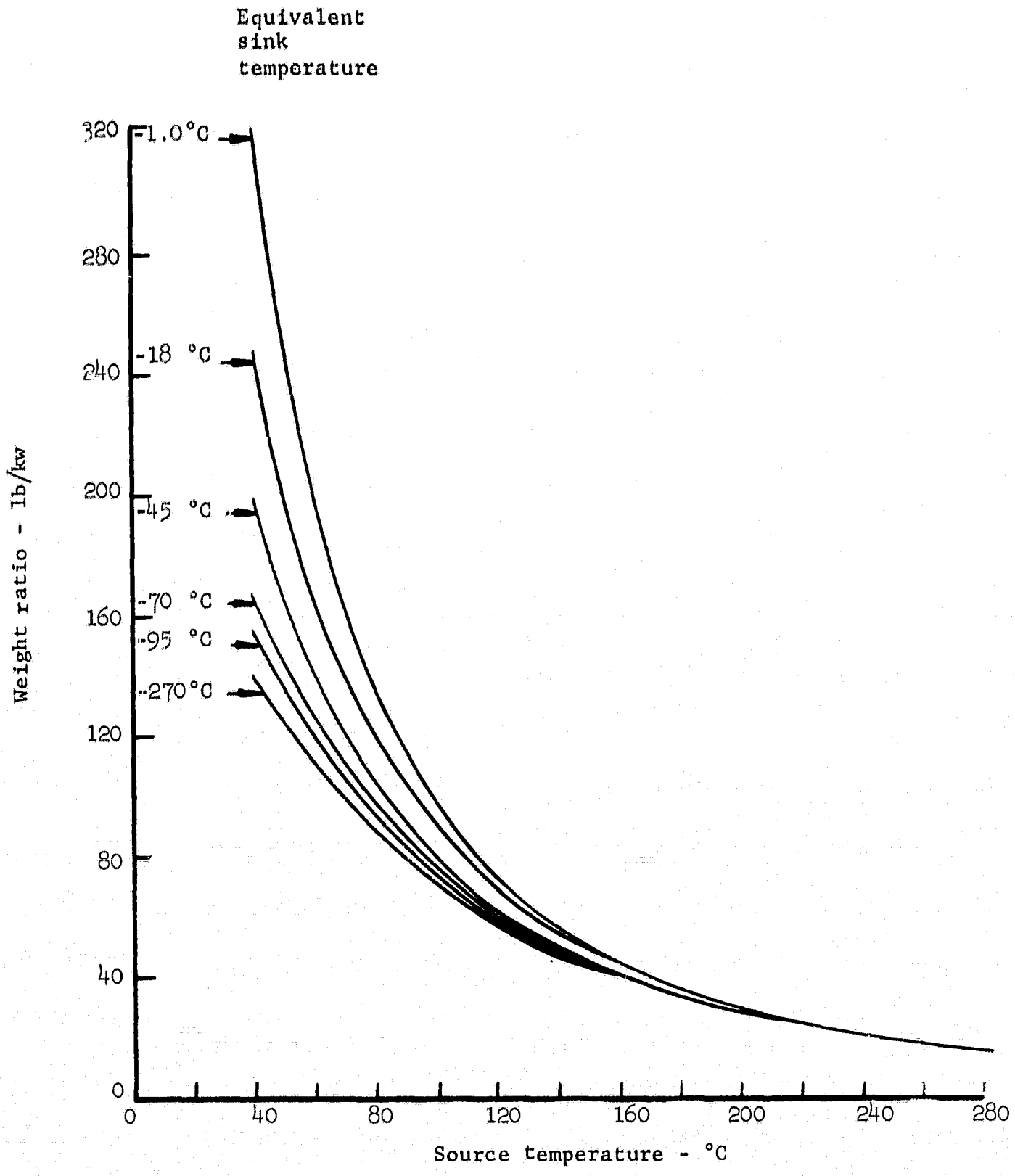

FIGURE 47 WEIGHT REQUIREMENTS FOR AN ISOTHERMAL RADIATOR

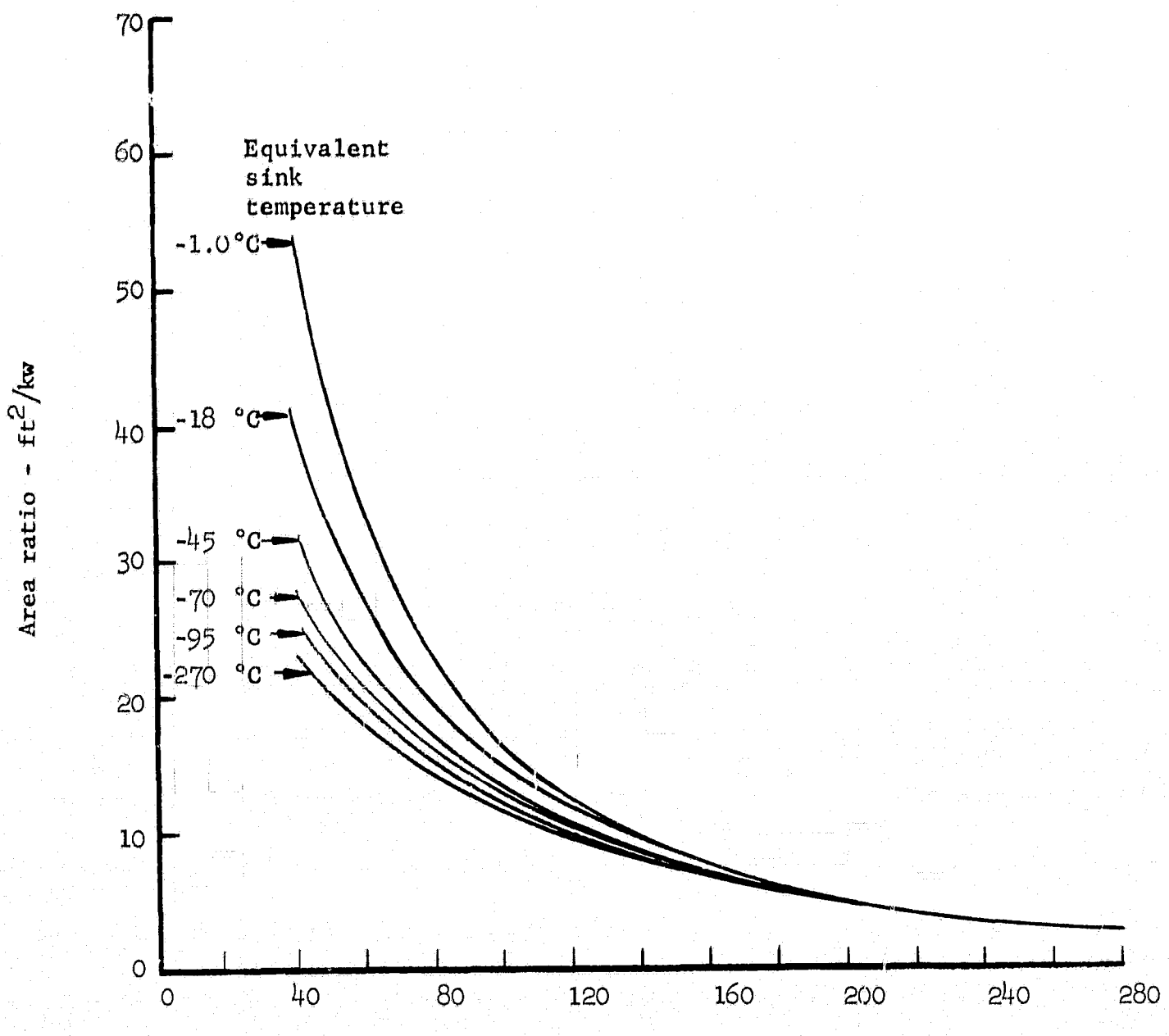

FIGURE 48 AREA REQUIREMENTS FOR AN ISOTHERMAL RADIATOR

The effect of sink temperature, T_s in equation (38), is also included.

The effect of incident solar energy on radiator temperature is taken care of by noting that the sink temperature, like the solar energy, is a term which provides a constant heat input over the radiator area. Thus, the sink temperature can be redefined as

$$T_s' = \sqrt[4]{T_s^4 + \frac{\alpha}{\epsilon\sigma} S \cos \psi} \qquad (39)$$

where T_s' = the new equivalent sink temperature
α = solar absorptivity
S = solar constant
ψ = angle between the sun's rays and the normal to the surface

The remaining symbols are as previously defined. Using this new sink temperature in equation (38) will now include the effect of impinging solar radiation. This approach must be taken because the effect of absorbed solar energy on the value of η in equation (38) is dependent upon sink temperature, as well as root temperature and geometry.

The surface finish chosen for the radiator should have as high a value of emissivity, ϵ, as possible to minimize radiator area and weight. The solar absorptivity, α, should be as low as possible to minimize the effect of absorbed solar energy. Although emissivity and absorptivity must have the same value at a given wavelength, the integrated values are usually different for different spectral distributions. The wide difference in the energy distribution in the infrared band (where the radiator emits) and the solar spectrum (through which a surface absorbs solar energy) can lead to wide differences in values of emissivity and solar absorptivity. The ratio α/ϵ in equation (39) can range from about 0.15 to well over 15. The effect of this ratio on the sink temperature, T_s', where T_s is taken

as zero, is shown in Figure 49. The lowest values of α/ϵ are obtained by overlaying a highly reflective material with one which has a high emissivity and a high transmittance to the solar spectrum. Hence, energy is radiated directly from the outer material, while incident solar energy passes through and is reflected by the bottom layer. This type of coating is very stable in a space environment, but, for some material combinations, the price may be prohibitive for large area radiators. Values of α/ϵ of less than 0.2 can be readily attained using certain paints. All paints tested to date, however, have shown at least some degree of degradation (increase in α) after exposure to ultraviolet and ionizing radiation. Thus, while paint is often the simplest coating, it is not always the best choice.

6.2 Thermal Design of the Internal Tube Structure

6.2.1 The UHF Amplifier

The internal thermal design of the UHF crossed-field amplifier is presented below.

6.2.1.1 Collector

The collector is made up of fifteen concentric rings in a space of 0.23" as shown in Figure 50. Under normal operating conditions, the dissipation is distributed over most of the rings. The condition can arise, however, where the beam falls on only four of the collector rings, producing the "worst" case condition. The temperature difference from the surface of the collector to the heat transfer ring was computed for this condition, allowing for a 1.2 kv heat load. Figure 51 shows the results as a function of temperature. The reason that the drop is such a strong temperature function is the temperature dependance of the thermal conductivity of beryllia. At 250°C, the thermal conductivity of pure beryllia is 0.295 cal/cm sec°C but is reduced more than 50% at 400°C. The thermal conductivity of copper, while it does change slightly, is relatively constant over the range.

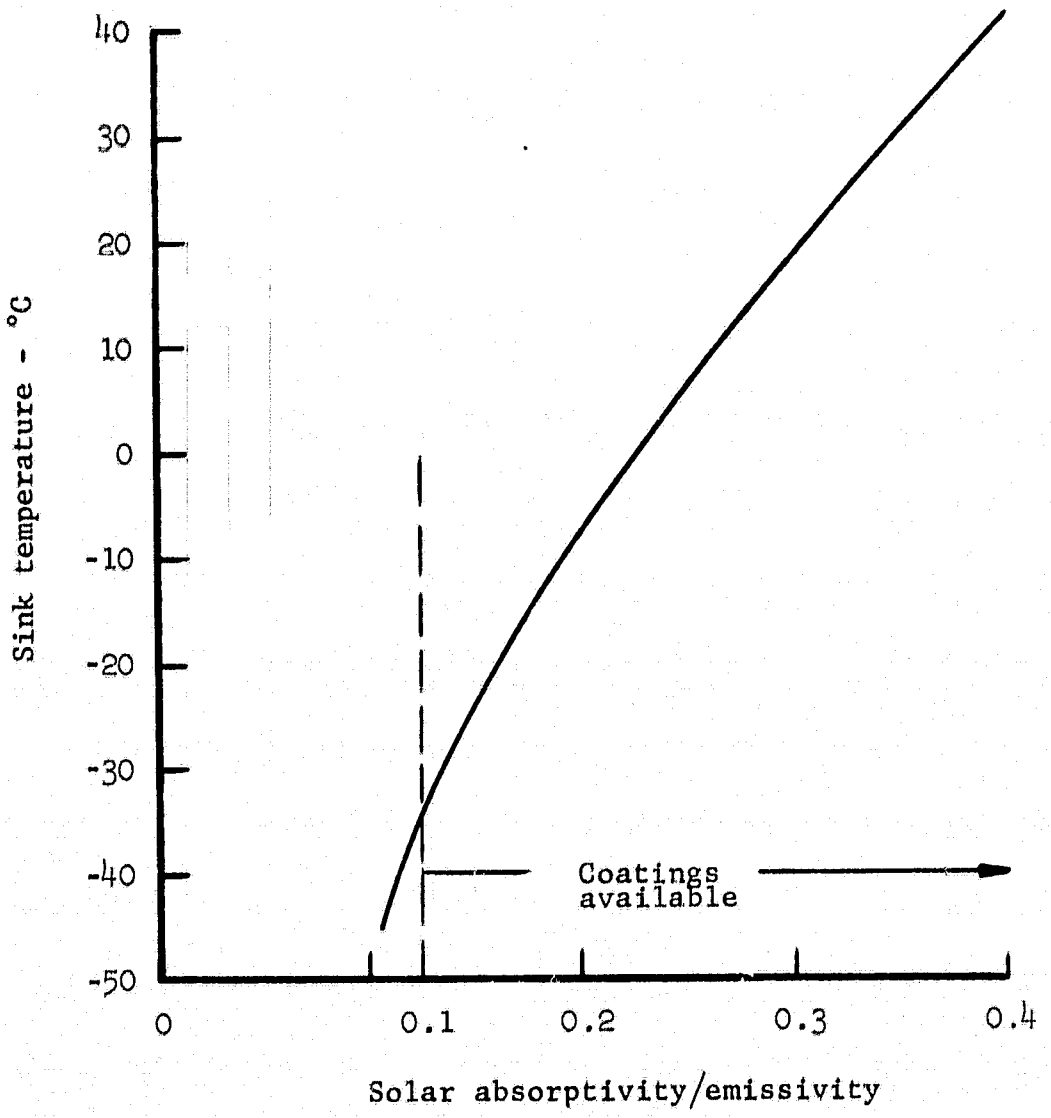

FIGURE 49 SINK TEMPERATURE FOR DIRECT SUN ILLUMINATION WITH DIFFERENTIAL ABSORPTIVITY AND EMISSIVITY

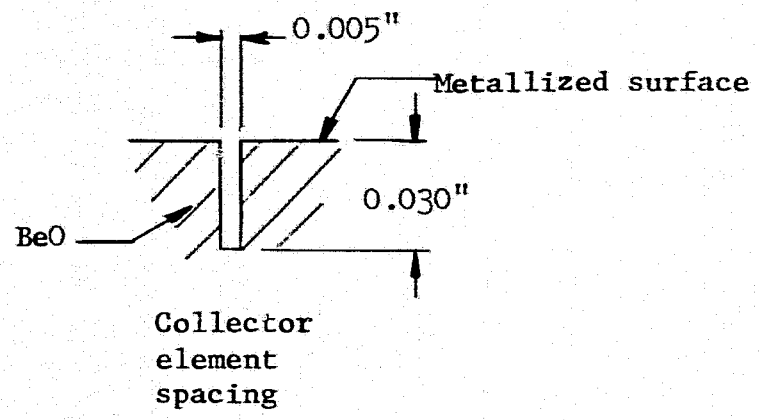

	Dimensions	
	UHF	S-band
A	0.23"	0.09"
R	3.5"	2"
D	0.534"	0.354"
d	0.053"	0.040"
Circuit bar	2"x0.14"	1"x0.06"
Collectors	15	10

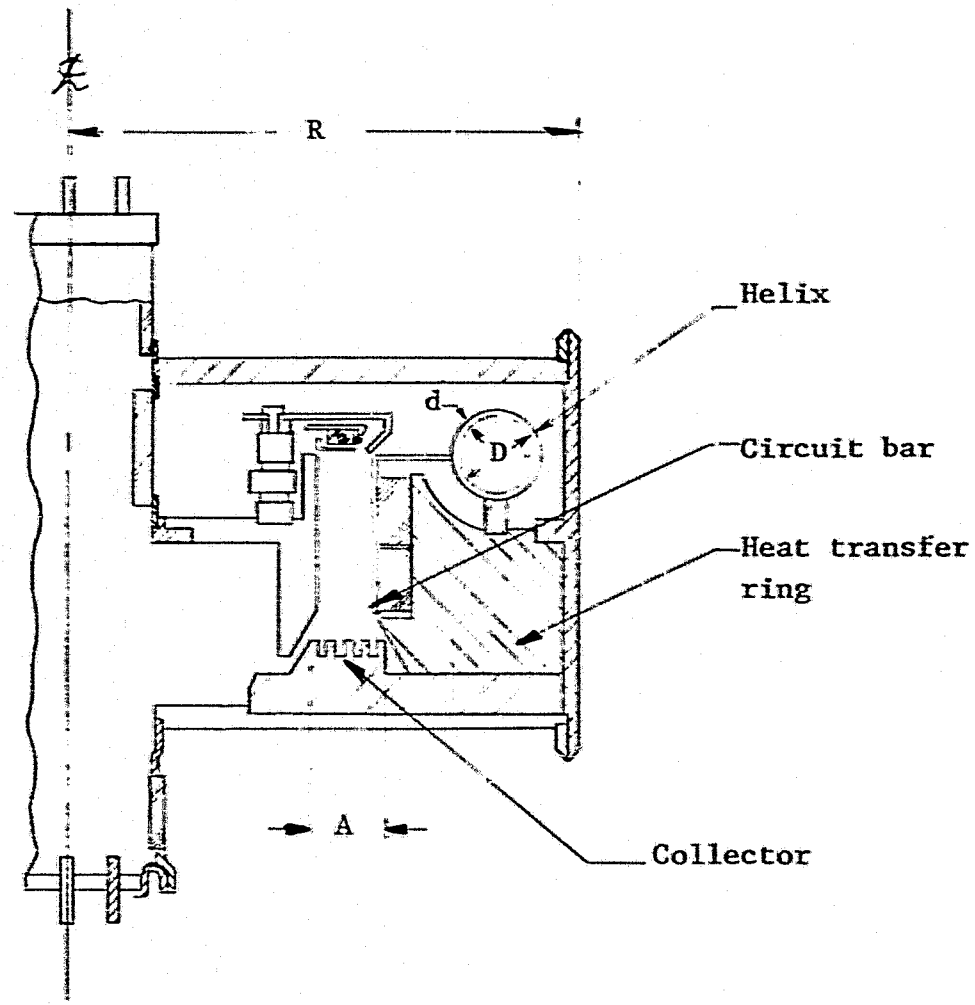

FIGURE 50 CFA CROSS-SECTION SHOWING THERMAL FLOW PATHS

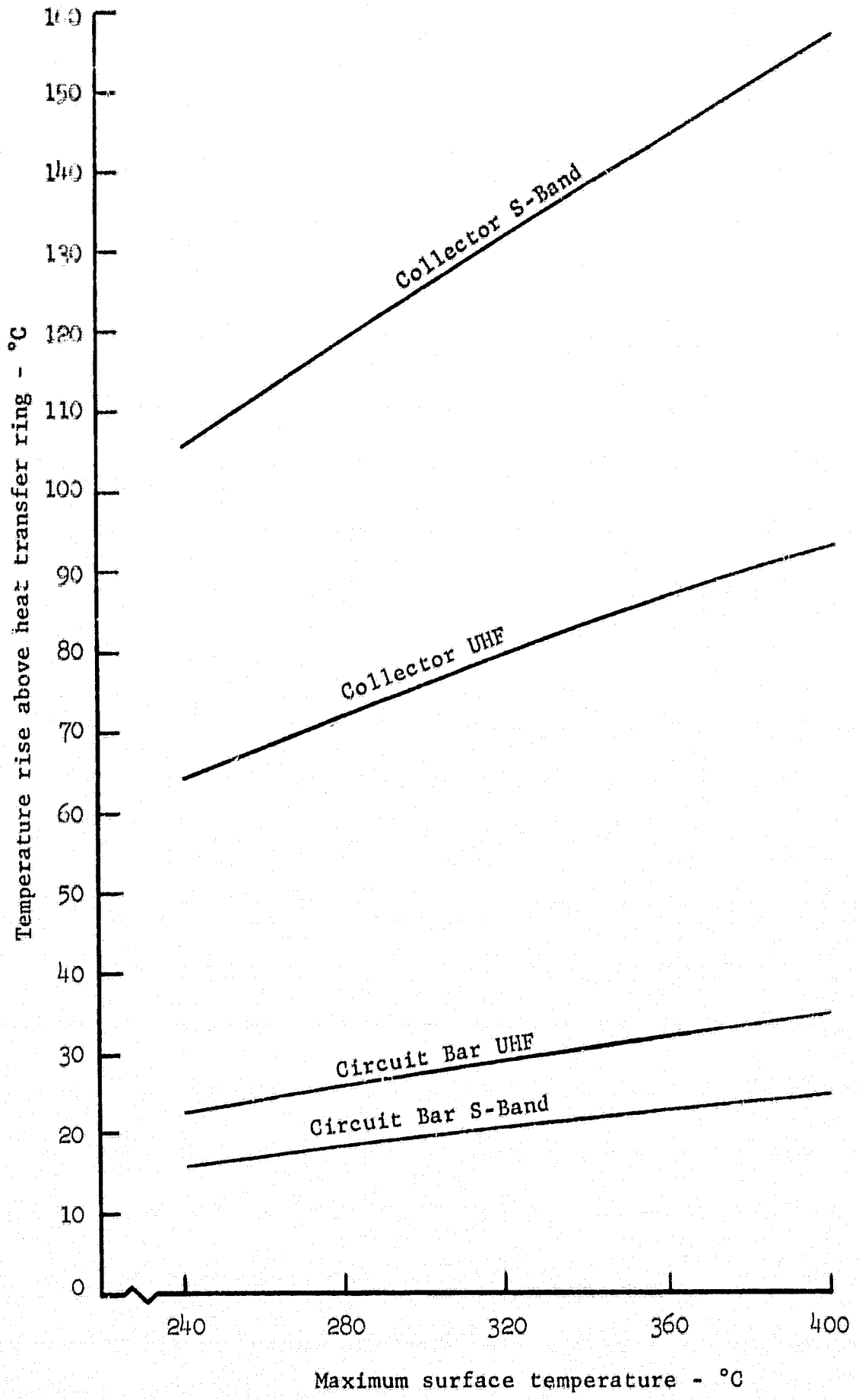

FIGURE 51 INTERNAL TEMPERATURE OF TUBE VERSUS RADIATOR TEMPERATURE

6.2.1.2 Circuit Bars

The 52 circuit bars are attached through beryllia supports to the heat transfer ring as shown in Figure 50. The "worst" case heat load on a given bar is estimated by allowing for a 1 kw heat load which is non-uniformly distributed over the bars. In this case, the maximum heat load on a given bar is 170% of the average heat load or approximately 33 watts. Figure 51 shows the relationship between the temperature differential between the heat transfer ring and the internal tube elements. The change in thermal conductivity of the beryllia support makes this differential temperature dependent.

6.2.1.3 Helix

The helix is a 0.534" diameter coil made up of 0.053" diameter copper clad stainless steel wire. Each turn is attached to the heat transfer ring by a beryllia support. This support also acts as a heat sink. By treating the heat transfer in the wire as a rod with uniform internal heat generation, the temperature rise in the wire can be computed as

$$\Delta T = \frac{Q}{2K} L^2 \qquad (40)$$

where ΔT = temperature rise along the wire
Q = volumetric heat generation rate
K = thermal conductivity of the wire
L = length of half turn of the helix

The temperature rise above the heat transfer ring in the helix for a heat generation rate of 0.5 watt per turn is 115°C for an all stainless steel wire and 9.1°C for solid copper through the beryllia support. Since the temperature rise for a heavily clad wire will be well below 115°C, this should not prove to be a problem. The cross-sectional area of the wire, however, should be 30% or more copper to prevent its temperature from exceeding the collector temperature.

From the preceding discussion and the results shown on Figure 51, it is evident that the maximum internal temperature will occur at the collector.

6.2.2 The S-band Amplifier

The thermal design of the CFA for operation at S-band is similar to that of the UHF device. Analysis of the three critical elements is given below.

6.2.2.1 Collector

The collector is made up of ten concentric rings in a space of 0.090" as shown in Figure 50. During periods of operation with no RF input, approximately 800 watts can be dissipated on three of the collector rings, which produces the peak power density and thus the highest collector temperature. As mentioned for the UHF tube, the temperature dependance of the thermal conductivity of beryllia causes a progressively higher temperature drop through the insulator resulting in the relationship shown on Figure 51.

6.2.2.2 Circuit Bars

Thermal analysis of the circuit bars is identical to that of the UHF tube, except the dimensions change as shown on Figure 50 and peak power on a given bar is reduced to 11.3 watts. The temperature drop from a circuit bar to heat transfer ring is shown on Figure 51.

6.2.2.3 Helix

For the S-band tube, the helix is 0.354" in diameter and made from 0.040" wire. The temperature rise in the coil from equation (40), is 125°C for stainless steel and 6.3°C for copper for a 0.5 watt per turn power dissipation. Since the copper cladding will provide sufficient thermal conductance to hold the rise well below the 125°C, the collector will have the limiting temperature.

6.3 Thermal Control System Integration and Selection of Final Operating Parameters

Interfacing the thermal control devices with the CFA and then integrating the entire package into a spacecraft can be done only after specific vehicle design parameters have been established. A specific design, however, is developed here for a heat rejection system of the capacity investigated in this study.

The preceding section shows the internal thermal design considerations for the UHF and S-band crossed-field amplifiers. Temperatures of the heat transfer ring were developed as a function of the maximum allowable temperature of any element in the tube. The radiator temperature will be somewhat lower than the temperature of the heat transfer ring due to additional drops encountered circumferentially and at the heat pipe interface. Under normal operating conditions, the circumferential temperature will be less than 8°C due to non-uniformity in the collector dissipation. Test results have shown that the total temperature drop, through a threaded interface of 0.50" stainless steel heat pipe to the condenser, is approximately 0.2°C/watt for a 1" evaporator. For copper, this can be reduced to 0.04°C/watt. Figure 52 shows the radiator temperature for the UHF and S-band configurations of the CFA as a function of the maximum operating temperature.

The radiator weight and area requirements can now be determined from the work of the preceding sections. First, the radiator coating must be chosen. The smaller the ratio of solar absorptivity to emissivity ratio, the less the effect of the sun on temperature. While coatings are available which will give a value of this ratio as low as 0.1, a value of 0.23 will be used since this is far more readily attained. The resulting sink temperature is 0°C. A cross plot of Figure 52 with Figures 45 through 48 for a 0°C sink shows the radiator requirements for 2 kw dissipation by the UHF tube (Figure 53) and 1 kw for the S-band tube (Figure 54).

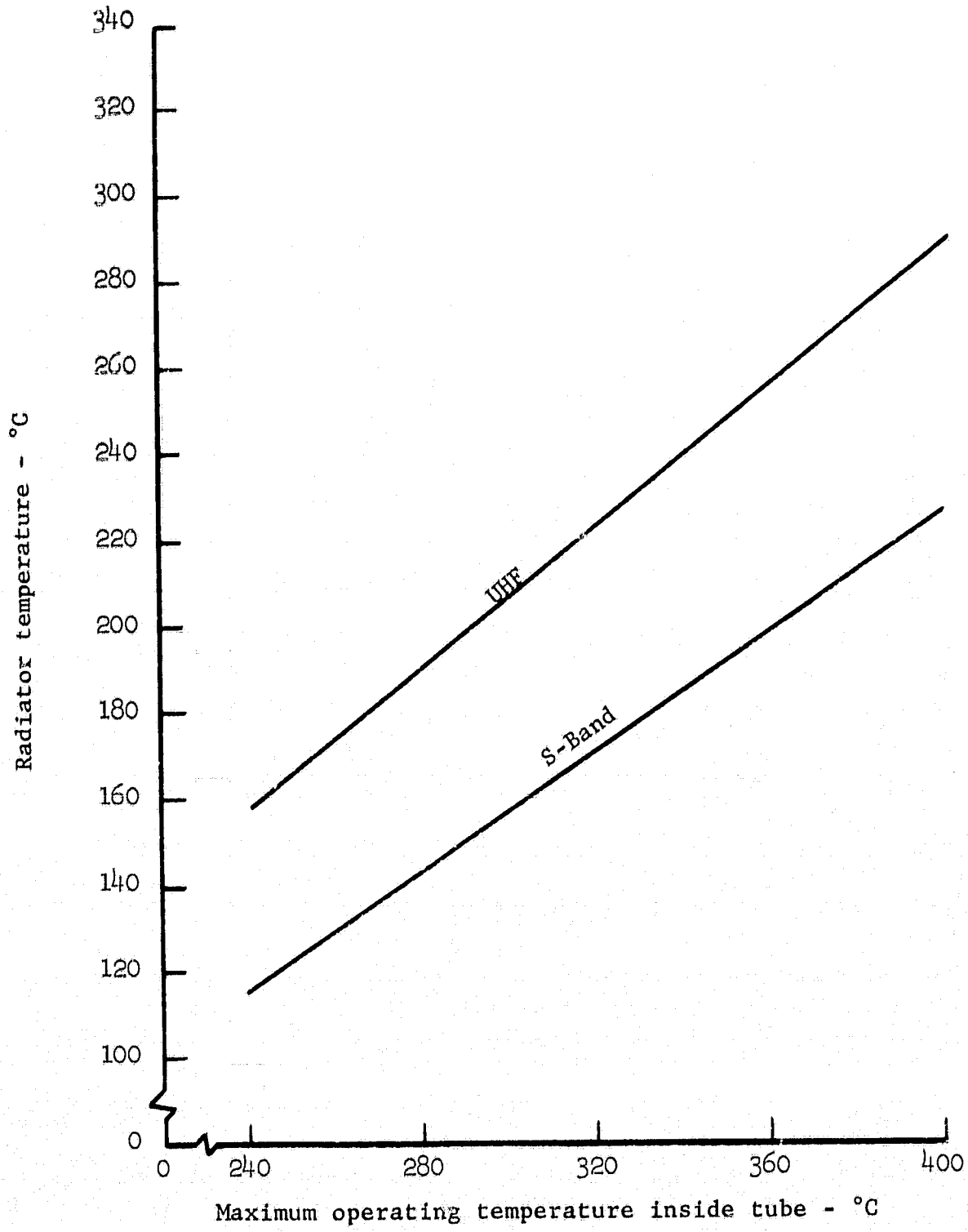

FIGURE 52 RADIATOR TEMPERATURE VARIATION WITH INTERNAL OPERATING TEMPERATURE

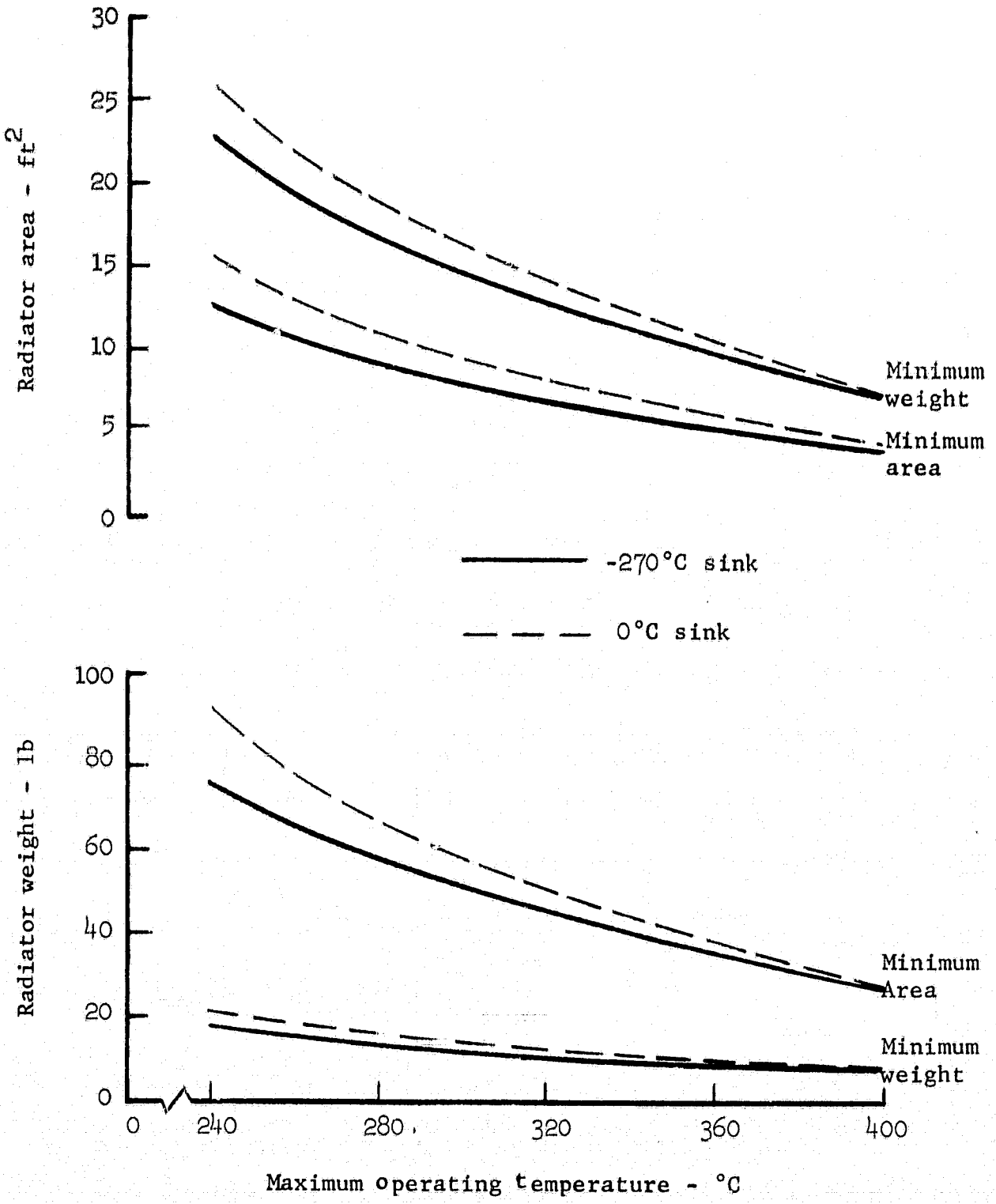

FIGURE 53 UHF RADIATOR REQUIREMENTS

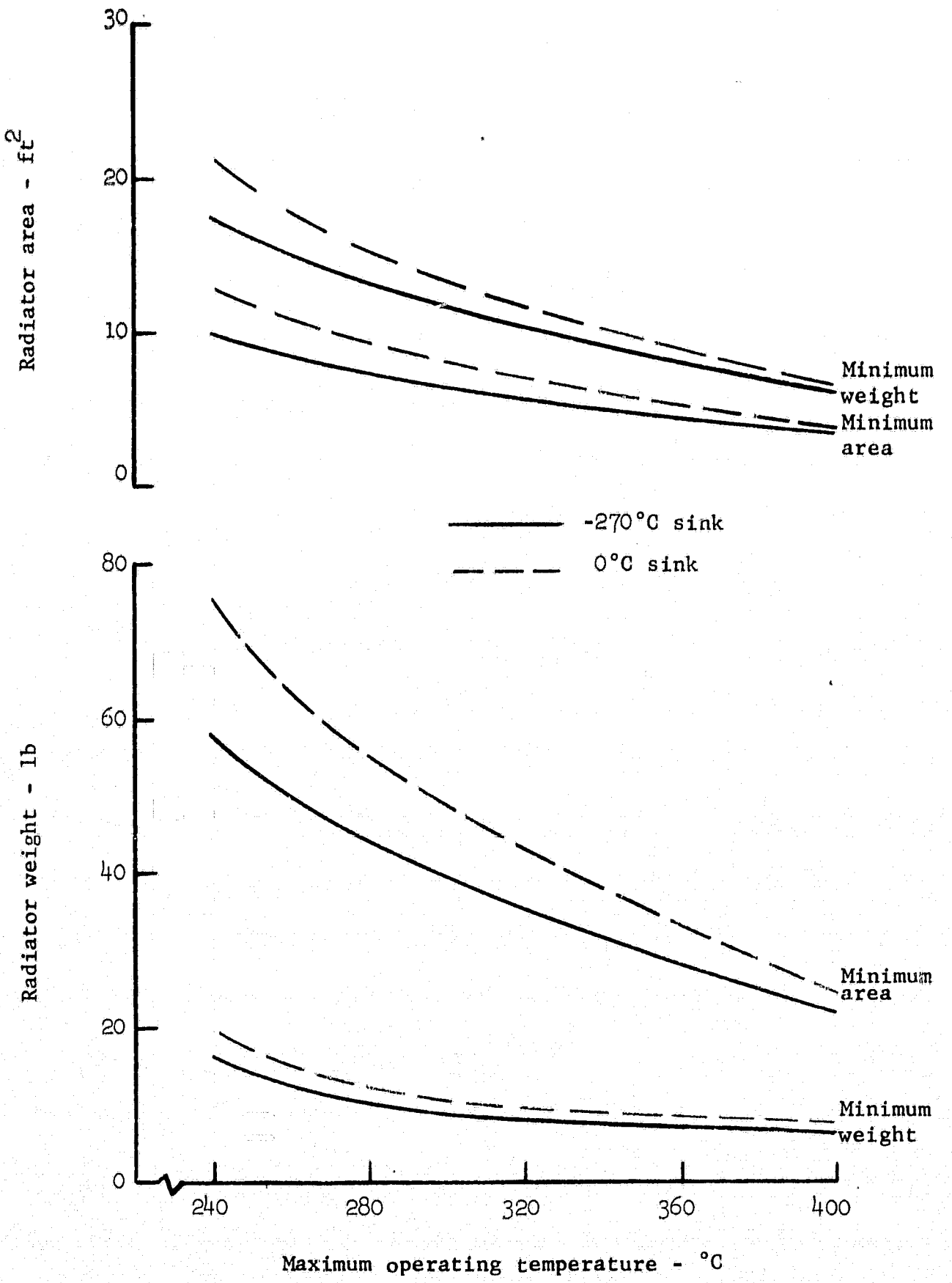

FIGURE 54 S-BAND RADIATOR REQUIREMENTS

To facilitate installation, the eight heat pipes are inserted through the shield. They are attached by threading them directly into the heat transfer ring as shown in Figure 55. An additional advantage is gained through this attachment technique since the heat pipes are completely separate from the CFA. Individual pipes can be replaced with a minimum of difficulty. An installation of this arrangement is shown in Figure 56. The operating parameters and resultant weight and geometry factors for eight 0.50" heat pipes and a 0.060" thick aluminum radiator are given in Table XVI. The heat pipes are periodically clamped to the radiator plate. While this system is not an optimum weight arrangement, the installation is simple and highly redundant as shown in Table XVII.

Thus the heat disposal system derived allows the maximum operating temperature within the amplifier tubes to remain at 300°C and thus maintains a very low evaporation rate of copper, so that the life expectancy of the amplifier will not be compromised. In addition, the system of connecting heat pipes clamped to a square aluminum radiator provides a system of radiation which has built into it sufficient redundancy so that failure of one or more heat pipes should not be fatal to the operation of the amplifier. The external components of the heat transfer system, the heat pipe and radiator plate can be disconnected from the tube proper itself. In addition the overall system has the virtue of being amenable to ground check-out which can be done by mounting the system, with the radiator plate held horizontally and, if need be, blowing cooling air across the surface of the plate. Use of selected coatings on the radiator plate protects the internal tube parts from excessive heat rise in those cases where solar radiation impinges directly upon the radiator surface. Under these conditions the maximum rise would be on the order of 15°C.

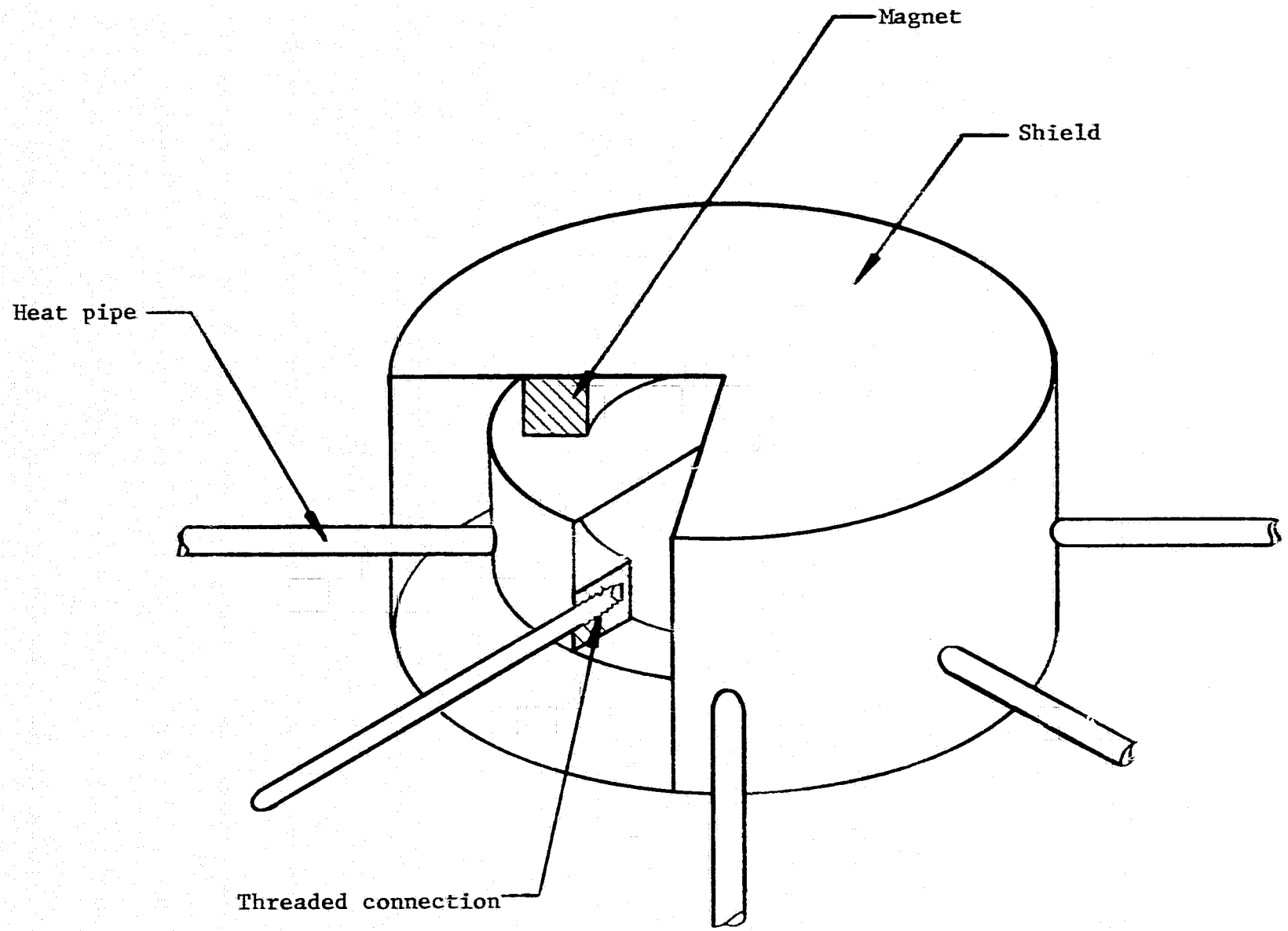

FIGURE 55 THERMAL INTERFACE

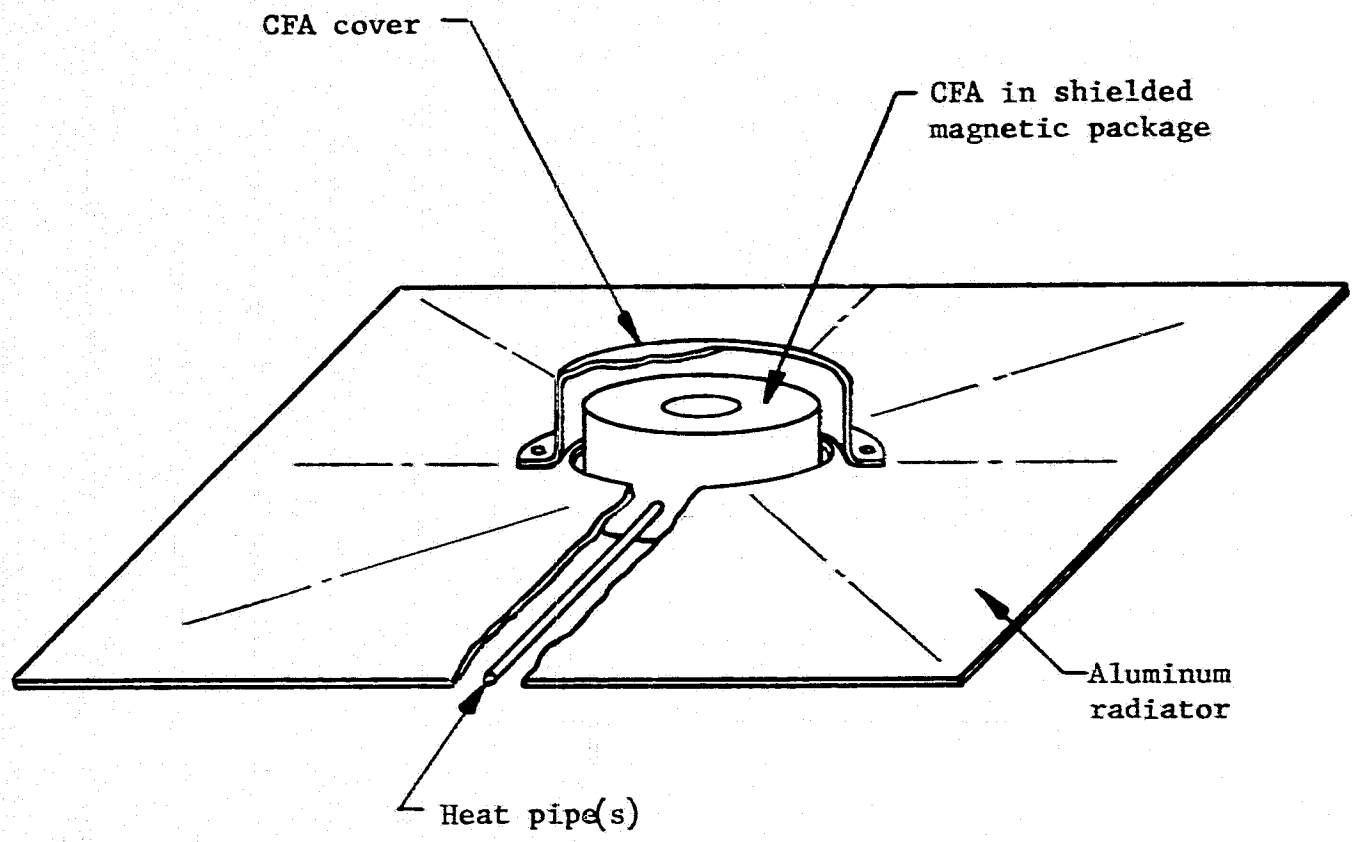

FIGURE 58 CFA RADIATOR ASSEMBLY

TABLE XVI

RADIATOR SYSTEM PARAMETERS AND GEOMETRY

	UHF Amplifier	S-band Amplifier
Radiator		
Weight (min), lb	12	14
Area, ft^2	14.5	17
Radiator temperature, ^oC	206	160
Collector temperature (worst case), ^oC	300	300
Circuit bar temperature, ^oC	249	194
Helix temperature (max), ^oC	286	230
Heat transfer ring temperature, ^oC	224	175

TABLE XVII

SYSTEM REDUNDANCY

Failure Mode	Maximum Component Temperature Rise (°C) UHF Amplifier	S-band Amplifier
No heat pipe failures	0	0
1 heat pipe failed	41	32
2 heat pipes failed (adjacent)	109	86
2 heat pipes failed (non-adjacent)	66	52

7.0 MECHANICAL DESIGN

The mechanical design of the axial injection CFA proposed for this program will result in a rugged, long life device. The materials selected and the assembly techniques will insure operation over the required 20,000 hours life. Time proven methods will be utilized in the machining, assembly and brazing operations, the vacuum processing, and the testing of the device. Environmental and life testing would finally check and document the reliability of the tube for its space mission.

Figures 57 and 58 are cross-sectional drawings of the proposed UHF and S-band amplifiers with the major piece parts and subassemblies identified. The S-band version of the tube is similar in construction to the UHF tube but is smaller in size. For reliability, conventional materials and state-of-the-art assembly techniques will be used wherever possible. New methods of construction and the possible use of new materials may be required for the circuit, the electron gun, and the collector assemblies. The vacuum envelope, matching sections, windows, sole assembly, and the magnetic package will present no problems in the design for a reliable long life device. Discussion of the mechanical design and manufacturing techniques which are planned to develop the circuit, axial injection gun, and collector assemblies follows.

7.1 The Slow Wave Circuit

The delay line chosen for the proposed amplifier is the helix coupled bar circuit described in Section 4.0. As can be seen in Figure 59, the bars and coupling helix of the delay line are supported from a ground plane by ceramic insulators. The ceramic details are metallized and brazes are made between the insulators and the metal details. In this manner the slow wave circuit is electrically insulated from the ground plane and, at the same time,

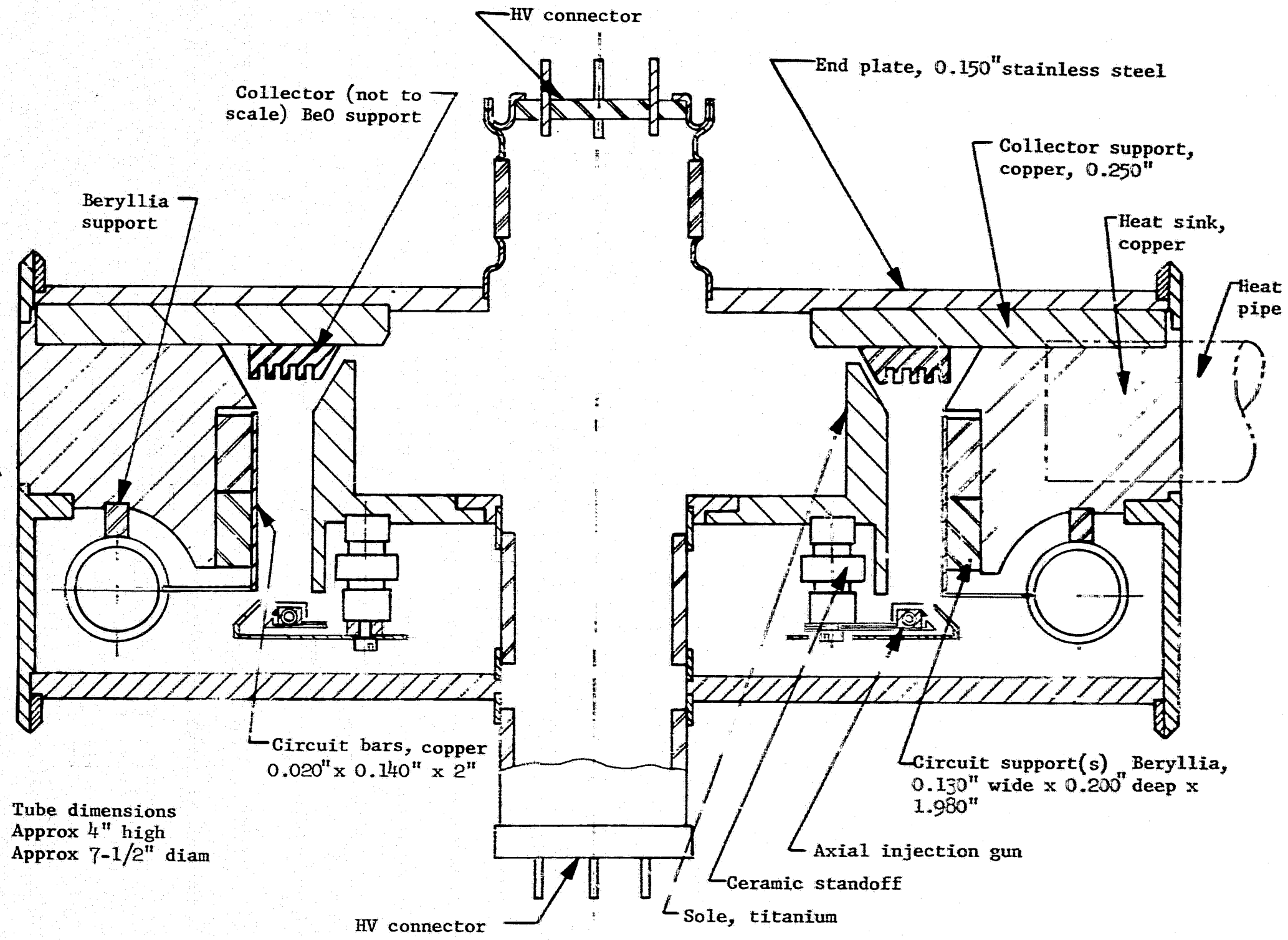

FIGURE 57 SCHEMATIC OF UHF AMPLIFIER

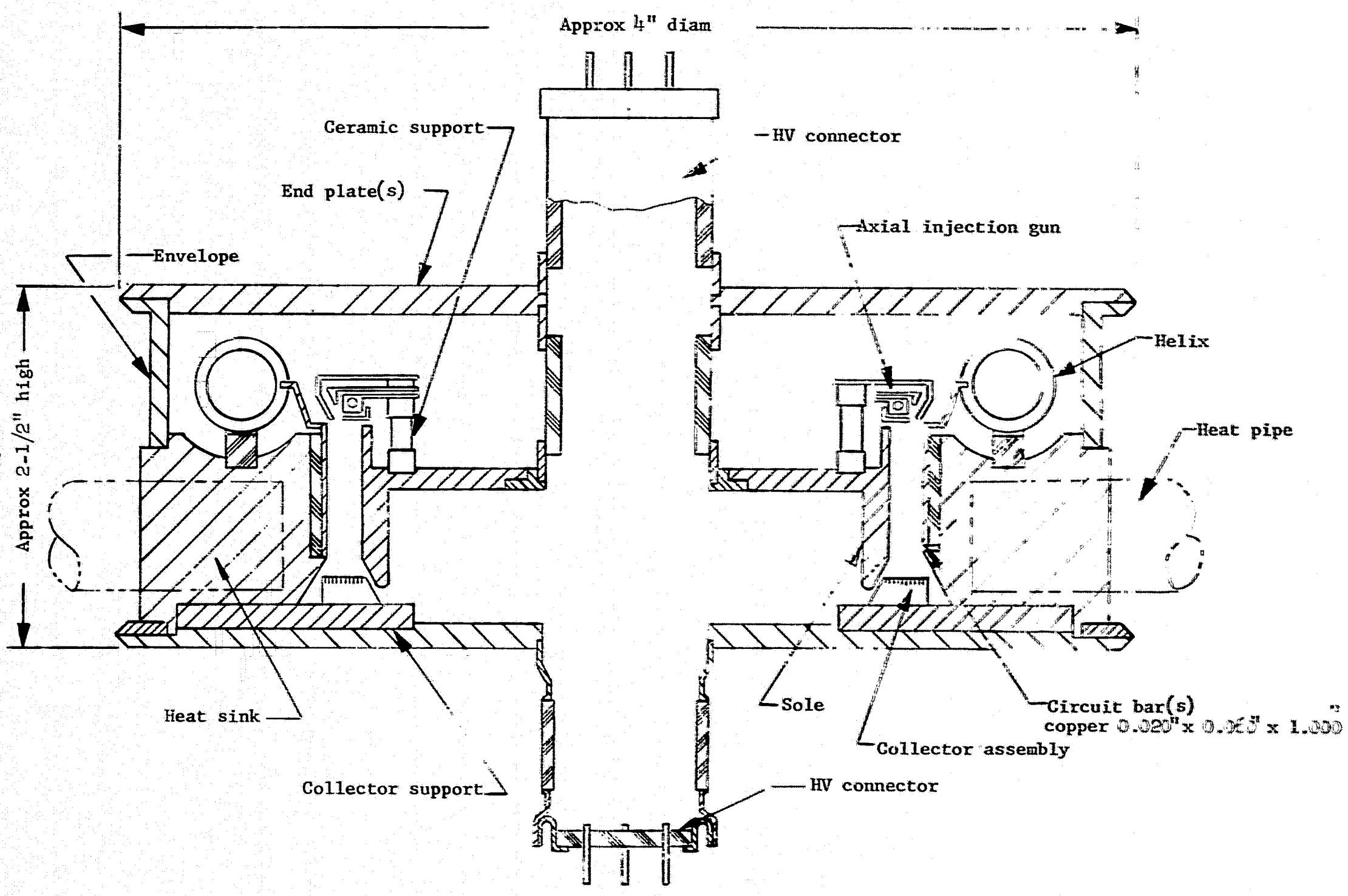

FIGURE 58 SCHEMATIC OF S-BAND AMPLIFIER

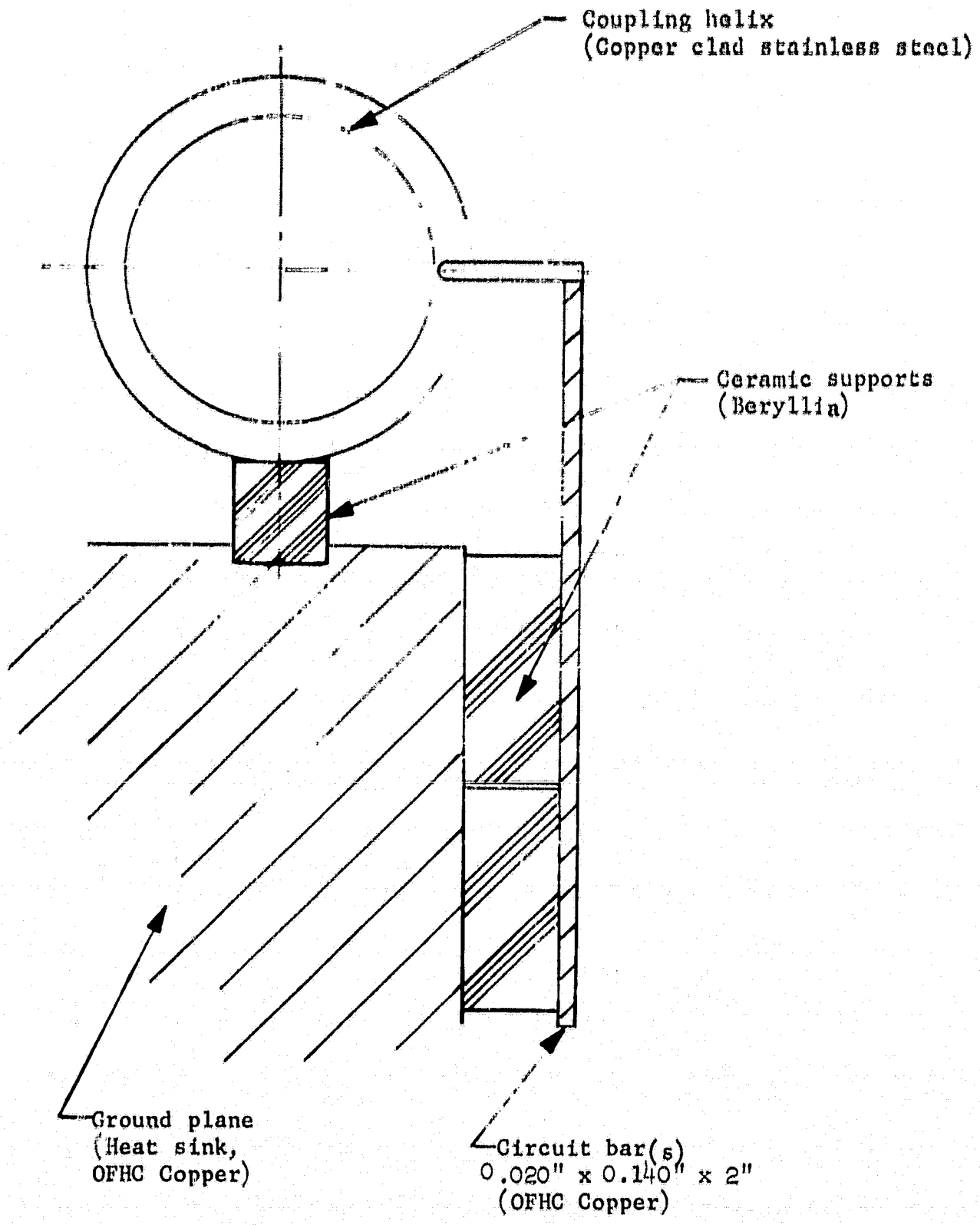

Not to scale

FIGURE 59 SKETCH OF HELIX COUPLED BAR CIRCUIT SHOWING MOUNTING TECHNIQUE

is thermally connected to a heat sink. Heat generated during operation of the tube is conducted through the metal-ceramic-metal assembly to the body of the tube where it will be dissipated with the aid of heat pipes. (Heat pipe design and theory were described in Section 6.0.)

Several ceramic materials could be used for the supports. The choice for this application is beryllium oxide after careful consideration of the thermal requirements. Of the usable ceramic materials, beryllium oxide has the highest thermal conductivity which, if the material is kept at an operating temperature of 250°C or lower, is about one-third that of copper. All other usable ceramics have one-twentieth to one-tenth the thermal conductivity of copper. When the bars and coupling helix are brazed to the supporting ceramics and then to the ground plane, an excellent thermal conduction path thus exists from the surface of the bars to the heat sink.

The techniques required for metal-ceramic sealing of the line support insulators are currently being evolved. A completely brazed assembly of the type of line proposed for this program is shown in Figure 60. The mean diameter of the circuit pictured is 8".

7.2 The Electron Gun

The electrical characteristics of the electron gun designed for use in the axial injection crossed-field amplifier was described in Section 5.0. The method of beam injection dictates that the diameter of the cathode ring be of the same magnitude as the diameter of the anode circuit. The emitting surface itself is rather small, being of the order of 0.080" in the UHF tube. Therefore, the cathode is a large diameter, thin ring component. The cathode to be used in the proposed amplifier will be the porous tungsten impregnated type and will be indirectly heated. Special care must be taken in the design of the supporting elements and in the use of heat reflecting shields to minimize heater power requirements. Sample calculations indicate that with the proper selection of a poor thermal conducting

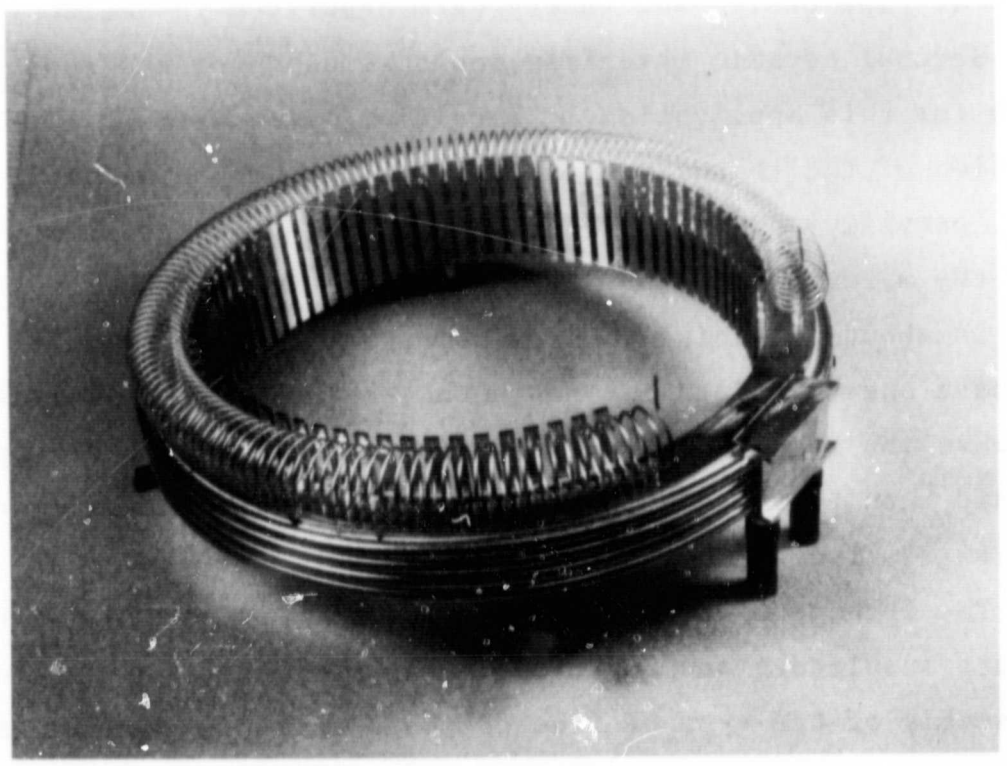

FIGURE 60 PHOTOGRAPH OF HELIX COUPLED BAR SLOW WAVE STRUCTURE

material for the cathode supporting members, it is possible to minimize conduction heat losses without sacrificing structural integrity. Thin members of stainless steel may be used. The addition of heat reflecting shields to reduce heat loss due to radiation from the high operating temperature of the cathode assembly further reduces heater power requirements.

Approximate dimensions for the proposed UHF and S-band cathode designs were assumed. Then equations (41) and (42) were used to determine heat loss. The heater power requirements resulting from these calculations are given in Table XVIII.

To calculate radiation losses:

$$P_r = \frac{\sigma A \epsilon_1 \epsilon_2 (T_1^4 - T_2^4)}{(\epsilon_2 + \epsilon_1)(1 - \epsilon_2)\frac{r_1}{r_2}} \qquad (41)$$

where P_r = energy loss due to radiation
A = area of radiating surface
ϵ_1 = emissivity of radiating surface
ϵ_2 = emissivity of absorbing surface
r_1 = radius of radiating surface
r_2 = radius of absorbing surface
σ = Stefan-Boltzmann constant
T_1 = absolute temperature of radiating surface
T_2 = absolute temperature of absorbing surface

To calculate conduction losses

$$P_c = \frac{T_1 - T_2}{R_T} \qquad (42)$$

TABLE XVIII

CATHODE-HEATER POWER REQUIREMENTS

Cathode	Cathode Temperature °C	Heater Power UHF Design watts	Heater Power S-band Design watts
Dispenser type	820	53	41
Oxide coated	720	40	32

where P_c = energy loss due to conduction
T_1 = temperature of hot body
T_2 = temperature of cold body
R_T = total thermal resistance of thermal path

It is possible that heater power may further be reduced through the use of a directly heated cathode in the form of tungsten wire which has been coated with a porous tungsten matrix. The matrix is then impregnated by conventional techniques. This new approach is currently under study at Semicon Associates, a subsidiary of Varian Associates. The cathode assembly, with its beam-forming and accelerating electrodes and its reflecting shields, is mounted from the sole on insulating ceramic supports, as shown in Figure 57.

7.3 The Collector

To obtain maximum beam efficiency, the collector is designed as a multiple element assembly, as described in Section 4.4. In both the UHF and S-band designs, it is important to accommodate as many collector rings or elements as is mechanically possible in the space allotted. These rings must be as close together as feasible and at the same time must be capable of accepting and dissipating the heat generated by electron bombardment. The collectors will be solidly mounted and brazed to beryllium oxide supports which will help transmit the heat to the heat sink and will electrically isolate one ring from the other. Several approaches to fabricating the multi-section assembly are being considered. Figures 61, 62, and 63 show three designs which may be used.

The design shown in Figure 61 consists of ten or more concentric rings and electrical leads attached to a beryllium oxide ceramic base. As the dimensions show, these rings must be precisely located on the ceramic substrate. To accomplish this, metallic rings can be deposited on the ceramic in a number of ways. Three convenient,

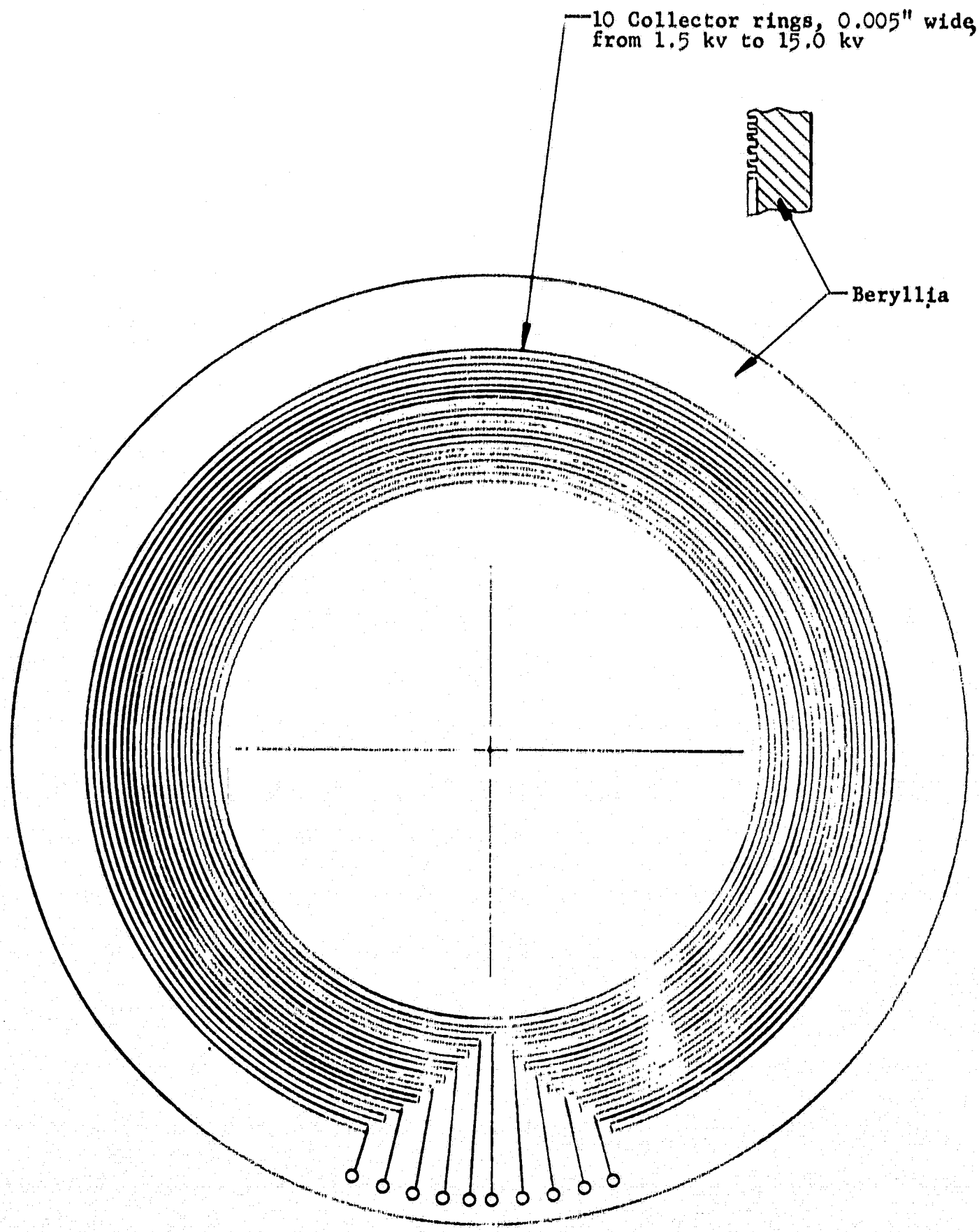

FIGURE 61 SCHEMATIC OF MULTI-ELEMENT COLLECTOR ASSEMBLY WITH CONNECTIONS

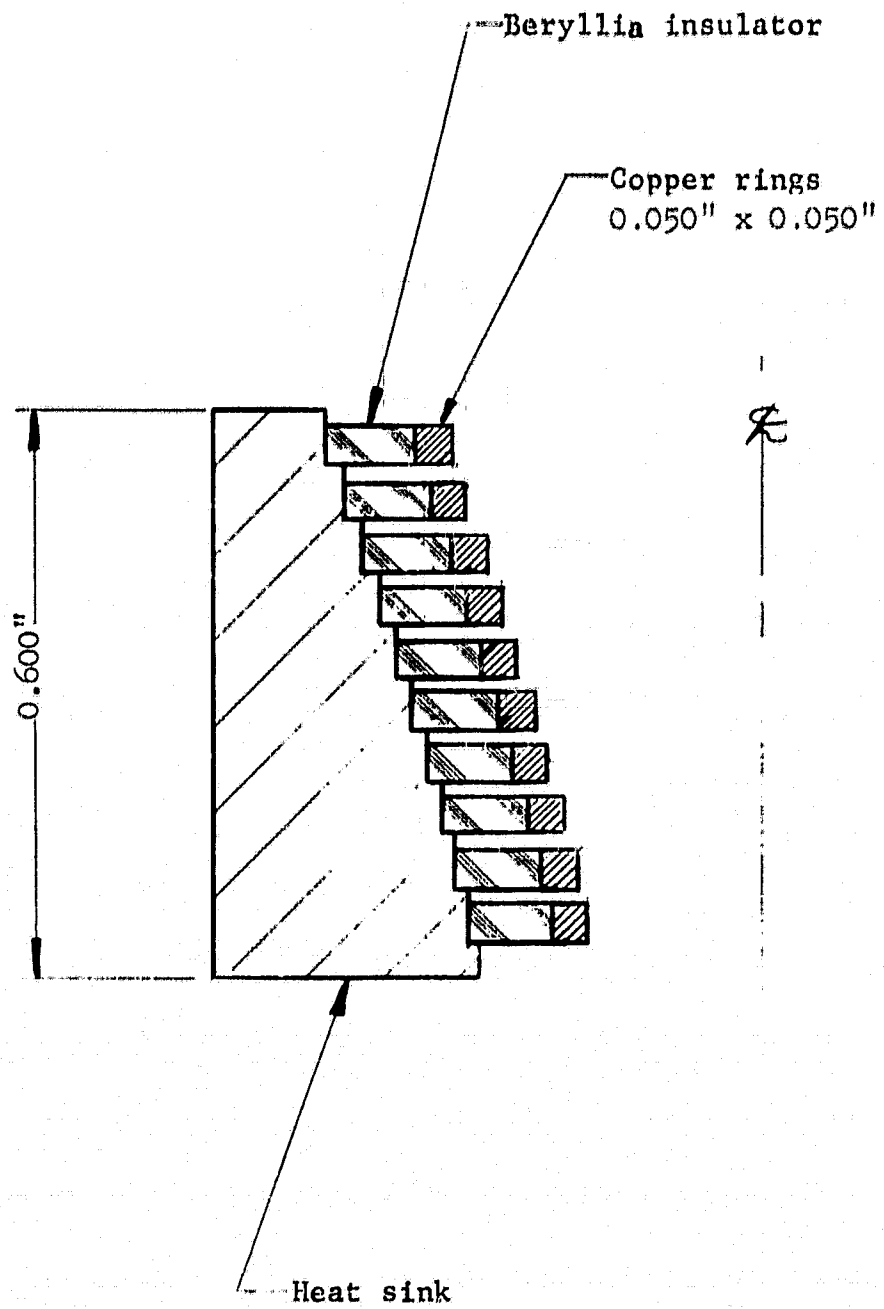

Not to scale

FIGURE 62 ALTERNATE COLLECTOR ASSEMBLY A

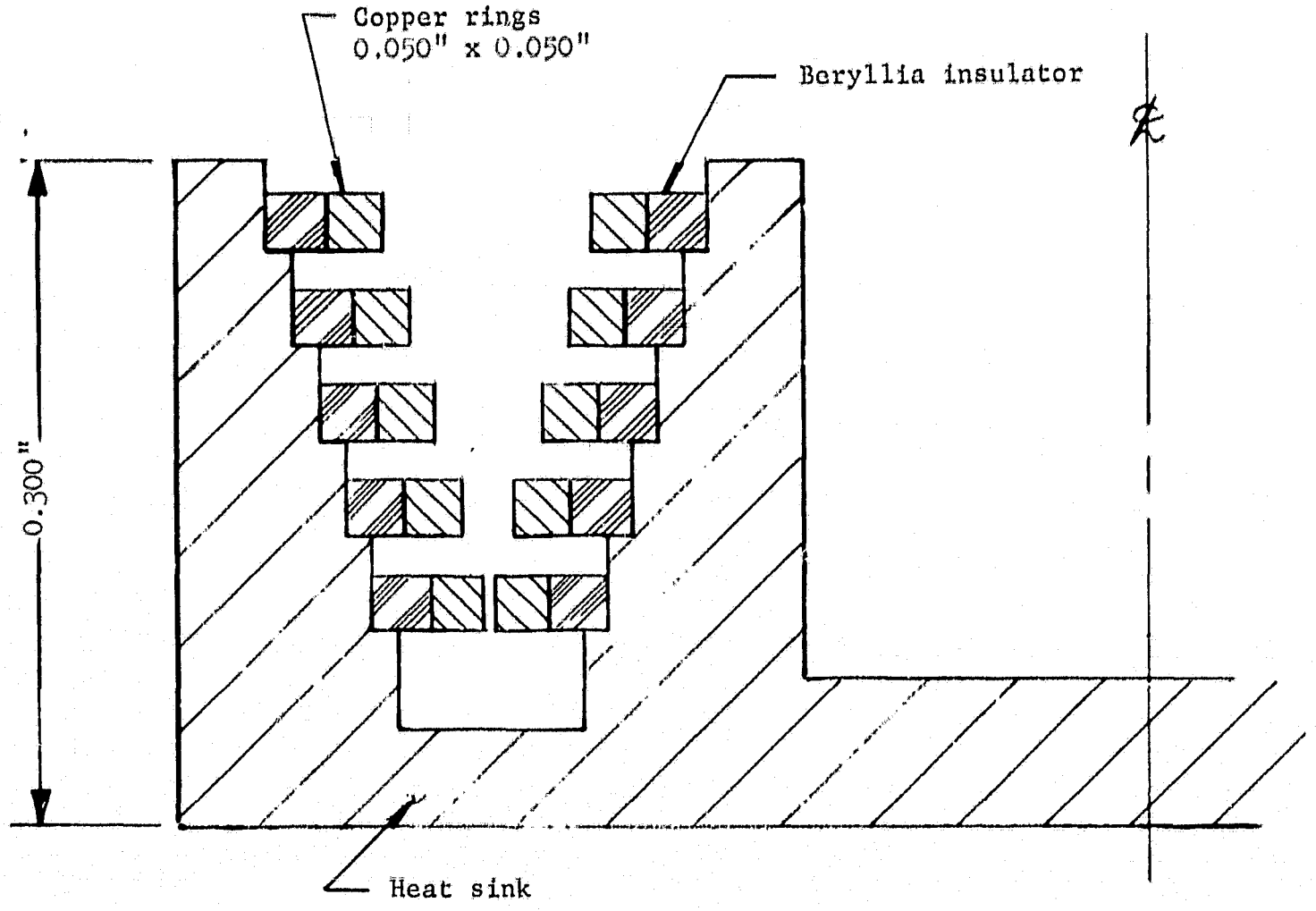

Not to scale

FIGURE 63 ALTERNATE COLLECTOR ASSEMBLY B

state-of-the-art techniques for depositing metal films on ceramic are by means of conventional vacuum evaporation, by ion plating, and by sputtering. After depositing a thin metal film, the thickness can be built to any desired height by plating or electroforming.

The selection of which method will be used will be dictated by the material to be deposited. The choice of material will depend upon the secondary emission coefficient, the resistivity, and the melting point. Lower melting point metals, such as copper and nickel, are deposited by vacuum evaporation or ion plating. In each of these techniques a filament source or electron beam bombardment is used to raise the temperature of the material to be deposited to the melting point. The method best suited for the higher melting point materials, such as molybdenum, tungsten, titanium or tantalum, is sputtering. Sputtering is the process in which a negatively charged element (cathode), in a partially evacuated chamber, is bombarded with positive ions which cause ejection of the surface atoms. These atoms are then deposited on the desired substrate. To prevent material from being deposited where it is not wanted, such as in the grooves shown, potting compounds may be used. If these compounds are found to be unsuitable for use under ion bombardment or at elevated temperatures, a technique for masking with photo etched metal masks can be used. Another method for getting the rings on the ceramic could be by metallizing with a conventional molybdenum-manganese solution. Control of this technique, however, is not as positive as the others for the critical dimensions required.

Two alternate solutions to closely packing the collector rings are seen in Figures 62 and 63. As shown, the collector elements are stacked in steps rather than being coplanar as in the previously discussed assembly. With stacked rings, there will be an increase in the magnetic gap length and special shaping of the collector faces will be required to inhibit secondary emission. Using the stacking

approach, the metal ring piece parts could be thicker and wider than those deposited on the ceramic base. Each of these collector rings is supported by a ring of ceramic as shown. As before, the ceramic is beryllium oxide to provide a good thermal path to the heat sink and to electrically insulate the collectors.

7.4 Environmental Testing

The tubes must meet certain environmental specifications for missile launch and earth orbit. The design and subsequent tests will then determine reliability in the mission. The mechanical configuration of the amplifiers will incorporate brazed and welded assemblies and will have support members similar to those used on several power tube programs successfully completed at S-F-D laboratories. During these programs, (which are classified), vibration and shock testing of all critical tube components, as well as complete tube packages, have proven the mechanical ruggedness and reliability of construction techniques. Amplifiers and high power magnetrons have been tested to more than the required 5 g to 15 g peak amplitude over 20-3000 Hz without damage to the units. The 8 msec, 30 g shock test is less than that required for many airborne operations in which crossed-field tubes are now employed. Environmental checks of these types of tubes have also included temperature testing from -40°C to +100°C and altitude and humidity tests.

The tubes, which would be manufactured for use on a proposed system, would be subjected to shock and vibration tests and to other environmental tests as specified. At each stage of the assembly, selected piece parts and subassemblies would be individually tested. Should failures occur, the design would then be modified and retested, as needed, until the specifications were met. In this manner, progression to a completely packaged device which passes all component tests would be achieved. Test reports of the failures, successes, and the modifications made would document the mechanical reliability of the package.

7.5 Tube Life

The 20,000 hours minimum life requirement will require a test program to determine life characteristics and reliability. Tube life will depend primarily on obtaining good cathode-heater reliability. The proper selection of tube materials and processing will also determine life limits. Many tube types in development and manufacture at S-F-D laboratories, use thermionic emitting cathodes such as proposed for this program. Quality conformance records show life times that consistently are thousands of hours. On several programs, records indicate that tubes have accumulated up to 8000 hours to 10,000 hours of operation. In all cases the cathode loading is as much as or higher than that required for the proposed tubes. Back bombardment can also play an important part in the ultimate life of a cathode. With the axial injection scheme, the back bombardment problem is non-existent. The selection and processing of the materials which are used in the construction of electron tubes is carefully considered. Materials with low vapor pressures are chosen. Rigorous controls over handling and processing of the raw material and the assemblies help to insure long operating life. Proper design to keep ambient temperature within the device at a moderate level will prevent evaporation or outgassing which can shorten operating life of the emitting surface of the cathode. It is the sum of careful attention to cathode design, to material selection, to fabrication and processing, and to temperature gradients which will make possible a tube life of more than 20,000 hours.

7.6 Size and Weight

The overall size of the two proposed packages are shown in Figures 64 for the UHF tube and in Figure 65 for the S-band design. Weight calculations have been made for both tube designs, and the results are given in Table XIX. The driver tube and circulator weight have been added to the weight of the tube package.

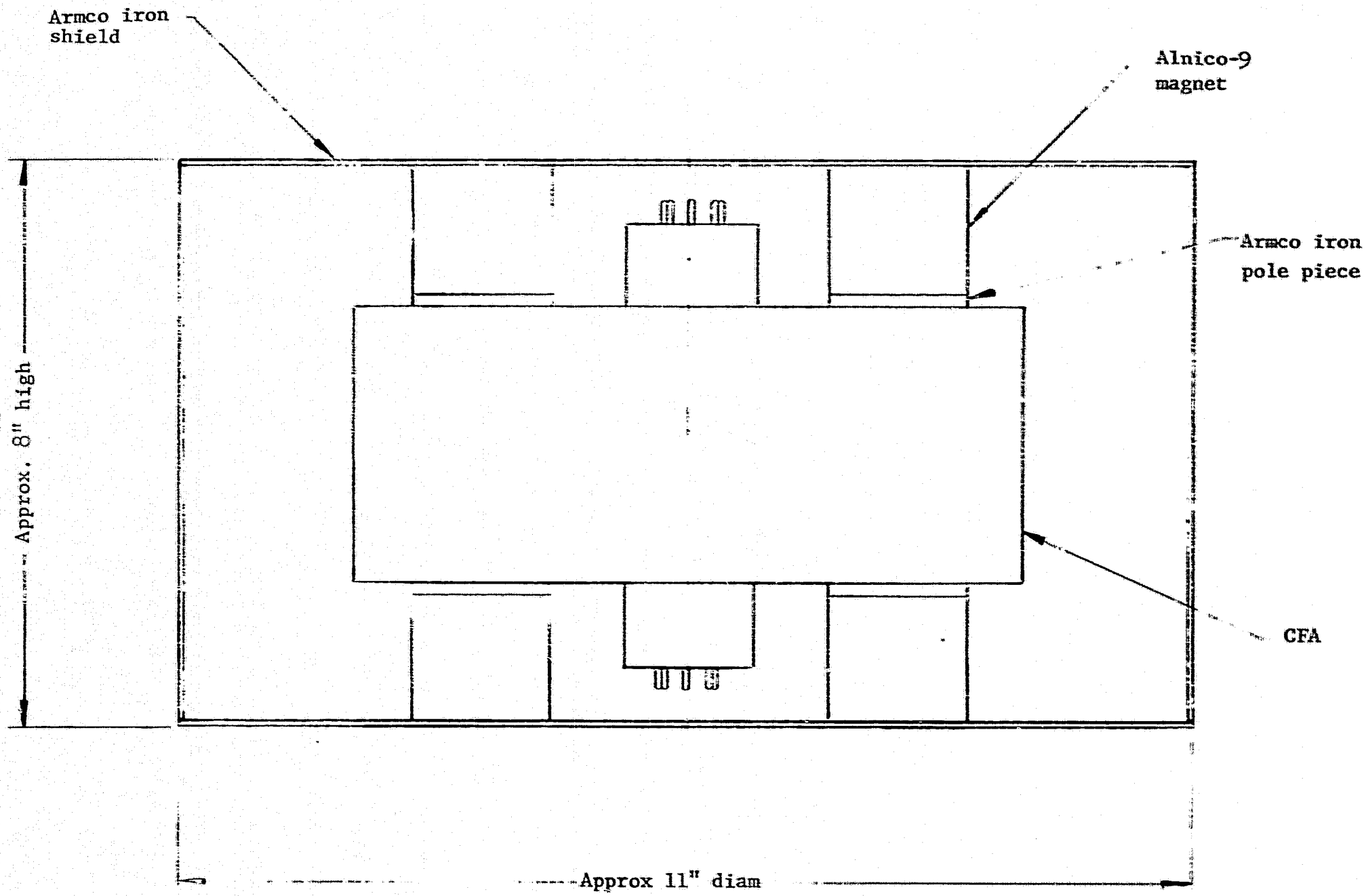

FIGURE 64 OUTLINE OF UHF AMPLIFIER AND MAGNETIC PACKAGE

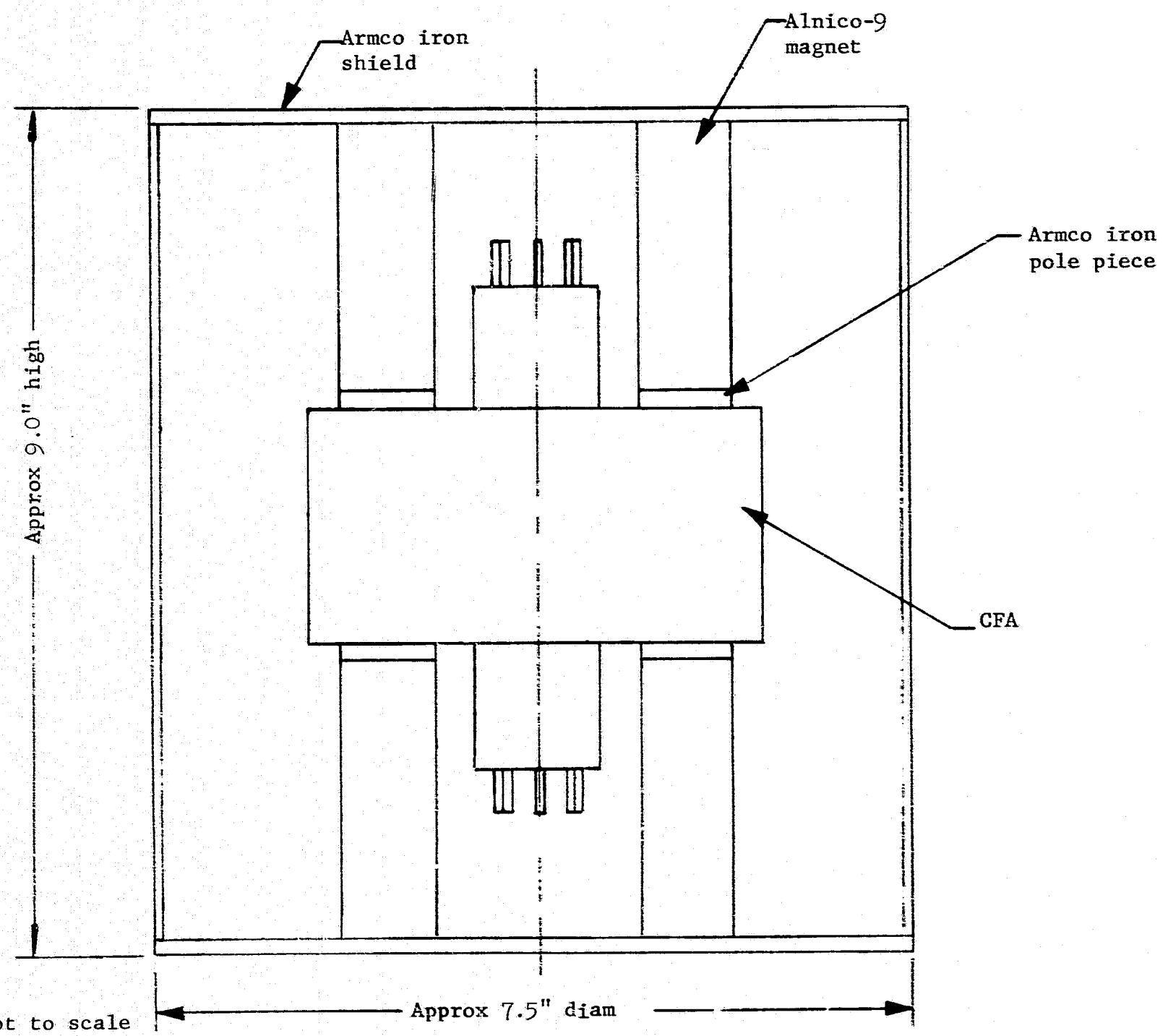

FIGURE 65 OUTLINE OF S-BAND AMPLIFIER AND MAGNETIC PACKAGE

TABLE XIX

WEIGHT ANALYSIS

	UHF Design		S-band Design	
Magnetic Circuit				
Magnets (Alnico-9)	22.00		13.70	
Shell (Armco Iron)	4.80		3.35	
End plates (Armco Iron)	4.90		2.43	
Pole pieces (Armco Iron)	1.20		0.49	
Total Magnetic Circuit		32.90		19.97
Tube Assemblies				
Tube envelope (Stainless Steel)	4.74		0.41	
Covers (Stainless Steel)	3.60		0.77	
Circuit support (OFHC Copper)	9.40		1.50	
Circuit bars (OFHC Copper)	0.24		0.10	
Sole (Titanium)	1.03		0.11	
Cathode (Molybdenum and Tungsten)	0.25		0.10	
Helix (Stainless Steel and OFHC Copper)	0.18		0.70	
Ceramic supports, windows, and connectors	1.00		0.70	
Total Tube Assemblies		20.44		4.39
Total Amplifier Package		53.34		24.36
Driver Tube	3.00*	10.00**	8.00	
Circulator	3.50	3.50	1.25	
Amplifier Package	53.34	53.34	24.36	
Total Package	59.84	66.84	33.61	

*Triode Driver
**Traveling Wave Tube Driver

In summary, the mechanical design of the crossed-field amplifier is based upon the use of materials and fabrication technique which are presently state-of-the-art or are in the development stage. The design of the circuit, the axial injection gun, and the collector assembly, are new concepts; however, these assemblies are manufacturable. The tube, which is proposed, will be a rugged assembly capable of meeting all environmental conditions through launch to orbit. The goal of a reliable 20,000 hour life device can be achieved through careful quality assurance of all materials and fabrication and processing techniques.

8.0 POWER CONDITIONER REQUIREMENTS

Summarized in Table XX are the voltage and current requirements for the UHF and S-band amplifiers. These determine the requirements imposed upon the power conditioning equipment. All voltages in the table are with reference to cathode potential. Physically, the anode structure is at the same dc potential as the vacuum envelope of the tube, which is at ground potential.

A typical power conditioning arrangement is sketched for the S-band crossed-field amplifier in Figure 66. This actually consists of several power supplied as discussed below. The appropriate ripple and regulation levels are shown in each case.

The cole-to-anode voltage must be well regulated, but does not draw any appreciable current. Therefore, a separate variable pulse width regulated converter may be used to supply a pre-regulated voltage to a corona voltage regulator. In this way, the pre-regulated voltage to the corona tube will tend to maintain constant corona current. This, in turn, keeps the corona voltage constant. Corona voltage regulators similar to the type indicated are manufactured by Victoreen and should be readily adaptable to this circuit.

The accelerator voltage is also a zero current supply. This may be derived from the same power supply as the heater voltage since neither one has stringent regulation requirements.

Finally, the collector supplies are shown as being derived from a common variable pulse width regulated converter which has multiple secondaries which are rectified, filtered, and connected in series. The cathode connection is the last negative tap on the collector supply. An alternate could be multiple, variable pulse width regulators for each collector element, if it were decided that each collector element should be regulated independently. The decision to use a single regulator or multiple regulators would depend on several factors. Among these are the reliability of multiple power

TABLE XX

VOLTAGE AND CURRENT REQUIREMENTS FOR UHF AND S-BAND AMPLIFIERS

(All voltages with reference to cathode potential)

	UHF Design	S-band Design
Anode voltage	14.2 kv	12 kv
Sole voltage	-7 kv	-6 kv
Number of collector elements	15	10
Collector voltages	890 v, 1780 v, ..., 13.3 kv*	1.1 kv, 2.2 kv, ..., 11.0 kv**
Cathode current	1.3 amps	1 amp
Accelerator voltage	~10 kv	~9 kv
Sole current	none	none
Accelerator current	none	none
Heater voltage	10 volts	10 volts
Heater current	4-5 amps	3-4 amps

*Voltage increases in steps of 890 v, from 890 v to 13.3 kv

**Voltage increases in steps of 1.1 kv, from 1.1 kv to 11.0 kv

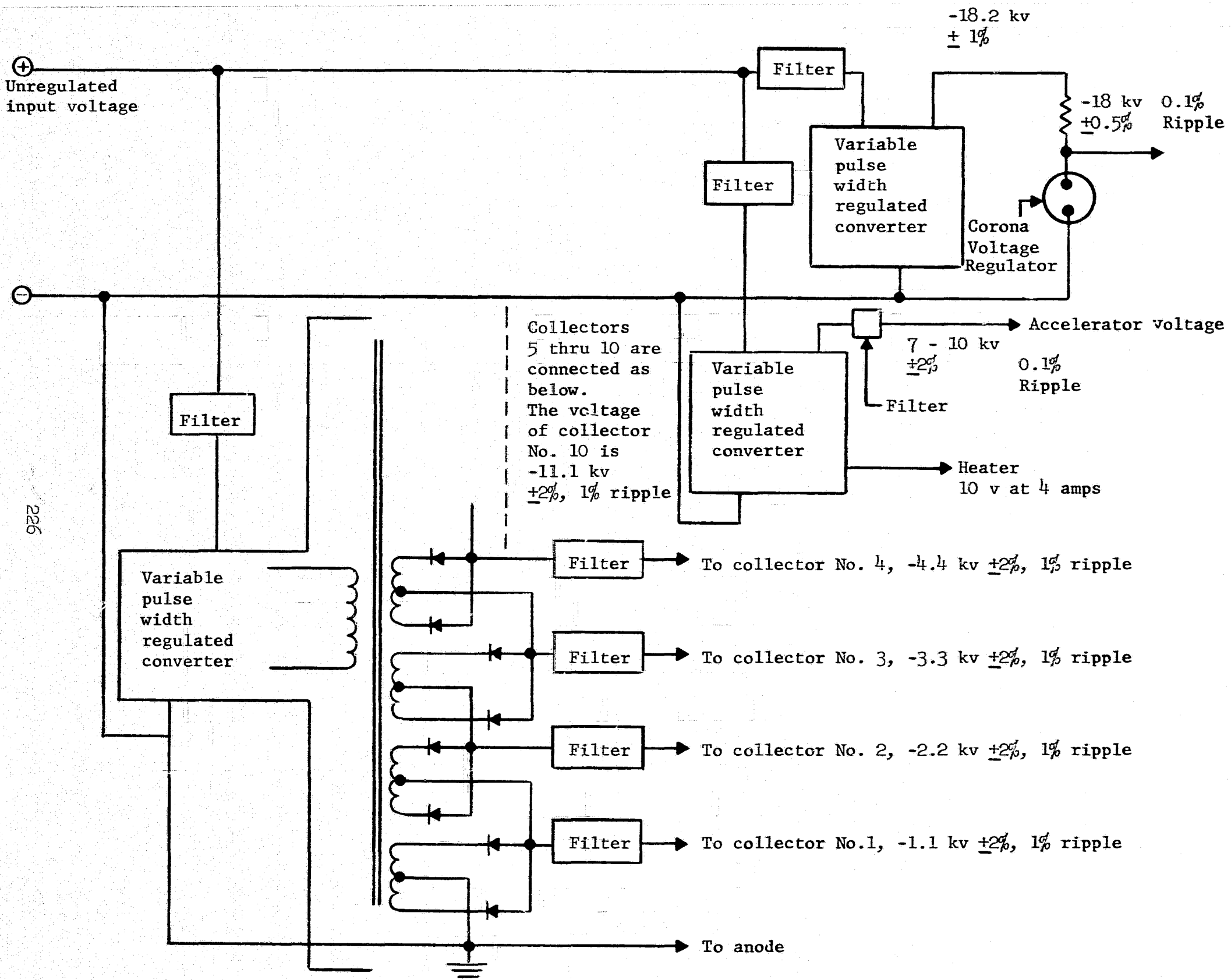

FIGURE 66 POWER SUPPLY FOR CROSSED-FIELD AMPLIFIER TUBE, S-BAND VERSION

supplies versus a single one, weight and thermal penalties of one approach over the other, and the maximum power that can be developed by a single regulator. This latter consideration is dependent on the capabilities of semiconductor switches and transformer cooling methods.

In addition, it is desirable to recover some of the power from electrons that impinge on collector elements that are at negative potential with respect to the cathode. These are electrons that have absorbed energy from the RF field. This power could be recovered if a regulated dc to dc converter were driven by this current. The output of the dc to dc converter would then be applied to the unregulated input bus and thus not lost. Figures 67 and 68 show how this might be accomplished for the case of a collector element operating at 31 kv below cathode potential.

Two points are made here. First, because of the high voltage, low current of the power, vacuum tubes similar to the Amperex neotron would be used for the converter. Second, the feedback signal for the regulator would be derived from the input voltage since we wish to keep the collector voltage constant (collector voltage is the input voltage in this case).

The requirements for the UHF power conditioning system can be met in a similar manner.

The possible arrangements discussed above were suggested by the General Electric, Space Technology Center.

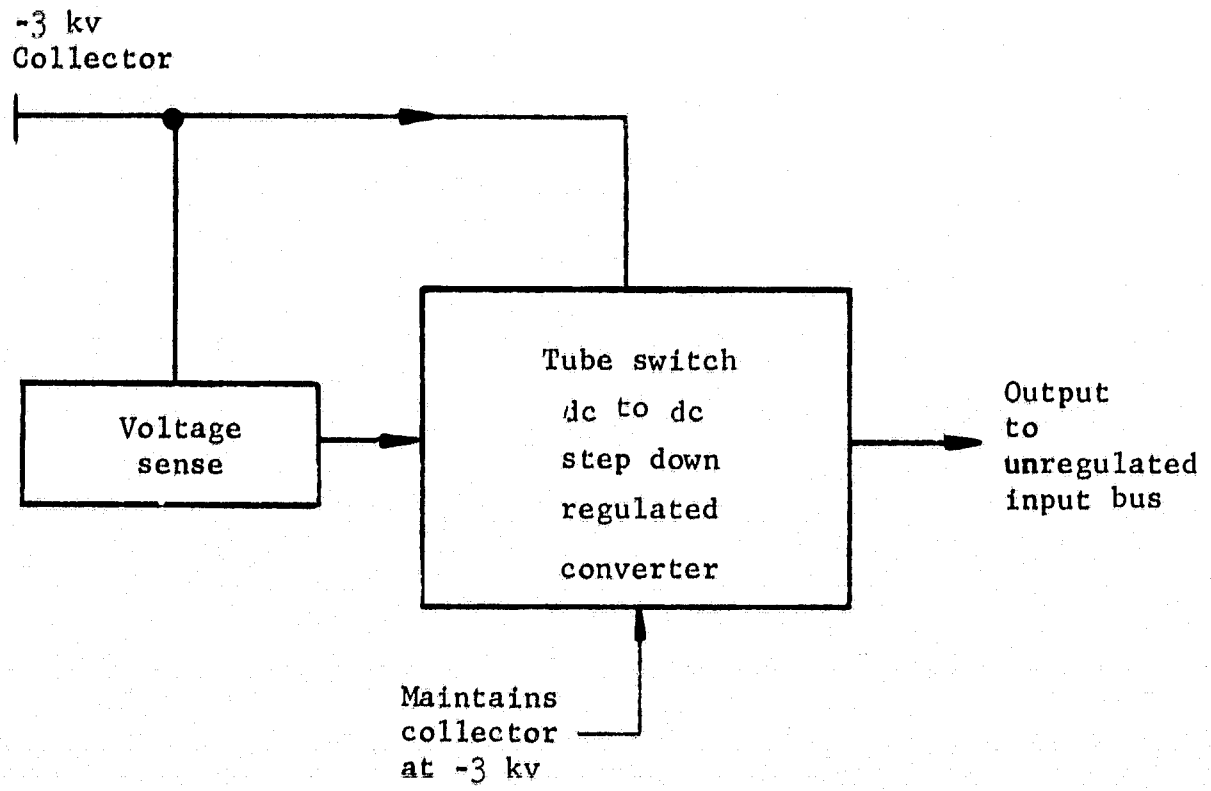

FIGURE 67 METHOD OF RECOVERING POWER FROM **NEGATIVE** COLLECTORS, BLOCK DIAGRAM

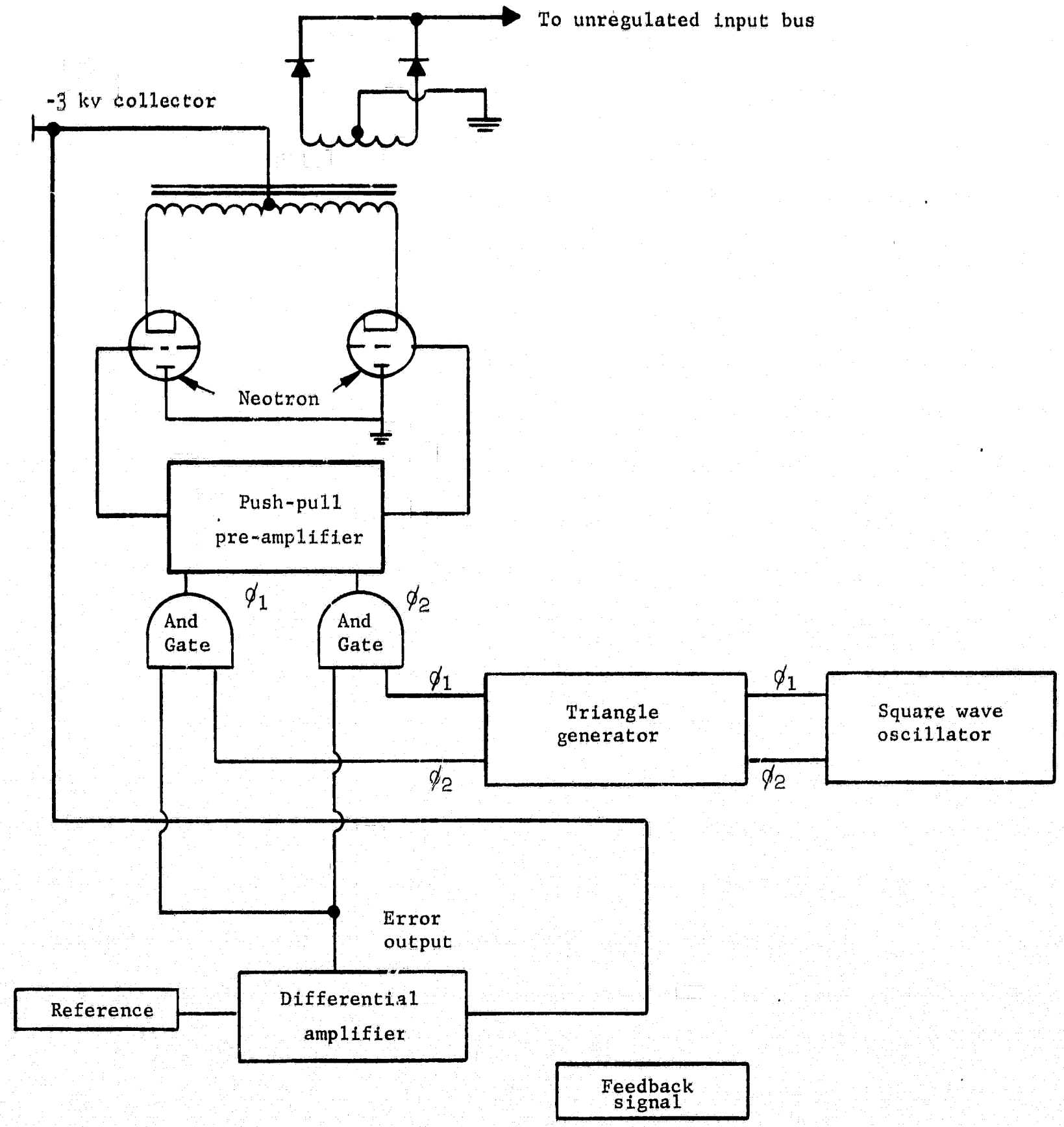

FIGURE 68 METHOD OF RECOVERING POWER FROM NEGATIVE COLLECTORS

9.0 SUMMARY OF DESIGN PARAMETERS AND DIMENSIONS

A summary of the design parameters and major dimensions is given in Tables XXI through XXIV.

Table XXI defines the electrical design parameters while Table XXII summarizes the electrical operating parameters. All voltages are with reference to cathode potential. The external dimensions are given in Table XXIII and the thermal system design appears in Table XXIV.

TABLE XXI

ELECTRICAL DESIGN PARAMETERS

	UHF Design	S-band Design
Frequency	850 MHz	2 GHz
Type of circuit	Helix loaded bar circuit	Helix loaded bar circuit
Magnetic field	1410 gauss	3300 gauss
Phase shift per circuit section	90°	90°
Interaction impedance	200 ohms	100 ohms
Surge impedance	372 ohms	190 ohms
Base period of circuit	0.213"	0.083"
Circuit height	2"	1"
Capacitive bar	2" high by 0.140" wide	1" high by 0.060" wide
Bar capacitance	1.01 pf	0.87 pf
Inductive coil	0.0632 μh (2 turns per circuit section)	0.0134 μh (1 turn per circuit section)
Coil diameter	0.534"	0.354"
Coil wire size	0.053"	0.040"
Circuit attenuation	0.29 db	1.2 db
Number of active circuit sections	52	76
Drift section	3 circuit wavelengths	3 circuit wavelengths
Circuit inside diameter	4.34"	2.33"
Sole outside diameter	3.64"	2.05"
Synchronous voltage	945 v	800 v
Circulating current	1.3 amps	1 amp
Gain per circuit wavelength	2.1 db	1.42 db
Distance from top of beam to delay line	0.202"	0.079"
Cathode diameter	3.9"	2.15"
Cathode length	0.083"	0.115"
Relative velocity slip in beam	0.07	0.05
Magnet material	Alnico-9 (shielded structure)	Alnico-9 (shielded structure)
Number of collector elements	15	10

TABLE XXII

ELECTRICAL OPERATING PARAMETERS

(Voltage referred to cathode potential)

	UHF Design	S-band Design
RF gain	20 db	20 db
RF output power		
saturation power	10 kw	6.6 kw
peak of synchronizing power	7.5 kw	5 kw
average power (for thermal design)	4.25 kw	2.8 kw
average signal power	2.6-3.0 kw	1.75-2.0 kw
Anode voltage	14.2 kv	12 kv
Cathode current	1.3 amps	1.0 amps
Sole voltage	-7 kv	-6 kv
Sole current	none	none
Number of collector elements, N_c	15	10
Collector voltages		
First collector voltage	890 v	1.1 kv
Voltage difference between two adjacent collector elements	890 v	1.1 kv
Nth collector voltage	13.3 kv	11 kv
Negative collectors (total of 3)	-890 v, -1980 v, -2670 v	-1.1 kv, -2.2 kv, -3.3 kv
Accelerator voltage	~10 kv	~9 kv
Accelerator current	none	none
Heater power	40-50 watts	30-40 watts
Estimated conversion efficiency		
Saturated output	84%	80%
Peak of synchronization	80%	77%
Peak picture	75%	68%
Average signal	70%	65%

TABLE XXIII

EXTERNAL DIMENSIONS

	UHF Design	S-band Design
Tube		
Diameter	7.0"	4.0"
Height	3.5"	2.3"
Shielded package with magnets		
Diameter	11"	7.5"
Height	8.0"	9.0"
Weight of packaged tube (Magnets + Shield)	53.4 lb	24.4 lb
Weight of amplifier chain (CFA + Driver + Circulator)	67 lb	34 lb

TABLE XXIV

THERMAL SYSTEM DESIGN

	UHF Design	S-band Design
External heat transfer system	8 heat pipes and aluminum radiator	8 heat pipes and aluminum radiator
Radiator		
Weight (min)	12 lb	14 lb
Area	14.5 sq ft	17 sq ft
Temperature	206°C	160°C
Collector temperature (worst case)	300°C	300°C
Circuit bar temperature	249°C	194°C
Coil temperature	286°C	230°C
Heat transfer ring temperature	224°C	175°C

10.0 CONCLUSIONS

This theoretical study program has developed the design parameters for a UHF and an S-band amplifier suitable for use in a satellite television relay system. The mode of modulation for the television signal was designated as vestigial side band amplitude modulation. A new form of crossed-field amplifier, which was invented at S-F-D laboratories, was used as the basis for evolving the design of the two amplifiers.

A number of new areas have been explored by this investigation. The result is that these crossed-field amplifiers have a combination of advantages not previously present simultaneously in any one crossed-field amplifier type. In addition they will have the capability of maintaining a high level of conversion efficiency over a wide range of RF drive levels. This is particularly significant since the average power level in an amplitude modulated television signal is approximately one-third of the peak synchronizing power level. The two power amplifiers as designed are each capable of 20 db gain. The peak synchronizing power for the 850 MHz amplifier is set at 7.5 kw and the peak synchronizing power for the 2 GHz amplifier is set at 5 kw. These new devices combine the reentrant stream, non-regenerative interaction format of the emitting sole crossed-field amplifier with a technique of space charge control. The system of control results from injection of the beam axially from one side of the interaction space, and collection of the beam at the other end of the interaction space by a multi-element collector. The space charge control leads to a large dynamic range and in addition, a very high efficiency. The conclusions reached based on the new areas that have been explored in this investigation are tabulated below.

10.1 Design Procedures and Trade-Off Calculations

An analytical design procedure for this new form of crossed-field amplifier has been synthesized from existing analyses that have been developed for the conventional injected beam amplifier. The validity of these design procedures has received some partial verification by experimental work carried on through S-F-D laboratories sponsored programs. In addition, a computer simulation model that was completed toward the end of this study program was utilized. Thus some verification of the design parameters was achieved by another mode of computation. The original analytical procedures were used to carry out a series of trade-off calculations. These led to the selection of an appropriate slow wave circuit for the amplifiers, as well as the selection of optimum operating parameters.

10.2 Noise Control and Zero Signal Stability using a Hollow Beam Axial Injection Gun

A hollow beam axial injection gun of the sort employed in some O-type tubes and in the voltage tunable magnetron is used. This results in a system of space charge control that eliminates the high level background noise that is characteristic of emitting sole crossed-field amplifiers. Thus, the available dynamic range of the CFA is greatly extended. The amplifier range then is suitable for an amplitude modulated signal with a designated dynamic range of 20 db. This is accomplished by the use of an electron collector in conjunction with the axial injection principle so that unused space charge is drained from the interaction space. Use of this scheme of injection also avoids the high current density cathodes and fine control grids that are sometimes employed in conventional injected beam CFAs.

10.3 Electron Recirculation

The principle of maintaining electron recirculation, as used in the emitting sole crossed-field amplifier, has been retained. This results in a high level of saturation efficiency, since partially interacted electrons can be reused. The saturation efficiency in both types of amplifiers is in excess of 80%. This, in combination with the maintenance of a high level of efficiency at reduced drive levels makes it possible to operate sufficiently far below the point of saturation of the amplifier, to meet the designated linearity requirements.

10.4 Programmed dc Power Input using Multi-Element Collector

The multi-element collector, as already indicated, serves the purpose of withdrawing unused space charge over a wide range of drive levels so that a low background noise and an adequate dynamic range are maintained. An outstanding capability provided by the multi-element collector is the programming of the dc power input into the amplifier so that the efficiency remains high as the RF drive level is reduced below the value needed to drive the tube into saturation. The principle is one of varying the effective anode voltage in a system of potential energy conversion as the RF drive level is varied. As a consequence, it is possible to make the following estimates. In the case of the UHF amplifier, the saturated efficiency of the amplifier might be 84%, the efficiency at peak of synchronizing power would be down to 80%, and at the average operating power level which is a full 5 db below the peak of synchronizing power, about 69% efficiency is expected. In the case of the S-band amplifier, the efficiency at saturated power output would be 80%, the efficiency at peak synchronizing power is estimated at 77%, and efficiency at peak picture power level would be about 68%. At the average power level, 5 db below peak of synchronizing power about 64% efficiency is estimated. Some of the computer model calculations

indicate efficiency numbers which are even a few percent higher than those quoted. These were indicated in Section 4.5.

10.5 Life Expectancy

The use of an external electron gun with a thermionically emitting cathode similar to that used in the voltage tunable magnetron and some O-type amplifiers has been explored for this program. The economic and technological requirements of the program are such that a life expectancy of two years is required. The thermionically emitting cathode is the only mechanism in electron tube technology that has accumulated the life test history necessary to predict a minimum of 20,000 hours of life. The use of a thermionic cathode eliminates the uncertainties that would be inherent in depending upon secondary emission from a metallic sole such as used in the classical emitting sole crossed-field amplifier. In addition, the generation of the electron stream from a large diameter, ring cathode results in the maintenance of low emission densities of about 200 ma/cm^2. Experience has shown that a low emission density is necessary to assure long life.

10.6 Linearity

The ability to operate below the saturation level of the amplifier with good conversion efficiency leads to the possibility of maintaining a linear mode of operation. Initial results from the computer simulation model indicate that the amplitude linearity requirements of this program can be met. The use of a non-dispersive delay line minimizes departures of phase linearity, and the ability to match these delay lines to the specified VSWR over the narrow frequency band involved minimizes any deviations in phase linearity due to multiple reflections.

10.7 High Impedance, Low Loss Circuit

The use of a high impedance, low loss circuit results in an optimum value of circuit efficiency which is necessary for maintaining the high conversion efficiency required by this program. In addition the selection of a relatively non-dispersive circuit also assures the maintenance of good phase linearity.

10.8 Permanent Magnets

The crossed-field amplifier format permits the use of permanent magnets to achieve the necessary magnetic field in the electron gun and in the interaction space. This eliminates the bulk, weight, and extra power consumption that is associated with the use of solenoids for obtaining a magnetic field. In addition a shield is provided as part of the permanent magnet package so that the magnetic field of the amplifier tubes does not disturb field sensitive elements in the spacecraft environment.

10.9 Low Thermal Impedance Circuit

The selection of a circuit, having a low thermal impedance between the active metallic elements of the circuit and a point of heat sink, results in a design which is compatible with the use of heat pipes and direct radiation into space. The use of the heat pipe radiator technology results in an internal tube temperature that is not much higher than that of the radiator itself. For an efficient radiator design, it is desirable that the operating temperature of the radiator not be much below 200°C. If the temperature rise from the point of heat sink to the tube elements were excessive, a high internal circuit element temperature or collector element temperature would compromise the life expectancy of the amplifier tube. Thus the selection of circuit type has made possible a compatible design of amplifier, heat pipe, and radiator system.

10.10 Multiple Voltages for the Collector System

The multiple voltages required for the collector system results in a more elaborate power conditioning system than would be required in the absence of such a collector structure. However, the presence of this multi-element collector system results in considerable gains in efficiency while utilizing power conditioning techniques that appear to be within the state-of-the-art. Only the voltage supply led between the sole and the anode of the tube must be critically regulated to maintain good conditions of synchronism within the interaction space of the tube. This voltage does not need to supply any current and, therefore, regulation and low ripple requirements are easily achieved.

10.11 Other Areas of Application

The design analyses which have been carried out for this study program were directed toward obtaining an optimum design for the program goal of processing an amplitude modulated signal. It is useful to point out, however, that nothing done in the design procedure is contrary to the optimal design requirements of an amplifier suitable for processing a frequency modulated signal. The bandwidths required to process a frequency modulated signal are inherent in the type of circuit chosen. In addition, the design evolved for the amplitude modulation service has been aimed at achieving the highest possible conversion efficiency at the saturation power level. An examination of the results of this study program therefore indicates that, if the goal had been to achieve an optimum design for a frequency modulation application, then essentially the same design would have resulted. This indicates another area of useful application for the axial injection crossed-field amplifier whose principles have been further explored and developed on this study program.

REFERENCES

1. J. Arnaud and A. O. Doehler, "Study of the Noise in Crossed-field Guns," J. App. Phys., Vol 33, Jan 1962, p 234

2. G. S. Kino, "A Design Method for Crossed-field Electron Guns," IRE Trans on Electron Devices, Vol ED-7, July 1960, pp 179-185

3. J. R. Pierce, TRAVELING WAVE TUBES, D. Van Nostrand and Co., 1950, p 95

4. R. W. Gould, "A Field Analysis of the M-type Backward Wave Oscillator," California Institute of Technology Electron Tube and Microwave Laboratory, Contract Nonr-220(13), Technical Report No. 3,

   Some of the above material is in Chapter 12, of R. Hutter, BEAM AND WAVE ELECTRONICS, D. Van Nostrand and Co., 1960, pp 234-291

5. HIGH POWER TUBE PROGRAM, Semi-Annual Technical Summary Report to the Advanced Research Projects Agency, 30 June 1961, Lincoln Laboratory, MIT, Air Force Contract AF19(604)-7400, pp 33-45

6. G. S. Kino and N. J. Taylor, "The Design and Performance of a Magnetron Injection Gun," IRE Trans on Electron Devices, Vol ED-9, Jan 1962, pp 1-11

7. Deverall, et al, "Orbital Heat Pipe Experiment," Los Alamos Scientific Laboratory Report LA-3714, June 1967

8. D. K. Anand, "Heat Pipe Application to a Gravity-Gradient Satellite (Explorer XXXVI)," Procedings of the ASME Aviation and Space Conference, June 1968

9. T. P. Cotter, "Theory of Heat Pipes," Los Alamos Scientific Laboratory Report, LA-3246-MS, 1965

10. H. R. Kunz, et al, "Vapor-Chamber Fin Studies, Transport Properties and Boiling Characteristics of Wicks," NASA CR-812

11. R. L. Chambers and E. V. Somers, "Radiator Fin Efficiency for One Dimensional Heat Flow in a Circular Fin," ASME Paper No. 59-HT-8, 1959

12. S. Lieblein, "Analysis of Temperature Distribution and Radiant Heat Transfer Along a Rectangular Fin of Constant Thickness," NASA TND-196, 1959

APPENDIX I
TRAVELING WAVE TUBE CHARACTERISTICS
(X1250 and EM1264 TWT's)

1.0 THE X1250 S-BAND, 50 WATT TWT

This S-band TWT, optimized for the 2.2-2.3 GHz space-ground telemetry band, was designed and built for JPL. It represents a second generation TWT for deep space missions. These include Voyager and Advanced Mariner spacecraft. Present units, qualified for space applications, are designed at the 20 watt level.

At 30% + overall efficiency (without optional output filtering) and 7.5 pounds, it exceeds the performance and form factor available in any other similar unit. It employs a welded, hermetically-sealed enclosure similar in concept to the other Eimac space qualified TWT's. This enclosure is responsible for a good portion of the form factor improvement. The basic design includes six outputs which can be used to remotely diagnose TWT performance.

The unit operates without degradation for input line voltages between 25 volts dc and 50 volts dc, temperatures of -10°C to +75°C, and standard NASA and Military shock and vibration environments associated with the ascent of present launch vehicles.

The requirements on life expectancy and reliability have not yet been assessed, although individual TWT's have been operated for periods up to 1000 hours.

The accompanying data are representative of that now available.

1.1 Engineering Model Data - X1250

TWT 118 without bandpass filter

Input voltage	30 volts
Input current	5.90 amps
Input power	177 watts
RF output power	17.25 = 53 watts
RF input power	-12.5 dbw = 0.563 watts
RF gain	29.75 db
Efficiency	30%

Parameter	Telemetry Voltage	Parameter Level
Helix current	14.20 volts	29.5 ma
Cathode current	7.382 volts	100 ma
Helix voltage	-4.007 volts	2029 volts
Collector voltage	-2.995 volts	1283 volts
Anode voltage	4.728 volts	2176 volts
Heater voltage	7.027 volts	13.2 volts

1.2 Power Budget - X1250

TWT beam power	150 watts
TWT heater power	4 watts
Total TWT power	154 watts
Power supply losses (at 88%)	21 watts
Typical TWT power	175 watts
Typical RF output power	56 watts
Typical efficiency	32.0%

1.3 Mechanical Configuration - X1250

Length	11-1/2 inches
Width	5-3/8 inches
Height	2-7/8 inches
Weight	7.8 pounds
RF connectors	TNC
dc connectors	Deutsch type 22650
Life, design	20,000 hours
MTBF, 3-year mission	50,000 hours

1.4 Design Requirements - X1250

Electrical

Input power (dc)	185 volts
Input voltage range	25-50 volts
Frequency range	2.29-2.30 GHz
RF output (fundamental)	50 watts
RF gain (saturation)	30 db
Harmonic level	-60 db
Input VSWR (operating)	1.2:1
Load VSWR (no damage)	5:1
Load VSWR (full operation)	1.3:1

Noise figure	35 db
Monitor points	Anode voltage Collector voltage Cathode voltage Collector temperature Helix current Collector current

Environmental

Operating pressure	Sea level to 10^{-6} mmHg
Operating temperature	$-10^{\circ}C$ to $+75^{\circ}C$
Shock	200 g 1'msec
Vibration	15 g rms (random)
Acceleration	14 g

2.0 THE EM1264 TWT

This TWT, optimized for the 2.2-2.3 GHz telemetry band, is a half-power version of the X1250 at the same nominal 30% overall efficiency. It is now in development. Being a 20 watt unit in a 50 watt frame, this unit represents a very conservative electrical and thermal design. Yet because of the advanced packaging concept used in the basic 50 watt TWT package and power supply, the 20 watt package is superior in form factor to other units now available.

All environmental ratings of the 20 watt unit are equal to that of the 50 watt unit. Life and reliability of the 20 watt unit, because of its 2:1 derating in power level will be appreciably enhanced.

As in the 50 watt TWT, special RF components, dc logic for system accessories, and configurations to further optimize the transmitter form factor can be provided. In all cases, components added are procured to appropriate high reliability specifications in the same manner as the basic tube and power supply parts.

2.1 Power Budget - EM1264

TWT beam power	56 watts
TWT heater power	4 watts
Total TWT power	60 watts
Power supply losses (at 80%)	8 watts
Typical TWT power	68 watts
Typical RF output power	22 watts
Typical efficiency	32.4%

2.2 Design Requirements - EM1264

Electrical

Input power (dc)	72 volts
Input voltage range	25-50 volts
Frequency range	2.29-2.30 GHz
RF output (fundamental)	22 watts
RF gain (saturation)	35 db
Harmonic level	-60 db
Input VSWR (operating)	1.2:1
Load VSWR (no damage)	5:1
Load VSWR (full operation)	1.3:1
Noise figure	35 db
Monitor points	Anode voltage Collector voltage Cathode voltage Collector temperature Helix current Collector current

Environmental

Operating pressure	Sea level to 10^{-6} mmHg
Operating temperature	-10^{o}C to $+75^{o}$C
Shock	200 g 1 msec
Vibration	15 g rms (random)
Acceleration	14 g

APPENDIX II

VELOCITY VARIATION IN CROSSED-FIELD HOLLOW ELECTRON BEAM

The electron gun design equations indicated in Section 4.2 can be used to calculate electron velocities. The variation of these velocities as a function of position, gun angle, and cathode current loading provides an insight into optimizing the gun design.

Recalling that

$$Z - Z_o = \frac{T^3}{6} \sin\theta \cos\theta \qquad (2\text{-}1)$$

then

$$\frac{dZ}{dt} = \omega\frac{T^2}{2} \sin\theta \cos\theta \left[\frac{Z}{\frac{T^3}{6}\sin\theta\cos\theta}\right]^{\frac{1}{3}}$$

or

$$\frac{dZ}{dt} = \frac{(6)^{\frac{2}{3}}}{2} \omega \sin^{\frac{1}{3}}\theta \cos^{\frac{1}{3}}\theta (Z)^{\frac{2}{3}} \qquad (2\text{-}2)$$

for the top of the beam, and

$$\frac{d(Z - Z_o)}{dt} = \frac{(6)^{\frac{2}{3}}}{2} \omega \sin^{\frac{1}{3}}\theta \cos^{\frac{1}{3}}\theta (Z - Z_o)^{\frac{2}{3}} \qquad (2\text{-}3)$$

for the bottom of the beam, where Z_o is the normalized cathode length. Since

$$z = \frac{\frac{e}{m} J_o}{\epsilon_o \omega^3} \gamma \qquad (2\text{-}4)$$

then

$$\frac{dz}{dt} = \frac{\frac{e}{m} J_o}{\epsilon_o \omega^3} \frac{dZ}{dt} = v_z$$

But

$$V_z = \frac{m}{2e} v_z^2$$

where V_z is the velocity expressed in electron volts of energy. Then

$$\Delta V_z = V_{z_{top}} - V_{z_{bott}} = \frac{m}{2e} (v^2_{z_{top}} - v^2_{z_{bott}}) \qquad (2\text{-}5)$$

or

$$\Delta V_z = \left(\frac{m}{2e} \frac{\frac{e}{m} J_o}{\epsilon_o \omega^3}\right)^2 \left\{ \left(\frac{dZ}{dt}\right)^2 - \left[\frac{d(Z - Z_o)}{dt}\right]^2 \right\}$$

$$\Delta V_z = \frac{e}{2m} \left(\frac{J_o}{\epsilon_o \omega^3}\right)^2 \left(\frac{m \epsilon_o \omega^3}{e J_o}\right)^{\frac{4}{3}} \frac{(6)^{\frac{4}{3}}}{4} \omega^2 \sin^{\frac{2}{3}} \theta \cos^{\frac{2}{3}} \theta (z_o)^{\frac{4}{3}} \left[\left(\frac{Z}{Z_o}\right)^{\frac{4}{3}} - \left(\frac{Z}{Z_o} - 1\right)^{\frac{4}{3}}\right] \qquad (2\text{-}6)$$

Let

$$F\left(\frac{Z}{Z_o}\right) = \left[\left(\frac{Z}{Z_o}\right)^{\frac{4}{3}} - \left(\frac{Z}{Z_o} - 1\right)^{\frac{4}{3}}\right] \qquad (2\text{-}7)$$

then

$$\Delta V_z = \frac{(6)^{\frac{4}{3}}}{8} \frac{\omega^2}{\left(\frac{e}{m}\right)^{\frac{1}{3}} \omega^2 \epsilon_o^{\frac{2}{3}}} (J_o \sin\theta \cos\theta)^{\frac{2}{3}} z_o^{\frac{4}{3}} F\left(\frac{Z}{Z_o}\right) \qquad (2\text{-}8)$$

Substituting constants in mks units

$$\Delta V_z = (5.7 \times 10^3) (J_o \sin\theta \cos\theta)^{\frac{2}{3}} z_o^{\frac{4}{3}} F\left(\frac{Z}{Z_o}\right) \qquad (2\text{-}9)$$

Let

$$\pi D Z_o J_o = I \qquad (2\text{-}10)$$

where D = cathode diameter

I = cathode current

$$\Delta V_z = 5.7 \times 10^3 \left(\frac{I}{\pi D}\right)^{\frac{4}{3}} \left(\frac{\sin\theta \cos\theta}{J_o}\right)^{\frac{2}{3}} F\left(\frac{Z}{Z_o}\right) \qquad (2\text{-}11)$$

Similarly, it can be shown that

$$V_{z_{top}} = 5.7 \times 10^3 \left(\frac{I}{\pi D}\right)^{\frac{4}{3}} \left(\frac{\sin\theta \cos\theta}{J_o}\right)^{\frac{2}{3}} \left(\frac{Z}{Z_o}\right)^{\frac{4}{3}} \qquad (2\text{-}12)$$

$$V_{z_{bott}} = 5.7 \times 10^3 \left(\frac{I}{\pi D}\right)^{\frac{4}{3}} \left(\frac{\sin\theta \cos\theta}{J_o}\right)^{\frac{2}{3}} \left(\frac{Z}{Z_o} - 1\right)^{\frac{4}{3}} \qquad (2\text{-}13)$$

Thus for set values of the ratio of sin θ/J_o, the difference in axial velocity for the top and bottom is determined as a function of the normalized axial displacement from the cathode.

LIST OF SYMBOLS

A = surface area

A = amplifier constant used in gain calculations

a = normalizing parameter used in electron gun calculations

a_n = current weighting factor

B = magnetic field

B = constant determined by amplifier parameters (used in gain calculations)

b = gain in nepers per wavelength

b = capillary geometry constant

C = capacitance of circuit bar to ground

c = speed of light

D = gain parameter

$\overline{D}$ = mean diameter

d = wire diameter

E = RF field strength

e = void fraction of wick

E_o = amplitude of fundamental space harmonic

E_{RF} = RF energy converted

e/m = charge to mass ratio

f = frequency, MHz

f_c = cyclotron frequency, MHz

G = amplifier gain

h = axial height of circuit bar

i = instantaneous current amplitude

I_C = capacitive or shunt current

I_c = circulating beam current

I_L = amplitude of series current

J_o = current density at cathode

K = interaction impedance

K = thermal conductivity

k = relative velocity slip in electron beam

k = factor to account for cycloiding beam

L = length

$\overline{L}$ = mean perimeter of helix turn

M = geometric factor for calculating space harmonic component of RF electric field

m = number of turns per circuit section

m_v = mass flow

N = number of wavelengths on circuit

n = number of active circuit sections

N_c = total number of collector elements

N_n = number of collector elements below cathode potential

N_p = number of collector elements above cathode potential

P = power flowing on slow wave circuit

p = pitch of circuit

P_c = energy loss due to conduction

P_d = power dissipated

P_{dc} = dc power input

P_i = RF power input

P_o = power output

P_r = energy loss due to radiation

P_{RL} = power summation of all charge rods in interaction space at end of run

P_{RR} = power summation of reentering rods

Q = parameter used in calculation of velocity slip

Q = rate of heat flow

q = net heat radiated

r = axial resistance

R_r = radial Reynolds number

R_s = effective series resistance

R_{s_1} = series resistance per unit length in the inductive coil

R_{s_2} = loss due to series current flowing across the height of the copper bars

R_{s_3} = loss due to shunt or capacitive charging current

R_{s_4} = effective series resistance representing dielectric losses in the BeO slab

R_T = total resistance

r_1 = radius of radiating surface

r_2 = radius of absorbing surface

r_w = outer radius of the wick

S = diocotron gain parameter

S = solar constant

s = spacing between adjacent helix turns

T = surface temperature

T = normalized transit time (used in electron gun design)

t = time

T_r = radiator temperature

T_s = equivalent sink temperature

T_s' = new equivalent sink temperature

T_1 = absolute temperature of radiating surface

T_2 = absolute temperature of absorbing surface

u_o = dc component of drift velocity corresponding to V_o

u_θ = instantaneous velocity amplitude in circumferential direction

u_r = instantaneous velocity amplitude in radial direction

V = voltage

v = velocity

V_a = anode potential with respect to cathode

V_o = synchronous voltage

V_r = lowest negative potential below cathode potential at which current collection will occur

v_g = group velocity of circuit wave

v_p = phase velocity of circuit wave

W = energy stored per unit length of circuit

w = width of circuit element

y = distance from outer surface of beam to anode

z = distance along delay line measured from input

Z_o = characteristic impedance

α = insertion loss

α = solar absorptivity

α_{tot} = total circuit insertion loss

β = propagation constant

γ = surface tension

ΔT = temperature differential

δ = secondary emission coefficient

ϵ = dielectric constant

ϵ = surface emissivity

ϵ_o = dielectric constant of free space

ϵ_1 = emissivity of radiating surface

ϵ_2 = emissivity of absorbing surface

η = conversion efficiency

η_c = circuit efficiency

η_e = electronic efficiency

η_ℓ = viscosity of liquid

η_v = viscosity of vapor

θ = phase shift per section, degrees

θ = contact angle between fluid and wick, degrees

λ = latent heat of vaporization

ρ = unit volumetric resistivity of metal

ρ_ℓ = density of liquid

ρ_v = density of vapor

σ = Stefan-Boltzmann constant

ϕ = phase shift per section, radians

ψ = angle between rays of sun and normal to surface

ω = radian signal frequency

ω_c = radian cyclotron frequency